6-17-2019

Investigating color additive molecules for pharmaceutical and cosmetic applications: A comparison of theoretical and experimental UV-visible absorbance spectra in tunable solvents

Jacqueline Casey Mohen
Rowan University

INVESTIGATING COLOR ADDITIVE MOLECULES FOR PHARMACEUTICAL AND COSMETIC APPLICATIONS: A COMPARISON OF THEORETICAL AND EXPERIMENTAL UV-VISIBLE ABSORBANCE SPECTRA IN TUNABLE SOLVENTS

by

Jacqueline C. Mohen

A Thesis

Submitted to the
Department of Chemistry & Biochemistry
College of Science and Mathematics
In partial fulfillment of the requirement
For the degree of
Master of Science in Pharmaceutical Sciences
at
Rowan University
May 9, 2019

Thesis Chair: Timothy D. Vaden, Ph.D.

Dedications

To Christine and Timothy,

for having faith in me against all odds, and the divine patience to wait for

a phenomenal outcome.

Acknowledgment

Special thanks to Nathalie Nicole Malinao, who went above and beyond to help me save this manuscript file from being compromised by an aggressive hacking attempt.

Abstract

Jacqueline C. Mohen
INVESTIGATING COLOR ADDITIVE MOLECULES FOR PHARMACEUTICAL AND COSMETIC APPLICATIONS:
A COMPARISON OF THEORETICAL AND EXPERIMENTAL UV-VISIBLE ABSORBANCE SPECTRA IN TUNABLE SOLVENTS
2018-2019
Timothy D. Vaden
Master of Science in Pharmaceutical Sciences

Color additive molecules have widespread applications ranging from ingestible foods and pharmaceutics to non-ingestible cosmetics and other naturally or synthetically-developed consumer products available worldwide. Certification for approved use of color additives varies globally; therefore, a feasible method to analyze existing color additives or to design novel color additive molecules with enhanced or otherwise desired physicochemical properties (such as hue) is in high demand for universal adoption. The studies herein provide sufficient proof that density functional theory and time-dependent density functional theory serve as effective predictive modeling techniques for generating theoretical maximum absorbance spectral peak responsivity for a single color additive molecule structure in the virtual workspace, as well as for multiple (heterodimeric and heterotrimeric) structures represented simultaneously. Furthermore, DFT and TD-DFT can be used to analyze changes in hue attributed to structural anomalies in molecules due to tautomerism, vibronic effects, intra- or intermolecular interactions, implicit or explicit solvation effects, or charge transfer effects on the structure represented in a given solvent or in vapor phase. Advancements in computational processing make incorporation of these and similar advanced *ab initio* quantum chemical methods more tangible for the modern pharmaceutical or cosmetic formulator to use in perfecting batch hue.

Table of Contents

List of Figures

List of Tables

Table Page

Introduction

The sensation of color has enchanted human beings ever since the earliest use of mineral pigments red ochre and charcoal in limestone cave paintings during the Paleolithic era to warn of predatory animals near human habitats [1]. Color is a physical stimulus [2], and is the result of the physical modification of light by chemical entities called chromophores [3] that exist within color molecules. Chromophores modify absorption and reflection of light that is detected by the human eye through a visual response process [2] or, more specifically, a signal transduction mechanism [4-7], which is interpreted in the brain, where it undergoes a perceptual process [2], which is more psychological in nature. Use of colorful molecules expanded from being advisory to decorative over 5,000 years ago in the Middle East with a twofold intention [8]: first, to serve functionally as a barrier in order to protect humans from the damages of a very arid, sun-drenched climate; and second, as a decorative method of enhancing the physical appearance to be more attractive to other human beings. The first intention gives way to the use of color in pharmaceutical formulations. Formulations by their very nature are defined as mixtures [9] of chemical substances designed to serve an intended purpose. A formulation is categorized as “pharmaceutical” if it contains active pharmaceutical ingredients (APIs) that may penetrate the epidermal layer to enter the bloodstream, functioning as drugs. Drugs alter the natural functioning of the machinery of cells within the human body or pathogen with the intention of repairing an imbalance that is causing disease [10]. Specifically, pharmaceutical chemistry pertains to the components within the molecular structure of a drug that cause it to affect cells in a particular way [10]. On the other hand, cosmetic formulations serve only to decorate, cover, conceal, or

temporarily change the visual appearance of the site of application but are not meant to affect the body's chemistry [11]. The concepts of color molecules and their interaction with other molecules found in formulations of either type are fundamental for humans to effectively distinguish among the wide variety of formulation products. Patients self-administering pharmaceutical or cosmetic formulation products do so on a regular basis. Color serves as an effective indicator, and helps maintain patient or client compliance when required to follow a recommended dosage regimen [12]. In today's more globalized manufacturing economy, the growing number of color molecules certified for use in specific regions also find their way into medical supplies, contact lenses, and wearable articles that touch the skin and hair [13]. Thus, there is significant overlap of certified color molecule applications. For these reasons, it is essential to understand the interaction of color molecules used in solvents applied in the formulation of both pharmaceutical and cosmetic products.

Cosmetic formulations have been essential to human civilization since our early history. The first cosmetic products were used in the Mesopotamian era to ward off against evil spirits entering the body through the nine vulnerable openings [14]. Later on, the ancient Egyptians extolled them for divination purposes and refined them, expanding most notably into development of ophthalmic products [14]. Their early "make-up" products consisted of mineral substances found beneath the earth's surface. These original "natural" products varied in value and toxicity to include cadmium for red hues (today a known inhibitor of calcium(II) ion absorption by bones [15, 16]), lapis lazuli, a mineral with a striking intense blue hue similar to ultramarine that is sold for nearly $100 per carat on today's market [17], and black "kohl" used in eyeliner that has historically

contained galena, consisting of lead (II) sulfide (PbS) and derivatives of other hazardous materials [14]. Considering the varied risk factors that ancient humans encountered upon using early colorful cosmetic and pharmaceutical formulations, it is no surprise that decorating oneself with chemical products of questionable origin and safety in order to better attract the opposite sex became denounced in the fourteenth century as "vanity" in Western religions [18]. This negative connotation lasted well into the early 20th century, as even foodstuffs containing (mostly yellow) color additive enhancers in order to approve their appearance and to prolong shelf-life were known to have toxic or deadly side effects upon human consumption [19, 20, 21]. In 1933, a woman known in court records as Ms. Brown had consented to have her eyelashes permanently dyed with *para*-phenylenediamene as a dyeing agent in an original "coal-tar" mascara product called Lash Lure [22]. This procedure resulted in Ms. Brown going blind—she had experienced severe symptoms of stinging and burning eyes, and by the following morning, her eyes had developed oozing ulcers, and then had swollen shut [22]. Fifteen similarly gruesome accounts of blindness and the death of a sixteenth user of Lash Lure prompted Congress to grant authority to the Food and Drug Administration to regulate cosmetic formulation products. As a result, the United States government introduced the Food, Drug, and Cosmetics Act of 1938 to begin to remedy the issues pertaining to all color molecules designated for use in food, pharmaceuticals, medical supplies, and any decorative or functional products applied topically to human skin, particularly cosmetics [20, 21]. All types of color molecules are tested for physical characteristics. Examples of qualities tested include their hue, chroma, saturation, fluorescence, colorfastness, lightfastness, and other desired properties when applied to, or used in conjunction with, various products.

Specific tests have been designed to help maintain color constancy, to prevent metamerism, and as a result, produce effective spectral matches [2, 4]. As experimental equipment has improved with the advancement of technology—and the expansion of health concerns harbored by manufacturers, retailers, and consumers has increased similarly—analytical testing now includes verification of health risk factors such as carcinogenicity since the 1970s and later mutagenicity (the ability of molecules to cause mutations of cells at the site of application) and teratogenicity (toxicity to the fetus) [21]. Today, bacterial assays are also performed on batches of finished cosmetic products to ensure they may successfully counter inoculation by microorganisms after repeated use [23] prior to commercial distribution. Because of the strong prevalence of colorful products for decorative (or edible) human use, diligent study of the interaction of novel or existing color additive molecules with any other molecules known to come in contact with color additives during the pharmaceutical or cosmetic formulation process is of pertinent interest to all scientists wishing to meet a higher standard of consumer product safety when utilizing colorful products regularly.

The definition of color molecules has evolved depending on their specific use. Color molecules are divided into two groups based on the method in which they add color to a given material. A “colorant” is a dye or a pigment molecule that is used in the process of coloring materials [2] but is not intended for human decoration or consumption. Alternatively, “color additive” molecule is a dye or pigment molecule that has been designed with the intent of coloring a product for human decoration or edible consumption [24]. Colorants and color additives are further classified based on their solubility properties. A dye is a water-soluble compound that exhibits its coloring ability

when dissolved in a solvent. Dyes appear colorful by selectively absorbing specific wavelengths of light and allow the remaining balance of wavelengths to be transmitted [21, 25]. A pigment is a color molecule that is not soluble in water, adding color by dispersion. Pigments function by selectively absorbing some wavelengths of light and reflecting others; this change in the proportion of wavelengths is perceived as color [25]. Generally, pigments serve to obscure the surface underneath, covering it to appear noticeably different. Insoluble pigments were originally available only as naturally-occurring inorganic compounds such as titanium dioxide, iron oxides, and ultramarine [23, 25]. Fifty years ago, the concept of synthetic insoluble color molecules called “lake pigments” was developed. These are manufactured by precipitating and adsorbing water-soluble dyes onto an insoluble substrate, usually alumina hydrate [23]. This chemical adhesion of the dye material onto the surface of the substrate renders the color molecule insoluble. The insolubility in this case prevents the coloring material from migrating, hence avoiding the most common problem associated with dyes in tablet-coating applications [25]. Note that particle size is particularly important with lake pigments as such materials produce color by the reflection of light from their surface area. The larger the surface area (thus the smaller the particle size), the more color is perceived [21]. As a result, dye and pigment molecules must be diligently selected to be effective for coloring their intended end use or application site.

The ability to distinguish among colors within the visible spectrum of light (400 nm to 800 nm) is a purely human phenomenon. Our species is able to distinguish among colors due to the mechanism of signal transduction of variable wavelengths of light, which in turn is unique among individuals. Light passes through the cornea, the

transparent outer layer of the eye and is refracted into the eyes' optical system through the lens [4]. Refractive errors are attributed to variations in the shape of the cornea pertaining to the shape and location of the retina. Myopia ("nearsightedness"), hyperopia ("farsightedness"), and astigmatism are attributed to such changes. Over one's lifetime, the lens absorbs and scatters short-wavelength (blue & violet) energy [4]; therefore, the lens becomes increasingly more yellow with age. As a result, we view the world through a yellow-tinted filter that becomes increasingly more yellow at a rate that varies among individual people. The effect is particularly evident during metameric color matching in which purple or blue objects are compared among color analysts. Generally, an older lens absorbs most of the blue energy reflected from a purple object but does not affect any of the red energy reflected from a purple object [4]. As a result, older observers will tend to report that the object is significantly more "red" than as reported by a younger observer with a lens that has been exposed to fewer short-wavelength (blue) light. For this reason, professionals evaluating color on a regular basis are required to have their sight analyzed using the Munsell color test [2, 4, 5] in order to indicate their ability to classify colors and to indicate potential issues with their perception of hue, chroma, and saturation. While many humans are able to observe a similar hue when viewing a given object, it is worth investigating a method to overcome the discrepancies of the "human element" of vision that emerge after non-quantifiable exposure to environmentally-induced light during one's lifetime, particularly among people of significant age difference.

In order to understand how an alternative method of discerning color might work, it is important to understand the basics of how human eyesight functions to depict imagery. The optical image formed by the eye is projected onto the retina, which is a thin

layer of cells (approximately the thickness of tissue paper) located at the back of the eye and incorporates the photosensitive cells called neurons, considered as part of the central nervous system (CNS) and initial signal processing and transmission "circuitry" [4]. The photoreceptors, mainly rods and cones, contribute to the signal transduction mechanism in which the information present in the optical image is converted into chemical and electrical signals that may be transmitted to the later stages of the visual system. These signals are then processed by an extended network of cells and transmitted to the brain via the optic nerve. A schematic diagram of the human eye optical signal processing mechanism is shown in Figure 1 below.

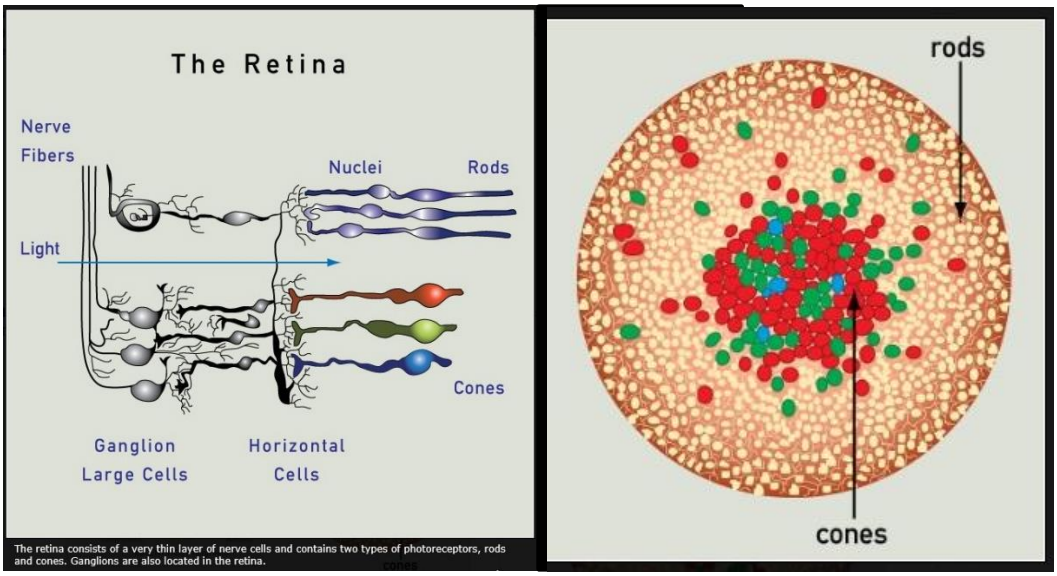

Fig. 1. [6] Generalized photoreceptor signal processing mechanism of the human eye (left) and distribution of rod and cone photoreceptors throughout the retina (right).

One noteworthy distinctive quality of human vision compared to that of nocturnal animals is the pigmented epithelium, the layer behind the retina. This is a dark, pigmented layer that absorbs any light that happens to pass through the retina without being absorbed by either rod or cone receptors. The pigmented epithelium serves to prevent light from being scattered back through the retina, thus reducing the sharpness and contrast of the perceived image. Humans with a pigmented epithelium as a result have improved image quality and sharpness whereas nocturnal animals without a pigmented epithelium have a highly-reflective "tapetum" that reflects light back to its source in order to provide a second chance for photoreceptors to absorb the energy [4]. The term "deer in headlights" arises from this light-reflecting sensation, and applies to other animal species with a "tapetum" that enables them to maneuver in dimly-lit environments at the expense of lower-quality visual imagery [4]. These distinct components of the eye contributing to human vision as described above enable us to view color at the seemingly instantaneous moment of light signal transduction.

Human color vision relies on systematic responses that are instantaneous at the moment of light-induced stimulation. Therefore, in order for an alternative method to provide useful data, these components must be isolated to focus on the parts of the eye most essential to vision: photoreceptors. It is important to understand the role of photoreceptors as transmitters of incident light in order for scientists to build effective theories for modeling human color vision. Photoreceptors are categorized based on the types of incident light wavelengths absorbed and later transduced for neural response. Two types of photoreceptors contribute to visual signal processing: rods, which contain the photopigment rhodopsin ("rhod"-opsin) consisting of both retinal and opsin, and

cones, which contain only opsin. Rods and cones contain photopigments with distinct protein structures that corresponding to the varied spectral responsivities observed in the cones. Rods tend to be long and slender while peripheral cones are conical in shape [4, 7, 26]. Cones exist in high density in the fovea, while rods exist in the area surrounding the fovea. The most important distinction between rods and cones is their visual function. Rods enable humans to see in dimly-lit conditions at shallow distances and at low luminance levels of less than 1 cd/m^2; cones enable human vision of higher luminance levels at greater than 100 cd/m^2, such as in brightly-lit, colorful environments and at vast distances [4]. At high luminance levels, only the cones function because the rods are effectively saturated. At intermediate luminance levels, both rods and cones function simultaneously and contribute to vision. At low luminance levels, only rods are active. The transition from rod to cone vision is one mechanism that enables our visual perception to successfully function over a large range of luminance levels. This is a unique characteristic of human vision compared to other living things. Vision relying on rod photoreceptors only is called scotopic vision; vision enabled by active cone receptors only is known as photopic vision [4, 26]. Mesotopic vision refers to vision when both rods and cones are active at intermediate luminance levels [4]. Each type of "cone" absorbing short (blue, β, or "S"), middle (green, γ, or "M"), or long (red, ρ, or "L") wavelengths of light contains a different form of opsin to absorb its corresponding wavelength. Each of the three cones has a distinct peak spectral responsivity, and all three are spread throughout the visible spectrum. Cones that absorb blue or short wavelengths (S-cone receptors) have a peak spectral responsivity at 420.3 ± 4.7 nm [5]. Cones that absorb green or middle-wavelengths (M-cone receptors) have a peak spectral responsivity

at 533.8 ± 3.7 nm [5]. Cones that absorb red or long-wavelength (L-cone receptors) have a peak spectral responsivity at 562.8 ± 4.7 nm [5]. Since there is only one type of rod receptor, rods have a peak responsivity of approximately 510 nm [4]. A third type of photoreceptor, containing the photopigment melanopsin, is beginning to be investigated as an intrinsically-activated photosensitive retinal ganglion cell (ipRGC) [4]. This means that rather than simply transmitting the signals produced from the rod and cone photoreceptor signal transmission, these ipRGCs transmit photosignals produced intrinsically, with peak spectral responses at approximately 480 nm, falling between S-cone peak signal response and rod signal response, with a width similar to the V(λ) function [4]. Thus, ipRGCs represent a third class of photoreceptors in the retina and will lead to interesting avenues for exploration as to their effect on human perception of color. By relating the signal transduction mechanism of human vision to sophisticated neural circuitry, it is understandable that advancement of computational processing power has rendered the modeling of human perception of color appearance more feasible. Note that the specific processing of visual stimulation by incident light resulting in signal transmission from the retina to the higher levels of the brain by the ganglion cells are not simple "point-wise" representations of the receptor signals. Each synapse between neural cells can effectively perform a basic mathematical operation (addition, subtraction, multiplication, or division) in addition to the amplification, "gain control", and nonlinearities that occur within the neural cells [4]. Therefore, the complexity of the human retinal signal processing can essentially serve as a sophisticated image computer. Information from 130 million photoreceptors can be reduced to signals in approximately one million ganglion cells without loss of visually meaningful data [4]. As a result,

computational chemistry serves as an effective method to explore the human perception of color.

Two spectral luminance efficiency functions developed by the Commission Internationale de l'Eclairage (CIE) indicate the overall sensitivity of rod and cone photoreceptors to different wavelengths of light with respect to the perceived brightness of various wavelengths. The function V'(λ) indicates the spectral responsivity of the rod receptor, depending largely on the spectral absorption of rhodopsin, its characteristic photosensitive pigment. The V(λ) function represents not a single cone type, rather, the collective spectral overlap of responsivity of all three cone receptors with their differing opsin photosensitive pigments. The graphical representation of both functions and corresponding S-, M-, L cone sensitivity ranges provide a visual representation indicating shifting of rod to cone photoreceptor function at low, intermediate, or high luminance levels. These functions explain human color vision when compared to the modern opponent colors theory developed by Vos and Walraven [27, 28], also known as "stage theory" in its division of signal transmission as distinct "stages". However, the V(λ) and V'(λ) functions have existed long before the modern color theories existed, and served to guide early color theorists as an experimental guide for devising theoretical mathematical models to quantify photoreceptor response to maximum absorbance spectra data.

Since the late 19th century, theoretical chemists have attempted to formulate mathematical relationships to explain the signal transduction mechanism that allows humans to perceive color. The first color theory to emerge was hypothesized by Maxwell, Young, and Helmholtz (1891, 1896) called "trichromatic theory", in which S-, M-, and L-cone receptors were distinctly separate, independent response mechanisms with a

characteristic response function [4], and each cone transmitted signals directly to the brain according to a "line element" known as the Riemannian Space [5]. The spectral response functions of the cones L, M, and S cones as $r(\lambda)$, $g(\lambda)$, and $b(\lambda)$ are represented as linear combinations of the three empirically determined color-matching functions $x(\lambda)$, $y(\lambda)$, $z(\lambda)$ developed by the Commission Internationale de l'Eclairage (CIE) such as those listed below:

$$r(\lambda) = a_{11}x(\lambda) + a_{12}y(\lambda) + a_{13}z(\lambda)$$

$$g(\lambda) = a_{21}x(\lambda) + a_{22}y(\lambda) + a_{23}z(\lambda)$$

$$b(\lambda) = a_{31}x(\lambda) + a_{32}y(\lambda) + a_{32}z(\lambda)$$

One color stimulus must be kept fixed and the other is changed relative to the first such that the distance between the two corresponding points in tristimulus space always represents a "just-perceptible" color difference, and the difference in color is characterized by a change in distance between points P_1 and P_2. Furthermore, in tristimulus space, an ellipsoidal shape centered at P_1 always exists. In addition, the characteristic embedding properties of a space are unaffected by any continuous transformation of the coordinates and are determined mathematically by the quantity known as the Gaussian curvature which is a function of the coefficients g_{ik} in the line element. In order to map one space into another of the same dimensions, and at the same time preserve distances, it is necessary and sufficient that the two spaces have the same Gaussian curvature at corresponding points. The Euclidean space has zero Gaussian curvature throughout. Thus if the three-dimensional color space is found to have nonzero curvature, it is impossible to map this space into a three-dimensional Euclidean space

without any ruptures or gaps. Thus, a Euclidean space of more than three, possibly six dimensions must be used, which does not exist. Therefore, the concept of embedding is of limited practical use and one applying Helmholtz's theory must be content to describe the color space and measure within it using the line element uniquely determined by its coefficient g_{ik}. Additionally, the resulting spectral response curves $r(\lambda)$, $g(\lambda)$, and $b(\lambda)$ which show two pronounced maxima, are completely incompatible with the spectral absorption curves that have now been measured for cone pigments in our current era. The line element is also not valid if the photoreceptors of each of the three mechanisms contain predominantly one pigment [5]. For this and other reasons, Helmholtz's theory was challenged later on by Schrödinger (1920). Schrödinger eliminated the limitations of the line element for multiple reasons, including the fact that Helmholtz's theory entails a luminous efficiency curve that is different from the directly-observed $V(\lambda)$ curve. According to Schrödinger, points P_1 and P_2 are supposedly joined by a line following any desired path in space, as opposed to the excessively linear model initially proposed by Helmholtz. In Schrödinger's theory, *R*, *G*, and *B* denote the responses of cone mechanisms that operate independently from one another. However, the contribution of each mechanism to the square of the perceived total difference depends on all three cone responses through the factor of:

$$\frac{1}{l_R R + l_G G + l_B B}$$

The brightness for this line element is proportional to $l_R R + l_G G + l_B B$, making a surface of constant brightness a plane in tristimulus space. Single-peak curves with maxima in the orange, green, and blue parts of the spectrum, not radically different from

more recent determinations of the fundamental response functions. With these fundamentals and a suitable choice of the relative values of the constants l_R, l_G, l_B brightnesses deduced from the Schrödinger line element agree approximately with luminances based on the experimentally determined luminous efficiency function V(λ). This concurrence and the additivity of brightness were considered by Schrödinger as the strong points of his line element, which he designed to achieve these ends. However, experimental tests conducted later on by Bouma and Heller (1935) and Rosemann (1938) showed that the model failed to predict correct experimental output of various kinds [5]. Therefore, this theory has not since been intensively studied.

The most elaborate line element that exists to explain the sensation of color vision signal transduction has been developed by Vos and Walraven in 1972. There are three assumptions underlying this theory: (i) Color stimuli are processed in two stages, occurring in a Helmholtz-type three-receptor zone, followed by a Hering-type neural conversion zone in which a luminance and two antagonistic chromatic signals are formed; (ii) Color discrimination is essentially photon-noise-limited. At higher luminances, "saturation" and "supersaturation" (or channel overloading) processes occur that keep color discrimination below the limit that photon noise alone would provide; and (iii) the signals emerging from the second zone, the neural conversion zone, combine in a positive and definite (quadratic) form to generate an output signal directly proportional to a just-noticeable difference between two given input stimuli [5, 27, 28]. Details regarding this mechanism are further discussed in Appendix B.

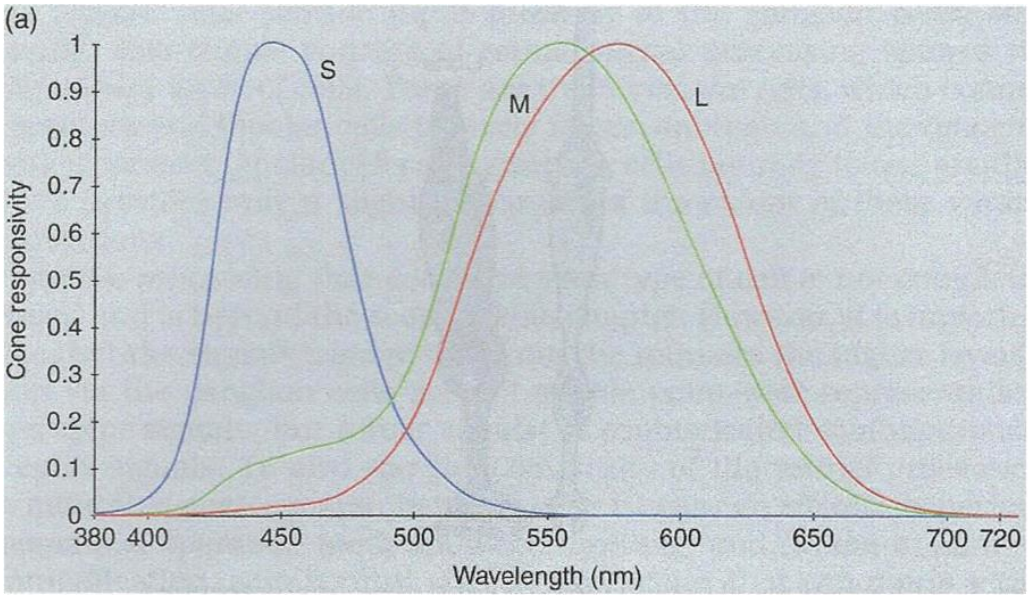

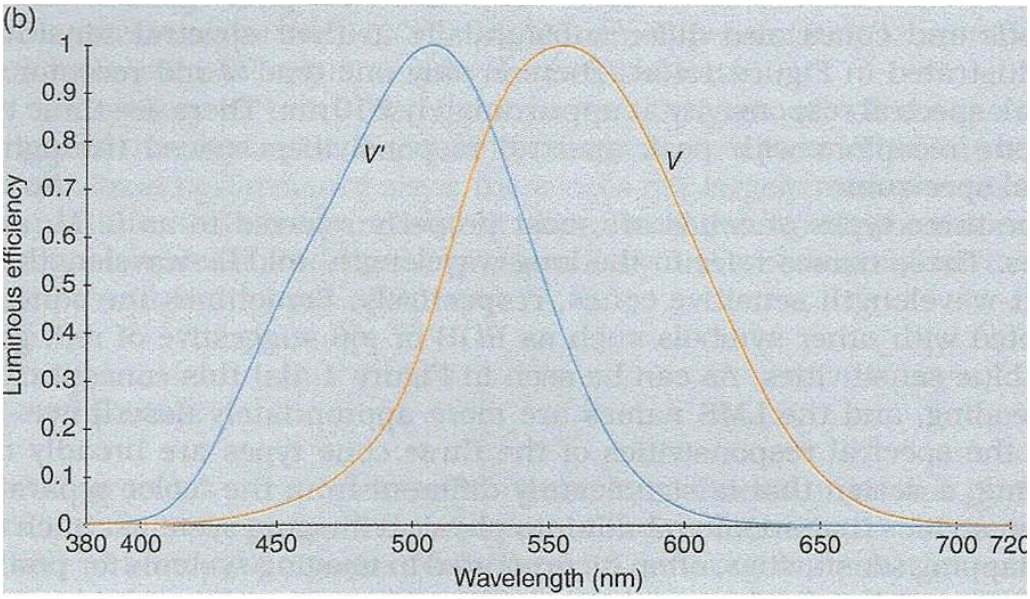

Fig. 2. V(λ) “rods” and V’(λ) “cones” absorbance spectra range [4].

A rudimentary sketch of the Vos and Walraven theory of color vision mechanism as described in Fairchild is depicted in Figure 2. Compared to experimental color discrimination data, this theory of color molecules finds reasonable agreement between prediction and experiment [5]. Note that this is an inductive line element theory, which explains the visual mechanism of color perception rather well using a mathematical model. However, inductive models make basic assumptions about color matching. Conversely, empirical line elements, such as those by MacAdam (1942, 1943) correctly reproduce standard deviations from the mean of repeated color matches but do not attempt explain the visual response mechanism responsible for color discrimination [5]. More advanced color theories have structured mathematical models to divide visual response mechanisms into Class I, II, or III component mechanisms--that are further classified as either simple or complex--which exhibit responses based on two or three tristimulus values [4, 5]. This integrated inductive and empirical model incorporates more physiological details into the calculations, including retinal end-organs that may contain more than one visual pigment or some interplay, usually neural, between end-organs with different visual pigments which occurs before the response is evaluated [5]. Or, a mechanism may incorporate itself in a differencing process or other inhibitory action such as the type proposed originally in the opponent color approach devised by Vos and Walraven [5, 27, 28]. It is interesting to note that throughout Wyszecki and Stiles' survey of color appearance models (2000), the authors mention a certain interchangeability between Poisson-type processes and Gaussian curvatures in the mathematical models discussed. Perhaps the Poisson models are more effective for the inductive modeling of the visual mechanism, whereas Gaussian curvature dominates when empirical models of

color matching properties are desired for objects that are known to be a specific color in the physical--yet non-biological--realm. Given the demonstrated efforts that theoretical and applied chemists and mathematicians have committed to demystifying the mechanism of sight using mathematical modeling techniques, equally detail-oriented theoretical computational studies on modern color additives serves to complement these theories by putting them into practice in order to determine if technological progression of computers can more adequately explain or predict results of color spectra analyses.

Further strides have been made to understand color appearance with the widespread use of computational software to construct novel or existing color molecule structures, and to assess their electronic, spectroscopic properties. Gaussian software has been used since its debut in 1994 to calculate linear combinations of atomic orbitals (LCAO-MOs) and to then determine their coefficients in the linear combination by a self-consistent field calculation (LCAO-MO-SCF). The set used to construct LCAO-MOs is called a "basis set" [29]. While basis sets applying Slater transition orbitals (STOs) to Hartree-Fock (HF) Theory were popular in the 1980s, today Gaussian functionals have outpaced STOs and are incorporated into the more popular advanced ab initio calculation method called Density Functional Theory (DFT) [29, 30]. In HF theory, a Slater determinant is constructed from a set of "N" single electron wave functions [29], but DFT is based on the concept that the overall electronic density is related to the total electronic energy. While the Thomas-Fermi model in the late 1920s was an approximate model that contained some of the basic elements, Hohenberg and Kohn in 1964 proved that ground state energy of a system and other properties of a system were uniquely defined by electron density. According to [30], this may be otherwise stated as the energy

E is a unique functional of ρ(r). Note that a "functional" enables a function to be mapped to a number and is usually written using square brackets [30]. Therefore,

$$Q[f(r)] = \int f(r)dr$$

Where, in the case of DFT, the function depends on electron density, making Q a functional of ρ(r). In the simplest case *f*(r) would be equivalent to the density ("rho" or ρ) so *f*(r) ≡ ρ(r). If the function *f*(r) were to depend in some way upon the gradients (or higher derivatives) of ρ(r), then the functional is referred to as being "non-local" or "gradient corrected" [30]. By contrast, a "local" functional would only have a simple dependence upon ρ(r). In DFT, the energy functional is written as a sum of two terms:

$$E[\rho(r)] = \int V_{ext}(r)\rho(r)\,dr + F[\rho(r)]$$

Where the term $V_{ext}(r)$ arises from the interaction of electrons with an external potential, typically due to the Coulomb interaction with the nuclei.

$F[\rho(r)]$ is the sum of the kinetic energy of the electrons and the contribution from inter-electronic interactions. The minimum value in the energy corresponds to the exact ground-state electron density, so enabling a variational approach to be used; as in, the best solution corresponds to the minimum of energy and an incorrect density gives an energy above the true energy [30].

There is a constraint on the electron density as the number of electrons (N) is fixed:

$$N = \int \rho(r)dr$$

In order to minimize the energy we introduce this constraint above as a Lagrangian multiplier (-μ), leading to:

$$\frac{\delta}{\delta\rho(r)}\left[E[\rho(r)] - \mu\int\rho(r)dr\right] = 0$$

From this, we can now write

$$\left(\frac{\delta E[\rho(r)]}{\delta\rho(r)}\right)_{Vext} = \mu$$

According to [30], this solution is the DFT equivalent to the Schrödinger equation.

It should be noted that the sensation of color stimulus is time-dependent; hence, time-dependent density functional theory (TD-DFT) is necessary to predict electronic excitation state energies for conversion to maximum absorbance spectral responsivity peaks. According to [31], the time-dependent Schrödinger equation is written including a Hamiltonian operator $\mathscr{H}$, set equal to the energy operator Ê as shown:

$$\mathscr{H}\Psi = \hat{E}\Psi$$

Where the Hamiltonian operator $\mathscr{H}$ is equivalent to the following function:

$$H(x,y,z,t) = -\frac{\hbar^2}{2m}\nabla^2 + V(x,y,z,t)$$

And the energy operator $\hat{E}$ (not to be confused with the scalar quantity of energy, *E*) on the right is equivalent to the following function:

$$\hat{\mathrm{E}} = i\hbar\frac{\partial}{\partial t}$$

Only ground state properties may be predicted using DFT, so development of time-dependent density functional theory allows for successful calculation of electronic excitations. In TD-DFT, the many-body time dependent Schrodinger equation is replaced by a set of time-dependent single particle equations whose orbitals yield the same time-dependent density [32]. This is possible because of the Runge-Gross theorem, which proves that for a given initial wavefunction, particle statistics and interaction, a given time-dependent density can arise from at most one time-dependent external potential. Therefore, the time-dependent potential (and all other properties) are a functional of the time-dependent density. With this in mind, the Kohn-Sham DFT, if refined for time dependent conditions, can describe non-interacting electrons that evolve in a time-dependent Kohn-Sham potential, but produce the same density as that of the interacting system of interest. Thus, as in the ground-state case, the demanding interacting time-dependent Schrodinger equation is replaced by a much simpler set of equations to propagate. The price of this simplification is that the exchange-correlation piece of the Kohn-Sham potential must be approximated.

According to [32], the most common time-dependent perturbation is a long-wavelength electric field, oscillating with frequency ω. In the usual situation, this field is a weak perturbation on the molecule, and one can perform a linear response analysis and can extract the optical absorption spectrum of the molecule due to electronic excitations. Thus, linear response TD-DFT predicts the transition frequencies to electronic excited states and many other properties. However, for conditions in which the ground-state excitation properties are inadequate for accurate measurement of electronic excited state properties, approximations have been created that both expedite calculations, lessen

computational processing time, and more importantly, serve to provide more accurate calculation of electronic excitation energies for further analyses. Among these include the Local Density Approximation (LDA) [30, 32], adiabatic local density approximation (ALDA) [32], and the Tamm-Dancoff Approximation (TDA) [33, 34]. In this body of work, the TDA approximation is most significant due to its effective modeling of charge transfer color spectral shifts exhibited in the pharmaceutical dye molecule Brilliant Cresyl Blue (see Chapter 3).

As computational processing power has advanced throughout the twentieth century, a series of researchers have contributed to the field of theoretical prediction of color molecule color spectra based on molecular structure. Woodward-Fieser explored these properties initially, developing the Woodward-Fieser Rules in 1941 for conjugated organic molecules which were eventually followed by the Fieser-Kuhn rules [35]. With the advancement of computer technology in the 1970s and 1980s [29], the field of computational chemistry rapidly expanded to develop a method for calculation of electronic excitation states in a more accurate fashion for larger quantities of atoms than the Woodward-Fieser rules could accommodate. Density Functional Theory (DFT) re-emerged as a method of calculating electronic energy in electron volts (eV) for large molecular structures to readily be converted into nanometers (nm) for comparison to experimental maximum absorbance (denoted λ_{max}) measurements determined using spectrophotometric analytical equipment. As computational speeds increased and processing power became readily accessible to the average consumer during the late 1990s to early twenty-first century [30], DFT had also evolved to meet the growing demand for more cost-effective accessibility of higher processing power for improved

parallelization, thus faster and more accurate Gaussian orbital calculations. Geometry conformations can be spread across a number of integrals equivalent to that of the number of atoms in the composite structure being analyzed. With formerly 32-bit processors--and now 64-bit processors becoming standard for personal laptop computers and beyond--chemists interested in designing molecules for industrial, pharmaceutical, and diverse consumer product applications can do so in a matter of weeks. These "custom-built" color molecules can be conceptualized in a computational workspace, and have their physical properties verified by performing theoretical calculations using DFT and TD-DFT to determine their electronic excitation state measurement for direct conversion into theoretical absorbance spectra values based on the Gaussian summation function. Upon conclusion of this streamlined process of data acquisition and exhibition, chemists designing a suitable color molecule for their pharmaceutical or cosmetic application can make a conscientious decision as to whether or not it is feasible to pursue development of the molecule. Alternatively, the chemist could decide to return to or the "drawing board" which is now literally represented as a computational workspace to make necessary amends to the molecule subject to analysis without excessive (or costly) experimental "trial-and-error" UV-visible maximum absorbance spectra analysis. Once adequate theoretical data is collected, experimental batches of the test samples can be prepared and further analyzed for effectiveness in conveying color appearance (in this case, hue) desired until a finite decision is made. Therefore, the application of computational methods to design and theoretically test color-inducing molecules streamlines color molecule development, enabling more efficient experimental testing of prepared batch samples.

The vibrant spectrum of colors that can be achieved by studying color molecule interactions with solvent molecules is called solvatochromism. A large quantity of research has been published in this field throughout the twentieth century [36-52]. Of particular interest is the work of Christian Reichardt, who conducted several experimental studies on amphoteric and zwitterionic molecules in common "stock" chemical solvents to observe their noticeably dramatic shifts in maximum absorbance spectra [48-52]. His varied works strongly emphasize the role of intermolecular interactions between solute and solvent, particularly due to intermolecular forces, dipole-dipole interactions, solvent polarity and acid-base interactions as strongly influential in the overall hue of the mixture (or the solution, when applicable) [52]. In the research being presented here, solvent interactions that affect perceived color spectra are being even more carefully investigated as contributors to changes in UV-visible spectral peak responsivities due to advances in quantum mechanical treatment of solvation effects. Solvation effects are no longer considered extraneous or out-of-reach in computational data collection; in fact, *in vacuo* ("in a vacuum") calculations are no longer considered sufficient and inclusion of solvation effects using continuum solvation models for conventional solvents as well as novel solvents for exploration is attaining heightened interest in the quantum chemical community. In particular, the Poisson-Boltzmann Finite (PBF) elements continuum model as used throughout this work is based on a solution of the Poisson-Boltzmann equation (PBE) until the electric potential on the molecular surface reaches equilibrium with contributions from the solvent and the solute molecule structure included or specified in the input parameters [53]. While geometry optimizations in solution are only possible with PBF because the appropriate energy gradients are contained in the PBF

model as of the edition of the software utilized at the time of this writing[1] , PBF gradients are not fully analytic, and as a consequence of the implicit dependence of the solution phase energy on the numerically-generated grid which is used to solve the Poisson-Boltzmann equation [53]. Despite this, PBF has no restrictions as to which basis set should be used, and empirical corrections are used to account for first solvation shell effects which are not captured by pure implicit solvation models. Recently, first shell effects in ions in aqueous media have been improved for PBF calculations such that the average solvation energy error for ionic species (evaluated on standard test sets) is approximately 3 kcal/mole [53], which is close to experimental error[2]. These significant advancements in computational technology have made quantum chemical analyses of physical properties of color and solvent molecules conducted using advanced ab initio methods very attractive in order to better design molecules for cosmetic and pharmaceutical end uses.

One avenue that leads to ample opportunity for exploration using combined computational, theoretical, and experimental studies has been the interplay of specific ions on certified color molecules so as to begin to attribute noticeable color shifts in experimental batch preparations of color molecules with various charge states to specific cation-anion combinations of ionic liquid solvents. The role of specific ions in solution with color additive molecules is increasingly more easily quantifiable using maximum absorbance spectra measurements obtained using advanced ab initio methods. However, in order for the computational data to be useful, experimental batch preparations in molar

[1] Schrödinger Jaguar 2015-2 edition using Maestro "Graphical User Interface" (GUI)
[2] Note that the experimental error for solvation of neutral species is smaller, around 1 kcal/mole, as reflected by similar error bars produced by PBF for these species [53].

equivalencies ought to be compared to theoretical calculations of molecular systems because one-to-one molar ratios serve as the most pragmatic virtual comparison. In recent years, ionic liquid solvents have been adopted by chemical manufacturing companies for their applicability as industrial lubricants. They are preferable over traditional uncharged solvents because of their variable physical properties—namely, viscosity [55-58], density [55, 58, 59], thermostability [55, 60-62], effects on solvation dynamics [63-68], glass transition temperature [58], melting and boiling point temperature [58,69], and conductivity [55, 56, 70-73]—which are customizable based on the cation-anion combination chosen. For this reason, the ionic liquid solvents have established a reputation as "designer solvents" throughout academia and beyond [54,57]. However, exploration of the photophysical properties of ionic liquids for industrial applications has not received as strong of focus among the other aforementioned physical properties that are "tunable" among ionic liquids (ILs). ILs have been integrated into pharmaceutical formulations to aid in drug delivery [74,75], improved surface interaction during emulsification [74, 76-79], and even in formulations containing sensory-stimulating perfume ingredients [80-82] or as a functional "green" additive for anti-pollution effects and carbon dioxide capture [83-90]. The potential of ILs for cosmetic applications is vastly expanding. Therefore, the need to be able to visualize or predict properties of ionic liquids with common pharmaceutical and cosmetic additives is increasingly important.

TD-DFT applications abound throughout contemporary chemical and biological research. Biological applications of TD-DFT include modeling of retinal photopigment chromophores and Schiff-base interactions within protein structures [91-95], modeling of green fluorescent proteins (GFP) [96-98] and bioluminescent protein *Photinus pyralis*

[99], and even flavonoid molecules [100-106] such as quercetin [107-109] and riboflavin [110-115] have been optimized with some success to determine physicochemical properties. TD-DFT has been effectively used to model chromophores of natural and synthetic nature [116-129], in addition to well-known dye and pigment molecules of various sizes and dye classes alone or in clay-like scaffold structures [130-157], but few studies exist to achieve strong comparisons of experimental batch preparations and spectroscopic testing to theoretical modeling. In fact, most theoretical studies classify absorbance spectra shifts determined by Gaussian summation functions to be either hypsochromic (leftward "blue shift" towards the ultraviolet region), or bathochromic (rightward "red shift" towards the infrared region) without clearly identifying the role of solvent interactions. As most of these studies have simulated molecules *in vacuo* (vapor phase), the assumptions made about their color appearance or physicochemical appearance are very impractical for the optical application of commonplace pharmaceutical or cosmetic formulations. This research seeks to begin to fill the void of TD-DFT studies on specific molecules in varied, charged solvents to explore the potential of using ionic liquids as alternatives to customary "stock" solvents for greater color variation and customizable physical properties. This work should create opportunities experiment with smaller amounts of color additives and solvents to achieve a wider range of colors to minimize the extraneous addition of unnecessary or nonsensical ingredients in order to achieve the same purpose.

It is important to note that while geometry optimizations were performed on molecules constructed in the workspace using both quantum mechanical and MM2 dynamic simulations in a computational workspace, the more modern form of "molecular

dynamics" was NOT performed in which large quantities of solvent molecules surrounded an individual solute molecule (or an equivalent quantity of solute-to-solvent molecules higher than one) to fill a boundary box or other specified area for observation of solute-solvent interaction studies. The initial and final "snapshots" of solute and solvent molecules optimized was used for necessary quantum mechanical calculations for determining theoretical absorbance spectra peak responsivities because the sensation of human color perception occurs at the instantaneous moment of electronic excitation from the *h*ighest *o*ccupied *m*olecular *o*rbital (HOMO) to the *l*owest *u*noccupied *m*olecular *o*rbital (LUMO) in molecules exhibiting conjugated pi-bonding (π-π* excitation) [3]. In addition, computational limitations on the types of solvent molecules that are available for the more sophisticated type of 3-D molecular dynamics modeling for pico-, nano-, micro-, or even millisecond timescales is not possible for custom molecules at this point in time. Only "pre-set" common solvent molecules such as those available as chemical stock solvents incorporated into a given workspace to surround a quantity of uniquely-constructed solute molecules, but not for individually-constructed and charged cation/anion pairs[3] . Regardless, the excessive computational processing time that would be required for such studies would still not emulate the ideal solvation conditions for each mixture of color molecule-solvent designed because solubility assumes 1:1 interaction of solute-to-solvent, at a rate that varies based on different physical properties--hence reinforcing that dissolution is a kinetic process, and solubility is a thermodynamic process. Despite this, perhaps computational chemistry software processes will improve in the near future to accommodate this emerging interest, allowing for more detailed

[3] As of November 8, 2018.

analyses of “designer solvents” to become a reality. In the meantime, it is possible to construct dye molecules in a computational workspace, calculate theoretical electronic excitation energies using these molecules, and subsequently compare theoretical spectra to both individual molecules and mixtures of molecules in a virtual setting for direct comparison to experimental batch preparations with reasonable, if not excellent, accuracy. Potential applications of the methods described herein abound. As form follows function in all design applications, hopefully use of advanced computational technology will enable ionic liquid mixtures to truly live up to their nickname as “designer solvents” by expanding their range as physical property modulators to include color for formulation chemistry applications.

References

[1] L. Schneider Adams, "The Art of Prehistory," in *Art Across Time Volume 1: Prehistory to the Fourteenth Century*, vol. 14 ed. New York: McGraw-Hill, 2011, p. 505.

[2] R. S. Berns, *Billmeyer and Saltzman's Principles of Color Technology*, 3rd ed. Wiley-Interscience, 2000.

[3] T. R. Engel, Philip, "Electronic Spectroscopy," in *Physical Chemistry* 3rd ed. Harlow: Pearson, 2012, pp. 609-612.

[4] M. Fairchild, *Color Appearance Models*, 3rd ed. (Wiley-IS&T Series in Imaging Science and Technology). Wiley, 2013, p. 472.

[5] G. S. Wyszecki, W.S., *Color Science: Concepts and Methods, Quantitative Data and Formulae*, 2nd ed. Wiley-Interscience, 2000, p. 968.

[6] M. Douma. (2008, November 7, 2018). *Causes of Color*. Available: http://www.webexhibits.org/causesofcolor/1.html

[7] D. Mustafi, A. H. Engel, and K. Palczewski, "Structure of cone photoreceptors," *Prog Retin Eye Res*, vol. 28, no. 4, pp. 289-302, Jul 2009.

[8] R. T. Korichi, Jean-Francois, "Decorative Products," in *Handbook of Cosmetic Science and Technology*, A. O. P. Barel, Marc; Maibach, Howard I. , Ed. 3rd ed. New York: Informa, 2013, pp. 391-406.

[9] G. A. Lewis, "Non Classical Experimental Designs in Pharmaceutical Formulation," *Drug Development and Industrial Pharmacy*, vol. 17, no. 12, pp. 1551-1570, 2008.

[10] D. G. Watson, Ed. *Pharmaceutical Chemistry*. Edinburgh: Elsevier, 2011, p. 641.

[11] M. M. Rieger, "Cosmetics," in *Kirk-Othmer Chemical Technology of Cosmetics*, A. Seidel, Ed. Hoboken: Wiley, 2013, pp. 1-48.

[12] A. T. S. More, R. K., "Aesthetic Considerations for pharmaceutical OTC (over-the-counter) products," in *Oxford Business & Economics Conference Program*, St. Hughes College, Oxford University, 2009, p. 22.

[13] D. Marmion, "Colorants for Foods, Drugs, and Cosmetics," in *Kirk-Othmer Chemical Technology of Cosmetics*, A. Seidel, Ed. Hoboken: Wiley, 2013, pp. 501-547.

[14] G. S. K. Velpandian T., *Pharmacology of Ocular Therapeutics*, V. T., ed., 2016. [Online]. Available.

[15] A. S. Sigel, Helmut; Sigel, Roland K.O., Ed. *Cadmium: From Toxicity to Essentiality* (Metal Ions in Life Sciences, no. 11). Springer, 2013, p. 560.

[16] E. J. B. Tokar, Windy A.; Freedman, Jonathan H.; Waalkes, Michael P., "Toxic Effects of Metals," in *Casarett & Doull's Toxicology: The Basic Science of Poisons*, C. Klaassen, Ed. 8th ed.: McGraw-Hill Medical, 2013, pp. 981-1031.

[17] R. W. Hughes. (2018, November 6, 2018). *Lapis Lazuli Buying Guide*. Available: http://www.palagems.com/lapis-lazuli-buying-guide/

[18] S. J. Downing, Beauty and Cosmetics 1550-1950. Shire, 2012, p. 64.

[19] U. S. F. a. D. Administration. (2015, November 7, 2018). *Color Additive Status List*. Available: https://www.fda.gov/ForIndustry/ColorAdditives/ColorAdditiveInventories/ucm106626.htm

[20] J. N. B. A. L. L. C. J. Bailey. (2003, November 7, 2018). *Color Additives: FDA's Regulatory Process and Historical Perspectives*.

[21] J. F. Senackerib, "Color Additives for foods, drugs, and cosmetics," in *Colorants for Non-Textile Applications*, A. T. P. H.S. Freeman, Ed. 1st ed. Amsterdam: Elsevier, 2000, pp. 131-187.

[22] T. Riordan, *Inventing Beauty: A history of the innovations that have made us beautiful*. Broadway, 2004.

[23] J. C. Hollenberg, *Color Cosmetics: A Practical Guide to Formulation*. Carol Stream: Allured, 2016.

[24] J. N. Barrows, "Absorbance Spectra Testing of Mixtures of D&C Color Molecules," ed, 2017.

[25] P. Smith. (2004, November 7, 2018). *The colouration of tablets and capsules*. Available: https://www.manufacturingchemist.com/news/article_page/The_colouration_of_tablets_and_capsules/34905

[26] *Color Chemistry: Syntheses, Properties, and Applications of Organic Dyes and Pigments*, 3rd ed. Wiley-VCH, 2001, p. 550.

[27] J. J. Vos and P. L. Walraven, "An analytical description of the line element in the zone-fluctuation model of colour vision—I. Basic concepts," *Vision Research*, vol. 12, no. 8, pp. 1327-1344, 1972.

[28] J. J. Vos and P. L. Walraven, "An analytical description of the line element in the zone-fluctuation model of colour vision—II. The derivation of the line element," *Vision Research*, vol. 12, no. 8, pp. 1345-1365, 1972.

[29] D. A. S. McQuarrie, John D., "Computational Quantum Chemistry," in *Physical Chemistry: A Molecular Approach* Sausalito: University Science, 1997, p. 1360.

[30] A. R. Leach, *Molecular Modelling: Principles and Applications*, 2nd ed. Harlow: Prentice Hall, 2001, p. 744.

[31] D. C. B. Harris, Michael D., *Symmetry and Spectroscopy: An Introduction to Vibrational and Electronic Spectroscopy*. New York: Dover, 1989, p. 550.

[32] P. Elliott, K. Burke, and F. Furche, "Excited states from time-dependent density functional theory," in *Reviews in Computational Chemistry*, vol. 26, K. B. C. Lipkowitz, T.R., Ed. New York: Wiley-VCH, 2007, pp. 91-167.

[33] S. Hirata and M. Head-Gordon, "Time-dependent density functional theory within the Tamm–Dancoff approximation," *Chemical Physics Letters*, vol. 314, no. 3-4, pp. 291-299, 1999.

[34] Y.-L. Wang and G.-S. Wu, "Improving the TDDFT calculation of low-lying excited states for polycyclic aromatic hydrocarbons using the Tamm–Dancoff approximation," *International Journal of Quantum Chemistry*, vol. 108, no. 3, pp. 430-439, 2008.

[35] A. Mehta. (2012, November 6, 2018). Ultraviolet-Visible (UV-Vis) Spectroscopy - Wooward-Fieser Rules to Calculate Wavelength of Maximum Absorption (Lambda-max) of Conjugated Dienes and Polyenes. Available: https://pharmaxchange.info/2012/08/ultraviolet-visible-uv-vis-spectroscopy-–-woodward-fieser-rules-to-calculate-wavelength-of-maximum-absorption-lambda-max-of-conjugated-dienes-and-polyenes/

[36] A. G. Gilani, M. Salmanpour, and T. Ghorbanpour, "Solvatochromism, dichroism and excited state dipole moment of azure A and methylene blue," *Journal of Molecular Liquids*, vol. 179, pp. 118-123, 2013.

[37] J. Katla et al., "Donor-Acceptor Styrylisoxazoles: Solvatochromism and Large First Hyperpolarizability," *ChemistrySelect*, vol. 3, no. 25, pp. 7416-7421, 2018.

[38] W. Liptay, "Electrochromism and Solvatochromism," *Angewandte Chemie International Edition in English*, vol. 8, no. 3, pp. 177-188, 1969.

[39] Z. M. S, G. A, and M. M, "Solvent Effects on the UV/ Visible Absorption Spectra of Some Aminoazobenzene Dyes," *Chemical Science Transactions*, vol. 1, no. 1, pp. 1-8, 2012.

[40] C. T. Martins, B. M. Sato, and O. A. Seoud, "First study on the thermo-solvatochromism in aqueous 1-(1-Butyl)-3-methylimidazolium tetrafluoroborate: a comparison between the solvation by an ionic liquid and by aqueous alcohols," *J Phys Chem B*, vol. 112, no. 28, pp. 8330-9, Jul 17 2008.

[41] M. Koel, "Solvatochromic Probes with Ionic Liquids," *Proc. Estonian Acad. Sci. Chem.*, vol. 54, no. 1, pp. 3-11, 2004.

[42] M. Koel, "Solvatochromic Study on Binary Solvent Mixtures with Ionic Liquids," 2006.

[43] J. R. Haak and J. B. F. N. Engberts, "Solvent polarity and solvation effects in highly aqueous mixed solvents. Application of the Dimroth-Reichardt ET(30) parameter," *Recueil des Travaux Chimiques des Pays-Bas*, vol. 105, no. 9, pp. 307-311, 2010.

[44] C. Florindo, A. J. S. McIntosh, T. Welton, L. C. Branco, and I. M. Marrucho, "A closer look into deep eutectic solvents: exploring intermolecular interactions using solvatochromic probes," *Phys Chem Chem Phys*, vol. 20, no. 1, pp. 206-213, Dec 20 2017.

[45] Z. M. S, G. A, and M. M, "Solvent Effects on the UV/ Visible Absorption Spectra of Some Aminoazobenzene Dyes," *Chemical Science Transactions*, vol. 1, no. 1, pp. 1-8, 2012.

[46] H. Weitman et al., "Solvatochromic Effects in the Electronic Absorption and Nuclear Magnetic Resonance Spectra of Hypericin in Organic Solvents and in Lipid Bilayers," *Photochemistry and Photobiology*, vol. 73, no. 2, pp. 110-118, 2007.

[47] B. M. Sato, C. G. de Oliveira, C. T. Martins, and O. A. El Seoud, "Thermo-solvatochromism in binary mixtures of water and ionic liquids: on the relative importance of solvophobic interactions," *Phys Chem Chem Phys*, vol. 12, no. 8, pp. 1764-71, Feb 28 2010.

[48] C. Reichardt, "Empirical Parameters of the Polarity of Solvents," *Angewandte Chemie International Edition in English*, vol. 4, no. 1, pp. 29-40, 1965.

[49] C. Reichardt, "Empirical Parameters of Solvent Polarity as Linear Free-Energy Relationships," *Angewandte Chemie International Edition in English*, vol. 18, no. 2, pp. 98-110, 1979.

[50] C. Reichardt, "Solvatochromism, thermochromism, piezochromism, halochromism, and chiro-solvatochromism of pyridinium N-phenoxide betaine dyes," *Chemical Society Reviews*, vol. 21, no. 3, 1992.

[51] C. Reichardt, "Polarity of ionic liquids determined empirically by means of solvatochromic pyridinium N-phenolate betaine dyes," *Green Chemistry*, vol. 7, no. 5, 2005.

[52] C. R. T. Welton, *Solvents and Solvent Effects in Organic Chemistry*, 4th ed. Weinheim: Wiley-VCH, 2011, p. 692.

[53] A. D. Bochevarov et al., "Jaguar: A high-performance quantum chemistry software program with strengths in life and materials sciences," *International Journal of Quantum Chemistry*, vol. 113, no. 18, pp. 2110-2142, 2013.

[54] P. W. Wasserscheid, T., *Ionic Liquids in Synthesis* (Green Chemistry). Erlangen: Wiley-VCH, 2008.

[55] K. Ueno, H. Tokuda, and M. Watanabe, "Ionicity in ionic liquids: correlation with ionic structure and physicochemical properties," *Phys Chem Chem Phys*, vol. 12, no. 8, pp. 1649-58, Feb 28 2010.

[56] E. I. Izgorodina, "Towards large-scale, fully ab initio calculations of ionic liquids," *Phys Chem Chem Phys*, vol. 13, no. 10, pp. 4189-207, Mar 14 2011.

[57] D. R. MacFarlane and K. R. Seddon, "Ionic Liquids—Progress on the Fundamental Issues," *Australian Journal of Chemistry*, vol. 60, no. 1, 2007.

[58] H. Saba, X. Zhu, Y. Chen, and Y. Zhang, "Determination of physical properties for the mixtures of [BMIM]Cl with different organic solvents," *Chinese Journal of Chemical Engineering*, vol. 23, no. 5, pp. 804-811, 2015.

[59] H. Niedermeyer, J. P. Hallett, I. J. Villar-Garcia, P. A. Hunt, and T. Welton, "Mixtures of ionic liquids," *Chem Soc Rev*, vol. 41, no. 23, pp. 7780-802, Dec 7 2012.

[60] F. Endres and S. Zein El Abedin, "Air and water stable ionic liquids in physical chemistry," *Phys Chem Chem Phys*, vol. 8, no. 18, pp. 2101-16, May 14 2006.

[61] R. M. Lynden-Bell, "Screening of pairs of ions dissolved in ionic liquids," *Phys Chem Chem Phys*, vol. 12, no. 8, pp. 1733-40, Feb 28 2010.

[62] B. M. Sato, C. G. de Oliveira, C. T. Martins, and O. A. El Seoud, "Thermo-solvatochromism in binary mixtures of water and ionic liquids: on the relative importance of solvophobic interactions," *Phys Chem Chem Phys*, vol. 12, no. 8, pp. 1764-71, Feb 28 2010.

[63] X. Song, "Solvation dynamics in ionic fluids: an extended Debye-Huckel dielectric continuum model," *J Chem Phys*, vol. 131, no. 4, p. 044503, Jul 28 2009.

[64] S. M. Urahata and M. C. Ribeiro, "Single particle dynamics in ionic liquids of 1-alkyl-3-methylimidazolium cations," *J Chem Phys*, vol. 122, no. 2, p. 024511, Jan 8 2005.

[65] Y. Shim, D. Jeong, M. Y. Choi, and H. J. Kim, "Rotational dynamics of a diatomic solute in the room-temperature ionic liquid 1-ethyl-3-methylimidazolium hexafluorophosphate," *J Chem Phys*, vol. 125, no. 6, p. 61102, Aug 14 2006.

[66] S. Arzhantsev, H. Jin, G. A. Baker, and M. Maroncelli, "Measurements of the complete solvation response in ionic liquids," *J Phys Chem B*, vol. 111, no. 18, pp. 4978-89, May 10 2007.

[67] K. Low, L. Wylie, D. L. A. Scarborough, and E. I. Izgorodina, "Is it possible to control kinetic rates of radical polymerisation in ionic liquids?," *Chem Commun (Camb)*, vol. 54, no. 80, pp. 11226-11243, Oct 4 2018.

[68] J. G. Huddleston, A. E. Visser, W. M. Reichert, H. D. Willauer, G. A. Broker, and R. D. Rogers, "Characterization and comparison of hydrophilic and hydrophobic room temperature ionic liquids incorporating the imidazolium cation," *Green Chemistry*, vol. 3, no. 4, pp. 156-164, 2001.

[69] M. H. Ghatee and Y. Ansari, "Ab initio molecular dynamics simulation of ionic liquids," *J Chem Phys*, vol. 126, no. 15, p. 154502, Apr 21 2007.

[70] T. Singh and A. Kumar, "Static dielectric constant of room temperature ionic liquids: internal pressure and cohesive energy density approach," *J Phys Chem B*, vol. 112, no. 41, pp. 12968-72, Oct 16 2008.

[71] M. V. Fedorov and A. A. Kornyshev, "Ionic liquids at electrified interfaces," *Chem Rev*, vol. 114, no. 5, pp. 2978-3036, Mar 12 2014.

[72] C. Schroder, T. Rudas, and O. Steinhauser, "Simulation studies of ionic liquids: orientational correlations and static dielectric properties," *J Chem Phys*, vol. 125, no. 24, p. 244506, Dec 28 2006.

[73] T. Singh and A. Kumar, "Static dielectric constant of room temperature ionic liquids: internal pressure and cohesive energy density approach," *J Phys Chem B*, vol. 112, no. 41, pp. 12968-72, Oct 16 2008.

[74] B. Wu, H. Shirota, S. Lall-Ramnarine, and E. W. Castner, "Structure of ionic liquids with cationic silicon-substitutions," *The Journal of Chemical Physics*, vol. 145, no. 11, 2016.

[75] Q. Zhang and S. Zhu, "Ionic Liquids: Versatile Media for Preparation of Vesicles from Polymerization-Induced Self-Assembly," *ACS Macro Letters*, vol. 4, no. 7, pp. 755-758, 2015.

[76] H. Epstein, "Skin Care Products," in *Handbook of Cosmetic Science and Technology*, A. O. P. Barel, Marc; Maibach, Howard I., Ed. 3rd ed. New York: Informa, 2009, pp. 121-134.

[77] Z. He and P. Alexandridis, "Nanoparticles in ionic liquids: interactions and organization," *Phys Chem Chem Phys*, vol. 17, no. 28, pp. 18238-61, Jul 28 2015.

[78] R. J. Bingham and P. Ballone, "Computational study of room-temperature ionic liquids interacting with a POPC phospholipid bilayer," *J Phys Chem B*, vol. 116, no. 36, pp. 11205-16, Sep 13 2012.

[79] J. G. Huddleston, A. E. Visser, W. M. Reichert, H. D. Willauer, G. A. Broker, and R. D. Rogers, "Characterization and comparison of hydrophilic and hydrophobic room temperature ionic liquids incorporating the imidazolium cation," *Green Chemistry*, vol. 3, no. 4, pp. 156-164, 2001.

[80] G. O. B. K. Richard and S. H. Q. N. Gunaratne, "Ionic Liquid Systems," United States of America Patent US 20160376522 A1, 2016. Available: https://www.google.com/patents/US20160376522.

[81] M. A. R. Martins, U. Domańska, B. Schröder, J. A. P. Coutinho, and S. P. Pinho, "Selection of Ionic Liquids to be Used as Separation Agents for Terpenes and Terpenoids," *ACS Sustainable Chemistry & Engineering*, vol. 4, no. 2, pp. 548-556, 2015.

[82] P. Berton, K. Bica, and R. D. Rogers, "Ionic liquids for consumer products: Dissolution, characterization, and controlled release of fragrance compositions," *Fluid Phase Equilibria*, vol. 450, pp. 51-56, 2017.

[83] D. Coleman and N. Gathergood, "Biodegradation studies of ionic liquids," *Chem Soc Rev*, vol. 39, no. 2, pp. 600-37, Feb 2010.

[84] M. Kanakubo, T. Makino, and T. Umecky, "CO2 solubility in and physical properties for ionic liquid mixtures of 1-butyl-3-methylimidazolium acetate and 1-butyl-3-methylimidazolium bis(trifluoromethanesulfonyl)amide," *Journal of Molecular Liquids*, vol. 217, pp. 112-119, 2016.

[85] M. Petkovic, K. R. Seddon, L. P. Rebelo, and C. Silva Pereira, "Ionic liquids: a pathway to environmental acceptability," *Chem Soc Rev*, vol. 40, no. 3, pp. 1383-403, Mar 2011.

[86] C. M. S. S. Neves, M. G. Freire, and J. A. P. Coutinho, "Improved recovery of ionic liquids from contaminated aqueous streams using aluminium-based salts," *RSC Advances*, vol. 2, no. 29, 2012.

[87] M. S. Raja Shahrom, C. D. Wilfred, and A. K. Z. Taha, "CO 2 capture by task specific ionic liquids (TSILs) and polymerized ionic liquids (PILs and AAPILs)," *Journal of Molecular Liquids*, vol. 219, pp. 306-312, 2016.

[88] M. B. Shiflett, D. W. Drew, R. A. Cantini, and A. Yokozeki, "Carbon Dioxide Capture Using Ionic Liquid 1-Butyl-3-methylimidazolium Acetate," *Energy & Fuels*, vol. 24, no. 10, pp. 5781-5789, 2010.

[89] M. Watanabe, D. Kodama, T. Makino, and M. Kanakubo, "CO2 absorption properties of imidazolium based ionic liquids using a magnetic suspension balance," *Fluid Phase Equilibria*, vol. 420, pp. 44-49, 2016.

[90] X. Zhang, X. Zhang, H. Dong, Z. Zhao, S. Zhang, and Y. Huang, "Carbon capture with ionic liquids: overview and progress," *Energy & Environmental Science*, vol. 5, no. 5, 2012.

[91] C. S. Lopez, O. N. Faza, S. L. Estevez, and A. R. de Lera, "Computation of vertical excitation energies of retinal and analogs: scope and limitations," *J Comput Chem*, vol. 27, no. 1, pp. 116-23, Jan 15 2006.

[92] L. A. Montero-Cabrera et al., "CNDOL: A fast and reliable method for the calculation of electronic properties of very large systems. Applications to retinal binding pocket in rhodopsin and gas phase porphine," *J Chem Phys*, vol. 127, no. 14, p. 145102, Oct 14 2007.

[93] I. V. Rostov, R. D. Amos, R. Kobayashi, G. Scalmani, and M. J. Frisch, "Studies of the ground and excited-state surfaces of the retinal chromophore using CAM-B3LYP," *J Phys Chem B*, vol. 114, no. 16, pp. 5547-55, Apr 29 2010.

[94] I. V. Rostov, R. Kobayashi, and R. D. Amos, "Comparing long-range corrected functionals in the cis–trans isomerisation of the retinal chromophore," *Molecular Physics*, vol. 110, no. 19-20, pp. 2329-2336, 2012.

[95] M. Sun, Y. Ding, G. Cui, and Y. Liu, "S1 and S2 excited states of gas-phase Schiff-base retinal chromophores: a time-dependent density functional theoretical investigation," *J Phys Chem A*, vol. 111, no. 15, pp. 2946-50, Apr 19 2007.

[96] C. C. Hsieh et al., "Comprehensive studies on an overall proton transfer cycle of the ortho-green fluorescent protein chromophore," *J Am Chem Soc*, vol. 133, no. 9, pp. 2932-43, Mar 9 2011.

[97] Q. K. Timerghazin, H. J. Carlson, C. Liang, R. E. Campbell, and A. Brown, "Computational prediction of absorbance maxima for a structurally diverse series of engineered green fluorescent protein chromophores," *J Phys Chem B*, vol. 112, no. 8, pp. 2533-41, Feb 28 2008.

[98] J. J. van Thor, "Photoreactions and dynamics of the green fluorescent protein," *Chem Soc Rev*, vol. 38, no. 10, pp. 2935-50, Oct 2009.

[99] L. Pinto da Silva and J. C. Esteves da Silva, "TD-DFT/molecular mechanics study of the Photinus pyralis bioluminescence system," *J Phys Chem B*, vol. 116, no. 6, pp. 2008-13, Feb 16 2012.

[100] S. Antonczak, "Electronic description of four flavonoids revisited by DFT method," *Journal of Molecular Structure: THEOCHEM*, vol. 856, no. 1-3, pp. 38-45, 2008.

[101] F. Di Meo, J. C. Sancho Garcia, O. Dangles, and P. Trouillas, "Highlights on Anthocyanin Pigmentation and Copigmentation: A Matter of Flavonoid pi-Stacking Complexation To Be Described by DFT-D," *J Chem Theory Comput*, vol. 8, no. 6, pp. 2034-43, Jun 12 2012.

[102] A. Amat, C. Clementi, C. Miliani, A. Romani, A. Sgamellotti, and S. Fantacci, "Complexation of apigenin and luteolin in weld lake: a DFT/TDDFT investigation," *Phys Chem Chem Phys*, vol. 12, no. 25, pp. 6672-84, Jul 7 2010.

[103] Y. Rong, Z. Wang, J. Wu, and B. Zhao, "A theoretical study on cellular antioxidant activity of selected flavonoids," *J Spectrochimica Acta Part A: Molecular Biomolecular Spectroscopy*, vol. 93, pp. 235-239, 2012.

[104] K. Sadasivam and R. Kumaresan, "Theoretical investigation on the antioxidant behavior of chrysoeriol and hispidulin flavonoid compounds – A DFT study," *Computational and Theoretical Chemistry*, vol. 963, no. 1, pp. 227-235, 2011.

[105] J. Tošović and S. Marković, "Reproduction and interpretation of the UV–vis spectra of some flavonoids," *J Chemical Papers*, vol. 71, no. 3, pp. 543-552, 2017.

[106] J. Tošović, Ž. Milošević, and S. Marković, "Simulation of the UV/Vis spectra of flavonoids," in *Bioinformatics and Bioengineering (BIBE)*, 2015 IEEE 15th International Conference on, 2015, pp. 1-6: IEEE.

[107] M. Leopoldini, N. Russo, S. Chiodo, and M. Toscano, "Iron chelation by the powerful antioxidant flavonoid quercetin," *Journal of agricultural food chemistry*, vol. 54, no. 17, pp. 6343-6351, 2006.

[108] S. Fiorucci, J. Golebiowski, D. Cabrol-Bass, and S. Antonczak, "Oxygenolysis of flavonoid compounds: DFT description of the mechanism for quercetin," *Chemphyschem*, vol. 5, no. 11, pp. 1726-33, Nov 12 2004.

[109] D. Jeevitha, K. Sadasivam, R. Praveena, and R. Jayaprakasam, "DFT study of glycosyl group reactivity in quercetin derivatives," *Journal of Molecular Structure*, vol. 1120, pp. 15-24, 2016.

[110] D. R. Cardoso, P. Homem-de-Mello, K. Olsen, A. B. da Silva, D. W. Franco, and L. H. Skibsted, "Deactivation of triplet-excited riboflavin by purine derivatives: Important role of uric acid in light-induced oxidation of milk sensitized by riboflavin," *Journal of agricultural food chemistry*, vol. 53, no. 9, pp. 3679-3684, 2005.

[111] D. R. Cardoso, S. H. Libardi, and L. H. Skibsted, "Riboflavin as a photosensitizer. Effects on human health and food quality," *J Food function*, vol. 3, no. 5, pp. 487-502, 2012.

[112] M. Insińska-Rak et al., "New photochemically stable riboflavin analogue—3-Methyl-riboflavin tetraacetate," *Journal of Photochemistry Photobiology A: Chemistry*, vol. 186, no. 1, pp. 14-23, 2007.

[113] H.-F. Ji and L. Shen, "A DFT study on deactivation of triplet excited state riboflavin by polyphenols," *J International journal of molecular sciences*, vol. 9, no. 10, pp. 1908-1914, 2008.

[114] B. Klaumünzer, D. Kröner, and P. J. T. J. o. P. C. B. Saalfrank, "(TD-) DFT calculation of vibrational and vibronic spectra of riboflavin in solution," vol. 114, no. 33, pp. 10826-10834, 2010.

[115] E. Sikorska et al., "Spectroscopy and photophysics of flavin related compounds: Riboflavin and iso-(6, 7)-riboflavin," *J Chemical physics*, vol. 314, no. 1-3, pp. 239-247, 2005.

[116] J. Mack, Y. Asano, N. Kobayashi, and M. J. Stillman, "Application of MCD spectroscopy and TD-DFT to a highly non-planar porphyrinoid ring system. New insights on red-shifted porphyrinoid spectral bands," *J Am Chem Soc*, vol. 127, no. 50, pp. 17697-711, Dec 21 2005.

[117] M. Sun, Y. Ding, G. Cui, and Y. Liu, "S1 and S2 excited states of gas-phase Schiff-base retinal chromophores: a time-dependent density functional theoretical investigation," *J Phys Chem A*, vol. 111, no. 15, pp. 2946-50, Apr 19 2007.

[118] L. A. Montero-Cabrera et al., "CNDOL: A fast and reliable method for the calculation of electronic properties of very large systems. Applications to retinal binding pocket in rhodopsin and gas phase porphine," *J Chem Phys*, vol. 127, no. 14, p. 145102, Oct 14 2007.

[119] F. J. Avila Ferrer, F. Santoro, and R. Improta, "The excited state behavior of cytosine in the gas phase: A TD-DFT study," *Computational and Theoretical Chemistry*, vol. 1040-1041, pp. 186-194, 2014.

[120] C. S. Lopez, O. N. Faza, S. L. Estevez, and A. R. de Lera, "Computation of vertical excitation energies of retinal and analogs: scope and limitations," *J Comput Chem*, vol. 27, no. 1, pp. 116-23, Jan 15 2006.

[121] L. Pinto da Silva and J. C. Esteves da Silva, "TD-DFT/molecular mechanics study of the Photinus pyralis bioluminescence system," *J Phys Chem B*, vol. 116, no. 6, pp. 2008-13, Feb 16 2012.

[122] R. Mera-Adasme and M. Dominguez, "A computationally-derived model for the solvatochromism of p-phenolates with high predictive power," *Phys Chem Chem Phys*, vol. 20, no. 26, pp. 18127-18132, Jul 4 2018.

[123] A. Charaf-Eddin, B. Le Guennic, and D. Jacquemin, "Excited-states of BODIPY–cyanines: ultimate TD-DFT challenges?," *RSC Adv.*, vol. 4, no. 90, pp. 49449-49456, 2014.

[124] I. Duchemin, C. A. Guido, D. Jacquemin, and X. Blase, "The Bethe-Salpeter formalism with polarisable continuum embedding: reconciling linear-response and state-specific features," *Chem Sci*, vol. 9, no. 19, pp. 4430-4443, May 21 2018.

[125] J. Gierschner, H.-G. Mack, L. Lüer, and D. Oelkrug, "Fluorescence and absorption spectra of oligophenylenevinylenes: Vibronic coupling, band shapes, and solvatochromism," *J Chem Phys*, vol. 116, no. 19, 2002.

[126] C. Adamo et al., "Exploring excited states using time dependent density functional theory and density-based indexes," *J Coordination Chemistry Reviews*, vol. 304, pp. 166-178, 2015.

[127] X. Blase, I. Duchemin, and D. Jacquemin, "The Bethe-Salpeter equation in chemistry: relations with TD-DFT, applications and challenges," *Chem Soc Rev*, vol. 47, no. 3, pp. 1022-1043, Feb 5 2018.

[128] A. Charaf-Eddin, T. Cauchy, F.-X. Felpin, and D. Jacquemin, "Vibronic spectra of organic electronic chromophores," *RSC Adv.*, vol. 4, no. 98, pp. 55466-55472, 2014.

[129] Z. C. Wong, W. Y. Fan, and T. S. Chwee, "Computational modelling of singlet excitation energy transfer: a DFT/TD-DFT study of the ground and excited state properties of a syn bimane dimer system using non-empirically tuned range-separated functionals," *New Journal of Chemistry*, vol. 42, no. 16, pp. 13732-13743, 2018.

[130] J. Fabian, "TDDFT-calculations of Vis/NIR absorbing compounds," *Dyes and Pigments*, vol. 84, no. 1, pp. 36-53, 2010.

[131] A. D. Laurent and D. Jacquemin, "TD-DFT benchmarks: A review," *International Journal of Quantum Chemistry*, vol. 113, no. 17, pp. 2019-2039, 2013.

[132] E. A. Perpete, C. Lambert, V. Wathelet, J. Preat, and D. Jacquemin, "Ab initio studies of the lambda(max) of naphthoquinones dyes," *Spectrochim Acta A Mol Biomol Spectrosc*, vol. 68, no. 5, pp. 1326-33, Dec 31 2007.

[133] D. Jacquemin, I. Duchemin, and X. Blase, "0-0 Energies Using Hybrid Schemes: Benchmarks of TD-DFT, CIS(D), ADC(2), CC2, and BSE/GW formalisms for 80 Real-Life Compounds," *J Chem Theory Comput*, vol. 11, no. 11, pp. 5340-59, Nov 10 2015.

[134] C. Adamo et al., "Exploring excited states using time dependent density functional theory and density-based indexes," *J Coordination Chemistry Reviews*, vol. 304, pp. 166-178, 2015.

[135] F. J. Avila Ferrer, J. Cerezo, J. Soto, R. Improta, and F. Santoro, "First-principle computation of absorption and fluorescence spectra in solution accounting for vibronic structure, temperature effects and solvent inhomogenous broadening," *Computational and Theoretical Chemistry*, vol. 1040-1041, pp. 328-337, 2014.

[136] V. Barone, M. Biczysko, J. Bloino, L. Carta, and A. Pedone, "Reprint of “Environmental and dynamical effects on the optical properties of molecular systems by time-independent and time-dependent approaches: Coumarin derivatives as test cases”," *Computational and Theoretical Chemistry*, vol. 1040-1041, pp. 144-157, 2014.

[137] X. Blase, I. Duchemin, and D. Jacquemin, "The Bethe-Salpeter equation in chemistry: relations with TD-DFT, applications and challenges," *Chem Soc Rev*, vol. 47, no. 3, pp. 1022-1043, Feb 5 2018.

[138] A. Chantzis, A. D. Laurent, C. Adamo, and D. Jacquemin, "Is the Tamm-Dancoff Approximation Reliable for the Calculation of Absorption and Fluorescence Band Shapes?," *J Chem Theory Comput*, vol. 9, no. 10, pp. 4517-25, Oct 8 2013.

[139] A. Charaf-Eddin, T. Cauchy, F.-X. Felpin, and D. Jacquemin, "Vibronic spectra of organic electronic chromophores," *RSC Adv.*, vol. 4, no. 98, pp. 55466-55472, 2014.

[140] D. Jacquemin and C. Adamo, "Computational Molecular Electronic Spectroscopy with TD-DFT," *Top Curr Chem*, vol. 368, pp. 347-75, 2016.

[141] D. Jacquemin, E. Bremond, A. Planchat, I. Ciofini, and C. Adamo, "TD-DFT Vibronic Couplings in Anthraquinones: From Basis Set and Functional Benchmarks to Applications for Industrial Dyes," *J Chem Theory Comput*, vol. 7, no. 6, pp. 1882-92, Jun 14 2011.

[142] D. Jacquemin, B. Mennucci, and C. Adamo, "Excited-state calculations with TD-DFT: from benchmarks to simulations in complex environments," *Phys Chem Chem Phys*, vol. 13, no. 38, pp. 16987-98, Oct 14 2011.

[143] D. Jacquemin, C. Peltier, and I. Ciofini, "Visible spectrum of naphthazarin investigated through Time-Dependent Density Functional Theory," *Chemical Physics Letters*, vol. 493, no. 1-3, pp. 67-71, 2010.

[144] D. Jacquemin and E. A. Perpète, "Ab initio calculations of the colour of closed-ring diarylethenes: TD-DFT estimates for molecular switches," *Chemical Physics Letters*, vol. 429, no. 1-3, pp. 147-152, 2006.

[145] D. Jacquemin, E. A. Perpete, I. Ciofini, and C. Adamo, "Accurate simulation of optical properties in dyes," *Acc Chem Res*, vol. 42, no. 2, pp. 326-34, Feb 17 2009.

[146] D. Jacquemin, E. A. Perpete, F. Maurel, and A. Perrier, "TD-DFT simulations of the electronic properties of star-shaped photochromes," *Phys Chem Chem Phys*, vol. 12, no. 28, pp. 7994-8000, Jul 28 2010.

[147] D. Jacquemin et al., "Time-dependent density functional theory investigation of the absorption, fluorescence, and phosphorescence spectra of solvated coumarins," *J Chem Phys*, vol. 125, no. 16, p. 164324, Oct 28 2006.

[148] D. Jacquemin, E. A. Perpete, G. E. Scuseria, I. Ciofini, and C. Adamo, "TD-DFT Performance for the Visible Absorption Spectra of Organic Dyes: Conventional versus Long-Range Hybrids," *J Chem Theory Comput*, vol. 4, no. 1, pp. 123-35, Jan 2008.

[149] D. Jacquemin, A. Planchat, C. Adamo, and B. Mennucci, "TD-DFT Assessment of Functionals for Optical 0-0 Transitions in Solvated Dyes," *J Chem Theory Comput*, vol. 8, no. 7, pp. 2359-72, Jul 10 2012.

[150] D. Jacquemin, J. Preat, V. Wathelet, and E. A. Perpète, "Time-dependent density functional theory determination of the absorption spectra of naphthoquinones," *Chemical Physics*, vol. 328, no. 1-3, pp. 324-332, 2006.

[151] E. A. Perpète and D. Jacquemin, "TD-DFT benchmark for indigoïd dyes," *Journal of Molecular Structure: THEOCHEM*, vol. 914, no. 1-3, pp. 100-105, 2009.

[152] E. A. Perpete, C. Lambert, V. Wathelet, J. Preat, and D. Jacquemin, "Ab initio studies of the lambda(max) of naphthoquinones dyes," *Spectrochim Acta A Mol Biomol Spectrosc*, vol. 68, no. 5, pp. 1326-33, Dec 31 2007.

[153] A. Prlj, M. E. Sandoval-Salinas, D. Casanova, D. Jacquemin, and C. Corminboeuf, "Low-Lying pipi* States of Heteroaromatic Molecules: A Challenge for Excited State Methods," *J Chem Theory Comput*, vol. 12, no. 6, pp. 2652-60, Jun 14 2016.

[154] D. Rivero, M. Á. Fernández-González, and L. M. Frutos, "Tuning molecular excitation energy with external forces," *Computational and Theoretical Chemistry*, vol. 1040-1041, pp. 106-111, 2014.

[155] K. Sakata, N. Saito, and T. Honda, "Ab initio study of molecular structures and excited states in anthocyanidins," *Tetrahedron*, vol. 62, no. 15, pp. 3721-3731, 2006.

[156] L. Shen, H.-F. Ji, and H.-Y. Zhang, "A TD-DFT study on triplet excited-state properties of curcumin and its implications in elucidating the photosensitizing mechanisms of the pigment," *Chemical Physics Letters*, vol. 409, no. 4-6, pp. 300-303, 2005.

[157] M. B. Vincenzo Barone, Camille Latouche, Andrea Pasti, "Virtual eyes for technology and cultural heritage: towards computational strategy for new and old indigo-based dyes," *Theo Chem Acc*, 2015.

Chapter 1

Predicting Color Appearance of Pharmaceutical and Cosmetic Color Additive Mixtures in Ethanol using TD-DFT Calculations

It is possible to predict the overall color appearance of mixtures of color additive molecules used in pharmaceutical or cosmetic formulations using a combination of advanced *ab initio* methods, namely (time-independent) density functional theory (DFT) and time-dependent density functional theory (TD-DFT). Ground-state properties such as geometric structural conformations determined using density-functional theory (DFT) and excited state predictions originating from calculating theoretical electronic excitations performed using the time-dependent density-functional theory (TD-DFT) provide insight into not only the overall hue of a single molecule, but a combination of molecules containing chromophores. While the number of reputable literature studies providing information on chromophore-containing molecules and their derivatives simulated in a virtual environment increases on a regular basis [1-65], a single study addressing the viability of using computational advanced ab initio methods to determine the overall hue of a group of color molecules has not yet been conducted at this time[4]. This poses a significant concern for those seeking practical applications of existing literature studies because formulators rarely use only a single color molecule to achieve a desired hue. Furthermore, many color or other sensory additive molecules have been simulated under theoretical vapor phase conditions or *in vacuo* [1-20] in order to minimize the complexity of the functionals used by excluding solvation effects, thus significantly expediting computational processing time duration. Unfortunately, this

[4] As of November 3, 2018.

literature trend provides data that is less useful for experiential formulators, who carefully select solvents based on their properties as vehicles[5], binders[6], stabilizers, and to provide the optimal sensory experience of the user [66-69] . Typically, liquid or aqueous media is used in practice, with the most common solvent of choice being water [73-75] followed by ethanol [76-78] with a nearly ubiquitous presence throughout countless formulations available [74-76]. This experiment sought to determine if the additional solvation effects, while computationally more demanding, were necessary for effective prediction of the maximum absorbance spectra peak of a single color additive molecule or a mixture of two to three color molecules, or if vapor phase calculations indeed produced sufficient data for further analysis.

Materials and Methods

Vertical excitation energies were calculated from restricted singlet excited states using the following density functional based on the Kohn-Sham DFT approximation [79]:

$$\rho(\mathrm{r}) = 2\sum_{i}^{occ.} |\psi_i(r)|^2$$

This functional was used to generate multiple theoretical single point energies in order to measure the maximum absorbance spectral peak to indicate the most prominent (or overall) hue of the color additive molecule or mixture simulated. In addition, the oscillator strength (*f*) was also calculated in TD-DFT using normalized eigenvectors to

[5] A vehicle is defined as a medium for the dispersion of particles. In color cosmetics, the term usually refers to the liquid carrier for the solid pigment and filler particles.[66]

[6] A binder is added to tablet formulations to add cohesiveness to powders, thus providing the necessary bonding to form granules, which under compaction form a cohesive mass or a compact which is referred to as a "tablet". [70] The encapsulation concept has also been applied in development of "nutraceuticals" in which vitamins, minerals, amino acids, hormones, or other isolated food ingredients beneficial for human health are encapsulated in tablet form and are delivered via oral ingestion. [71,72]

determine if the theoretical intensity could be comparable to experimentally-measurable quantities of fluorescence. Due to the high saturation of commercially-available color molecules used in this study, experimental fluorescence data was not able to be compared to theoretical numerical values of oscillator strength. Therefore, this phenomenon is outside the scope of this work as the main objective is to investigate an ideal method of using DFT and TD-DFT to measure the hue of an individual molecule or its mixture with other molecules.

The basis set 6-31+G* was used for both DFT and TD-DFT calculations. The 6-31+G* basis set describes the following conditions regarding calculations being performed. The number "6" indicates that the inner-shell or "1s" orbital on the carbon atom is given by the sum of 6 Gaussian functions (hence "G" for Gaussian). The hyphen indicates a split valence (SV) basis set [80-81], which tells us that the valence 2s and 2p orbitals are each represented by a pair of Slater orbitals. One of these Slater orbitals, the smaller one, (2s), is represented by a sum of 3 Gaussian functions (hence the number 3). The larger Slater orbital (2p), is represented by a single Gaussian function—hence the number "1". The time required to evaluate the elements of the "secular determinant" depends on the number of functionals used. Today, Gaussian orbitals are more widely used throughout computational chemistry as opposed to their predecessor Slater transition orbitals (STOs) that are more typical of Hartree-Fock theory. Using HF theory is now considered passé due to the less accurate calculation using STOs (see reference [80]). Basis sets generated from a sum of two Slater orbitals with different orbital exponents are called double-zeta basis sets because each orbital in the basis set is the sum of two Slater orbitals that differ only in their value of the orbital exponent, ζ (zeta) [80,81]. In general,

only the valence orbitals are expressed by a double-zeta representation. The inner-shell electrons are still described by a single Slater orbital. Basis sets that describe the inner shell electrons by a single Slater orbital and the valence shell electrons by a sum of Slater orbitals are commonly referred to as "split valence" basis sets. McQuarrie [80] has a thoroughly detailed discussion of the basics of STOs and Gaussian orbitals used in common basis sets. This work will exemplify the use of the 6-31+G* basis set to model a large quantity of atoms combined within a single workspace in order to verify their use as an advanced ab initio method to approximate the individual and combined excitation energies of color additives using DFT and TD-DFT calculations for reliable maximum absorbance spectral peak responsivity ranges at inexpensive computational cost.

In this study, the hybrid functional basis set Becke-3-Lee-Yang-Parr (abbreviated B3LYP) was used. This exchange correlation functional was originally refined by Becke to eliminate the term U_{XC}^{0} because the electron gas model is not appropriate to use as one approaches the exchange-only limit of $\lambda = 0$ for molecular bonds [82]. By employing the Lee-Yang-Parr correlation functional with gradient term and the standard local correlation functional using Vosko, Wilk, and Nusair (VWN), we arrive at the B3LYP hybrid density functional:

$$E_{XC}^{B3LYP} = (1 - a_0)E_X^{LSDA} + a_0 E_X^{HF} + a_X \Delta E_X^{B88} + a_C E_C^{LYP} + (1 - a_c)E_C^{VWN}$$

This hybrid density functional is used to calculate "zero-point" energies, also known as "single-point" energies as they are referred to throughout this body of work. According to Leach [82], one of the most important developments for practical application of DFT were methods for calculating analytical gradients of the energy with

respect to the nuclear coordinates, this enables geometries to be optimized. A potential problem when using DFT is that the use of grid-based integration "schemes" makes it difficult to provide an exact expression for the gradients However, errors are generally very small and do not pose a significant problem [82]. Numerous studies have reported the success of hybrid functionals for modeling excitation energies of molecular structures that vary widely [1-9,20,21,25-27,30-33,35-47,49-52,55,58-64], therefore the B3LYP functional was applied for theoretical calculations presented here.

Polarization terms, represented as "p" or an asterisk (*) in a basis set, exist to account for the fact that electron distribution around each hydrogen atom does not remain spherically symmetrical as two hydrogen atoms approach each other. According to [80], this can be accounted for using the following methodology: if we let the axis between nuclei or "internuclei axis" be the z-axis, we can construct a molecular orbital form a linear combination of a 1s orbital and a $2p_z$ orbital on each hydrogen atom instead of from just a 1s orbital. This allows us to account for the fact that atomic orbitals distort as atoms are brought together. Such an effect is called a "polarization effect".

Polarization is accounted for by adding orbitals of higher orbital angular momentum quantum number l to the mathematical expression for a given atomic orbital, just as we added a $2p_z$ orbital to a 1s hydrogen orbital previously. For example, *d* character can be added to the description of the valence electrons in 2p orbitals, thereby providing a representation of the asymmetric shape of the electron density along the chemical bonds involving 2p orbitals. The addition of 3d orbitals to the 2p orbitals of the atoms in the 2nd row elements of the periodic table is denoted by a single asterisk, * (as in the basis set used throughout this work, 6-31+G*). Since unpolarized basis sets give

poor results for other properties such as bond lengths and energies, their use is generally discouraged nowadays [81]. Some basis sets have more than one asterisk represented[7]. For instance, a 6-31G** basis set is used for systems in which hydrogen bonding is known to occur. However, in this work, only addition of a single set of Gaussian 3d functions was added to the split valence basis set description of each non-hydrogen atom.

By adding a single set of polarization functions to non-hydrogen atoms, the split-valence results for valence excitations can be considerably improved at still moderate computational cost [81]. There is also a dramatic improvement in the oscillator strength of the dipole-allowed transition from a valence shell of l quantum number l_v generally involves orbitals with L-quantum number lv+1 [80,81,83] Basis sets of split-valence polarization, abbreviated SV(P) or similar quality are often the first choice for TD-DFT applications to large systems [81], especially if only the lowest states are of interest and or diffuse excitations are quenched (such as in the case of a polar environment)[8]. Today, triple- and quadruple zeta basis sets are commonplace and have been used to simulate a variety of chromophore-containing molecules [2,6,7,9,21,22,26,27,30,32,35-37,39,40-47,49-50,56,58-60,64]. In this work, due to the large quantity of molecules of varied dye classes—thus of varied molecular structure and constituent atoms of color-inducing functional groups—and the range of atoms extending from hydrogen to sulfur (as in the sulfonated salt groups $[SO_3]^-$ as indicated in other molecules studied), the 6-31G basis set

[7] A double asterisk indicates that polarization is also being taken into account for orbital descriptors on hydrogen atoms by adding 2p orbitals to hydrogen 1s orbitals. [80]

[8] Split valence polarized (SVP) basis sets mainly describe carbon-hydrogen σ* type excitation in molecules which usually occur in the far ultraviolet and are rarely studied in applications. This is useful for low-lying π-π* excitation states that closely resemble ground-state excitation energies. In an example of naphthalene TD-DFT calculations [81], going from SV(P) to SVP has no significant effect. This may be different for molecules containing strongly polarized hydrogen-element or hydrogen bridge bonds, or strong charge transfer (CT) properties as will be further discussed in the forthcoming chapters.

was utilized throughout to maintain consistency among large data sets and to simplify analysis.

"Diffuse functions" are another function that is indicated in the choice of basis set. Adding a [1*s*1*p*1*d*1*f*] set of primitive Gaussian functionals with small exponents are called "diffuse functions". The effect of diffuse augmentation is that a moderate downward shift of less than 0.1 eV for the first two singlet excitation energies is noted [81]. This behavior is typical of lower valence excited states having a similar extent as the ground state. Diffuse functions can have a significant effect on higher excitations as well. See [81] for some examples of this effect.

While polarization functions are necessary for a qualitatively correct description of transition dipole moments, additional diffuse polarization functions can account for radial nodes in the first-order Kohn-Sham orbitals, which further improves computed transition moments and oscillator strengths. These benefits have to be contrasted with a significant increase of the computational cost. In the naphthalene example explored by [81], using the aug-SV(P) basis increases computational time by a factor of four. In molecules with more than 30 to 40 atoms, most excitations of interest are valence excitations, and the use of diffuse augmentation may become prohibitively expensive because the large extent of these functions confounds integral prescreening [81]. This work required calculation of both geometry optimizations and excitations in gas phase and with relevant solvent effects of molecules containing between 30 and 97 atoms at any given time, representing the total number of constituent atoms in the indigo molecule and the heterotrimer, respectively. Therefore, this study serves as an indication of the feasibility of applying polarization functions to calculate useful transition moments and

approximate oscillator strengths of the realistic structures of color additive molecules in their entirety while also gauging computational processing time throughout all simulations.

Polarization (* or "p") and diffuse (+ or "s") functions can be used to determine more accurate geometry optimizations of color additives in vapor phase and in ethanol solvent using a "Poisson-Boltzmann Finite" elements (PBF) continuum solvation model. PBF is based on an iterative solution of the Poisson-Boltzmann equation until the electric potential on the molecular surface—with contributions from the solvent and the solute—reaches equilibrium [84]. This model uses empirical corrections to account for first solvation shell effects, which are not captured by pure implicit solvation models, and calculations exhibit very small average solvation energy errors[9] (particularly for ionic species) that are comparable to experimental errors in practice [84]. In this study, the input parameters selected to simulate solvation effects using the Poisson-Boltzmann Finite elements according to the computational software utilized are listed in Table 1. Note that probe radius (Å, Angstroms) was calculated automatically based on the structure(s) present in the workspace and thus was not input manually.

TABLE I

Input parameters for solvation effects using PBF elements according to Schrodinger Maestro Jaguar software[10]

Solvent	ϵ_0	Molecular Weight (g/mol)	Density (g/cm^3)
Water	80.37	18.02	0.99823
Ethanol	24.85	46.07	0.785

[9] Namely, approximately 3 kcal/mole for ionic species, and ~1 kcal/mole for neutral species) [84].
[10] Numerical values obtained from Schrodinger Maestro Jaguar Preset value, 2015-2 edition. Jaguar, Schrödinger, LLC, New York, NY, 2015. [84]

At times, effective core potential (ECP) using the Los Alamos basis set LAV2P was incorporated into the basis set for calculations. This basis set calculates linear combinations of molecular orbitals using Gaussian functionals according to the same 6-31+G* basis set as described above, but differs in that effective core potential provides adequate data for systems with large anions containing atoms ranging from hydrogen (H) to krypton (Kr) [85]. More specifically, the atoms hydrogen through argon are described with the 6-31G family of basis sets while the heavier atoms are modeled using the LANL2DZ basis set (with a neon core for sodium through argon) applying effective core potential for all atoms larger than neon. Due to the variety of elements constituting the color additive molecules analyzed, ECP was incorporated for structures containing heavier atoms with larger numbers of electrons such that the existing diffuse functions indicated by "+" are not sufficient.

These advanced *ab initio* methods were used to investigate the properties of three FDA-certified color additive compounds approved for externally-applied drugs: (i) D&C Blue No. 6, commonly known as "Indigo" [86-89,90], (ii) D&C Yellow No. 11, also known as "SS Quinoline Yellow" [88-92], and (iii) D&C Red No. 36, also known as "Pigment Red 4" or "American Vermillion" [88-89,93]. Their characteristic structures were built in a computational workspace as shown in Figures 3, 4, and 5, respectively. Individual color additive molecules, heterodimers, and a heterotrimer (containing all three of the molecules in a single workspace) were simulated in order to theoretically measure their corresponding optical properties.

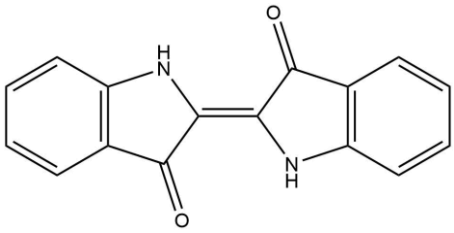

Fig. 3. D&C Blue No. 6 “Indigo” structure

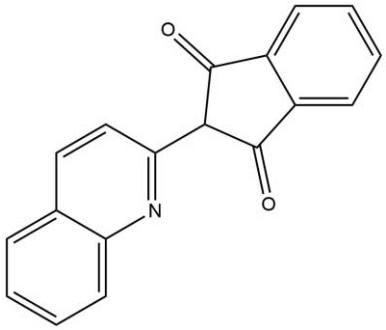

Fig. 4. D&C Yellow No. 11 “SS Quinoline Yellow” structure

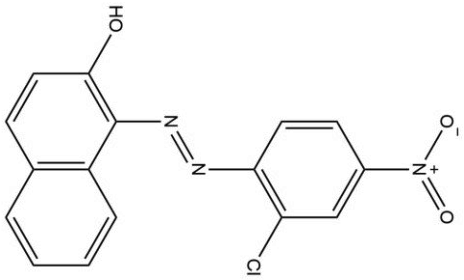

Fig. 5. D&C Red No. 36 “American Vermillion” structure

Optimal conformational structures in vapor phase and ethanol solvent were modeled using the empirical [94] molecular mechanics method MM2. The output file generated using MM2 methods was then submitted as the input file for DFT geometry optimizations using the double-zeta hybrid functional B3LYP/6-31+G*. The resulting output file served as the input file for subsequent TD-DFT single-point-energy (SPE) calculations used to generate three restricted singlet excitation states to predict vertical

excitations. The three single point energy values generated theoretical maximum absorption peak spectral responsivities ("theoretical" λ_{max}) and oscillator strengths (*f*) that were input into a mean Gaussian normalization function created using Microsoft Excel to then generate the overall theoretical maximum absorption peak spectral responsivities ("theoretical" λ_{max}) and oscillator strengths (*f*) for the molecule(s) simulated.

TABLE II

Experimental concentrations prepared of D&C Blue No. 6, D&C Yellow No. 11, and D&C Red No. 36 batches in ethanol solvent.

Concentration	mM	M
10 mM	10	1×10^{1}
1 mM	1	1×10^{0}
0.1 mM	0.1	1×10^{-1}

For practical comparison, batch samples of dilute (1 mM) and saturated (10 mM) color additive mixtures were prepared in ethanol solvent in order to measure "experimental" λ_{max} values using a conventional UV-visible spectrophotometer. Concentrations of the individual color additives and their heterodimeric and -trimeric mixtures were prepared according to the molar conversions as shown in Table 2.

Experimental Data

The figure below shows the color appearance of mixtures of individual color molecules in ethanol solvent. D&C Blue No. 6, D&C Yellow No. 11, and D&C Red No. 36 are shown from left to right in 5 mL of ethanol solvent. Each color additive-solvent mixture has a noticeably distinct color appearance; therefore, these experimental batches will provide λ_{max} values that will serve as a "benchmark" for comparison to theoretical data generated using computational means.

Fig. 6. Individual color additive molecule experimental batches prepared in ethanol solvent.

Figure 7 depicts the color appearance of heterodimeric mixtures of the color molecules selected for analysis in this study. These are combinations of two different molecules with ethanol solvent, as shown from left to right: D&C Blue No. 6 and D&C Yellow No. 11 (Indigo—SS Quinoline Yellow), D&C Blue No. 6 and D&C Red No. 36 (Indigo—American Vermillion), and D&C Yellow No. 11 and D&C Red No. 36 (SS Quinoline Yellow—American Vermillion). The overall hues are clearly discernable, however the challenge here is to see if DFT and TD-DFT provide adequate vertical

excitation data that can successfully be converted into theoretical λ_{max} values for experimental comparison.

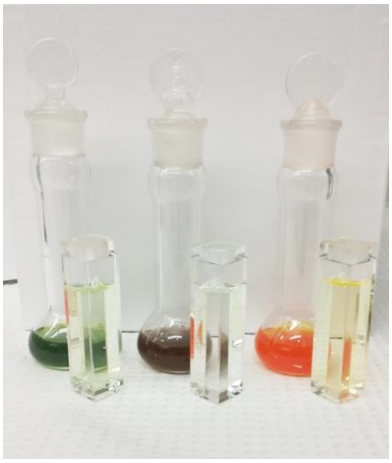

Fig. 7. Heterodimeric mixtures of color additive molecule experimental batches prepared in ethanol solvent

Figure 8 indicates the overall color appearance of the heterotrimeric mixture of all three color molecules analyzed in ethanol solvent.

Fig. 8. Heterotrimeric mixture of color additive molecule experimental batches prepared in ethanol solvent.

The hue of this mixture was a little puzzling considering the subtractive method of mixing states that the three primary colors should indicate a dull brown or black hue when mixed in equal quantities [95]. The preparation in the cuvette has an experimental

λ_{max} value that is nearly identical to the Despite this “irregularity”, this observation made further analysis of the optical properties of this mixture using computational methods all the more interesting.

Theoretical Data

The following theoretical data was generated from DFT geometry calculations incorporating no solvation effects (“gas” or “vapor phase”) or the effects of ethanol solvent using the PBF continuum model as discussed earlier. The data from these output files served as the input file for TD-DFT SPE calculations of three theoretical singlet excited states. TD-DFT SPE calculations were also calculated using either no solvation effects (for simulation in gas or vapor phase), or using ethanol solvation effects using the PBF elements continuum model. As described above, comparison of the theoretical λ_{max} value obtained to the experimental λ_{max} served to indicate whether the computational input parameters utilized were truly effective at predicting realistic values of maximum absorbance spectral peak responsivity of an individual color additive or a combination of color additive molecules.

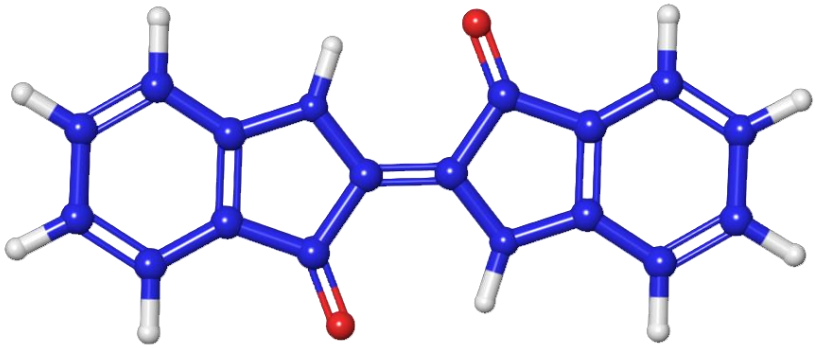

Fig. 9. D&C Blue No. 6 “Indigo” single-point-energy (SPE) output file

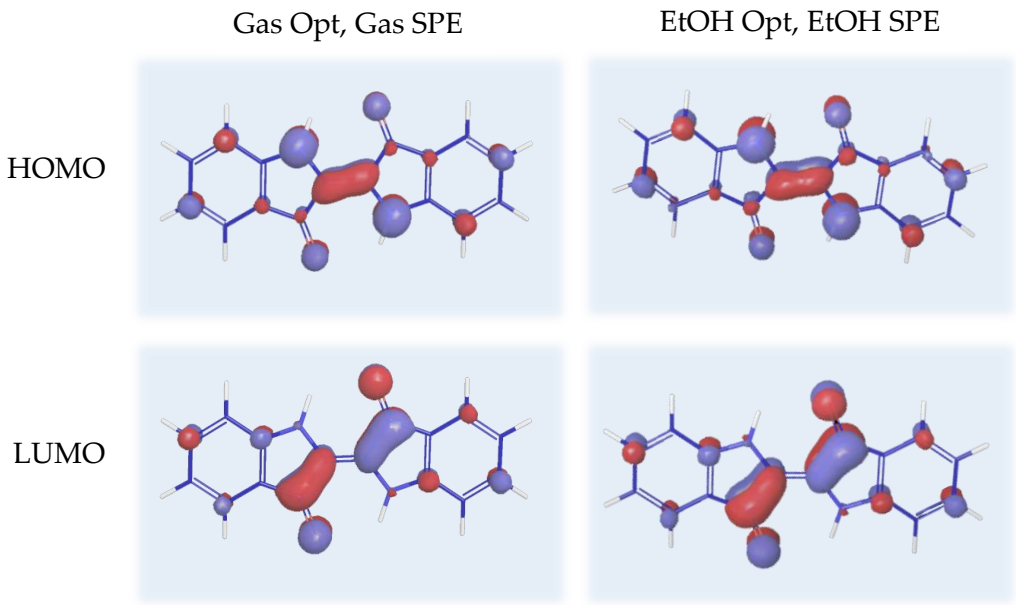

Fig. 10. D&C Blue No. 6 “Indigo” single-point-energy (SPE) output file containing calculated HOMO and LUMO surfaces

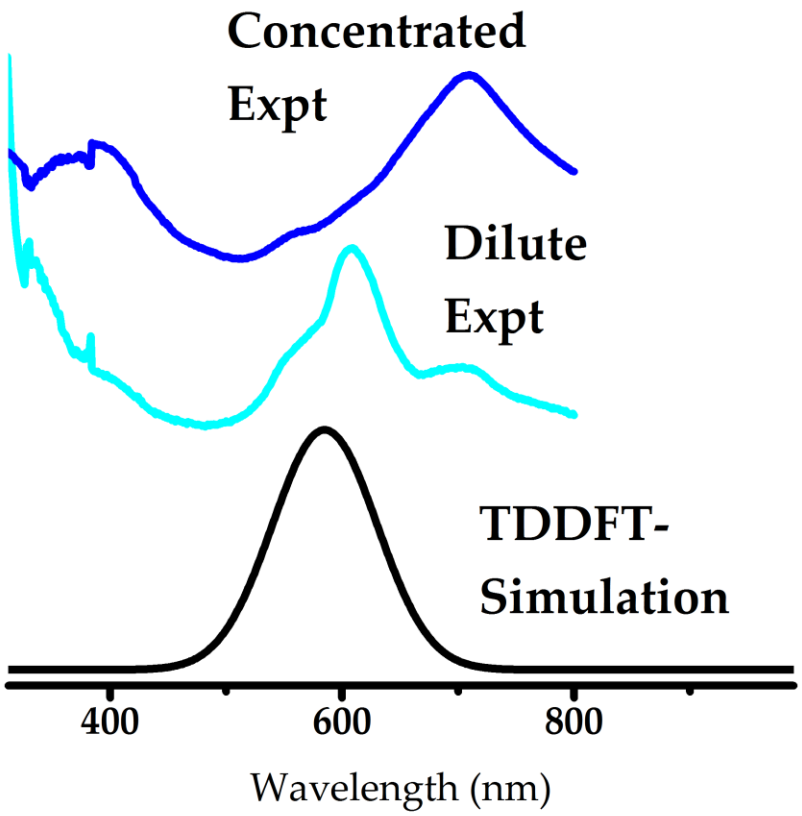

Fig. 11. D&C Blue No. 6 concentrated, dilute, and TD-DFT simulation absorbance spectra data

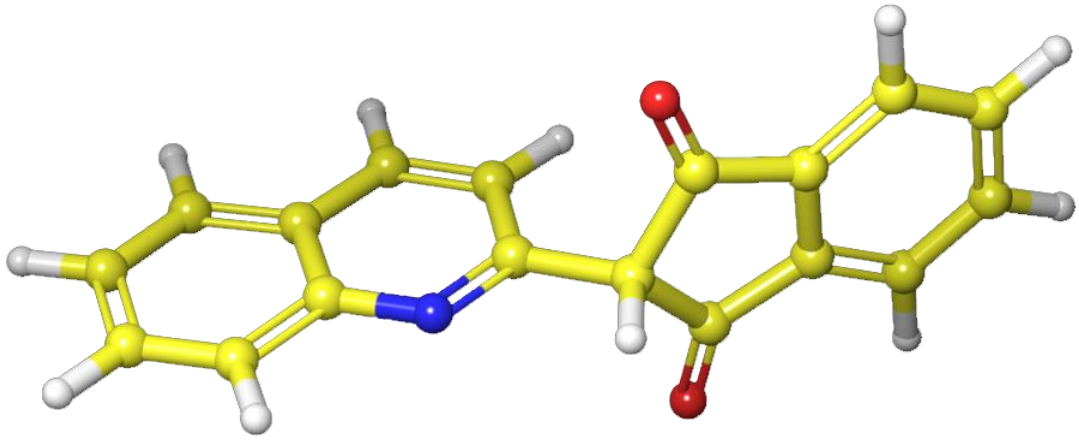

Fig. 12. D&C Yellow No. 11 “SS Quinoline Yellow” single-point-energy (SPE) output file.

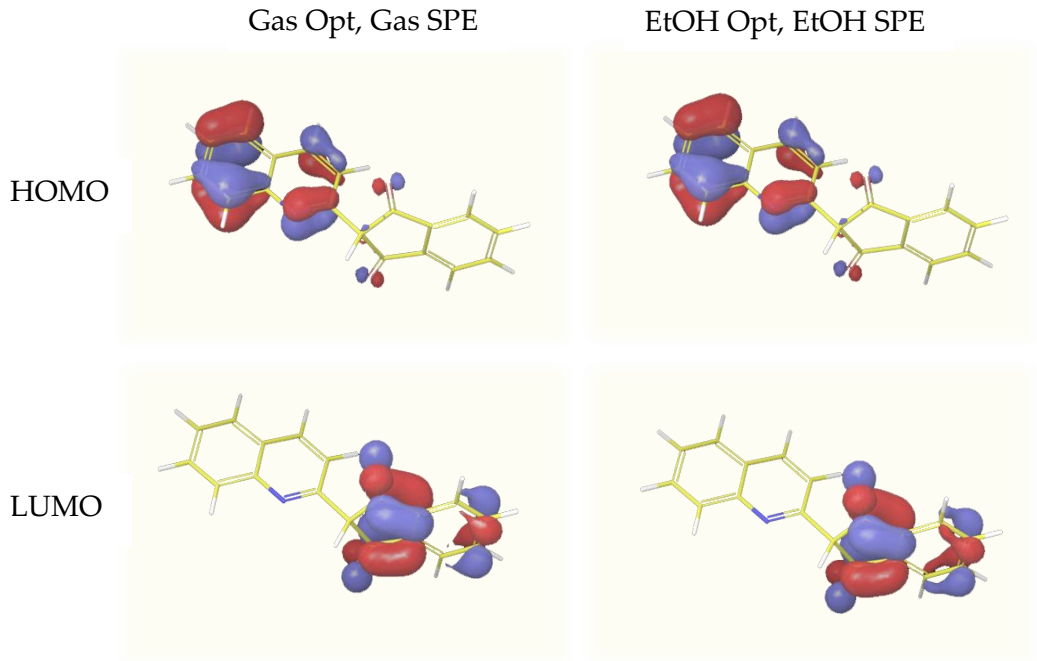

Fig. 13. D&C Yellow No. 11 “SS Quinoline Yellow” single-point-energy (SPE) output file containing calculated HOMO and LUMO surfaces.

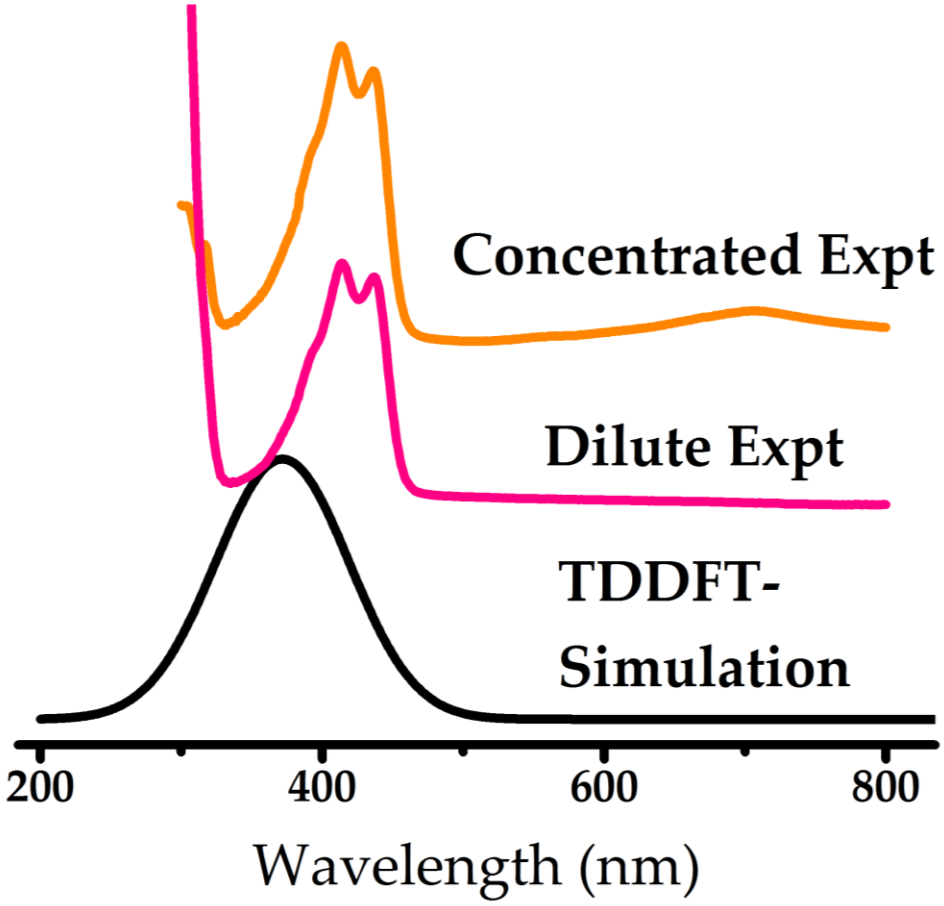

Fig. 14. D&C Yellow No. 11 concentrated, dilute, and TD-DFT simulation absorbance spectra data.

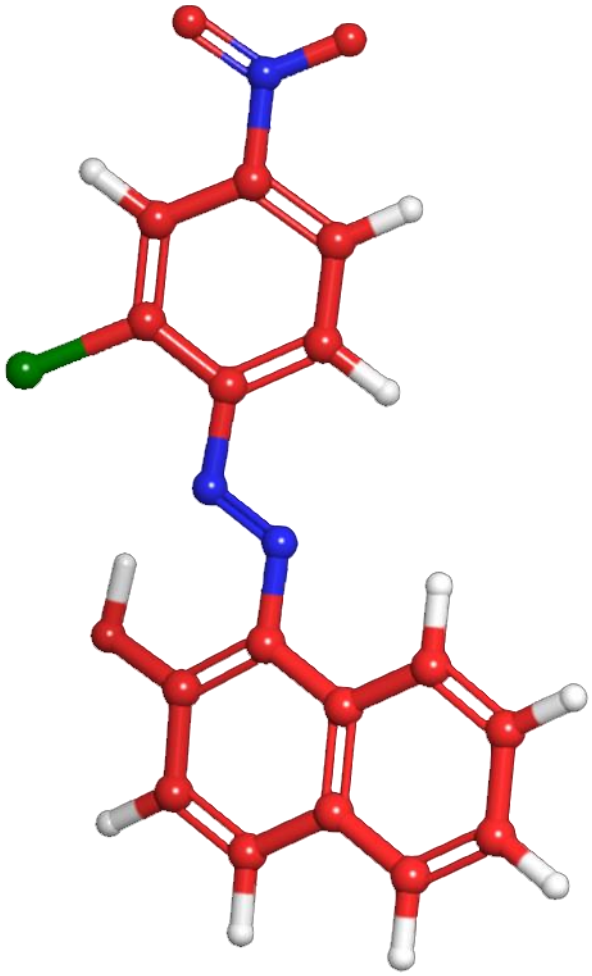

Fig. 15. D&C Red No. 36 “Pigment Red 4” single-point energy (SPE) output file.

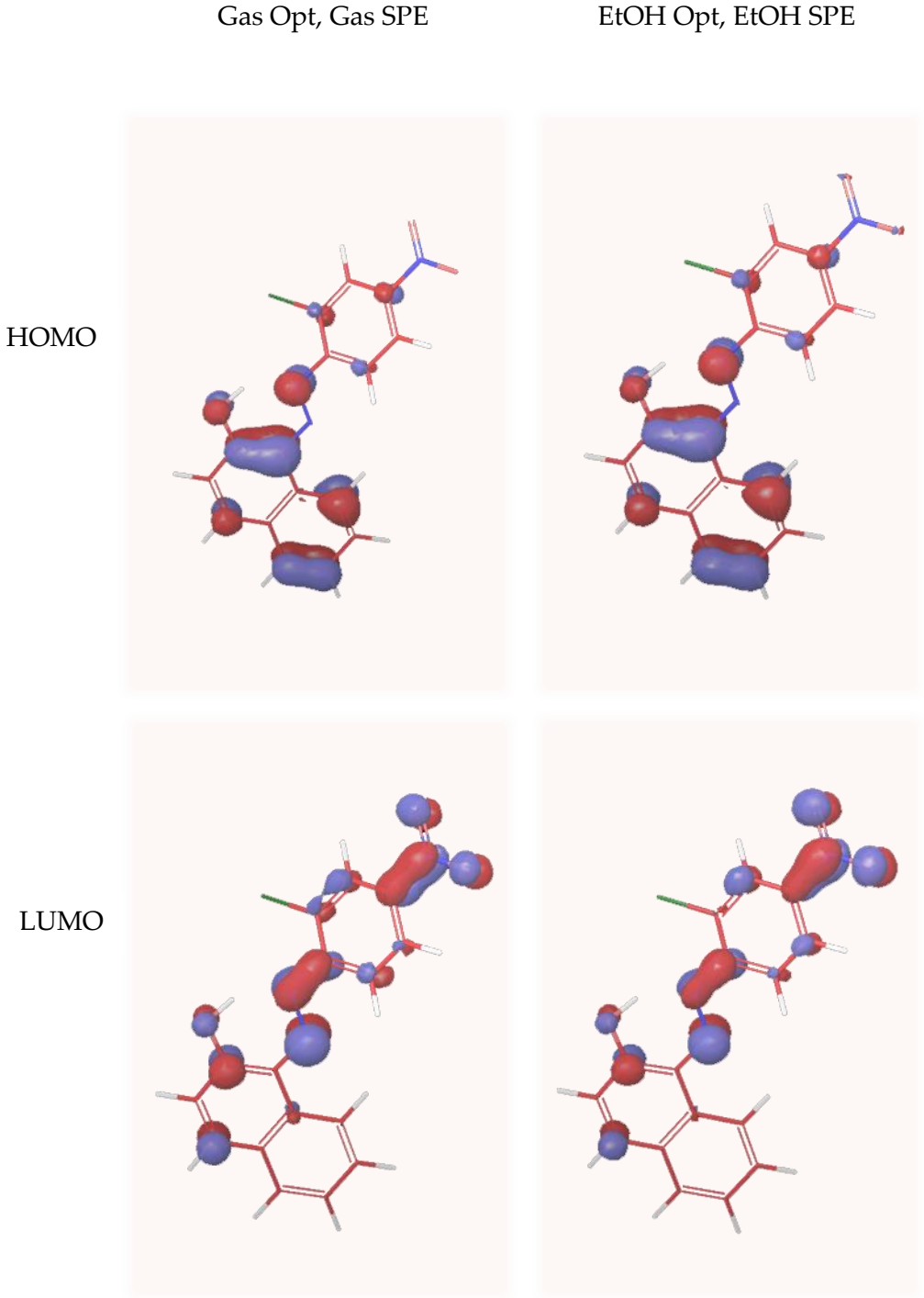

Fig. 16. D&C Red No. 36 “Pigment Red 4” single-point-energy (SPE) output file containing calculated HOMO and LUMO surfaces.

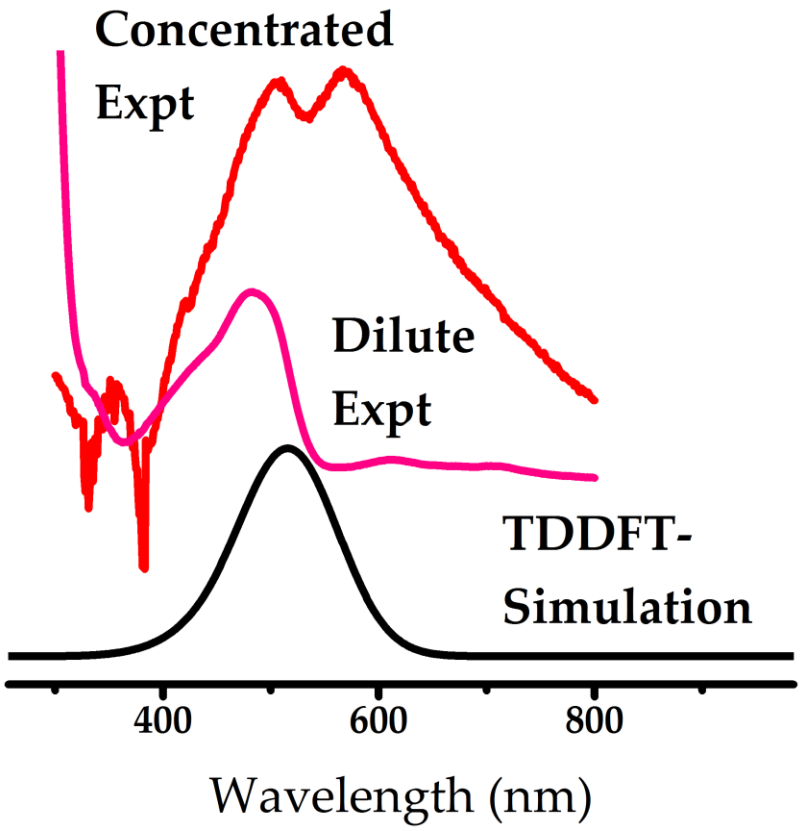

Fig. 17. D&C Red No. 36 concentrated, dilute, and TD-DFT simulation absorbance spectra data.

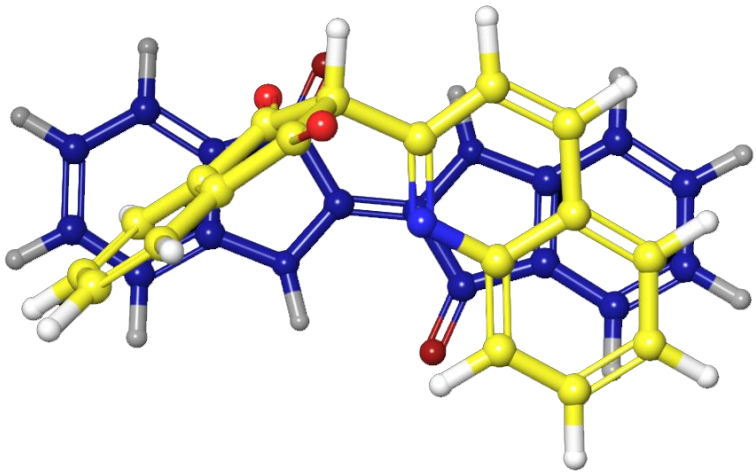

Fig. 18. D&C Blue No. 6 and D&C Yellow No. 11 heterodimeric mixture single-point energy (SPE) output file.

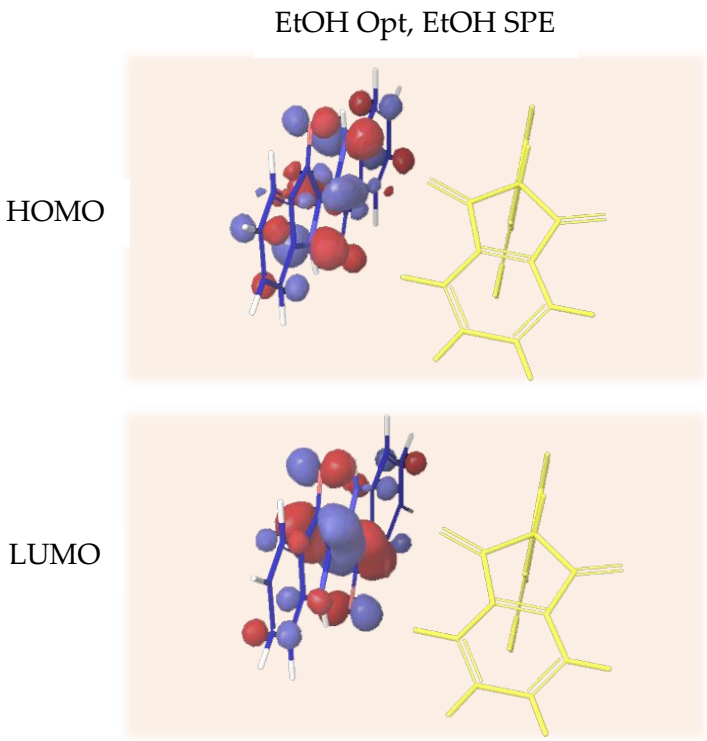

Fig. 19. D&C Blue No. 6 and D&C Yellow No. 11 single-point-energy (SPE) output file containing calculated HOMO and LUMO surfaces.

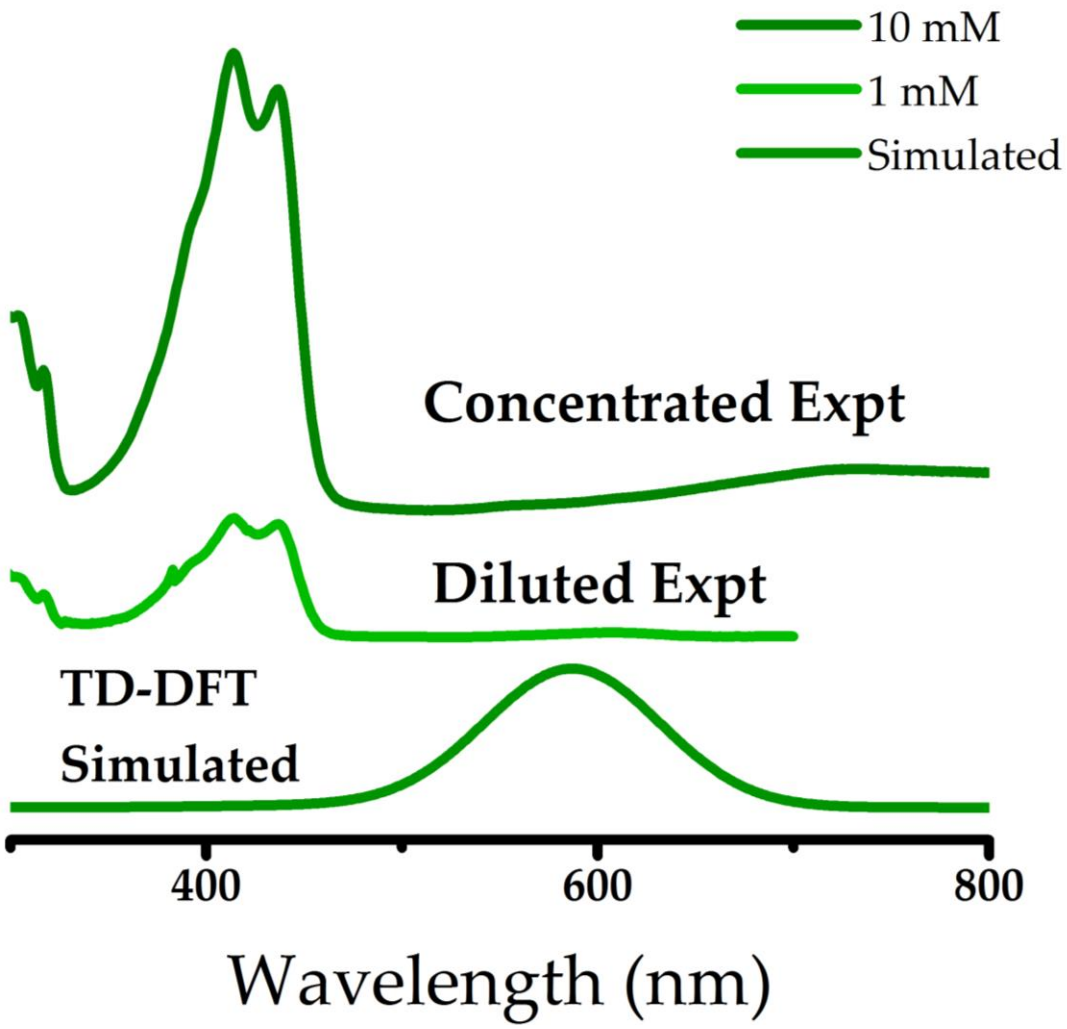

Fig. 20. D&C Blue No. 6 and D&C Yellow No. 11 heterodimeric mixture concentrated, dilute, and TD-DFT simulation absorbance spectra data.

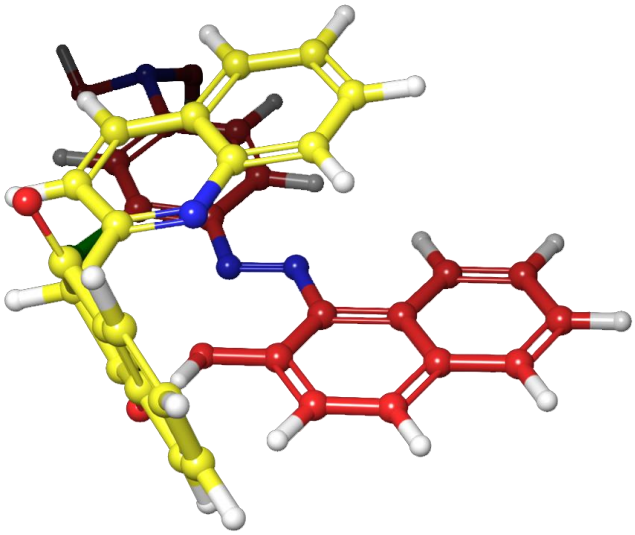

Fig. 21. D&C Yellow No. 11 and D&C Red No. 36 heterodimeric mixture single-point energy (SPE) output file.

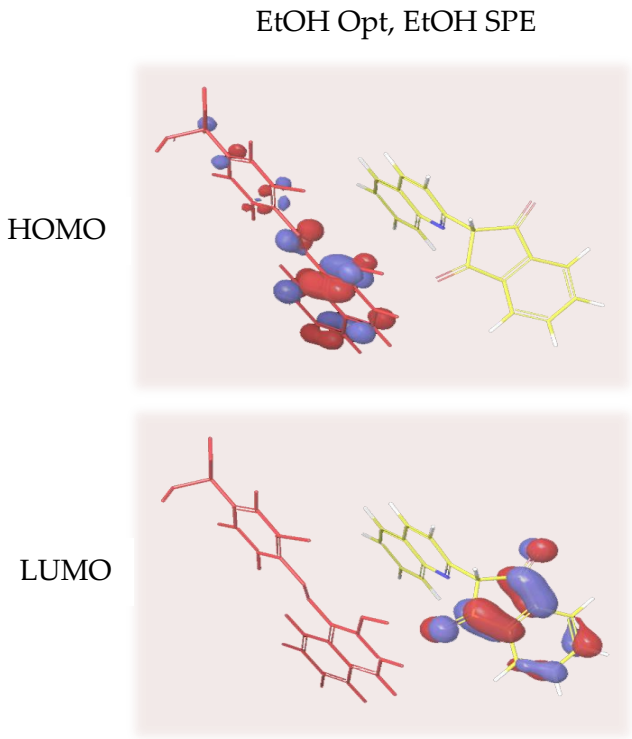

Fig. 22. D&C Yellow No. 11 and D&C Red No. 36 single-point-energy (SPE) output file containing calculated HOMO and LUMO surfaces.

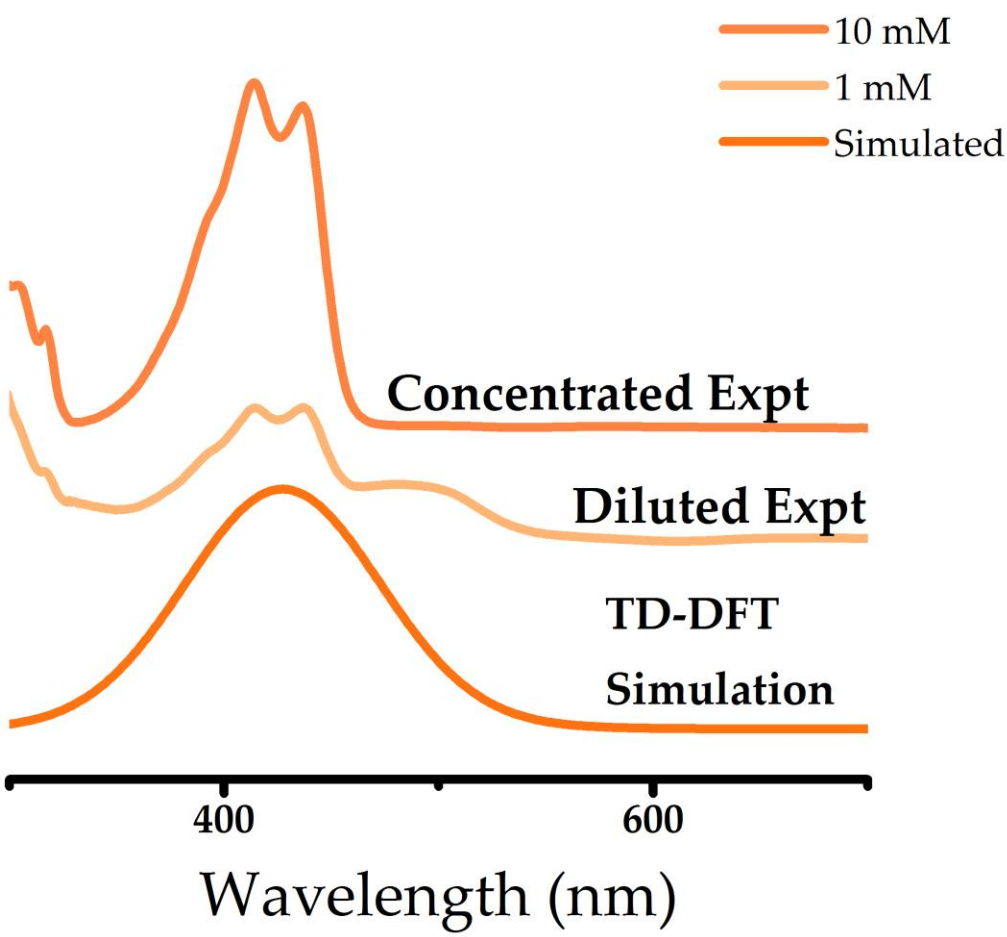

Fig. 23. D&C Yellow No. 11 and D&C Red No. 36 heterodimeric mixture concentrated, dilute, and TD-DFT simulation absorbance spectra data.

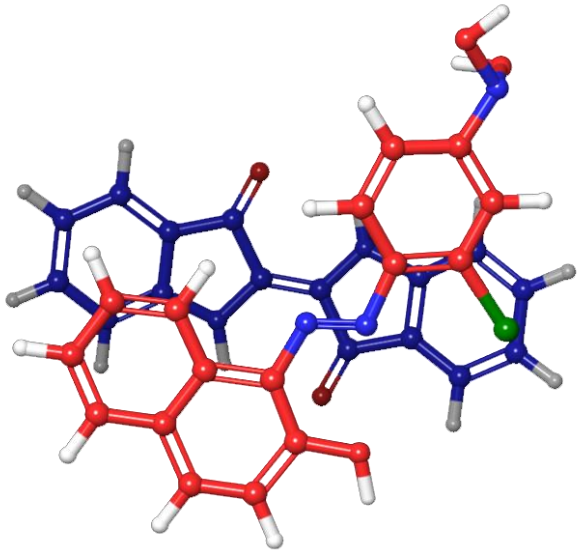

Fig. 24. D&C Blue No. 6 and D&C Red No. 36 heterodimeric mixture single-point energy (SPE) output file.

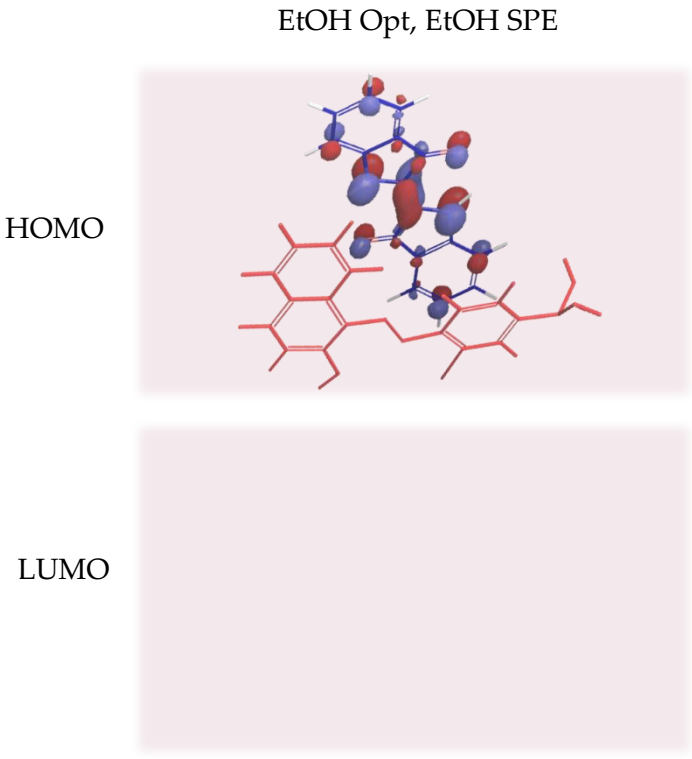

Fig. 25. D&C Blue No. 6 and D&C Red No. 36 single-point-energy (SPE) output file containing calculated HOMO and LUMO surfaces.

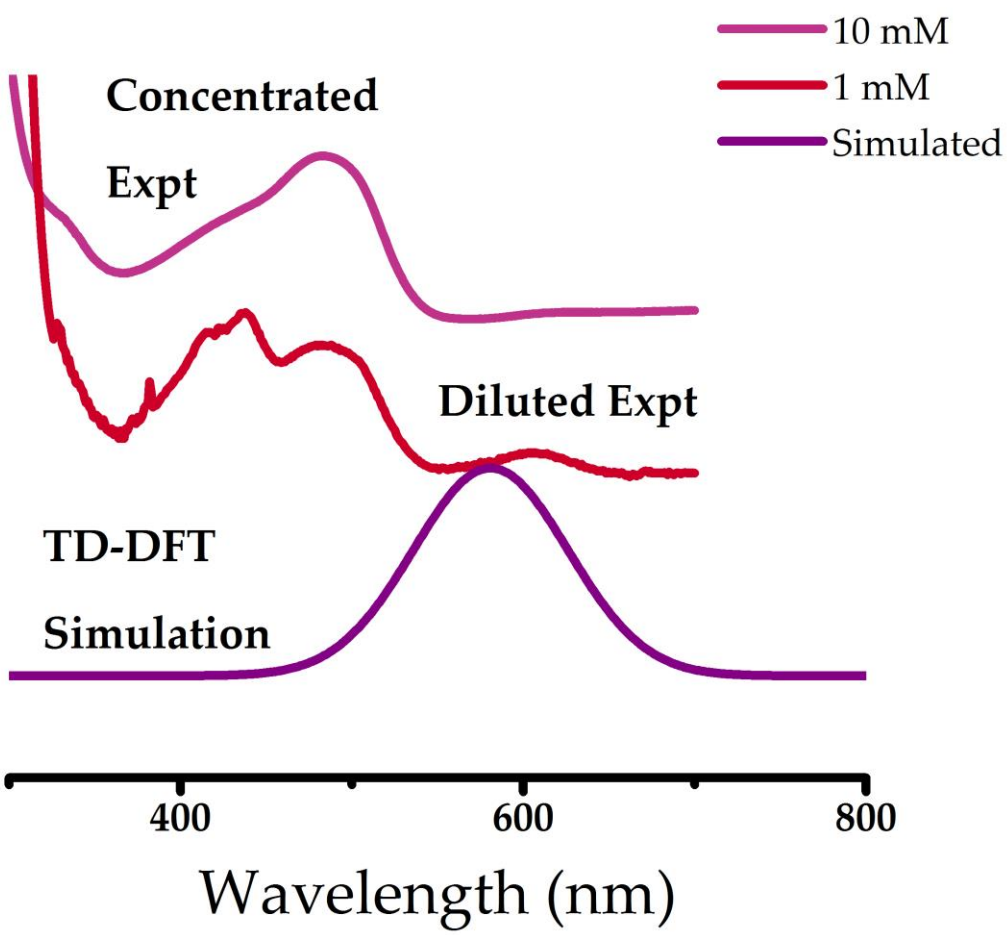

Fig. 26. D&C Blue No. 6 and D&C Red No. 36 heterodimeric mixture concentrated, dilute, and TD-DFT simulation absorbance spectra data

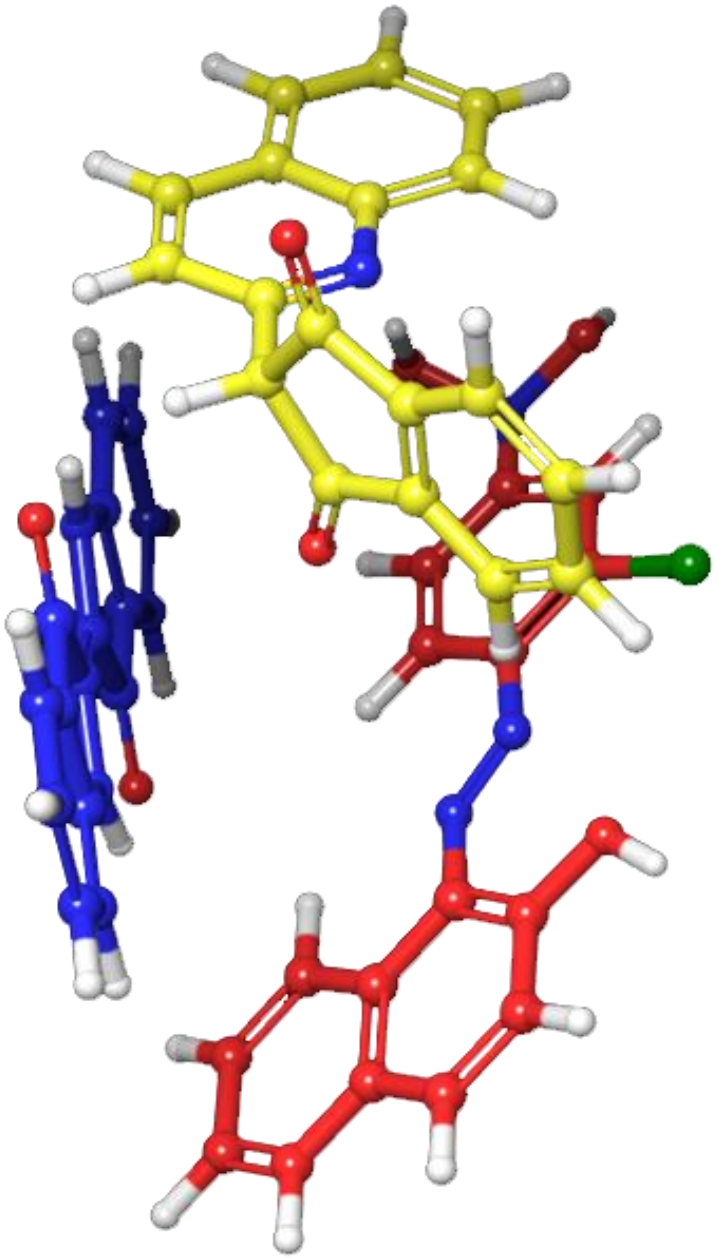

Fig. 27. D&C Blue No. 6, D&C Yellow No. 11, and D&C Red No. 36 heterotrimeric mixture single-point energy (SPE) output file

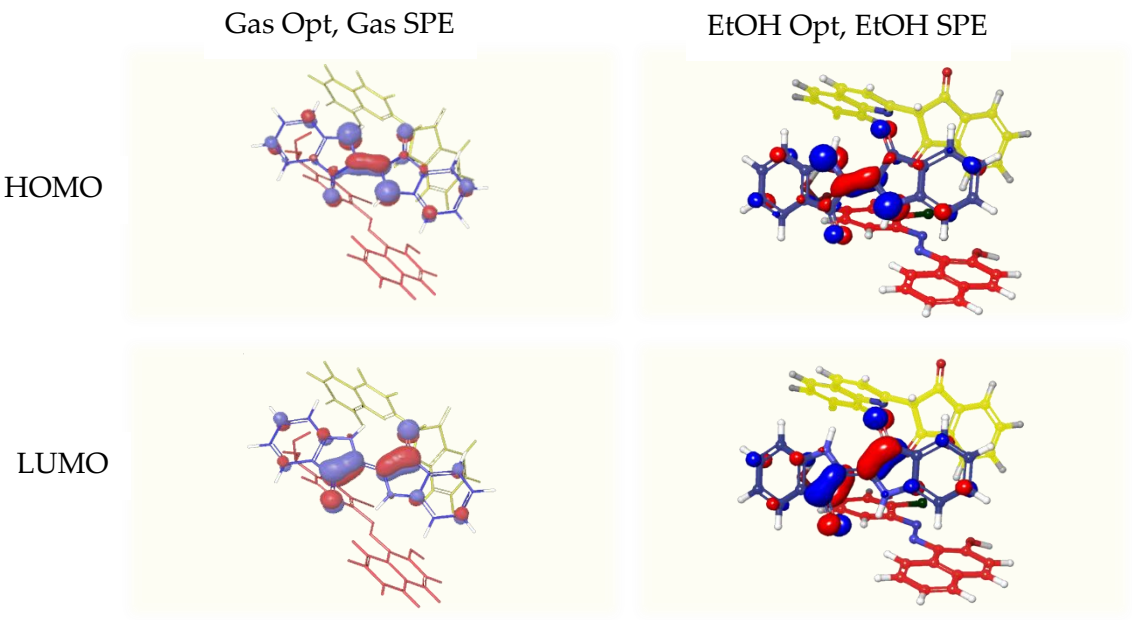

Fig. 28. D&C Blue No. 6, D&C Yellow No. 11, and D&C Red No. 36 single-point-energy (SPE) output file containing calculated HOMO and LUMO surfaces.

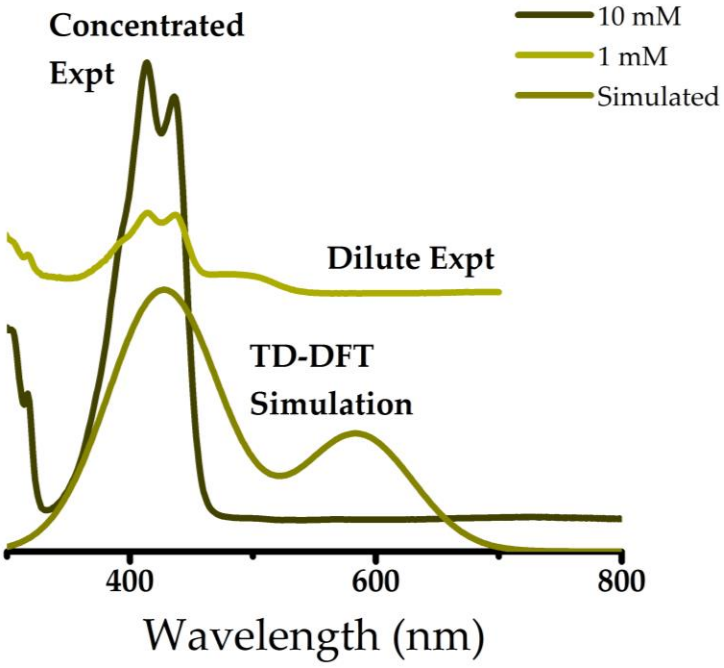

Fig. 29. D&C Blue No. 6, D&C Yellow No. 11, and D&C Red No. 36 heterotrimeric mixture concentrated, dilute, and TD-DFT simulation absorbance spectra data.

Individual Color Additive Molecules. Experimental λ_{max} comparison to theoretical TD-DFT simulation maximum absorbance spectral peak responsivity (λ_{max}) under 3 simulation conditions.

TABLE III

Individual color additive molecule experimental λ_{max} comparison to theoretical λ_{max} using gas phase geometry optimization followed by gas phase single-point energy (SPE) calculation.

D&C Molecule Name	Single-Point Energy Restricted Singlet Excited States (Gas Opt, Gas SPE)			TD-DFT Theoretical λmax	Dilute Experimental λmax	Concentrated Experimental λmax	Dilute – TD-DFT Δλmax Δintensity	Concentrated – TD-DFT Δλmax Δintensity
D&C Blue No. 6	552.16 (*f*=0.2789)	457.64 (*f*=0.0000)	433.70 (*f*=0.0000)	551.90 (*f*=0.2807)	608.55 (*f*=0.0379) [IP: 582.45 (0.0261)] 708.73 (*f*=0.0195) [IP: 667.70 (0.0181)]	709.68 (*f*=0.0599)	+56.65 (-0.2428) [+30.55 (-0.2546)], +156.83 (-0.2612) [+115.80 (0.2626)]	+157.78 (-0.2208)
D&C Yellow No. 11	399.98 (*f*=0.0034)	353.29 (*f*=0.0013)	349.56 (*f*=0.0001)	388.73 (*f*=0.0044)	414.31 (*f*=0.2937), 437.23 (*f*=0.2780)	413.62 (*f*=0.2236), 436.71 (*f*=0.2038)	+25.58 (+0.2893), +48.50 (+0.2736)	+24.89 (+0.2192), 47.98 (+0.1994)
D&C Red No. 36	491.61 (*f*=0.2640)	471.95 (*f*=0.2067)	410.79 (*f*=0.0554)	480.78 (*f*=0.4800)	483.34 (*f*=0.1579)	506.15 (*f*=0.0100), 566.56 (*f*=0.0102)	+2.56 (-0.3221)	+25.37 (-0.4700), +85.78 (-0.4698)

TABLE IV

Individual color additive molecule experimental λ_{max} comparison to theoretical λ_{max} using gas phase geometry optimization followed by ethanol solvation effects in single-point energy (SPE) calculation.

D&C Molecule Name	Single-Point Energy Restricted Singlet Excited States (Gas Opt, Ethanol SPE)			TD-DFT Theoretical λ_{max}	Dilute Experimental λ_{max}	Concentrated Experimental λ_{max}	Dilute – TD-DFT $\Delta\lambda_{max}$ Δintensity	Concentrated – TD-DFT $\Delta\lambda_{max}$ Δintensity
D&C Blue No. 6	584.02 (*f*=0.2615)	491.68 (*f*=0.0000)	415.04 (*f*=0.0000)	584.48 (*f*=0.2634)	608.55 (*f*=0.0379) [IP: 582.45 (0.0261)] 708.73 (*f*=0.0195) [IP: 667.70 (0.0181)]	709.68 (*f*=0.0599)	+24.07 (-0.2255) [-2.03 (-0.2373)], +124.25 (-0.2439) [+83.22 (0.2453)]	+125.20 (-0.2035)
D&C Yellow No. 11	375.57 (*f*=0.0056)	348.23 (*f*=0.0037)	324.58 (*f*=0.0001)	364.22 (*f*=0.0090)	414.31 (*f*=0.2937), 437.23 (*f*=0.2780)	413.62 (*f*=0.2236) 436.71 (*f*=0.2038)	+50.09 (+0.2847) +73.01 (+0.2690)	+49.40 (0.2146) +72.49 (+0.1948)
D&C Red No. 36	509.72 (f=0.4325)	487.21 (f=0.0307)	429.51 (f=0.0414)	507.21 (f=0.4737)	483.34 (f=0.1579)	506.15 (f=0.0100), 566.56 (f=0.0102)	-23.87 (-0.3158)	-1.06 (-0.4637) +59.35 (-0.4635)

TABLE V

Individual color additive molecule experimental λ_{max} comparison to theoretical λ_{max} using ethanol solvation effects in geometry optimization followed by ethanol solvation effects in single-point energy (SPE) calculation.

D&C Molecule Name	Single-Point Energy Restricted Singlet Excited States (Ethanol Opt, Ethanol SPE)			TD-DFT Theoretical λ_{max}	Dilute Experimental λ_{max}	Concentrated Experimental λ_{max}	Dilute – TD-DFT $\Delta\lambda_{max}$ Δintensity	Concentrated – TD-DFT $\Delta\lambda_{max}$ Δintensity
D&C Blue No. 6	585.02 (*f*=0.2619)	495.05 (*f*=0.0000)	420.36 (*f*=0.0000)	584.48 (*f*=0.2648)	608.55 (f=0.0379) [IP: 582.45 (0.0261)] 708.73 (f=0.0195) [IP: 667.70 (0.0181)]	709.68 (*f*=0.0599)	+24.07 (-0.2269) [-2.03 (-0.2387)], +124.25 (-0.2453) [+83.22 (-0.2467)]	+125.20 (-0.2049)
D&C Yellow No. 11	382.48 (f=0.0049)	355.54 (f=0.0031)	327.90 (f=0.0001)	371.91 (f=0.0078)	414.31 (f=0.2937), 437.23 (f=0.2780)	413.62 (f=0.2236), 436.71 (f=0.2038)	+42.40 (+0.2859) +65.32 (+0.2702)	+41.71 (+0.2158) +64.80 (+0.1960)
D&C Red No. 36	518.05 (f=0.4842)	500.73 (f=0.0154)	440.65 (f=0.0432)	515.38 (f=0.5134)	483.34 (f=0.1579)	506.15 (f=0.0100), 566.56 (f=0.0102)	-32.04 (-0.3555)	-9.23 (-0.5034) +51.18 (-0.5032)

Heterodimeric Mixtures. Experimental λ_{max} comparison to theoretical TD-DFT simulation maximum absorbance spectral peak responsivity (λ_{max}) under 3 simulation conditions.

TABLE VI

Heterodimeric mixtures of color additive molecules experimental (λ_{max}) data comparison to theoretical λ_{max} using gas phase geometry optimization followed by gas phase single point energy (SPE) calculation.

D&C Molecule Name	Single-Point Energy Restricted Singlet Excited States (Gas Opt, Gas SPE)						TD-DFT Theoretical λ_{max}	Dilute Experimental λ_{max}	Concentrated Experimental λ_{max}	Dilute – TD-DFT $\Delta\lambda_{max}$ Δintensity	Concentrated – TD-DFT $\Delta\lambda_{max}$ Δintensity
D&C Blue No. 6 & D&C Yellow No. 11	555.07 (*f*=0.0229)	500.53 (*f*=0.0065)	450.19 (*f*=0.0004)	431.09 (*f*=0.0002)	425.28 (*f*=0.0054)	408.88 (*f*=0.0054)	554.69 (*f*=0.2282)	414.30 (*f*=0.2013) 437.11 (*f*=0.1921)	414.00 (*f*=0.8255) 436.83 (*f*=0.7698)	-140.39 (-0.0269) -117.58 (-0.0361)	-140.69 (+0.5973) -117.86 (+0.5416)
D&C Yellow No. 11 & D&C Red No. 36	563.19 (*f*=0.0015)	548.44 (*f*=0.0007)	493.97 (*f*=0.0023)	448.71 (*f*=0.0002)	426.56 (*f*=0.4874)	420.20 (*f*=0.0203)	426.00 (*f*=0.5127)	414.70 (*f*=0.2891), 437.21 (*f*=0.2898), 488.57 (*f*=0.1417)	414.15 (*f*=0.6861), 436.87 (*f*=0.6401)	-11.30 (-0.2236) +11.21 (-0.2229) +62.57 (-0.3710)	-11.85 (+0.1734) +10.87 (+0.1274)
D&C Blue No. 6 & D&C Red No. 36	661.19 (*f*=0.0017)	576.22 (*f*=0.1892)	541.29 (*f*=0.0460)	522.02 (*f*=0.0065)	477.71 (*f*=0.0015)	467.70 (*f*=0.0015)	569.20 (*f*=0.2322)	488.32 (*f*=0.0249), 438.11 (*f*=0.0300), 414.89 (*f*=0.0268), 607.16 (*f*=0.0097)	484.25 (*f*=0.5031)	-80.88 (-0.2073) -131.09 (-0.2022) -154.31 (-0.2054) +37.96 (-0.2225)	-84.95 (+0.2709)

TABLE VII

Heterodimeric mixtures of color additive molecules experimental λ_{max} comparison to theoretical λ_{max} using gas phase geometry optimization followed by ethanol solvation effects in single-point energy (SPE) calculation.

D&C Molecule Name	Single-Point Energy Restricted Singlet Excited States (Gas Opt, Ethanol SPE)						TD-DFT Theoretical λmax	Dilute Experimental λmax	Concentrated Experimental λmax	Dilute – TD-DFT Δλmax Δintensity	Concentrated – TD-DFT Δλmax Δintensity
D&C Blue No. 6 & D&C Yellow No. 11	585.02 (*f*=0.2126)	486.05 (*f*=0.0034)	485.73 (*f*=0.0010)	441.28 (*f*=0.0032	415.62 (*f*=0.0000)	404.43 (*f*=0.0007)	585.34 (*f*=0.2150)	414.30 (f=0.2013) 437.11 (f=0.1921)	414.00 (f=0.8255), 436.83 (*f*=0.7698)	-171.04 (-0.0137) -148.23 (-0.0229)	-171.34 (+0.6105) -148.51 (+0.5548)
D&C Yellow No. 11 & D&C Red No. 36	530.86 (*f*=0.0025)	474.25 (*f*=0.0019)	430.68 (*f*=0.4905)	407.19 (*f*=0.0058)	393.58 (*f*=0.0109)	384.51 (*f*=0.0004)	430.71 (*f*=0.5089)	414.31 (*f*=0.2937), 437.23 (*f*=0.2780)	414.15 (*f*=0.6861), 436.87 (*f*=0.6401)	+16.40 (-0.2152) +6.52 (-0.2309)	-16.56 (+0.1772) +6.16 (+0.1312)
D&C Blue No. 6 & D&C Red No. 36	651.68 (*f*=0.0015)	598.58 (*f*=0.1831)	531.16 (*f*=0.0629)	503.51 (*f*=0.0024)	497.63 (*f*=0.0058)	492.20 (*f*=0.0019)	589.96 (*f*=0.2101)	488.32 (*f*=0.0249), 438.11 (*f*=0.0300), 414.89 (*f*=0.0268), 607.16 (*f*=0.0097)	484.25 (*f*=0.5031)	-101.64 (-0.1852), -151.85 (-0.1801), -175.07 (-0.1833), +17.20 (-0.2004)	-105.71 (+0.2930)

TABLE VIII

Heterodimeric mixtures of color additive molecules experimental λ_{max} comparison to theoretical λ_{max} using ethanol solvation effects in geometry optimization followed by ethanol solvation effects in single-point energy (SPE) calculation.

D&C Molecule Name	Single-Point Energy Restricted Singlet Excited States (Ethanol Opt, Ethanol SPE)						TD-DFT Theoretical λ_{max}	Dilute Experimental λ_{max}	Concentrated Experimental λ_{max}	Dilute – TD-DFT $\Delta\lambda_{max}$ Δintensity	Concentrated – TD-DFT $\Delta\lambda_{max}$ Δintensity
D&C Blue No. 6 & D&C Yellow No. 11	587.06 (*f*=0.2161)	491.38 (*f*=0.0004)	480.05 (*f*=0.0015)	446.98 (*f*=0.0013)	419.15 (*f*=0.0001)	400.74 (*f*=0.0006)	586.88 (*f*=0.2648)	414.30 (*f*=0.2013) 437.11 (*f*=0.1921)	414.00 (*f*=0.8255) 436.83 (*f*=0.7698)	-172.58 (-0.0171) -149.77 (-0.0263)	-172.88 (+0.6071) -150.05 (+0.5514)
D&C Yellow No. 11 & D&C Red No. 36	523.38 (*f*=0.0034)	465.34 (*f*=0.0017)	428.00 (*f*=0.4633)	399.36 (*f*=0.0079)	395.35 (*f*=0.0066)	378.77 (*f*=0.0005)	427.53 (*f*=0.4818)	414.31 (*f*=0.2937), 437.23 (*f*=0.2780)	414.15 (*f*=0.6861), 436.87 (*f*=0.6401)	-13.22 (-0.1881) +9.70 (-0.2038)	-13.38 (+0.2043) +9.34 (+0.1583)
D&C Blue No. 6 & D&C Red No. 36	581.04 (*f*=0.2115)	565.45 (*f*=0.0004)	535.42 (*f*=0.0004)	492.15 (*f*=0.0000)	491.08 (*f*=0.0001)	483.16 (*f*=0.0000)	581.40 (*f*=0.2140)	488.32 (*f*=0.0249) 438.11 (*f*=0.0300) 414.89 (*f*=0.0268) 607.16 (*f*=0.0097)	484.25 (*f*=0.5031)	-93.08 (-0.1891) -143.29 (-0.1840) -166.51 (-0.1872) +25.76 (-0.2043)	-97.15 (+0.2891)

Heterotrimeric Mixture. Experimental λ_{max} comparison to theoretical TD-DFT simulation maximum absorbance spectral peak responsivity (λ_{max}) under 3 simulation conditions.

TABLE IX

Heterotrimeric mixture of color additive molecules experimental λ_{max} comparison to theoretical λ_{max} using gas phase geometry optimization followed by gas phase single-point energy (SPE) calculation.

D&C Molecule Name	Single-Point Energy Restricted Singlet Excited States (Gas Opt, Gas SPE)									TD-DFT Theoretical λmax	Dilute Experimental λmax	Concentrated Experimental λmax
D&C Blue No. 6, D&C Yellow No. 11, & D&C Red No. 36	569.21 (f=0.1833)	531.68 (f=0.0003)	527.37 (f=0.0029)	502.97 (f=0.0012)	484.80 (f=0.0001)	465.78 (f=0.0001)	447.74 (f=0.0010)	429.98 (f=0.0002)	415.14 (f=0.4409)	416.10 (f=0.4462) 567.95 (f=0.1899)	414.43 (f=0.1385) 437.38 (f=0.1349)	313.91 (f=0.7775) 336.21 (f=0.7233)

TABLE X

Change in (λ_{max}) and intensity for dilute and concentrated heterotrimer mixture of color additive molecules in ethanol solvent compared to theoretical TD-DFT simulation (λ_{max}) using gas phase geometry optimization followed by gas phase single-point energy (SPE) calculation.

D&C Molecule Name	Dilute – TD-DFT Δλmax (Δintensity)	Concentrated – TD-DFT Δλmax (Δintensity)
D&C Blue No. 6, D&C Yellow No. 11, & D&C Red No. 36	-1.67 (-0.3077), +21.28 (-0.3113) -153.52 (-0.0514), -130.57 (-0.0550)	-102.19 (+0.3313), -79.89 (+0.2771) -254.04 (+0.5876), -231.74 (+0.5334)

TABLE XI

Heterotrimeric mixture of color additive molecules experimental λ_{max} comparison to theoretical λ_{max} using gas phase geometry optimization followed by ethanol solvation effects in single-point energy (SPE) calculation.

D&C Molecule Name	Single-Point Energy Restricted Singlet Excited States (Gas Opt, Ethanol SPE)									TD-DFT Theoretical λmax	Dilute Experimental λmax	Concentrated Experimental λmax
D&C Blue No. 6, D&C Yellow No. 11, & D&C Red No. 36	587.45 (f=0.1633)	566.24 (f=0.0145)	520.72 (f=0.0003)	492.68 (f=0.0000)	492.29 (f=0.0016)	486.97 (f=0.0000)	446.29 (f=0.0010)	432.96 (f=0.0001)	423.53 (f=0.4010)	423.64 (f=0.4066) 586.88 (f=0.1804)	414.43 (f=0.1385) 437.38 (f=0.1349)	313.91 (f=0.7775) 336.21 (f=0.7233)

TABLE XII.

Change in (λ_{max}) and intensity for dilute and concentrated heterotrimer mixture of color additive molecules in ethanol solvent compared to theoretical TD-DFT simulation (λ_{max}) using gas phase geometry optimization followed by ethanol solvation effects in single-point energy (SPE) calculation.

D&C Molecule Name	Dilute – TD-DFT Δλmax (Δintensity)	Concentrated – TD-DFT Δλmax (Δintensity)
D&C Blue No. 6, D&C Yellow No. 11, & D&C Red No. 36	-9.21 (-0.2681), +13.74 (-0.2717) -172.45 (-0.0419), -149.50 (-0.0455)	-109.73 (+0.3709), -87.43 (+0.3167) -272.97 (+0.5971), -250.67 (+0.5429)

TABLE XIII

Heterotrimeric mixture of color additive molecules experimental λ_{max} comparison to theoretical λ_{max} using ethanol solvation effects in geometry optimization followed by ethanol solvation effects in single point energy (SPE) calculation.

D&C Molecule Name	Single-Point Energy Restricted Singlet Excited States (Ethanol Opt, Ethanol SPE)									TD-DFT Theoretical λmax	Dilute Experimental λmax	Concentrated Experimental λmax
D&C Blue No. 6, D&C Yellow No. 11, & D&C Red No. 36	585.42 (f=0.1797)	558.76 (f=0.0071)	528.27 (f=0.0015)	495.44 (f=0.0012)	486.36 (f=0.0000)	479.60 (f=0.0000)	454.35 (f=0.0005)	428.80 (f=0.0009)	427.51 (f=0.4132)	427.53 (f=0.4194) 584.29 (f=0.1911)	414.43 (f=0.1385) 437.38 (f=0.1349)	313.91 (f=0.7775) 336.21 (f=0.7233)

TABLE XIV

Change in (λ_{max}) and intensity for dilute and concentrated heterotrimer mixture of color additive molecules in ethanol solvent compared to theoretical TD-DFT simulation (λ_{max}) using ethanol solvation effects in geometry optimization followed by ethanol solvation effects in single-point energy (SPE) calculation.

D&C Molecule Name	Dilute – TD-DFT Δλmax (Δintensity)	Concentrated – TD-DFT Δλmax (Δintensity)
D&C Blue No. 6, D&C Yellow No. 11, & D&C Red No. 36	-13.10 (-0.2809), +9.85 (-0.2845) -169.86 (-0.0526), -146.91 (-0.0562)	-113.62 (+0.3581), -91.32 (+0.3039) -270.38 (+0.5864), -248.08 (+0.5322)

Discussion

Based on the data produced computationally, it may be deduced that distinct classes of color additive mixtures may be theoretically "mixed" in a virtual workspace and analyzed using DFT and TD-DFT to achieve a reasonable perspective of how the overall hue of the color mixture should ultimately appear to the user. Distinct classes of color additive molecules may be "mixed" if simulated using DFT in both vapor phase and ethanol solvent to predict maximum absorbance spectra peak responsivity (λ_{max}) comparable to the color appearance of traditional batch preparations. However, it should be noted that the effectiveness of the combination of DFT and TD-DFT in these cases may be utilized further to explain hidden issues of solubility among solute and solvent molecules that are typically observed over long periods of time by formulators after multiple color molecules are mixed. In this way, DFT with TD-DFT can also be used as an effective method to prevent unnecessary waste due to dissatisfactory color additive performance encountered during formulation product development.

Individual Color Additive Molecules. It is evident that theoretical and experimental maximum absorbance spectra for individual color additive molecules exhibit differences based on their respective dye class. Existing literature describes noteworthy patterns of numerical variation in simulated λ_{max} values based on their constituent chromophores which are indicative of their dye class categorization. Such combinations of chromophores present in a molecule affect the location within the visible region in which both experimental and theoretical maximum absorbance spectral peak responsivities may appear. This work indicates the issues that may arise when studying

one color additive molecule in addition to other color additives containing chromophores indicative of different dye and pigment classes.

D&C Blue No. 6 "Indigo". Select molecules within the indigoid class of color molecules have been extensively studied in vapor phase [1,96], in solvent [87,96], or in conjunction with other historical pigments of cultural significance [97,98] using computational quantum chemical methods. Perhaps the most famous example, called D&C Blue No. 6 or "Indigo", has been used in this study. Indigo is a water insoluble pigment derived naturally from the indigo plant [88,89] originally cultivated in India [98]. Its rigid, planar structure as seen in Figure 9 contains the characteristic N-H donor groups and carbonyl (C=O) acceptor groups representative of the indigoid dye class, and cause the molecule to act as a pigment [89]. As visible in the molecular orbital diagrams in Figure 10, both $\pi \rightarrow \pi^*$ and $n \rightarrow \pi^*$ transitions occur. $\pi \rightarrow \pi^*$ transitions occur due to the presence of nitro groups and carbon-carbon double bonds. $n \rightarrow \pi^*$ transitions appear as a result of carbonyl groups, however are considered "forbidden" transitions when certain simplifications of the Hamiltonian are taken into account during approximation [99]. $\pi \rightarrow \pi^*$ transitions typically indicate hypsochromic (blue) shifts because the excited state is less dipolar but more polarizable than the ground state. Thus, the resulting decrease in the quantity of the dipole leads to a hypsochromic shift with increasing solvent polarity because the electrostatic dipole/dipole interactions stabilize the dipolar ground state more than the less dipolar S_1 excited state [100]. As one *n*-electron is promoted to a more diffuse, excited π orbital, which is more polarizable, the S_1 excited state then has a larger polarizability than the S_0 ground state. Therefore, the dispersion interaction of the excited carbonyl solute with the solvent will be larger than the

dispersion interaction of the less-polarizable ground state solute with the solvent included in spectroscopic measurement (or approximation). The electronic excitation energy decreases, resulting in a bathochromic (towards infrared, or "red") shift of the $n \rightarrow \pi^*$ absorption band. $n \rightarrow \pi^*$ transitions are typically symmetry-forbidden transitions as seen for pyridazine. However, they can be enabled by vibronic interactions of weak intensity. In protic solvents, such as ethanol, hydrogen bond formation with the oxygen lone pairs of a carbonyl group lower the energy of the *n*-state, whereas the first approximation of the energy of the (excited) π^* state is not modified by intermolecular hydrogen bonding. Therefore, this specific carbonyl-containing solute-solvent interaction should lead to a hypsochromic (towards ultraviolet, or "blue") shift of the $n \rightarrow \pi^*$ absorption band.

Some researchers theorize that vibronic effects are more suitable for computational study of the indigoid dye alone. However, the significantly larger rigidity of the central C=C bond which resists twisting—unlike its derivatives [87]—infers that the first bright excited states are more likely attributed to electronic singlet intermolecular proton transfer (ESIPT) than vibronic effects. This is noticeable in the HOMO-LUMO-1 transitions between adjacent N-H and carbonyl groups. Nitrogen atoms become more acidic upon electronic excitation due to electronic transfer towards more basic carbonyl groups, facilitating a proton transfer [87]. This contrasts with vibronic effects because, in such cases, the forbidden transitions acquire intensity by coupling to the vibrations of the molecule [99]. Vibronic effects may be an acceptable route for computational and experimental spectral comparisons to more concentrated mixtures containing indigo, in which computational studies must be performed on homodimers (two of the same indigo

monomer in the workspace) for accurate comparison. See [86,87] for further discussion of the viability of this method.

$\pi \rightarrow \pi^*$ transitions are of much greater intensity than $n \rightarrow \pi^*$ transitions due to a larger magnitude of μ_g [11] and collinear absorbance μ_e [100]. In going from a nonpolar to a polar solvent, $\pi \rightarrow \pi^*$ absorption should undergo a bathochromic shift, while $n \rightarrow \pi^*$ undergoes a hypsochromic shift. This contradictory behavior of absorbance bands changes with solvent polarity. In strongly acidic media, $n \rightarrow \pi^*$ transitions being superimposed by larger, stronger $\pi \rightarrow \pi^*$ transitions yield large "positive" solvatochromic band shifts, and may indicate that electron pair donor/acceptor interactions between the aromatic chromophoric groups occur, such as between a phenol and a ketone.

When analyzing theoretical spectra of monomeric contributions to the color additive-solvent mixtures presented, TD-DFT more closely approximates λ_{max} of dilute concentrations of indigo mixed with ethanol solvent. Restricted singlet excited state calculations reveal that in gas phase, D&C Blue No. 6 theoretical λ_{max} is lower than experimental λ_{max} in ethanol solvent. This is due to the presence of multiple (two) carbonyl groups exhibiting the $n \rightarrow \pi^*$ transitions which denote hypsochromic shifts in the absorbance band if they are not solvated in polar protic solvent. Pi-bonding indicates $\pi \rightarrow \pi^*$ transitions, which indicate bathochromic (towards infrared, or red) shifts that generally are of higher intensity than $n \rightarrow \pi^*$ shifts; thereby rendering them as comparatively weaker electronic transitions [101]. In gas phase, generally van der Waals

[11] See benzophenone example published by source 104 in [100] showing μ_e has over 33% increase in magnitude of $\tilde{\nu}$ and approximately a 35 nm bathochromic shift in λ_{max} in polar solvents compared to μ_g.

dispersion forces contribute to solvation of the color additive molecule. These forces cause a small bathochromic shift [101]. The amine group NH is a proton donor group; therefore, as indicated by Reichardt and Welton (2011), electron pair-donor/acceptor effects occur [101] between the solute containing the donor group and the polar protic solvent (ethanol) containing the acceptor groups.

Since indigo is dipolar, the dipole/induced dipole of the solute increases with solvent polarity during the electronic transition. As a result, the Franck-Condon excited state is more solvated by dipole-solvent polarization, and a bathochromic red shift—depending on the solvent refractive index *n* and the change in solute dipole moment—is expected [101]. The Franck-Condon excited state is less solvated if the solute dipole moment decreases during the electronic transition, so a hypsochromic (blue) shift, again proportional to the two aforementioned factors, is also expected. In the latter case, the resultant shift may be red or blue depending on the relative magnitude of the red shift caused by polarization compared to the blue shift caused by excited state decay.

As shown in Table 3, gas phase exhibits greater hypsochromic shifts than experimental spectra comparison because experiments were carried out in polar protic solvent (ethanol). Thus, the change in λ_{max} and change in intensity are greater in gas phase computational simulations than in combined Gas DFT Opt/EtOH TD-DFT SPE and EtOH Opt/EtOH SPE. Lower intensity is approximated for both cases of EtOH SPE compared to the Gas Opt/Gas SPE yet is overestimated compared to experimental oscillator strength. This is due to overestimation of the Stokes shift with increasing solvent polarity (in this case, theoretical gas phase comparison to the ethanol solvent data). When the dipole moment of a fluorescent molecule is larger in the excited state

than in the ground state, $\mu_g < \mu_e$, then the differential solvation of the two states by solvents of varying polarity gives rise to an increase in the Stokes Shift with increasing solvent polarity [102]. Ethanol SPE calculations show more favorable changes in λ_{max} and changes in intensity. It is important to note that dilute (1 mM) concentrations provide data that is more favorable comparison to computational simulations of the indigo monomer than to the more saturated (10 mM) "concentrated" indigo-ethanol mixture. This is because the presence of isosbestic points (IPs) in experimental spectra is evidence that dimer complexation occurs, to yield more saturated (yet less intense, more dull) hue at 582.45 nm (f=0.0261) prior to reaching dilute λ_{max} at 608.55 (f=0.0379). It is worth noting that theoretical λ_{max} is very close to the IP value, therefore may correctly indicate the correct λ_{max} for the indigo monomer at 1:1 mM molar concentration. On the other hand, the second significant absorbance peak observed experimentally indicates that dimer complexation at higher concentrations occurs at 709.68 nm (f=0.0599). Other research has discussed the significance of isosbestic points and shoulder peaks in determining monomer-dimer complexation of dye aggregates in solution (see Chapters 2 and 3). This computational study proves that the point of dye aggregation is not only qualitatively discernable with experimental absorbance spectra observation but also quantifiable using DFT and TD-DFT theoretical methods.

Despite the obvious distinction of the concentrated experimental λ_{max} measured for the 10 mM Indigo-ethanol mixture, TD-DFT is able to simulate a theoretical λ_{max} value well within the appropriate maximum absorbance spectral range to reflect dark blue, emulating the isosbestic point evident in the absorbance curve generated by dilute

concentration of Indigo after particle filtration[12]. D&C Blue No. 6 exhibits dilute experimental absorbance spectra that is in close proximity to theoretical spectra simulated using TD-DFT with a change in λ_{max} of +24.07 nm when ethanol solvation effects are applied using PBF elements in both DFT geometry optimizations and single-point energy excited state calculations. However, more saturated mixtures of the molecule exhibit a stronger bathochromic (right-ward, or "red") shifts of +124.25 nm with lower intensity. As theorized by Barone [87], it may be necessary in cases where more concentrated experimental batches must be further analyzed at the molecular or atomic level using computational data, the dimerization of two planar indigo monomers must be explored for satisfactorily explaining the significant ~100 nm bathochromic shift in maximum absorbance peak responsivity compared to the well-documented λ_{max} of indigo monomers of approximately 609 nm in ethanol [87]. Other studies have noted the presence of a "shoulder" peak or isosbestic point in more concentrated experimental absorbance spectra, which further implicates the role of a monomer producing maximum absorbance spectra at one responsivity while the dimer contributes to more pronounced maximum absorbance peak at a more right-ward λ_{max} at approximately 708 nm with higher intensity [87]. In the concentrated and dilute experimental spectra for indigo shown in Figure 11, an isosbestic point is visible where the slope changes at 582.45 nm for the dilute concentration absorbance spectral curve. In comparison to theoretical data, the simulated TD-DFT spectra produces a λ_{max} peak at 584.48 nm for Gas Opt/EtOH SPE and EtOH Opt/EtOH SPE mixtures, indicating that indigo monomers produce a λ_{max} value at this wavelength, and begin to form dimer complexes to produce the higher intensity and

[12] The color additive-ethanol mixture was considered "diluted" when drawn into a 3 mL syringe and ejected through a Whatman 1.0 μM GF/B w/GMF particle filter into a cuvette for further UV-visible spectrophotometric analysis.

darker blue hue (more red-shifted absorbance λ_{max} value) at greater concentrations when mixed in ethanol solvent. The effect of choice of solvent on the λ_{max} of color additive molecules in computational simulation and experimental preparations has a twofold significance: solvent effects lead to both a modification of the ground-state geometry as an indirect effect, and modification of the electronic structure as a direct effect [96]. DFT and TD-DFT calculations incorporating ethanol solvation effects using PBF proves that spectral ranges of theoretical absorbance data are indeed reliable. For this reason, DFT and TD-DFT can be used confidently to model theoretical spectra of the indigo color additive molecule.

D&C Yellow No. 11 "SS Quinoline Yellow". Other dye classes have yet to have adequate data produced to explain theoretical versus experimental spectra anomalies. D&C Yellow No. 11, aptly named "SS Quinoline Yellow" as a member of the quinoline dye class. This color additive is considered a "solvent-soluble" dye molecule because it is soluble in solvents other than water[13], including ethanol, glycerol, methanol, ethanol, petroleum jelly, toluene, stearic acid, oleic acid, mineral oil, (di)ethyl ether, acetone, and butyl acetate [88,89]. This structure is derived from quinaldine by condensation with phthalic anhydride [88]. D&C Yellow No. 11 is clearly soluble in ethanol as evidenced by its noteworthy change in geometry conformation after DFT calculations have been performed on the molecule. According to Atkins and Friedman (2011), π-π* transitions in double-bonded carbon atoms are allowed for carbon-carbon double bonds and in this case, the transition dipole moment is directed along the internuclear axis (z-axis). As a result, the transition reduces the strength of the carbon-carbon bond because a bonding

[13] Its sulfonated-derivative, D&C Yellow No. 10, on the other hand, *is* water soluble [88,89].

electron is transferred from a bonding orbital into an antibonding orbital. The reduction in strength is so great that the bonded groups twist about the bond direction in order to minimize the antibonding effect. This results in *cis-trans* photoisomerization as a result of the twisting of the central carbon-carbon double bond [99, 103]. Using the example of ethylene, the CH_2 groups would be perpendicular in the excited state [99]. In D&C Yellow No. 11, the central carbon-carbon double bonds reorient the planar, cyclic structures on opposite sides of the molecule across the C=C bond so that their planes are oriented perpendicular to one another, as seen in Figure 12. In addition, conjugated carbon-carbon double bonds are prevalent throughout the dye molecule structure in the cyclic regions of the molecule, facilitating higher electron density and enhanced photoelectronic response to light stimulus.

Furthermore, there is an amine group on the left side of the molecule as shown in Figure 12 that promotes an interesting photoelectronic effect. When an electron is stimulated by incident light (becomes "excited") to move from the *h*ighest *o*ccupied *m*olecular *o*rbital (HOMO) to the *l*owest *u*noccupied *m*olecular *o*rbital (LUMO) as shown in Figure 13, the molecular orbitals shift from the left side of the dye molecule containing the amine group (N-H) and carbon-carbon double bonds to the right side of the molecule where two carbonyl groups exist in addition to more carbon-carbon double bonds. The carbonyl group experiences an $n \rightarrow \pi^*$ transition, involving the transfer of some electron density from the oxygen atom to the carbon atom, because the *n* orbital is largely confined to the oxygen atom whereas the antibonding π^* orbital spreads over both atoms. This migration of charge helps explain the shift to higher absorption frequencies that occur when this dye molecule is immersed in a polar solvent (ethanol) since the ground

state of the molecule favors a particular arrangement of solvent molecules. This higher absorption frequency can also be noticed in Figure 14 where the experimental excitation generates a maximum absorbance spectral peak responsivity of greater magnitude than that predicted in the TD-DFT simulation.

Theoretical and experimental spectral comparisons using Tables 3-5 for this molecule indicate that there is a +25.58 to +48.50 nm absorbance band shift in spectra for gas phase optimization followed by gas phase SPE, a +50.09 to +73.01 nm band shift under Gas Optimization/EtOH SPE simulation conditions, and a +41.70 to +65.32 absorbance band shift using EtOH solvation effects for both DFT optimization and TD-DFT simulated spectra. Upon simulation in polar ethanol solvent, the absorbance spectra exhibit a bathochromic shift of +42.40 and +65.32 nm because of the positive solvatochromism if the excited state is more dipolar than the ground state [104].

Theoretical data provided indicates that hypsochromic shifts ranging from +25-73.01 nm using TD-DFT approximation occur when compared to experimental spectra. See Tables 3-5 for $\Delta\lambda_{max}$ and Δintensity for direct comparison to dilute and concentrated color additive-ethanol mixtures. As shown in Tables 3-4, DFT and TD-DFT calculations incorporating gas phase (or no solvation) effects indicate larger shifts that are higher (Gas Opt/Gas SPE) or lower (Gas Opt/EtOH SPE) than the theoretical λ_{max} and intensity predicted for ethanol optimization DFT and ethanol single point energy TD-DFT. This is due to the mostly hypsochromic shifts when electronic transitions that occur in gas phase are considered, namely, $n \rightarrow \pi^*$ due to the unsolvated carbonyl groups. However, $\pi \rightarrow \pi^*$ transitions are not only of greater intensity than $n \rightarrow \pi^*$ transitions, but they are also higher in magnitude for dipolar solute molecules in increasingly polar solvent, such as

ethanol [104]. While substantial evidence suggests here that the bathochromic shift should dominate theoretical spectra and its experimental counterpart, the amine group on the left side of the molecule contributes to an $n \rightarrow \sigma^*$ shift because amine groups contain lone pairs of electrons as solvated heteroatoms. $n \rightarrow \sigma^*$ transitions cause notable hypsochromic (blue) shifts, especially in protic solvents such as ethanol. Therefore, in theoretical calculations, the hypsochromic transitions are more dominant, especially where gas phase DFT geometry optimizations and TD-DFT single point energy calculations are applied to the D&C Yellow No. 11 structure. Moreover, in solvent, solvent polarity effects contribute strongly to higher intensity and magnitude of the oscillator strength due to the large electronic transition that affects the geometry of the molecule, rotating it about the z-axis. In all experimental data, this energy is the highest among the three color additive molecules studied, and even among their corresponding mixtures. However, theoretical data largely underestimates this otherwise high oscillator strength.

Vibronic transitions also contribute to the high intensity of the solvated D&C Yellow No. 11 molecule. The geometry conformational change along the internuclear z-axis incurred upon solvation of the dye molecule in ethanol causes elimination of the center of symmetry within the molecule by an asymmetrical vibration [105]. Properties of the electronic dipole transition moment, as shown in the integral below, establish symmetry-based selection rules that follow the Laporte selection rule for centrosymmetric molecules (those with a center of inversion, not only linear molecules) that govern which transitions are permissible for a given molecule [105].

$$\mu_{fi} = \int \psi_f^* \hat{\mu} \psi_i d\tau$$

The z-component, the component parallel to the axis of the molecules of the electric dipole moment operator, is responsible for $\Sigma \leftrightarrow \Sigma$ transitions. The z-component of μ has (+) symmetry with respect to reflection in a plane containing the internuclear axis (z-axis) [105]. Therefore, for a (+) ↔ (-) transition, the overall symmetry of the integrand is so the integral must be zero; hence $\Sigma^+ \leftrightarrow \Sigma^-$ transitions are not allowed [105]. However, integrands for $\Sigma^+ \leftrightarrow \Sigma^+$ and $\Sigma^- \leftrightarrow \Sigma^-$ are allowed because the integrands are not necessarily zero. In this case, otherwise "forbidden" electronic transitions can be allowed, which acquire intensity by coupling to the vibrations of the molecule [99]. Such "forbidden" transitions that are allowed include $n \rightarrow \pi^*$ transitions, which are typically symmetry-forbidden but can be enabled by vibronic interactions of weak intensity [99,100,103,105]. In protic solvents, such as ethanol, hydrogen bond formation with the oxygen lone pairs of a carbonyl group lower the energy of the *n*-state, whereas the first approximation of the energy of the (excited) π^* state is not modified by intermolecular hydrogen bonding [Reichardt]. Therefore, this specific carbonyl-containing solute-solvent interaction should lead to a hypsochromic (towards ultraviolet, or "blue") shift of the $n \rightarrow \pi^*$ absorption band. The vibronic transitions result in two peaks of differing intensity as shown in Figure 14, with the difference in peak height based on the magnitude of the transitions coupled to vibrations within each alternating structure, as this molecule exhibits keto-enol tautomerism.

In theoretical absorbance spectra simulations, $n \rightarrow \pi^*$ transitions theoretically do not account for the transition state $[>C\text{--}O\cdot]^{\ddagger}$ of the singlet electron to the more diffuse π^* orbital after the carbonyl group is dissolved in ethanol solvent. The dispersion interaction of the excited state containing the solvated carbonyl-containing color additive (dye) solute will be larger than the dispersion interaction of the less-polarizable ground state solute in the same solvent. Therefore, the electronic excitation energy decreases, resulting in a bathochromic (red) shift of the experimental absorbance band. This effect could be increased due to the presence of multiple carbonyl groups that may undergo similar, if not identical, electronic transitions upon solvation. Theoretical calculations have likely predicted the spectra of an unsolvated "ground state" structure of D&C Yellow No. 11 based on Figures 12-14 submitted for calculation, which is less useful for practical formulators in applications of this molecule in common (polar protic) formulation solvents. Future computational development has sought to correct this issue by improving theoretical prediction of transition state structures based on enthalpy and likelihood of reactivity [106]. Later investigation of distinct keto and enol tautomeric forms of D&C Yellow No. 11 in Chapter 2 may serve to better clarify intermolecular interactions between alternating structural forms of this color additive solute and the solvent of choice.

Figure 14 also graphically depicts an important aspect of the D&C Yellow No. 11 dye molecule—the existence of seemingly two maximum absorbance peaks. This output is typical for the molecule in that two structures are being represented simultaneously in the experimental spectra: quinolyl indandione [91,92] and quinolyl indendione [107], the keto and enol forms of the molecule, respectively [108]. Because different molecules

have natural frequencies of vibration that also differ, the molecules will selectively absorb different frequencies of incident visible light [108]. Therefore, the "double" or "forked" peaks represent resonance between two distinct electronic configurations of the "same" molecule. The difference in electronic transitions produces distinct vibronic transitions of different intensities as a result of coupling of the electronic transition to a vibrational mode [99]. These noticeable electronic and vibrational spectroscopic effects of D&C Yellow No. 11 upon photoactivation with incident light will arise in the experimental absorbance spectra in mixtures with other color additives analyzed in this study. Computational data using DFT followed by TD-DFT with appropriate solvation effects using PBF elements provides a helpful glimpse into the photoisomerization exhibited in this color additive molecule upon solvation.

D&C Red No. 36 "American Vermillion". D&C Red No. 36, "American Vermillion", is classified as a nitrophenyl azo dye [93] due to the presence of one or more azo bonds (-N=N-) and an amphoterically-charged nitro (NO_2) group attached to a phenyl ring [88]. The azo class of color additive molecules is the largest and among the oldest classes of dye molecules in existence [109]. Azo dyes and pigments are also among the most commonly simulated due to the abundance of literature data supporting the anticipated "red-shifts" associated with error margins encountered using computational methods [1]. In fact, a "diazo-substituted" azo dye of similar structure attempted by Fabian (2010) for theoretical simulation of absorbance spectral peaks using TD-DFT calculations incorporating the same basis set but no solvation effects yielded poor results due to its cationic nature. In theory, this is not an "intrinsic" azo molecule, rather a diazo-substituted molecule with charge transfer properties that would render

theoretical calculations problematic. However, as this molecule is quite commonly encountered in formulations and even in cosmetic preparations, this work aims to report an assessment of the feasibility of using more modern DFT and TD-DFT with solvation effects to simulate the absorbance spectra of this molecule. This study gladly reports more accurate λ_{max} calculations in all three theoretical conditions: 480.78 nm (Gas Opt/Gas SPE), 507.21 nm (Gas Opt/EtOH SPE), and 515.38 nm (EtOH Opt/EtOH SPE). Theoretical intensity values as indicated by oscillator strength *f* vary significantly in comparison to experimental data collected in ethanol solvent, but do not widely deviate from one another in either the theoretical or experimental case in this study.

Due to the low solubility in conventional formulation solvents, this pigment molecule can be modeled surprisingly well in simulations incorporating gas phase. DFT and TD-DFT yield structures with nearly identical λ_{max} in dilute concentrations (+2.56 nm) using Gas Opt/Gas SPE and even more similar λ_{max} data for concentrated D&C Red No. 36—ethanol mixtures (+1.06 nm) using Gas Opt/EtOH SPE. TD-DFT seems to effectively model absorbance spectral peaks for realistic formulation mixtures, likely due to the similar HOMO-LUMO transitions in both Gas Opt and Ethanol Opt as seen in Figure 16. On the left side of the namesake azo (-N=N-) bond of the molecule, a change in geometry conformation occurs upon electronic excitation: the side of the molecule with two aromatic rings is slightly rotated, which shifts the electronic transitions in HOMO to the opposite side, containing the nitro group, in LUMO. In HOMO, $\pi \rightarrow \pi^*$ transitions indicated by carbon-carbon double bonds in the conjugated aromatic ring structures and a less polar dipole at a phenyl hydroxyl group near the central azo bond have molecular orbital surface areas of significant proportion. Upon electronic excitation

of a singlet electron to enter the LUMO, the large energy transfer causes high absorbance frequency (thus high oscillator strength *f*) and slight rotation about the azo bond. The amphoterically-charged nitro group contains an additional $n \rightarrow \pi^*$ hypsochromic transition. Furthermore, the zwitterionic nitro (NO_2) group causes the ground state to be more dipolar than the excited state ($\mu_g > \mu_e$) also known collectively as exhibiting "negative solvatochromism" [104]. In addition, there are $\pi \rightarrow \pi^*$ transitions in both the HOMO and the LUMO surface map images (Figure 16), but are located on opposite sides of the azo bond. This is due to the high energy of the transition dipole moment of the $\pi \rightarrow \pi^*$ transition about the azo bond. This is aided in part by the zwitterionic nitro group.

NO_2 has been known to produce a bathochromic (red) shift in absorbance spectra with increasing wavelength of excitation or increasing pressure [110]. According to Sidebottom et. al. (1972), the double peak observed in the experimental absorbance spectra exhibited in Figure 17 arises from the mixture of vibronic level of the NO_2 (nitro) group excited state with those of another electronic state. In order for the magnitude of the lifetime of the excited state to increase, the perturbing state must have a high density of suitable vibrational levels compared to the excited state near the energy level being considered, and it must mix wll with these states [110]. Therfore, the coupling of higher energy electronic states of the NO_2 group to vibrational modes of the D&C Red No. 36 molecule in polar solvent enables otherwise "forbidden" $n \rightarrow \pi^*$ transitions to be allowed, as shown by the HOMO-LUMO surfaces covering the excited N=O bonds in the nitro group in Figure 16 [99]. The bathochromic shift in absorbance spectra is one contribution of the nitro group; a second important contribution includes vibronic effects,

inducing the presence of multiple peaks in the more concentrated pigment-solvent mixture data as shown in Figure 18.

Polar solvent effects employ $n \rightarrow \sigma^*$ transitions as well due to the numerous nitrogen atoms carrying lone electron pairs throughout the molecule, shifting the otherwise strongly bathochromic absorbance spectra towards the blue range (in a hypsochromic shift). In this case, the shift can be interpreted as slightly overestimated for ethanol solvation because D&C Red No. 36 is sparingly soluble in ethanol [88,89]. Also, these theoretically high energy transitions are overestimated by TD-DFT with regard to oscillator strengths, but the simulation of λ_{max} is significantly improved with modern computational software.

D&C Red No. 36 caused difficulty in analysis because of its molecular properties which were quickly observed in experimental trials. D&C Red No. 36 is an unsulfonated pigment that contains no groups capable of salt formation and is thus insoluble and precipitates directly upon coupling [88] of the electronic and vibrational modes of the molecule [99]. As seen in Figure 15, it contains a chlorine group in ortho position to the azo group, which results in a sterically-hindered molecule with low solubility and excellent light stability. As a result, D&C Red No. 36 is not soluble in any of the common formulation solvents, however exhibits a slight solubility of less than 1% in steric acid, oleic acid, mineral oil, mineral wax, glycerol, and petroleum jelly if dispersed by grinding or otherwise homogenizing, and an equally sparing solubility in ethanol, methanol, and acetone according to Senackerib [89]. In this work, the experimental batch samples were sonicated and vortexed in order to achieve the effect of homogenizing in the small quantities prepared. Due to the molecule's ability to accumulate in the human

body, it is restricted for use in quantities not to exceed 3% w/w for externally-applied cosmetics or drugs [88]. More specifically, if used as a color additive in an orally-ingested drug other than mouthwashes and dentrifices, D&C Red No. 36 can only be applied for the maximal amount of 1.7 mg/d dose of drug if the drug is being taken continuously for less than one year [88,89]. If the drug is administered for longer than one year, only 1.0 mg/d dose of drug is permitted for use of the color additive in the pharmaceutical product [88,89]. Otherwise, it is strictly limited to external applications. The unique physicochemical behavior of this unusual color additive structure will serve to produce intriguing computational data during analysis of the heterodimeric and heterotrimeric mixtures.

The presence of the second λ_{max} peak in the experimental absorbance spectra curve of the American Vermillion—ethanol mixture is likely due to the existence of a mesomeric or constitutional isomer-like alternative structure as a result of its zwitterionic nature. The change in the electronic nature of the molecule that affects intramolecular bonding contributes to a charge-transfer phenomenon. The chlorine atom of significant atomic mass and, more importantly, of higher electron density does not exhibit any large effect on HOMO-LUMO character due to its “size”. Effective core potential incorporated into TD-DFT SPE values may have overestimated the high energy transition of this molecule if the chlorine atom and the nitro group charges worked in tandem to cause overestimation of oscillator strength (intensity, in this case). Furthermore, this may have caused a discrepancy in the simulated λ_{max} of this color additive with ethanol solvation effects in both DFT and TD-DFT as shown in Table 6 since ethanol is a polar protic solvent and the chlorine ion is a strong nucleophile.

Heterodimeric Mixtures. Heterodimeric mixtures in this study consist of only two of the three color additive molecules simulated as mixtures in ethanol solvent. These results ought to interest the computational chemist or bench-top formulator because in each case, the two molecules selected are part of distinct dye classes. The combination of multiple color additive molecules for quantum chemical simulation using DFT and TD-DFT calculations has presented some issues in interpretation due to the limitation of the maximum number of HOMO-LUMO surfaces that can be approximated for molecules in a given workspace for a single computational job. However, a discussion of the likely electronic transitions that occur is still relevant based on the distinguished TD-DFT theoretical λ_{max} calculated for each combination of molecules in a given workspace despite the software limitation of MO surface depiction.

D&C Blue No. 6 and D&C Yellow No. 11. D&C Blue No. 6 and D&C Yellow No. 11 make a combination that appears a deep green hue to the observer. Experimental and theoretical λ_{max} data seem to be in poor agreement at first glance; however, the combined analysis of the data provided by the experimental batches is actually supported by computational data to help more accurately explain photochemical phenomena that occurs when the molecules are mixed instantaneously, as well as when they settle out as precipitates. Quantum mechanical TD-DFT calculations tell us that based on the sum of the six singlet excited states values approximated at the instantaneous sensation of excitation of one electron from the ground state to the excited state, the "average" value. In this case, the simulated λ_{max} peak with the highest intensity as oscillator strength obtained as a result of mean Gaussian distribution indicates that upon immediate mixing, the heterodimer appears green (586.88 nm). If the same mixture is diluted or left for the

particles to settle, or if this process is expedited as occurred in this study using a particle filter to obtain a less saturated sample for UV-visible spectroscopic analysis, the mixture will have an experimental λ_{max} value of 414.00 nm with a $\lambda_{shoulder}$ value of 437.11 nm. This indicates that D&C Yellow No. 11 is more soluble in ethanol than D&C Blue No. 6 because indigo is an insoluble pigment, so eventually indigo will precipitate out of the mixture. The solubility issues are also evident in Figure 19 showing the molecular orbital surfaces calculated for the structures in that MOs are calculated for one molecule, (D&C Blue No. 6), but not the other (D&C Yellow No. 11) molecule. Using DFT, D&C Blue No. 6 (pigment) experiences the HOMO-LUMO transition but the D&C Yellow No. 11 (dye) structure has reproduced the significant rotation about the internuclear axis indicating electronic excitation in the polar solvent. As a result, the yellow dye is soluble in ethanol, producing a high intensity, but the blue pigment has greater, more numerous electronic transitions that push the absorbance spectra further right in a bathochromic shift (towards infrared range). Thus, the two colors are represented simultaneously to the viewer as a green mixture, but the indigo will eventually settle out as a (blue) precipitate, leaving the D&C Yellow No. 11 molecule to ultimately remain as the overall hue of the ethanol solvent. This important comparison helps shed light on the quantum chemical properties of heterodimeric mixtures of color additives that are commonplace in formulations but have variable color solubility properties which are rarely analyzed in such computational depth before a product is marketed with a desired hue.

As previously discussed, the individual color additive molecule D&C Blue No. 6 exhibits two $n \rightarrow \pi^*$ electronic transitions from carbonyl groups that contribute to hypsochromic shifts unless solvated in polar solvent, when the solvated carbonyl would

cause a bathochromic shift in the absorbance curve. Upon solvation in ethanol, numerous $\pi \rightarrow \pi^*$ transitions from carbon-carbon double bonds throughout the molecule cause bathochromic shifts, and an amine group with a lone pair of electrons acts as a proton donor in a polar protic solvent, contributing to electron pair donor/acceptor activity resulting in hypsochromic shift of greater magnitude than unsolvated carbonyl groups that would cause a decrease in dipole moment. Solvated carbonyls have larger dispersion interactions in the excited state than in the ground state, so the electronic excitation energy decreases and results in a bathochromic shift of the absorbance band. In the case of D&C Yellow No. 11, the transition dipole moment is such a high energy transition that nearly perpendicular rotation about the internuclear axis (z-axis) occurs as a result of ethanol solvation. This transition causes a hypsochromic shift. Furthermore, the amine group on the DC Yellow No. 11 molecule in protic solvent, like D&C Blue No. 6, contributes to an increased hypsochromic shift in polar protic solvent. D&C Blue No. 6 is a pigment with no geometry conformational changes observed as a result of its rigid, planar structure. However, the indigo molecule contains additional carbon-carbon double bonds that upon electronic excitation exhibit $\pi \rightarrow \pi^*$ antibonding activity during the HOMO-LUMO transition with solvation effects applied. This results in an increased bathochromic shift of the overall absorbance spectral band in combination with mainly hypsochromic D&C Yellow No. 11 transitions, so the color-additive mixture appears green at the instantaneous moment of mixing. This is correctly predicted by TD-DFT according to Tables 6-8.

The high intensity of D&C Yellow No. 11 is preserved in the heterodimeric mixture is due to vibronic effects, as apparent in the measured absorbance spectra

frequency (measured in terms of oscillator strength *f*) and discernible visually in Figures 18 and 19. As electrons in the molecule move from a ground state to an excited state, the geometry conformational change induces electronic coupling to asymmetrical vibrational modes as a result of the shift in the center of symmetry along the z-axis of the molecule [99, 105]. This high-intensity electronic coupling to vibrational modes produces a high intensity vibronic effect, which is preserved in the heterodimeric mixture of the yellow dye with indigo. The intensity of D&C Yellow No. 11 cannot be camouflaged or superseded by indigo, especially after attempted particle filtration to attain higher concentration of color additive molecule combinations in the mixture. Therefore, the brightness of the green mixture increases considerably in both dilute and concentrated batches, especially as the indigo pigment gradually settles out as a precipitate.

D&C Yellow No. 11 and D&C Red No. 36. Similar observations can be made when observing the hue of the heterodimeric mixture of D&C Yellow No. 11 and D&C Red No. 36 in ethanol solvent. In this case, D&C Red No. 36 is the unsulfonated insoluble pigment molecule, well known to have limited solubility in polar solvents. Due to the sterically-hindered chromophores that prevent any necessary electronic coupling in solvent, it functions as a pigment. However, the nitro group has a significant role in that it is strongly electron-withdrawing and induces vibronic effects, which jointly contribute to $\pi \rightarrow \pi^*$ and (otherwise forbidden) $n \rightarrow \pi^*$ transitions that are responsible for its distinct orange-red hue.

The molecular orbital surfaces paint an interesting picture for us regarding the interaction of these colorful molecules. The highest occupied molecular orbital HOMO structures in the heterodimeric mixture show that only the pigment molecule (D&C Red

No. 36) has anti-bonding orbitals of interest. However, the LUMO structure shows the right side of the yellow dye (D&C Yellow No. 11) containing the carbonyl groups and cyclic conjugated π-bonded carbon atoms as having antibonding orbitals throughout its structure. Note that the yellow dye structure is also bent as a result of the electronic transition dipole moment, producing the antibonding effect. There is significant bond-twisting along the internuclear axis (z-axis) again, as occurred with the heterodimeric mixture of the blue pigment with the yellow pigment. This shows that, once more, the pigment-dye-solvent combination instantaneously produces an electronic excitation and absorbance spectra that we visually discern as the red pigment and yellow dye appearing simultaneously as a bright orange mixture.

The concentrated spectra exhibits the competing electronic transitions of the dye-pigment-solvent mixture in an interesting fashion: one λ_{max} peak at 414.80 nm indicates the presence of the yellow molecule, and a distinguished "shoulder" peak of higher intensity appears in the orange range (437.19 nm) when the solution is concentrated at 10 mM. On the other hand, the dilute 1mM concentration shows that the red pigment is clearly able to reflect red light (hence the perturbation at approximately 489 nm) but the high intensity of the yellow dye pigment in ethanol solvent causes a hypsochromic (rightward, towards ultraviolet) shift in the overall absorbance spectra, thus yields a maximum absorbance peak responsivity value that is smaller than the simulated TD-DFT spectral peak responsivity. As discussed earlier, the emergence of the two "forked" spectral peak responsivities indicate the beginning of separation of the red pigment from the yellow dye in the overall solvent mixture. Over time, the red pigment will precipitate out, leaving the yellow dye solvated in ethanol. Thus, a single pigment molecule and a

single dye molecule will instantaneously appear to be successfully “mixed” in solution at first glance; however, the pigment will precipitate out eventually, leaving the solvent mixture to appear the hue of the soluble dye molecule. Therefore, the computational data for this heterodimeric mixture proves that precipitation or solvation of a given color additive or group of color additives may be visualized using molecular orbital surfaces calculated based on their geometry optimization using DFT. Furthermore, the instantaneous hue of the mixture is estimated within the correct spectral region using TD-DFT single-point energy calculations with relevant solvation effects applied.

In HOMO, the molecular orbital surfaces are calculated on only the D&C Red No. 36 molecule, mainly in the region of the molecule containing two fused aromatic rings exhibiting antibonding orbitals and $\pi \rightarrow \pi^*$ transitions contributing to an overall bathochromic shift. The significant perpendicular rotation of the D&C Yellow No. 11 molecule about the z-axis has occurred to produce the aforementioned vibronic effect, but no molecular orbitals are evident in the figure. The size of the molecular orbital surfaces mapped on the amphoterically-charged nitro [NO_2] group is surprisingly minimal, contributing less to the overall absorbance spectral band shift than expected. In LUMO, on the other hand, the molecular orbitals are mapped exclusively onto the “right” side of the D&C Yellow No. 11 molecule containing the two carbonyl groups but without the amine group. Therefore, the combination of these two molecules reveals that although the red diazo-substituted nitrophenyl azo pigment has strong $\pi \rightarrow \pi^*$ electronic transitions and a notable cationic nature that dominate the absorbance spectral curve numerical approximation when modeled independently, the combination of the red molecule with the D&C Yellow No. 11 molecule shifts the overall absorbance spectral curve towards

the blue range (a hypsochromic shift) upon instantaneous mixing. Like its combination with the D&C Blue No. 6 molecule, D&C Yellow No. 11 contributes to the heightened intensity of this mixture overall in both theoretical and experimental mixtures.

D&C Blue No. 6 and D&C Red No. 36. The final heterodimeric mixture of D&C Blue No. 6 and D&C Red No. 36 provides an even simpler conclusion based on the properties of the two pigment molecules of distinct dye classes. The blue pigment, D&C Blue No. 6, and the red pigment D&C Red No. 36, show no conformational changes when solvation effects are applied in ethanol solvent. Their structures remain rigid because the groups susceptible to electronic coupling in polar solvents are too sterically-hindered to engage in solvent interactions, thus eliminating any evidence of rotation about their internuclear axes which would indicate noteworthy anti-bonding interactions leading to measurable absorbance spectra. Eventually, after a reasonable time duration, both the red and the blue pigment molecules would precipitate out of the ethanol solvent mixture to yield a purple precipitate and a colorless ethanol solvent. This interesting phenomena is predicted with a simulated TD-DFT spectra in the blue range, but concentrated color additive combination in ethanol solvent produces λ_{max} in the red range. Dilute color additive combination in ethanol solvent tells a more complete story over time as both red (at 488 nm) and blue (607 nm) peaks emerge in absorbance spectra data. In this case, less pronounced peaks appearing as uneven ruptures in the absorbance spectral curve within the yellow range are actually indicative of the red monomer as originally depicted in Figure 17.

Upon instantaneous mixing, D&C Blue No. 6 and D&C Red No. 36 have competing $\pi \rightarrow \pi^*$ electronic transitions that result in mostly bathochromic shifts of the

overall absorbance spectra. In this combination, there is a strong hypsochromic shift due to the zwitterionic nature of the amphoterically-charged nitro group of the red pigment, causing a $n \rightarrow \sigma^*$ electronic transition that also complements that of the amine group on the planar indigo molecule (see Figures 9, 10, and 24) upon ethanol solvation. Due to the sterically-hindered nature of the functional groups on the D&C Red No. 36 molecule, and the large chlorine atom, the American Vermillion acts like an insoluble pigment in ethanol solvent. D&C Blue No. 6 is a rigid and planar molecule but has more favorable solvent interactions upon instantaneous mixing than D&C Red No. 36, resulting in diminished intensity of the mixture as shown for oscillator strength calculations in both theoretical conditions and experimental settings. In higher concentrations, the indigo molecule eventually separates from the ethanol molecules to form a precipitate, leaving the more concentrated experimental spectra to largely depict D&C Red No. 36 absorbance of higher intensity.

The presence of λ_{max} peaks at 438.11 and 414.89 nm are likely results of experimental error due to frequent usage of the same cuvette for UV-visible spectroscopic analysis. Despite repeated cleaning between trials, the equipment utilized was sensitive enough to detect residual D&C Yellow No. 11 absorbance peaks in only the dilute spectral curve. These errors were not carried into higher concentrations of the DC Blue No. 6—D&C Red No. 36 color additive mixtures.

Heterotrimeric Mixture

D&C Blue No. 6, D&C Yellow No. 11, and D&C Red No. 36. The heterotrimeric mixture provides perhaps the most intriguing conclusions of all batches prepared herein. The heterotrimeric mixture, upon instantaneous mixing of all three color additives in ethanol solvent, appears a dull brown hue which theoretically adheres to the subtractive method of color mixing [95]. This is further evidenced by the high singlet excitation state λ_{max} from TD-DFT simulation which falls into the (dull) orange-brown range, comparable to a sepia-like hue. So why would the particle-filtered, "diluted" experimental λ_{max} appear an intense yellow? The experimental λ_{max} peaks indicate the following: First, that D&C Yellow No. 11 is the most soluble color additive molecule in the ethanol solvent mixture compared to indigo and much less soluble American Vermillion. Second, as shown in Figure 28, the molecular orbitals as depicted only show calculation of $\pi \rightarrow \pi^*$ excitation on the yellow molecule; hence proving that, ultimately, this molecule will have electronic- and vibronic coupling in the (polar) solvent that can sustain the large electronic transition after the other molecules precipitate out of the mixture. D&C Blue No. 6 and D&C Red No. 36 have chromophores that are too sterically-hindered to promote favorable solvation effects with the third color additive, so the mixture will ultimately appear as if only D&C Yellow No. 11 exists in solution with a purple precipitate.

While D&C Blue No. 6 successfully diminishes the oscillator strengths to lower the overall intensity of the theoretical and dilute experimental batches, the spectra of the color additive combination shows that the larger energy transition dipole moment of D&C Yellow No. 11 largely dominates, increasing the oscillator strength dramatically

and hypsochromically shifting the spectra into the yellow-green range. The hypsochromic shifts are more numerous and of greater intensity than the bathochromic transitions of the more rigid, planar, stable indigo structure. D&C Red No. 36 is very insoluble, however the more numerous $\pi \rightarrow \pi^*$ transitions due to the two fused aromatic rings contribute to a noticeable bathochromic shift to indicate the higher intensity presence of the molecule, but steric hindrance as a result of bulky functional groups such as the large chlorine atom and the zwitterionic nitro group hinder solvent interactions with ethanol as well as solute interactions among the blue and yellow color additives. What is also interesting is that theoretical data indicate the presence of two λ_{max} peaks, indicating competing structures in the mixture. In Gas Opt/Gas SPE (shown in Table 10), TD-DFT simulated λ_{max} shows one peak that indicates D&C Yellow No. 11 is prevalent at high intensity, but the second theoretical λ_{max} peak closely mimics the second of the two peaks shown in experimental data for the red molecule in dilute concentration in ethanol (see Table 6). Perhaps a mesomeric or otherwise charged structure predominates the heterotrimeric mixture that is distinct from the form selected as the monomer in this study, depicted in Figure 15.

In computational studies applying ethanol solvation effects to TD-DFT following gas phase geometry optimizations using DFT, (Gas Opt/EtOH SPE) shown in Table 10, the first peak of the theoretical heterotrimer—ethanol mixture indicates that D&C Yellow No. 11 absorbance spectra dominates because of the characteristic lambda max region and high intensity, however the second theoretical peak (586.88 nm) closely reflects indigo monomer absorbance spectra calculations and its experimental λ_{max} measurement at the isosbestic point on the dilute concentration curve. This data indicates that if it were possible to measure gas phase UV-visible absorbance spectra, the heterotrimer would

likely appear sepia-like (dull reddish-brown) in hue. However, as the experimental batches analyzed were conducted in ethanol solvent only, the mixture exhibits spectral curves that indicate the polar protic solvent effects incurred by the distinct high-intensity yellow molecule and the blue indigo molecule in ethanol dominate the heterotrimeric mixture while D&C Red No. 36 settles out of the mixture as a precipitate.

Note that all mixtures containing D&C Yellow No. 11 in any capacity (alone or in combination with other color additive molecules) exhibit a double- or forked-peak. It is well-known that high-intensity electronic transition dipole moments derived from an asymmetrical vibration of a molecule in polar solvent can enable otherwise forbidden transitions to occur, thus exhibiting absorbance spectra that appears "forked" in curvature alluding to the presence of vibronic effects. In addition, there is known keto-enol tautomerism that exists within the molecule. Both the keto and enol structures are present in the mixture simultaneously, and each contributes to a separate, distinct absorbance peak [108]. The less-intense (shorter) of the two peaks is known as the "shoulder" peak ($\lambda_{shoulder}$), whereas the highest of the two peaks is considered the "true" maximum absorbance value (λ_{max}). This topic will be explored in greater detail in the forthcoming chapters and using varied molecules of even more distinct dye classes in different solvents that exhibit this same effect or other spectral anomalies in experimental absorbance spectra measuring using conventional UV-visible spectroscopic methods. D&C Red No. 36 exhibits a similar double-peak in experimental spectra, however this is likely due to changes in electronic charge distribution among the atoms contained in the nitrophenyl group of the molecule. The nitro group is strongly electron-withdrawing as an amphoterically-charged functional group and chromophore. As a result, the nitro

group competes with the two distinct electronic configurations of the keto-enol forms of D&C Yellow No. 11. This “competition” is portrayed graphically with the high intensity absorbance peaks in the blue absorbance (yellow reflectance) range, and a smaller but nonetheless existent maximum absorbance peak in the blue region (reflects orange-red) based on the contribution of the nitro group to the simulated TD-DFT spectra. The nitro group-instigated bathochromic shift evident in the photographed dull “sepia”-colored experimental batch appearance of the heterotrimeric color additive-ethanol mixture (as shown in Figure 8) is more accurately portrayed by the TD-DFT simulation than by either the concentrated or dilute experimental batch absorbance spectral projections measured by conventional UV-visible spectroscopy.

Conclusion

DFT & TD-DFT serve as valuable tools to analyze quantum chemical properties of molecules that cannot be fully understood, or even correctly assumed, using experimental spectroscopic methods alone. Optimized geometry conformations and molecular orbital surface area calculations of color additive molecules existing independently or in conjunction with other color additive molecules in mixture-like environments demystifies their physicochemical behavior attributes by allowing the computational chemist or practical formulator to observe their intermolecular interactions. In this way, a combined DFT & TD-DFT approach clarifies subtleties which arise from typical spectroscopic analysis of experimental absorbance spectra. Electronic excitation energies of singlet excited states can provide valuable insight on the physicochemical behavior of structures constructed virtually. Such data is readily comparable to effects observed in experimental batches over time using much more

diminutive quantities of color additive molecules and formulation solvent than would be required by traditional benchtop analytical methods. Furthermore, theoretical data has effectively conveyed the lack of solubility of certain color additives in mixtures containing other color additive molecules in a common (polar) formulation solvent when simulated (TD-DFT) maximum absorbance peak spectral responsivity was calculated. As this is the first known report of the success of TD-DFT to predict the instantaneous absorbance spectra of mixtures of distinct classes of color additive molecules and to also provide thoughtful insight on their interaction with a solvent of choice over time based on MO character and relevant transitions, hopefully this work will serve to improve the reputation of computational approaches to formulation development among the applied scientific community.

On a more practical level, use of DFT and TD-DFT to predict and anticipate color additive-solvent mixture compatibility reduces the amount of chemical waste produced in formulation development considerably. Use of computational methods would considerably expedite the process of determining long-term product stability. In a typical industrial setting, formulated products, especially cosmetics, sensory additives are the final touches added to a batch [67]. Even if all functional aspects of the formulation are satisfactory, if the color appearance is incorrect or unsightly in any way, the entire batch is discarded, entailing frequent generation and disposal of large quantities of chemical waste of “unsatisfactory” batches. After successful completion of a satisfactory formulation, a large quantity of the finished product is left in a sealed container in temperature- and pressure-controlled storage rooms to monitor product decay after a period of six months to one year [68]. This procedure is performed as another criteria of

formulation development in order to detect inconsistencies or undesirable properties of the formulation that may emerge after long term use and storage of the product. Based on the computational data presented in this work, the process of detecting precipitation of lesser-known or esoteric sensory additive molecules may be reduced to a matter of days or weeks[14]. For these reasons, it is increasingly important to incorporate meaningful computational quantum mechanical methods as analytical tools in our current era of rapidly-advancing technology to streamline formulation conceptualization as well as molecule design and development, to ensure immediate satisfaction the prototype, and to guarantee optimal long-term formulation product performance and aesthetic value of products containing color additive molecules for consumer use.

[14] Time duration of computational job processing depends on a variety of factors, including, but not limited to, the quantity of atoms in molecular structures simulated, their combination with the other molecules to be analyzed, and/or the computational processing power available.

References

[1] J. Fabian, "TDDFT-calculations of Vis/NIR absorbing compounds," *Dyes and Pigments*, vol. 84, no. 1, pp. 36-53, 2010.

[2] D. Jacquemin, I. Duchemin, and X. Blase, "0-0 Energies Using Hybrid Schemes: Benchmarks of TD-DFT, CIS(D), ADC(2), CC2, and BSE/GW formalisms for 80 Real-Life Compounds," *J Chem Theory Comput*, vol. 11, no. 11, pp. 5340-59, Nov 10 2015.

[3] A. D. Katharyn Fletcher, Shirin Faraji, "Potential energy surfaces and approximate kinetic model for the excited state dynamics of Pigment Yellow 101," *Computational and Theoretical Chemistry*, vol. 1040-1041, pp. 177-185, April 4, 2014 2014.

[4] R. M. Cammi, Benedetta; Tomasi, Jacopo, "Fast Evaluation of Geometries and Properties of Excited Molecules in Solution: A Tamm-Dancoff Model with Application to 4-Dimethylaminobenzonitrile," *J. Phys. Chem. A*, vol. 104, pp. 5631-5637, 2000.

[5] S. G. Maja Parac, "A TDDFT study of the lowest excitation energies of polycyclic aromatic hydrocarbons," *Chemical Physics*, vol. 292, pp. 11-21, February 4, 2003 2003.

[6] L. Shen, H.-F. Ji, and H.-Y. Zhang, "A TD-DFT study on triplet excited-state properties of curcumin and its implications in elucidating the photosensitizing mechanisms of the pigment," *Chemical Physics Letters*, vol. 409, no. 4-6, pp. 300-303, 2005.

[7] D. Jacquemin and E. A. Perpète, "Ab initio calculations of the colour of closed-ring diarylethenes: TD-DFT estimates for molecular switches," *Chemical Physics Letters*, vol. 429, no. 1-3, pp. 147-152, 2006.

[8] A. M.-L. Samuel Frutos-Puerto, M. Elena Martin, Manuel A. Aguilar, "Theoretical study of the absorption and emission spectra of tha anionic p-coumaric methyl ester in gas phase and in solution," *Computational and Theoretical Chemistry*, pp. 287-294, April 25 2014 2014.

[9] X. Lopez, M. A. Marques, A. Castro, and A. Rubio, "Optical absorption of the blue fluorescent protein: a first-principles study," *J Am Chem Soc*, vol. 127, no. 35, pp. 12329-37, Sep 7 2005.

[10] M. A. Marques, X. Lopez, D. Varsano, A. Castro, and A. Rubio, "Time-dependent density-functional approach for biological chromophores: the case of the green fluorescent protein," *Phys Rev Lett*, vol. 90, no. 25 Pt 1, p. 258101, Jun 27 2003.

[11] N. S. U. Lourderaj; Manoj K. Harbola, "Time-dependent density functional theoretical study of low lying excited states of F_2," *Chemical Physics Letters*, vol. 366, pp. 88-94, September 17 2002 2002.

[12] M. Guillaume, V. Liégeois, B. Champagne, and F. Zutterman, "Time-dependent density functional theory investigation of the absorption and emission spectra of a cyanine dye," *Chemical Physics Letters*, vol. 446, no. 1-3, pp. 165-169, 2007.

[13] S. Fantacci, F. De Angelis, A. Sgamellotti, A. Marrone, and N. Re, "Photophysical properties of [Ru(phen)2(dppz)]2+ intercalated into DNA: an integrated Car-Parrinello and TDDFT study," *J Am Chem Soc*, vol. 127, no. 41, pp. 14144-5, Oct 19 2005.

[14] M. A. R. M. Clara C.S. Sousa, Victor M.F. Morais, "Energetics and stability of azulene: from experimental thermochemistry to high-level quantum chemical calculations," *J. Chem. Thermodynamics*, vol. 73, pp. 101-109, November 11 2013 2014.

[15] J. C. Ling-Jun He, Fu-Quan Bai, Ran Jia, Jian Wang, Hong-Xing Zhang, "Fine-tuning pi-spacer for high efficiency performance DSSC: a theoretical exploration with D-pi-A based organic dye," *Dyes and Pigments*, vol. 141, pp. 251-261, February 13, 2017 2017.

[16] X. A. Thibaud Etienne, Antonio Monari, "QM/MM calculation of absorption spectra of complex systems: the case of human serum albumin," *Computational and Theoretical Chemistry*, vol. 1040-1041, pp. 360-366, January 7 2014 2014.

[17] E. C. Daniele Varsano, Olivia Pulci, Adriano Mosca Conte, Leonardo Guidoni, "Ground state structures and electronic excitations of biological chromophores at Quantum Monte Carolo/Many Body Green's Function Theory level," *Computational and Theoretical Chemistry*, vol. 1040-1041, pp. 338-346, March 6, 2014 2014.

[18] Y. Zhao and D. G. Truhlar, "Density functional for spectroscopy: no long-range self-interaction error, good performance for Rydberg and charge-transfer states, and better performance on average than B3LYP for ground states," *J Phys Chem A*, vol. 110, no. 49, pp. 13126-30, Dec 14 2006.

[19] S. D. Sema Caglar, Zerrin Heren, Orhan Buyukgungor, "Crystal structures, thermal, spectroscopic properties and DFT/TD-DFT based investigation of [M(bba)2(phen)] (M= Cu and Zn, bba = 2-benzoylbenzoato, phen = 1,10-phenanthroline)," *Polyhedron*, vol. 30, pp. 1389-1395, February 21 2011 2011.

[20] A. Chantzis, A. D. Laurent, C. Adamo, and D. Jacquemin, "Is the Tamm-Dancoff Approximation Reliable for the Calculation of Absorption and Fluorescence Band Shapes?," *J Chem Theory Comput*, vol. 9, no. 10, pp. 4517-25, Oct 8 2013.

[21] E. A. Perpete, C. Lambert, V. Wathelet, J. Preat, and D. Jacquemin, "Ab initio studies of the lambda(max) of naphthoquinones dyes," *Spectrochim Acta A Mol Biomol Spectrosc*, vol. 68, no. 5, pp. 1326-33, Dec 31 2007.

[22] K. L. Meguellati, Sylvain; Spichty, Martin, "A conceptually improved TD-DFT approach for predicting the maximum absorption wavelength of cyanine dyes," *Dyes and Pigments*, vol. 90, pp. 114-118, December 3 2010 2010.

[23] C. Loison, R. Antoine, M. Broyer, P. Dugourd, J. Guthmuller, and D. Simon, "Microsolvation effects on the optical properties of crystal violet," *Chemistry*, vol. 14, no. 24, pp. 7351-7, 2008.

[24] C. C. Maria Vega Canamares, Ronald L. Birke, John R. Lombardi, "DFT, SERS, and Single-Molecule SERS of Crystal Violet," *J. Phys. Chem. C*, vol. 112, pp. 20295-20300, Dec 17, 2018 2008.

[25] Lili Lin, Zhongjie Wang, Jianzhong Fan, and C. Want, "Theoretical insights on the electroluminescent mechanism of thermally activated delayed fluorescence emitters," *Organic Electronics*, vol. 41, pp. 17-25, December 17, 2018 2017.

[26] Y. G. S. Isa Sidir, "Experimental and Theoretical Investigation of the molecular, electronic structure and solvatohromism of phenyl salicylate: External electric field effect on the electronic structure," *Journal of Molecular Structure*, vol. 1147, pp. 206-216, June 21, 2017 2017.

[27] J. P. Denis Jacquemin, Eric A. Perpete, "A TD-DFT study of the absorption spectra of fast dye salts," *Chemical Physics Letters*, vol. 410, pp. 254-259, April 28, 2005 2005.

[28] A. H. Tobias Risthaus, Stefan Grimme, "Excited States using the simplified Tamm-Dancoff Approach for range-separated hybrid density functionals: development and application," *Physical Chemistry Chemical Physics*, vol. 16, pp. 14408-14419, 2013.

[29] S. C. Silvio Pipolo, Roberto Cammi, "The cavity electromagnetic field within the polarizable continuum model of solvation: an application to the real-time time-dependent density functional theory," *Computational and Theoretical Chemistry*, vol. 1040-1041, pp. 112-119, February 28 2014 2014.

[30] A. D. Laurent and D. Jacquemin, "TD-DFT benchmarks: A review," *International Journal of Quantum Chemistry*, vol. 113, no. 17, pp. 2019-2039, 2013.

[31] C. Adamo et al., "Exploring excited states using time dependent density functional theory and density-based indexes," *J Coordination Chemistry Reviews*, vol. 304, pp. 166-178, 2015.

[32] F. J. Avila Ferrer, J. Cerezo, J. Soto, R. Improta, and F. Santoro, "First-principle computation of absorption and fluorescence spectra in solution accounting for vibronic structure, temperature effects and solvent inhomogenous broadening," *Computational and Theoretical Chemistry*, vol. 1040-1041, pp. 328-337, 2014.

[33] V. Barone, M. Biczysko, J. Bloino, L. Carta, and A. Pedone, "Reprint of "Environmental and dynamical effects on the optical properties of molecular systems by time-independent and time-dependent approaches: Coumarin derivatives as test cases"," *Computational and Theoretical Chemistry*, vol. 1040-1041, pp. 144-157, 2014.

[34] X. Blase, I. Duchemin, and D. Jacquemin, "The Bethe-Salpeter equation in chemistry: relations with TD-DFT, applications and challenges," *Chem Soc Rev*, vol. 47, no. 3, pp. 1022-1043, Feb 5 2018.

[35] A. Charaf-Eddin, T. Cauchy, F.-X. Felpin, and D. Jacquemin, "Vibronic spectra of organic electronic chromophores," *RSC Adv.*, vol. 4, no. 98, pp. 55466-55472, 2014.

[36] D. Jacquemin and C. Adamo, "Computational Molecular Electronic Spectroscopy with TD-DFT," *Top Curr Chem*, vol. 368, pp. 347-75, 2016.

[37] D. Jacquemin, E. Bremond, A. Planchat, I. Ciofini, and C. Adamo, "TD-DFT Vibronic Couplings in Anthraquinones: From Basis Set and Functional Benchmarks to Applications for Industrial Dyes," *J Chem Theory Comput*, vol. 7, no. 6, pp. 1882-92, Jun 14 2011.

[38] D. Jacquemin, B. Mennucci, and C. Adamo, "Excited-state calculations with TD-DFT: from benchmarks to simulations in complex environments," *Phys Chem Chem Phys*, vol. 13, no. 38, pp. 16987-98, Oct 14 2011.

[39] D. Jacquemin, C. Peltier, and I. Ciofini, "Visible spectrum of naphthazarin investigated through Time-Dependent Density Functional Theory," *Chemical Physics Letters*, vol. 493, no. 1-3, pp. 67-71, 2010.

[40] D. Jacquemin, E. A. Perpete, I. Ciofini, and C. Adamo, "Accurate simulation of optical properties in dyes," *Acc Chem Res*, vol. 42, no. 2, pp. 326-34, Feb 17 2009.

[41] D. Jacquemin, E. A. Perpete, F. Maurel, and A. Perrier, "TD-DFT simulations of the electronic properties of star-shaped photochromes," *Phys Chem Chem Phys*, vol. 12, no. 28, pp. 7994-8000, Jul 28 2010.

[42] D. Jacquemin et al., "Time-dependent density functional theory investigation of the absorption, fluorescence, and phosphorescence spectra of solvated coumarins," *J Chem Phys*, vol. 125, no. 16, p. 164324, Oct 28 2006.

[43] D. Jacquemin, E. A. Perpete, G. E. Scuseria, I. Ciofini, and C. Adamo, "TD-DFT Performance for the Visible Absorption Spectra of Organic Dyes: Conventional versus Long-Range Hybrids," *J Chem Theory Comput*, vol. 4, no. 1, pp. 123-35, Jan 2008.

[44] D. Jacquemin, A. Planchat, C. Adamo, and B. Mennucci, "TD-DFT Assessment of Functionals for Optical 0-0 Transitions in Solvated Dyes," *J Chem Theory Comput*, vol. 8, no. 7, pp. 2359-72, Jul 10 2012.

[45] D. Jacquemin, J. Preat, V. Wathelet, and E. A. Perpète, "Time-dependent density functional theory determination of the absorption spectra of naphthoquinones," *Chemical Physics*, vol. 328, no. 1-3, pp. 324-332, 2006.

[46] E. A. Perpète and D. Jacquemin, "TD-DFT benchmark for indigoïd dyes," *Journal of Molecular Structure*: THEOCHEM, vol. 914, no. 1-3, pp. 100-105, 2009.

[47] E. A. Perpete, C. Lambert, V. Wathelet, J. Preat, and D. Jacquemin, "Ab initio studies of the lambda(max) of naphthoquinones dyes," *Spectrochim Acta A Mol Biomol Spectrosc*, vol. 68, no. 5, pp. 1326-33, Dec 31 2007.

[48] A. Prlj, M. E. Sandoval-Salinas, D. Casanova, D. Jacquemin, and C. Corminboeuf, "Low-Lying pipi* States of Heteroaromatic Molecules: A Challenge for Excited State Methods," *J Chem Theory Comput*, vol. 12, no. 6, pp. 2652-60, Jun 14 2016.

[49] D. Rivero, M. Á. Fernández-González, and L. M. Frutos, "Tuning molecular excitation energy with external forces," *Computational and Theoretical Chemistry*, vol. 1040-1041, pp. 106-111, 2014.

[50] K. Sakata, N. Saito, and T. Honda, "Ab initio study of molecular structures and excited states in anthocyanidins," *Tetrahedron*, vol. 62, no. 15, pp. 3721-3731, 2006.

[51] L. Shen, H.-F. Ji, and H.-Y. Zhang, "A TD-DFT study on triplet excited-state properties of curcumin and its implications in elucidating the photosensitizing mechanisms of the pigment," *Chemical Physics Letters*, vol. 409, no. 4-6, pp. 300-303, 2005.

[52] M. B. Vincenzo Barone, Camille Latouche, Andrea Pasti, "Virtual eyes for technology and cultural heritage: towards computational strategy for new and old indigo-based dyes," *Theo Chem Acc*, 2015.

[53] K. I. Pryadarsini, "Photophysics, photochemistry and photobiology of curcumin: Studies from organic solutions, biomimetics and living cells," *Journal of Photochemistry and Photobiology C: Photochemistry Reviews*, vol. 80, pp. 81-95, May 11 2009 2009.

[54] S. K. Jessie A. Key, Qadir K. Timerghazin, Alex Brown, Christopher W. Cairo, "Photophysical characterization of triazole-substituted coumarin fluorophores," *Dyes and Pigments*, vol. 82, pp. 196-203, January 5 2009 2009.

[55] H.-F. J. Liang Shen, Hong-Yu Zhang, "A TD-DFT study on photo-physicochemical properties of hypocrellin A and its implications for elucidating the photosensitizing mechanisms of the pigment," *Journal of photochemistry and photobiology A: Chemistry*, vol. 180, pp. 65-68, September 21 2005 2006.

[56] H.-F. J. Liang Shen, "Theoretical study on physicochemical properties of curcumin," *Spectrochim Acta Part A*, vol. 67, pp. 619-623, August 15 2006 2007.

[57] G. G. Valentina Cantatore, Maurizio Persico, "Simulation of the pi-pi* photodynamics of azobenzene: Decoherence and solvent effects," *Computational and Theoretical Chemistry*, vol. 1040-1041, pp. 126-135, February 10 2014 2014.

[58] F. J. Avila Ferrer, J. Cerezo, J. Soto, R. Improta, and F. Santoro, "First-principle computation of absorption and fluorescence spectra in solution accounting for vibronic structure, temperature effects and solvent inhomogenous broadening," *Computational and Theoretical Chemistry*, vol. 1040-1041, pp. 328-337, 2014.

[59] V. Barone, M. Biczysko, J. Bloino, L. Carta, and A. Pedone, "Reprint of “Environmental and dynamical effects on the optical properties of molecular systems by time-independent and time-dependent approaches: Coumarin derivatives as test cases”," *Computational and Theoretical Chemistry*, vol. 1040-1041, pp. 144-157, 2014.

[60] A. P. Santu Biswas, Pranab Sarkar, "Effect of additional donor group on the charge transfer/recombination dynamics of a photoactive organic dye: a quantum mechanical investigation," *Computational and Theoretical Chemistry*, vol. 1103, pp. 38-47, January 10 2017 2017.

[61] N. S. Xian-Fu Zhang, Xulin Lu, Wenyu Jia, "Benzoate-modified rhodamine dyes: large change in fluorescence properties due to photoinduced electron transfer," *Journal of Luminescence*, vol. 179, pp. 511-517, July 20 2016 2016.

[62] U. R. Marika Savarese, Raolo A. Netti, Carlo Adamo, Ilaria Ciofini, Nadia Rega, "Modeling of charge transfer processes to understand photophysical signatures: The case of Rhodamine 110," *Chemical Physics Letters*, vol. 610-611, pp. 148-152, July 9 2014 2014.

[63] S. Chibani, D. Jacquemin, and A. D. Laurent, "Modelling solvent effects on the absorption and emission spectra of constrained cyanines with both implicit and explicit QM/EFP models," *Computational and Theoretical Chemistry*, vol. 1040-1041, pp. 321-327, 2014.

[64] A. H. S. Maarten T.P. Beerepoot, Kenneth Ruud, Jogvan Magnus Haugaard Olsen, Jacob Kongsted, "Convergence of environmental polarization effects in multiscale modeling of excitation energies," *Computational and Theoretical Chemistry*, vol. 1040-1041, pp. 304-311, March 17 2014 2014.

[65] G. J. Zhao et al., "Photoinduced intramolecular charge transfer and S2 fluorescence in thiophene-pi-conjugated donor-acceptor systems: experimental and TDDFT studies," Chemistry, vol. 14, no. 23, pp. 6935-47, 2008.

[66] J. C. Hollenberg, *Color Cosmetics: A Practical Guide to Formulation*. Carol Stream: Allured, 2016.

[67] P. Gupta, "Cosmetic Science," Spring 2016 semester course pertaining to biological, chemical, and pharmaceutical concepts utilized in cosmetic formulation development. ed. Philadelphia: University of the Sciences in Philadelphia, 2016.

[68] P. Romanowsky, "Practical Cosmetic & Product Development," Continuing and Professional Education course ed. New York: Society of Cosmetic Chemists, 2016.

[69] Handbook of Cosmetic Science and Technology, 3rd ed. New York: Informa Healthcare, 2009, p. 869.

[70] S. Pál, "Pharmaceutical Excipients of solid dosage forms," Institute of Pharmaceutical Technology and Biopharmacy, Web. December 18, 2018 2017.

[71] (2009, December 18, 2018). Nutriceutical definition. Available: https://medical-dictionary.thefreedictionary.com/nutriceutical

[72] (2012, December 18, 2018). Nutriceutical definition. Available: https://medical-dictionary.thefreedictionary.com/nutriceutical

[73] M. M. Reiger, "Cosmetics," in *Kirk-Othmer Chemical Technology of Cosmetics*, A. Seidel, Ed. Hoboken: Wiley, 2013, pp. 1-48.

[74] E. W. Flick, *Cosmetic and Toiletry Formulations*, 2nd ed. Norwich: Noyes, 2001, p. 378.

[75] E. W. Flick, *Cosmetic and Toiletry Formulations*, 2nd ed. Park Ridge: Noyes, 1989, p. 971.

[76] M. V. D. Michalun, Joseph, *Milady Skin Care and Cosmetic Ingredients Dictionary*, 4th ed. Clifton Park: Cengage Learning, 2015, p. 339.

[77] S. M. G. Ming Shin Neo, Tahir Mehmood Khan, Manish Gupta, "Quantification of Ethanol Content in Traditional Herbal Cough Syrups," *Pharmacogn. J.*, vol. 9, no. 6, pp. 821-827, 2017.

[78] R. U. P. E. W. J. A. R. D. Howes, "Fate of Ethanol Topically Applied To Skin," *Food Chem Toxicol*, vol. 39, no. 2, pp. 169-174, 2001.

[79] "Jaguar 8.8 User Manual," Schrodinger L.L.C. Web: Schrodinger Press, 2015.

[80] D. A. S. McQuarrie, John D., "Computational Quantum Chemistry," in *Physical Chemistry: A Molecular Approach* Sausalito: University Science, 1997, p. 1360.

[81] P. Elliott, K. Burke, and F. Furche, "Excited states from time-dependent density functional theory," in *Reviews in Computational Chemistry*, vol. 26, K. B. C. Lipkowitz, T.R., Ed. New York: Wiley-VCH, 2007, pp. 91-167.

[82] A. R. Leach, "Advanced Ab Initio Methods, Density Functional Theory, and Solid-State Quantum Mechanics," in *Molecular Modelling: Principles and Applications* 2nd ed. Harlow: Prentice Hall, 2001, pp. 108-164.

[83] P. F. Atkins, Ronald, *Molecular Quantum Mechanics*, 5th ed. Oxford: Oxford University Press, 2011, p. 537.

[84] A. D. Bochevarov et al., "Jaguar: A high-performance quantum chemistry software program with strengths in life and materials sciences," *International Journal of Quantum Chemistry*, vol. 113, no. 18, pp. 2110-2142, 2013.

[85] japan@wavefun.com. (2014, April 2, 2017). Spartan '14 Help: Questions about Basis Sets. Available: http://www.wavefun.com/japan/support/help/BasisSetFAQ.html

[86] E. A. Perpète and D. Jacquemin, "TD-DFT benchmark for indigoïd dyes," *Journal of Molecular Structure*: THEOCHEM, vol. 914, no. 1-3, pp. 100-105, 2009.

[87] M. B. Vincenzo Barone, Camille Latouche, Andrea Pasti, "Virtual eyes for technology and cultural heritage: towards computational strategy for new and old indigo-based dyes," *Theo Chem Acc*, 2015.

[88] D. Marmion, "Colorants for Foods, Drugs, and Cosmetics," in *Kirk-Othmer Chemical Technology of Cosmetics*, A. Seidel, Ed. Hoboken: Wiley, 2013, pp. 501-547.

[89] J. F. Senackerib, "Color Additives for foods, drugs, and cosmetics," in *Colorants for Non-Textile Applications*, A. T. P. H.S. Freeman, Ed. 1 ed. Amsterdam: Elsevier, 2000, pp. 131-187.

[90] PubChem. (2018, Dec 17, 2018). Indigo. Available: https://pubchem.ncbi.nlm.nih.gov/compound/5318432

[91] PubChem. (2018, December 17 2018). DC Yellow No. 11. Available: https://pubchem.ncbi.nlm.nih.gov/compound/6731#section=Top

[92] ToxNet. (2012, December 17, 2018). HSDB: D & C YELLOW NO. 11 Available: https://toxnet.nlm.nih.gov/cgi-bin/sis/search2/f?./temp/~1JyHiT:2

[93] PubChem. (2018, Dec 17, 2018). DC Red No. 36. Available: https://pubchem.ncbi.nlm.nih.gov/compound/5720319

[94] A. R. Leach, "Empirical Force Field Models: Molecular Mechanics," in *Molecular Modelling: Principles and Applications* 2nd ed. Harlow: Prentice Hall, 2001, pp. 165-252.

[95] R. S. Berns, "Producing Color," in *Billmeyer and Saltzman's Principles of Color Technology* 3rd ed.: Wiley, 2000, pp. 149-197.

[96] J. P. Denis Jacquemin, Valerie Wathelet, Eric A. Perpete, "Theoretical investigation of the absorption spectrum of thioindigo dyes," *Journal of Molecular Structure*: THEOCHEM, vol. 731, pp. 67-72, June 29, 2005 2005.

[97] N. D. Bernardino, S. Brown-Xu, T. L. Gustafson, and D. L. A. de Faria, "Time-Resolved Spectroscopy of Indigo and of a Maya Blue Simulant," *The Journal of Physical Chemistry C*, vol. 120, no. 38, pp. 21905-21914, 2016.

[98] B. Schaefer, "Colorants," in *Natural Products in the Chemical Industry*: Springer, 2014, pp. 13-44.

[99] P. F. Atkins, Ronald, "Molecular Electronic Transitions," in *Molecular Quantum Mechanics* 5th ed. Oxford: Oxford University Press, 2011, pp. 382-406.

[100] C. W. Reichardt, Thomas, "Specific Solvent Effects on UV/Vis Absorption Spectra," in *Solvents and Solvent Effects in Organic Chemistry* 4th ed. Weinheim: Wiley-VCH, 2011, pp. 380-384.

[101] C. W. Reichardt, Thomas, "Theory of Solvent Effects on UV/Vis Absorption Spectra," in *Solvents and Solvent Effects in Organic Chemistry* 4th ed. Weinheim: Wiley-VCH, 2011, pp. 371-380.

[102] C. W. Reichardt, Thomas, "Solvent Effects on Fluorescence Spectra," in *Solvents and Solvent Effects in Organic Chemistry* 4th ed. Weinheim: Wiley-VCH, 2011, pp. 384-393.

[103] C. W. Reichardt, Thomas, "Solvent Effects on Position of Homogenous Chemical Equilibrium," in *Solvents and Solvent Effects in Organic Chemistry* 4th ed. Weinheim: Wiley-VCH, 2011, pp. 107-156.

[104] C. W. Reichardt, Thomas, "Solvatochromic Compounds," in *Solvents and Solvent Effects in Organic Chemistry* 4th ed. Weinheim: Wiley-VCH, 2011, pp. 360-371.

[105] P. A. J. d. J. Keeler, *Physical Chemistry*, 11th ed. Oxford: Oxford University Press, 2018, p. 908.

[106] A. D. Bochevarov, "Automated Quantum Chemical Reactivity Predictions for the Predefined Reaction Types," ed. Web: Schrodinger L.L.C., 2018.

[107] ToxNet. (2018, December 17, 2018). 3-Hydroxy-2-(2-quinolinyl)-1H-inden-1-one. Available: https://chem.nlm.nih.gov/chemidplus/rn/5662-02-2

[108] S. Harfouch, "Quinoline Absorbance Peaks," J. Mohen, 2017, p. 2.

[109] H. Zollinger, "Azo Dyes and Pigments," in *Color Chemistry: Syntheses, Properties, and Applications of Organic Dyes and Pigments* 3rd ed.: Wiley-VCH, 2001, pp. 165-253.

[110] H. Sidebottom, K. Otsuka, A. Horowitz, J. Calvert, B. Rabe, and E. Damon, "Vibronic effects in the decay of the fluorescence excited in SO2 and NO2," *Chemical Physics Letters*, vol. 13, no. 4, pp. 337-343, 1972.

Chapter 2

Solvent Effects on Interaction Energies of Alternating Color Additive Molecular Structures in Conventional and Ionic Liquid Solvents Calculated using TD-DFT

Scientists familiar with the most rudimentary analysis of ultraviolet-visible spectroscopic spectral peak responsivity are typically advised to look for a single smooth curve that is discernible within the visible region, indicative of the hue of the mixture analyzed. Historically, compendulums have been published [1] to exist as reference guides for identification of color molecules based on their molecular structure and characteristic functional groups. In current era, online databases [2,3] are becoming available to complement the existing resources in order to serve as more contemporary "guides" for comparison of the UV-visible spectral peak responsivity of novel color additives in addition to those used since antiquity[15]. While most observers of the experimental peaks of various chromophore-containing groups will notice the prevalence of a single peak within the measured spectral range, an astute researcher will notice that experimental absorbance spectral data for other molecules exhibits very interesting anomalies. These may include "double-" or even "forked" peaks in which two nearly identical peaks are situated side-by-side, or a "plateau"-like rupture in the (usually left) side of the otherwise clearly-indicated single maximum absorbance peak. Some of these anomalies may be prevalent in certain formulation solvents, but not in others. The objective of this series of applied and theoretical chemical experiments in this study is to investigate the seemingly abnormal qualities of color additive-solvent mixture spectral

[15] Modern examples include [2] and [3], published by the National Institute of Standards and Technology (NIST) in the United States, available online and updated regularly as of September 2018.

peak responsivities of molecules of distinct dye classes using a similar computational approach--applying density functional theory--as discussed in detail in the prior chapter. However, in this study, solvent molecules will also be analyzed more thoroughly using both experimental and computational methods to explain their interaction with the color additive molecules selected.

One common source of visible anomalies or ruptures in the absorbance spectral curve can be attributed to the presence of known tautomerism or tautomer-like structural changes in solute molecules that occur when such molecules are mixed in a given solvent. These result from shifts in solution equilibria due to changes in solvent polarity [4-18], charge-transfer effects [5-7,13-15,18-22], or the acidity or basicity of the solution [4,12,18,23-25]. Countless studies have pursued experimental measurements to attempt to quantify the spectral shifts with increasing accuracy as more solute molecules are analyzed. In the historical works, the solvents utilized are restricted to chemical stock solutions. In more recent publications from the beginning of the twenty-first century until now, solvent choice has been taken under greater consideration with the advent of ionic liquids that have customizable properties based on combinations of the constituent ions comprising their binary mixture. In addition, ionic liquids are desirable alternatives to conventional “stock” solvents because they exhibit improved separation, distillation, and extraction properties which are strongly desirable in industrial settings readily applicable to food, pharmaceutical, cosmetic and other consumer product development. Furthermore, the effect of ions on excitation transitions has been noted in previous studies of molecules of smaller size [4,9,12,19,25-30]. Because ions can affect properties of chemical equilibria, this study has included three different ionic liquids with diverse

anion combinations to investigate the spectral shifts that may occur with common color additives approved for use in drugs, cosmetics, and/or food products. This study attempts to go further than experimental spectral analyses to determine if theoretical advanced ab initio methods have truly advanced enough to more directly correlate changes in color additive molecule bonding, charges, and structural isomerism to clearly explain causes of spectral anomalies. To verify the spontaneity of a particular structure being more dominant in a given mixture, interaction energies have been theoretically calculated using DFT to determine which structure is most prevalent in an analyte solution based on changes in enthalpy, entropy, and Gibbs free energy. A synthesis of the results pertaining to analyses of the three color additive molecules selected will reveal the interactions at play in chemical equilibria by comparing the effects of both conventional and alternative formulation solvents using theoretical data to explain experimental discrepancies in absorbance spectra.

Changes in hue as a result of the choice of solvent is a phenomenon known as solvatochromism, initially explored in the 1920s by scientists such as Holmes [31,32] and expanded upon significantly in the mid- to late twentieth century by Christian Reichardt [33-37]. The term “solvatochromism” applies when exploring color molecules that exhibit changes in the position of the absorption band and/or the molar extinction constant (ε) that accompanies a change in the polarity of the medium–and thus, in apparent hue and intensity, respectively—as a result of solvent interactions [17,31,32,38, 39]. A hypsochromic (blue) shift occurs with increasing solvent polarity, and typically higher frequency of wavelength emissions due to higher energy of electronic excitation transitions. In this case, the mixture is said to exhibit “negative solvatochromism”;

conversely, a bathochromic (red) shift occurs when there is a decrease in solvent polarity, and is known as “positive solvatochromism” [38]. The size of molecules studied has strongly affected the types of molecules surveyed. For example, coumarin has been a popular test molecule for theoretical and computational analyses due to its relatively small size [26-30]. In addition, certain authors warn that experimental limitations exist in analyzing mixtures containing molecules of different chromophore classes [40]. Reichardt focused exclusively on betaines in a number of studies [34,36,37]; in particular, betaine dye 30 has been named “Reichardt’s Dye” in honor of the famous researcher [12]. Mikhel Koel analyzed solvatochromism among several members of the oxazine dye class [41,42]. Oxazine dyes were also analyzed by [43] and [44], but as is evident in these studies, one common name may be used to refer to molecules exhibiting seemingly minor structural changes that may in fact largely impact noteworthy spectral shifts in different solvents. This generalization of molecules’ structural attributes must be carefully considered before making broad comparisons to model experimental spectra with accuracy. Furthermore, much literature data pertaining to spectra is limited to the most common formulation solvents. However, further questions lie at the structural level in which quantum chemical calculations are apt to provide insight. First, it is unknown exactly which structures contribute to the perceived hue during solvation. If there is a change in the color additive molecule structure, or perhaps a color additive-solvent molecule interaction occurring at the atomic level, it is invisible to the naked eye. Thus, computational data of the color additive structure as well as useful thermodynamic data in solvent obtained from DFT calculations of the optimal geometry conformation may begin to answer pertinent questions. Second, the prevalence of multiple peaks garners

interest in the question of whether or not multiple structures of quantifiable maximum absorbance spectra can be emulated in theoretical data--and if not, if isolating specific structures for computational analysis is possible to understand their physicochemical behavior in solution.

Materials and Methods

Computational advanced *ab initio* methods were used as described in Chapter 1. Geometry optimizations using density functional theory (DFT), and restricted singlet excited state theoretical calculations were carried out using its time-dependent counterpart (TD-DFT). The basis set B3LYP/6-31+G* was used in conjunction with a Los Alamos basis set LAV2P applying effective core potential (ECP) for determining properties related to electron density for heavy atoms in which diffuse functions (+ or "s") alone were not sufficient. While it is true that triple- and quadruple zeta basis sets are becoming commonplace in computational studies throughout relevant literature [9, 20, 45-69], in this work, due to the large quantity of molecules of varied dye classes—and thus of varied molecular structure and constituent atoms of color-inducing functional groups—as well as the range of atoms extending from hydrogen to sulfur (as in the sulfonated salt groups $[SO_3]^-$ as indicated in other molecules studied[16]), the 6-31G basis set was utilized throughout to maintain consistency among large data sets and to simplify analysis among the color additive molecules studied in order to notice anomalies pertaining to their isomeric structural characteristics.

[16] See Appendix G for additional examples of common water-soluble color additive molecules containing sulfonated salt groups.

In this study, three color additive molecules were selected for analysis based on the existence of clearly discernible absorbance spectral anomalies during repeated experimental trials:

(i) FD&C Red No. 40, more commonly referred to as Allura Red [70-72],

(ii) D&C Yellow No. 11 or "SS Quinoline Yellow" [70,73-75] , and

(iii) Brilliant Cresyl Blue [76-81].

Each of the three structures contains either a plateau or a double- or forked peak in its absorbance spectra that may contribute to noticeable experimental spectral anomalies as referenced in prior literature [1,2,31-32,72,76]. To determine the role of possible constitutional isomer formation within solute-solvent color additive mixtures to shift the equilibrium of the analyte mixture, two alternating structures of each color additive molecule listed above were assembled virtually in a computational workspace in order to generate theoretical absorbance spectra for later comparison to experimental spectral batch data. Representative chemical structures of each color additive molecule and its alternative structure analyzed are shown in Figures 30-32. Each alternating structure, referred to as "structure 1" (S1) and "structure 2" (S2) throughout this study, was constructed individually as a single input file for sequential quantum mechanical DFT calculations.

Five solvents were chosen for analysis in order to assess solvent effects on experimental batches for further investigation using computationally-derived data: water, ethanol, and three ionic liquids: 1-butyl-3-methylimidazolium chloride, (abbreviated

[BMIM]Cl), 1-butyl-3-methylimidazolium tetrafluoroborate (abbreviated [BMIM]BF_4), and 1-ethyl-3-methylimidazolium acetate (abbreviated [EMIM]OAc). Because ionic liquids exist as binary mixtures of pairs of oppositely-charged ions in solution [82], they exist as constructed in Figure 33 for ease of visual representation only. In this study, only implicit solvation effects using measurable solvent input parameters as variables for the Poisson Boltzmann Finite elements polarizable continuum model were incorporated into theoretical calculations. Explicit representations of the solvent molecules are combined with implicit data in another study [83].

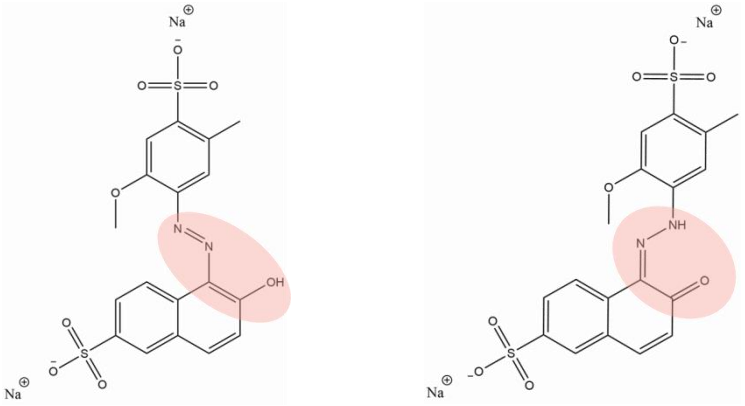

A **B**

Fig. 30. (a) FD&C Red No. 40 "azo" Structure 1 (S1) and (b) "hydrazone" Structure 2 (S2)

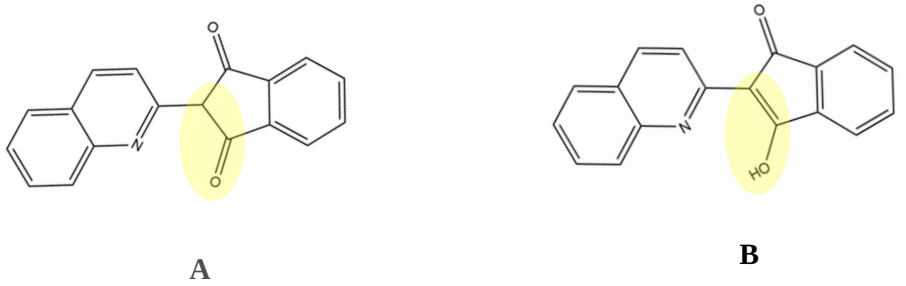

A **B**

Fig. 31. (a) D&C Yellow No. 11 "keto" Structure 1 (S1) and (b) "enol" Structure 2 (S2).

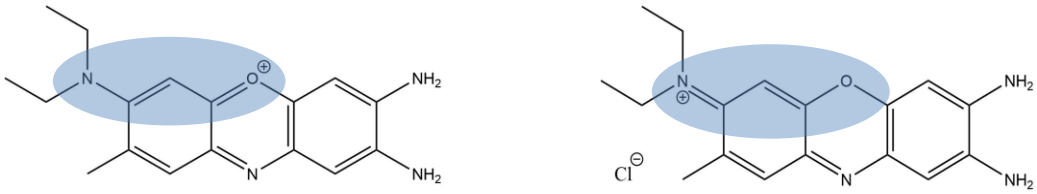

A **B**

Fig. 32. (a) Brilliant Cresyl Blue "BB" Structure 1 (S1) and (b) "C" Structure 2 (S2).

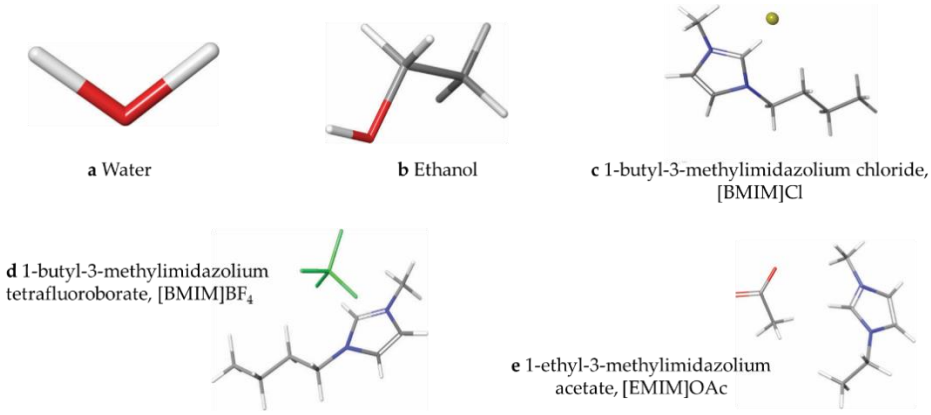

Fig. 33. Visual representations of solvent molecule structures provided for emphasis of implicit solvation effects data generated using molecular modeling and quantum mechanics calculations: (a) water, (b) ethanol, (c) 1-butyl-3-methylimidazolium chloride (abbreviated [BMIM]Cl), (d) 1-butyl-3-methylimidazolium tetrafluoroborate (abbreviated [BMIM]BF_4), and (e) 1-ethyl-3-methylimidazolium acetate (abbreviated [EMIM]OAc)

Geometry conformations initially modeled in vapor phase were calculated to generate optimal theoretical structural conformations in space using DFT. The resulting output file was used to model solvation effects on geometry conformations using the Poisson-Boltzmann Finite (PBF) elements continuum model [84]. To apply solvation effects, quantified input parameters including molecular weight, density, static dielectric constant (ϵ_0), and probe radius (in Å, Angstroms) were specified based on chemical supplier specifications, measured experimental quantities published in reputable literature, or as calculated using the capabilities of the Schrödinger software package[17] . The input parameters are listed as shown in Table 15. Ionic liquid solvent input parameters were selected from contemporary literature studies [85-88] due to their recent popularity as novel, recyclable alternatives to more conventional formulation solvents due to their customizable physicochemical properties [82,25,86-147] and sustainable

[17] Schrödinger Jaguar 2015-2 software with Maestro graphical interface was used to calculate probe radius (Å) and for QM calculations throughout this study.

[7,28,34,35,41,42,82,89,91,100,103,104,109,110,111,119,120,122,123,126,133,136,144, 146,148-152] characteristics.

TABLE XV

List of theoretical input parameters used for Poisson-Boltzmann Finite (PBF) elements solvation effects in DFT and TD-DFT calculations for color additive structures 1 and 2[18]

Solvent	ϵ_0	Molecular Weight (g/mol)	Density (g/cm^3)
Water	80.37[d]	18.02[d]	0.99823[d]
Ethanol	24.85[d]	46.07[d]	0.785[d]
[BMIM]Cl	14	174.67[c]	1.08[b,c]
[BMIM]BF_4	13.9 ± 0.4[a]	226.02[c]	1.21[c]
[EMIM]OAc	12	170.21[c]	1.027[c]

Interaction energies, including enthalpy, entropy, and Gibbs free energy values, were calculated using self-consistent field (SCF) energies generated based on the aforementioned (theoretical) solvation effects. These values were compared to both theoretical and experimental spectra to deduce the dominant structure in each solvent analyzed.

Experimental Data

Small-scale batch preparations of color additive-solvent mixtures were prepared by using the following procedure. 0.5 mL of the solvent of choice was added to a 1.0 mL Eppendorf tube. A mole fraction of color additive molecule (solid, dry, powder form) was then added to the existing 0.5 mL volume of solvent based on the increments listed in

[18] Numerical values obtained from: [a] [85] [b] [86] [c] Sigma-Aldrich Safety Data Sheets (SDS) for 1-butyl-3-methylimidazolium chloride [153], 1-butyl-3-methylimidazolium tetrafluoroborate [154], and 1-ethyl-3-methylimidazolium acetate [155] [d] Schrödinger Maestro Jaguar Preset value, 2015-2 edition. Jaguar, Schrödinger, LLC, New York, NY, 2015 [84].

Table 16. An additional 0.5 mL of the same solvent used initially was added to the color additive-solvent mixture to create a 1.0 mL volume batch. The mixture was vortexed for approximately 10 seconds, and sonicated for approximately 25 minutes to ensure complete dissolution of color additive solute into solvent analyte.

TABLE XVI

Experimental concentrations of FD&C Red No. 40, D&C Yellow No. 11, and Brilliant Cresyl Blue batches prepared in varied solvents

Concentration	μM	M
10 μM	10	1×10^{-5}
1 μM	1	1×10^{-6}
0.1 μM	1×10^{-1}	1×10^{-7}

This procedure was followed for preparation of experimental batches containing FD&C Red No. 40, D&C Yellow No. 11, and Brilliant Cresyl Blue in five distinct solvents: water, ethanol, [BMIM]Cl, [BMIM]BF_4, and [EMIM]OAc. Satisfactory mixtures were transferred onto a 0.1 mm path length cuvette for further spectroscopic analysis using a conventional UV-visible spectrophotometer.

FD&C Red No. 40 absorbance spectral data generated from experimental UV-visible spectroscopic analyses within the 400 nm-700 nm range is depicted in Figure 34. Relevant λ_{max} values are listed for numerical comparison in Table 17. D&C Yellow No. 11 absorbance spectral data generated from experimental UV-visible spectroscopic analyses between 300 nm-700 nm is shown in Figure 35. Relevant λ_{max} values are listed for numerical comparison in Table 18. Brilliant Cresyl Blue absorbance spectral data generated from experimental UV-visible spectroscopic analyses within the 400 nm-700

nm range is indicated in Figure 36. Relevant λ_{max} values are listed for numerical comparison in Table 19.

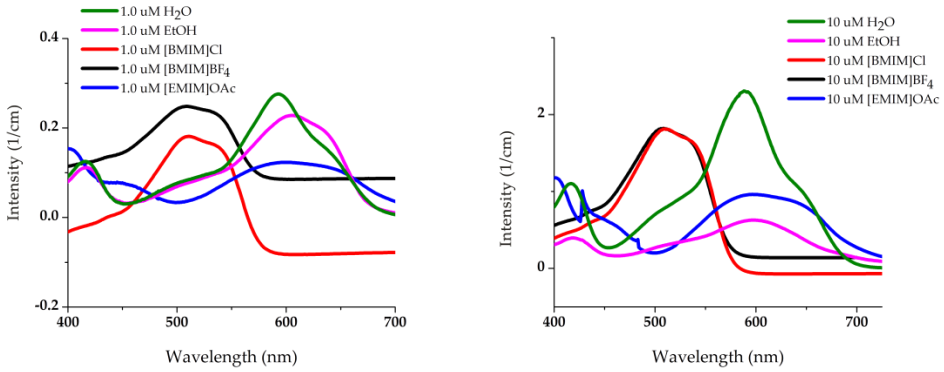

Fig. 34. 1.0 µM and 10 µM concentrations of FD&C Red No. 40 experimental maximum absorbance spectral peak responsivity (λ_{max}) in five solvents

TABLE XVII

FD&C Red No. 40 experimental maximum absorbance spectral peak responsivity (λ_{max}) comparison among five solvents

Solvent	$\lambda_{1\,\mu M}$	$\lambda_{10\,\mu M}$	$\Delta\lambda$(nm)
Water	592	586.5	-5.5
Ethanol	605, 634	599.3	-5.7
[BMIM]Cl	509.4, 534.1	509.5, 536	0.1, 1.9
[BMIM]BF_4	506.4, 531.7	506.4, 530.23	0, -1.47
[EMIM]OAc	602.5	592.73, 633.13	-9.77

"Allura red" exhibits relatively small changes in λ_{max} when comparing 1 µM (1 micromolar) and 10 µM concentrations of the same solvent, with the exception being ionic liquid [EMIM]OAc, in which case a larger hypsochromic shift is seen with increased color additive concentration in [EMIM]OAc. In addition, [BMIM]Cl and [BMIM]BF_4 both exhibit plateau-like spectra that differ in spectral range from

[EMIM]OAc and polar ethanol by a bathochromic (rightward, red) shift of approximately 100 nm. Less polar water solvent exhibits a more clearly-defined λ_{max} at 592 nm, closer in spectral range to ethanol and [EMIM]OAc counterparts. Theoretical absorption spectra will serve to clarify the phenomenon contributing to the distinct changes in absorbance spectra due to the solvent in which the color additive molecule is analyzed.

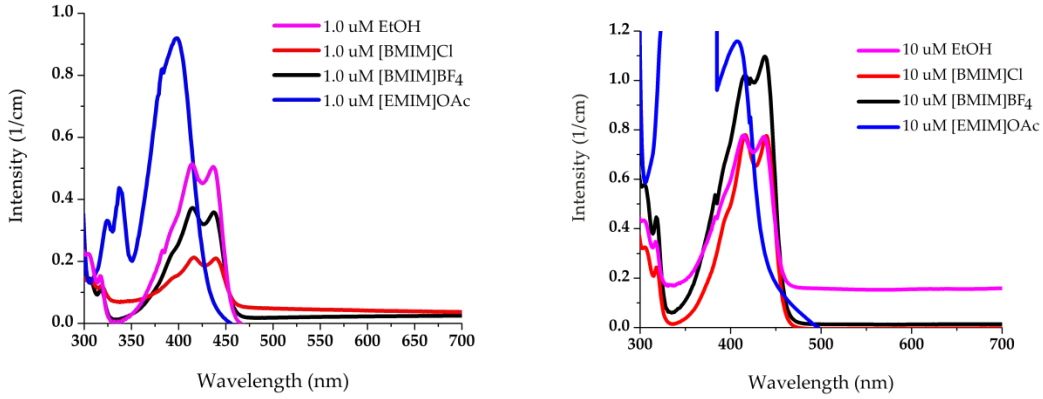

Fig. 35. 1.0 µM and 10 µM concentrations of D&C Yellow No. 11 experimental maximum absorbance spectral peak responsivity (λ_{max}) in five solvents

TABLE XVIII

D&C Yellow No. 11 experimental maximum absorbance spectral peak responsivity (λ_{max}) comparison among four solvents

Solvent	$\lambda_{1\,\mu M}$	$\lambda_{10\,\mu M}$	$\Delta\lambda$ (nm)
Ethanol	415, 437	415, 438	0, 1
[BMIM]Cl	415, 437.5	416, 439	1, 1.5
[BMIM]BF_4	415, 437.5	417, 438	2, 0.5
[EMIM]OAc	382, 398	407.6	9.6

The experimental data reveals multiple vibronic peaks of pronounced intensity, yet differing height, based on solvent selection. D&C Yellow No. 11 is known for being exceptionally soluble in most common formulation solvents, except for water [71,76].

This was proven to be the case during experimental trials, and was even troublesome during computational simulation at times, thus water solubility data for this molecule has been excluded from analysis. The structures shown in Figure 31(a) and (b) indicate that keto-enol tautomerism clearly exists [1,2,156-157]. However, theoretical calculations will be necessary to quantitatively deduce the most favorable structure in the given mixture as well as designate each peak as indicative of a particular isomer.

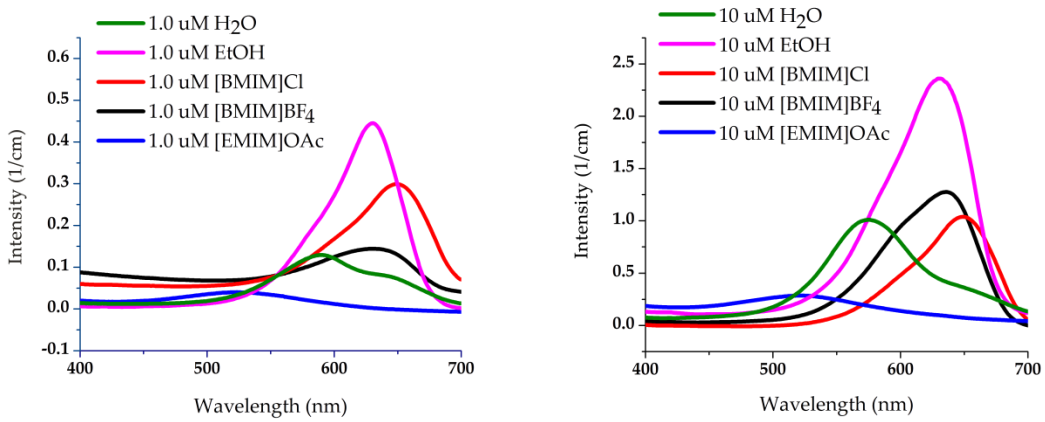

Fig. 36. 1.0 µM and 10 µM concentrations of Brilliant Cresyl Blue experimental maximum absorbance spectral peak responsivity (λ_{max}) in five solvents

TABLE XIX

Brilliant Cresyl Blue experimental maximum absorbance spectral peak responsivity (λ_{max}) comparison among five solvents

Solvent	$\lambda_{1\,\mu M}$	$\lambda_{10\,\mu M}$	$\Delta\lambda$ (nm)
Water	588.15	573.73	-14.42
Ethanol	630.2	630.84	0.64
[BMIM]Cl	650.7	648.87	-1.83
[BMIM]BF_4	635.024	636.25	1.226
[EMIM]OAc	519.6	515.46	-4.14

Spectral data for this molecule indicates a wide variety of hues appear based on choice of solvent. Water has an intense blue hue that exhibits a hypsochromic (blue) shift

with increased concentration. However, the ethanol and [BMIM]BF_4 values exhibit different projects of absorbance spectra with very small changes in λ_{max}, as well as a slight bathochromic (red) shift. [BMIM]Cl has a noticeably right-shifted λ_{max}, possibly as a result of greater hydrogen bond acceptor (HBA) capability of the chlorine anion [12,18,89]. [EMIM]OAc data produces the most shocking result—a deep red hue that is a stark contrast to the intense blue appearance of Brilliant Cresyl Blue in other solvents. Theoretical calculations will serve to better clarify solvatochromic effects and other influences contributing to such a significant difference in hue.

Theoretical Data

Ball-and-stick structural models of FD&C Red No. 40, D&C Yellow No. 11, and Brilliant Cresyl Blue are shown in Figures 37-39, respectively. These theoretical structures are based on optimized geometry conformations to reflect accurate bond angles and orientations of each atom in (a virtual) space.

Density functional theory calculations shed light on aspects of solution equilibria effects that are themselves invisible to the naked eye, yet produce visual effects that are universally agreed upon as existent. While initial optimizations incorporated an ideal geometric conformation in vapor phase, they were followed by solvation effects using the Poisson Boltzmann Finite elements continuum model. Table 15 lists constants and calculated values that were necessary input parameters for determining solvent effects on molecules in the computational workspace and theoretical conditions discussed herein.

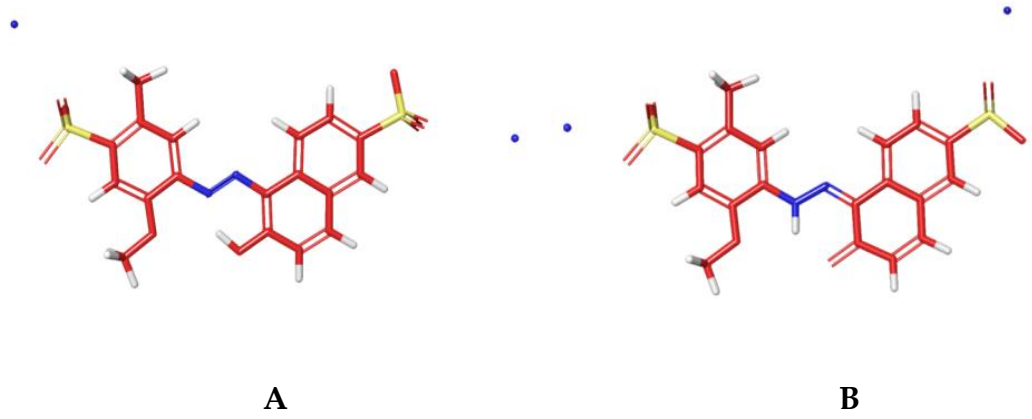

A **B**

Fig. 37. Three-dimensional visualization of optimal geometry conformation of FD&C Red No. 40 (a) Structure 1 “azo” form in water, and tautomeric (b) Structure 2 “hydrazone” form in [BMIM]BF_4.

A **B**

Fig. 38. Three-dimensional visualization of optimal geometry conformation of D&C Yellow No. 11 (a) Structure 1 “keto” form in [EMIM]OAc (12), and tautomeric (b) Structure 2 “enol” form in vapor phase.

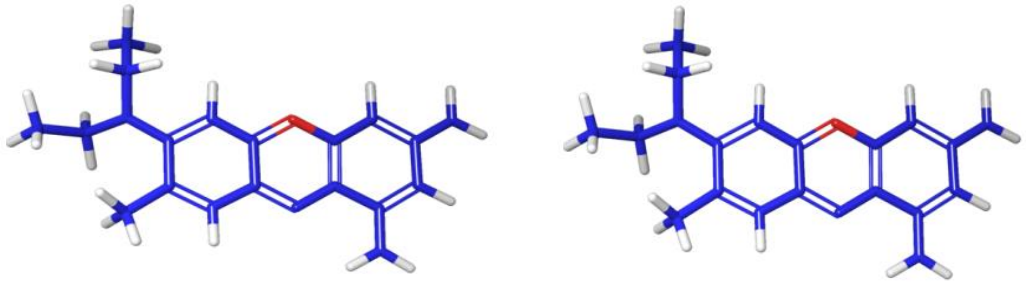

A **B**

Fig. 39. Three-dimensional visualization of optimal geometry conformation of Brilliant Cresyl Blue (a) Structure 1 “BB” form containing a charged oxygen atom in ethanol, and tautomeric (b) Structure 2 “C” form containing a charged nitrogen atom in water.

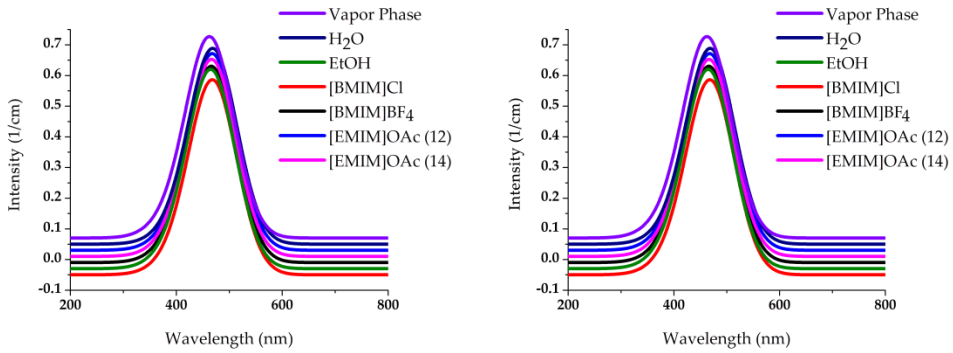

Fig. 40. TD-DFT simulation maximum absorbance spectral peak responsivity (λ_{max}) of FD&C Red No. 40 structures 1 and 2 in five solvents and in vapor phase.

TABLE XX

FD&C Red No. 40 theoretical TD-DFT simulation maximum absorbance spectral peak responsivity (λ_{max}) comparison among five solvents

Solvent	λ_{S1}	$\lambda_{Tautomer}$	$\Delta\lambda$(nm)
Water	451.97	467.98	16.01
Ethanol	454.13	464.95	10.82
[BMIM]Cl	451.11	467.98	16.87
[BMIM]BF_4	452.26	464.95	12.69
[EMIM]OAc (ϵ_0=12)	451.97	467.98	16.01
[EMIM]OAc (ϵ_0=14)	449.66	466.39	16.73
Vapor Phase	450.96	462.79	11.83

TABLE XXI

FD&C Red No. 40 experimental and theoretical TD-DFT simulation maximum absorbance spectral peak responsivity (λ_{max}) comparison in five solvents

Solvent	$\Delta\lambda_{Exp}$ (nm) ($\lambda_{10\ uM}$-$\lambda_{1\ uM}$)	Solvent	$\Delta\lambda_{max}$ (nm) (λ_{Expt}-λ_{Theo})			
			$\lambda_{1\mu M}$-λ_{S1}	$\lambda_{10\mu M}$-λ_{S1}	$\lambda_{1\mu M}$-$\lambda_{Tautomer}$	$\lambda_{10\mu M}$-$\lambda_{Tautomer}$
Water	-5.5	Water	140.03	134.53	124.02	118.52
Ethanol	-5.7	Ethanol	150.87, 179.87	145.17	140.05, 169.05	134.35
[BMIM]Cl	0.1, 1.9	[BMIM]Cl	58.29, 82.99	58.39, 84.89	41.42, 66.12	41.52, 68.02
[BMIM]BF_4	0, -1.47	[BMIM]BF_4	54.14, 79.44	54.14, 77.97	41.45, 66.75	41.45, 65.28
[EMIM]OAc	-9.77	[EMIM]OAc (ϵ_0=12)	150.53	140.76, 181.16	134.52	124.75, 165.15
		[EMIM]OAc (ϵ_0=14)	152.84	143.07, 183.47	136.11	126.34, 166.74

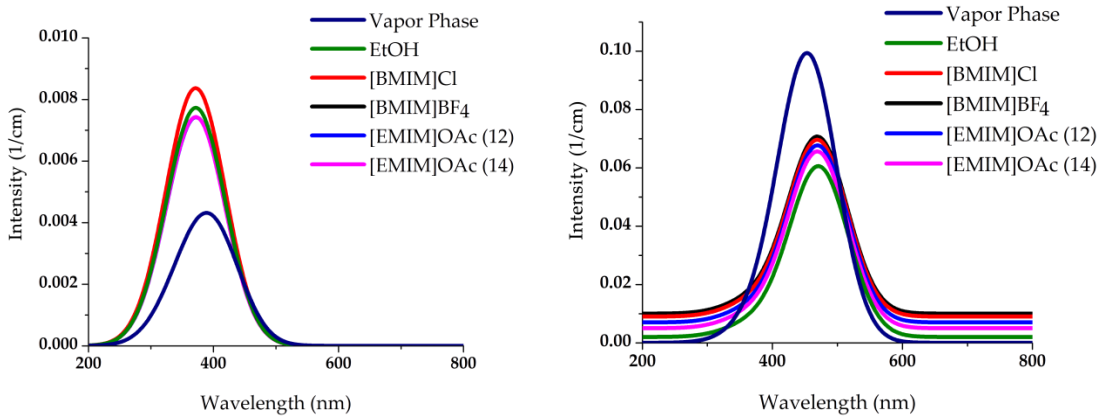

Fig. 41. TD-DFT simulation maximum absorbance spectral peak responsivity (λ_{max}) of D&C Yellow No.11 structures 1 and 2 in five solvents and in vapor phase.

TABLE XXII

D&C Yellow No. 11 theoretical TD-DFT simulation maximum absorbance spectral peak responsivity (λ_{max}) comparison among four solvents (and in vapor phase)

Solvent	λ_{S1}	$\lambda_{Tautomer}$	$\Delta\lambda$(nm)
Ethanol	370.76	469.28	98.52
[BMIM]Cl	371.35	469.28	97.93
$[BMIM]BF_4$	371.49	469.28	97.79
[EMIM]OAc (ϵ_0=12)	371.49	469.28	97.79
[EMIM]OAc (ϵ_0=14)	371.49	469.28	97.79
Vapor Phase	389.95	452.55	62.60

TABLE XXIII

D&C Yellow No. 11 experimental and theoretical TD-DFT simulation maximum absorbance spectral peak responsivity (λ_{max}) comparison in four solvents

Solvent	$\Delta\lambda_{Exp}$ (nm) ($\lambda_{10\ uM}$-$\lambda_{1\ uM}$)	Solvent	$\Delta\lambda_{max}$ (nm) (λ_{Expt}-λ_{Theo})			
			$\lambda_{1\mu M}$-λ_{S1}	$\lambda_{10\mu M}$-λ_{S1}	$\lambda_{1\mu M}$-$\lambda_{Tautomer}$	$\lambda_{10\mu M}$-$\lambda_{Tautomer}$
Ethanol	0, 1	Ethanol	44.24, 66.24	44.24, 67.24	-54.28, -32.28	-54.28, -31.28
[BMIM]Cl	1, 1.5	[BMIM]Cl	43.65,66.15	44.65, 67.65	-54.28, -31.78	-53.28, -30.28
$[BMIM]BF_4$	2, 0.5	$[BMIM]BF_4$	43.51, 66.01	45.51, 66.51	-54.28, -31.78	-52.28, -31.28
[EMIM]OAc	9.6 nm	[EMIM]OAc (ϵ_0=12)	10.51, 26.51	36.11	-87.28, -71.28	-61.68
		[EMIM]OAc (ϵ_0=14)	10.51, 26.51	36.11	-87.28, -71.28	-61.68

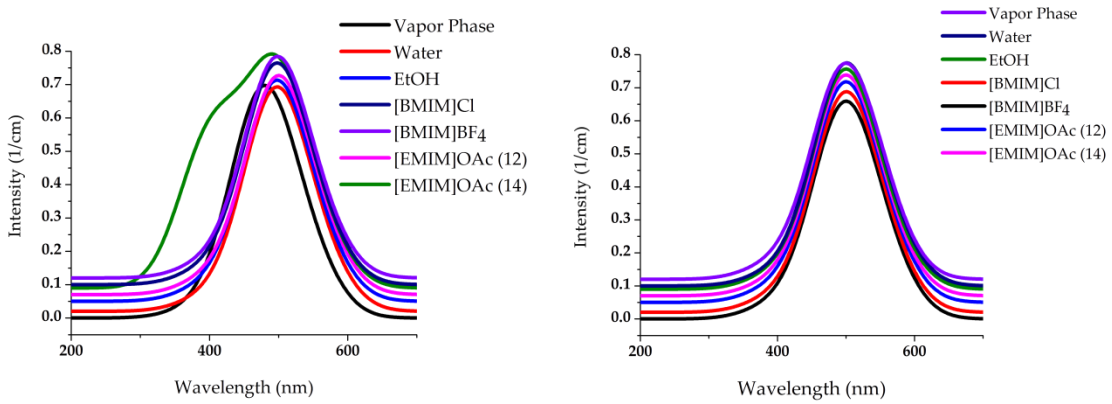

Fig. 42. TD-DFT simulation maximum absorbance spectral peak responsivity (λ_{max}) of Brilliant Cresyl Blue BB (structure 1, left) and C (structure 2, right) in five solvents and in vapor phase

TABLE XXIV

Brilliant Cresyl Blue theoretical TD-DFT simulation maximum absorbance spectral peak responsivity (λ_{max}) comparison in five solvents

Solvent	λ_{S1}	$\lambda_{Tautomer}$	$\Delta\lambda$ (nm)
Water	499.52	501.56	2.04
Ethanol	498.56	499.52	0.96
[BMIM]Cl	498.56	501.44	2.88
$[BMIM]BF_4$	499	499.52	0.52
[EMIM]OAc (ϵ_0=12)	498.56	500.6	2.04
[EMIM]OAc (ϵ_0=14)	489.54	499.52	9.98
Vapor Phase	479.57	499.52	19.95

TABLE XXV

Brilliant Cresyl Blue experimental and theoretical TD-DFT simulation maximum absorbance spectral peak responsivity (λ_{max}) comparison in five solvents

Solvent	$\Delta\lambda_{Exp}$ (nm) ($\lambda_{10\,\mu M}$-$\lambda_{1\,\mu M}$)	Solvent	$\Delta\lambda_{max}$ (nm) (λ_{Expt}-λ_{Theo})			
			$\lambda_{1\mu M}$-λ_{S1}	$\lambda_{10\mu M}$-λ_{S1}	$\lambda_{1\mu M}$-$\lambda_{Tautomer}$	$\lambda_{10\mu M}$-$\lambda_{Tautomer}$
Water	-14.42	Water	138.63	74.21	86.59	72.17
Ethanol	0.64	Ethanol	131.64	132.28	130.68	131.32
[BMIM]Cl	-1.83	[BMIM]Cl	152.14	186.31	149.26	183.43
$[BMIM]BF_4$	1.226	$[BMIM]BF_4$	136.024	137.25	135.504	136.73
[EMIM]OAc	-4.14	[EMIM]OAc (ϵ_0=12)	21.04	16.9	19.0	14.86
		[EMIM]OAc (ϵ_0=14)	30.06	25.92	20.08	15.94

HOMO-LUMO Surface Maps

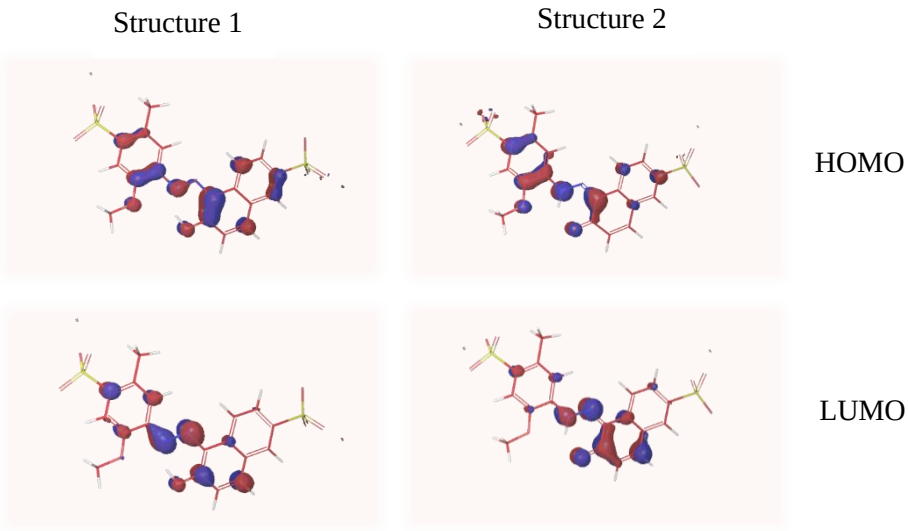

Fig. 43. FD&C Red No. 40 single-point-energy (SPE) output file containing calculated HOMO and LUMO surfaces in vapor phase.

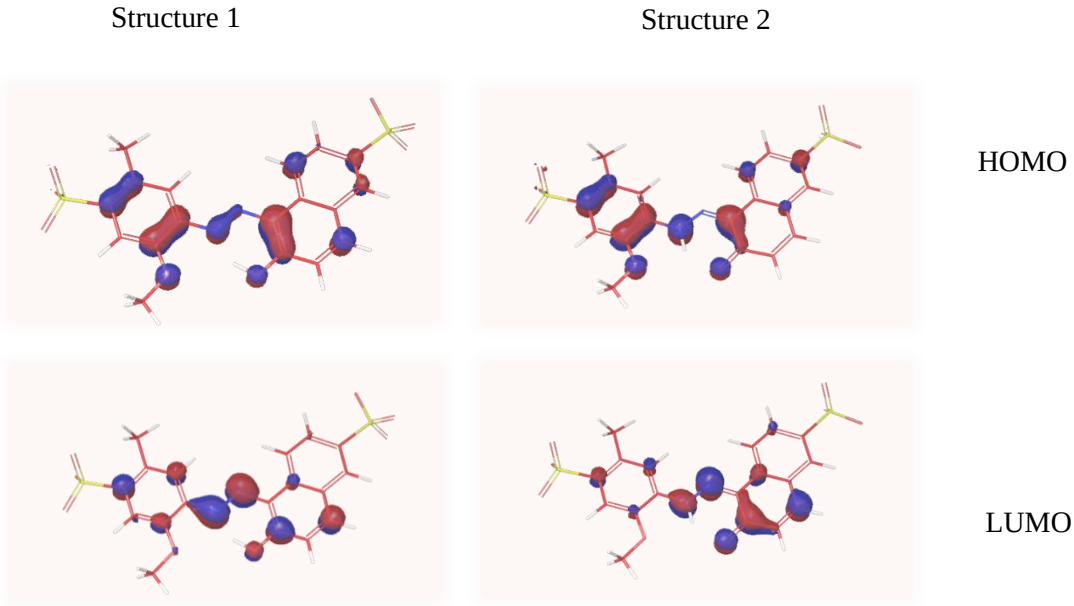

Fig. 44. FD&C Red No. 40 single-point-energy (SPE) output file containing calculated HOMO and LUMO surfaces with water solvation effects

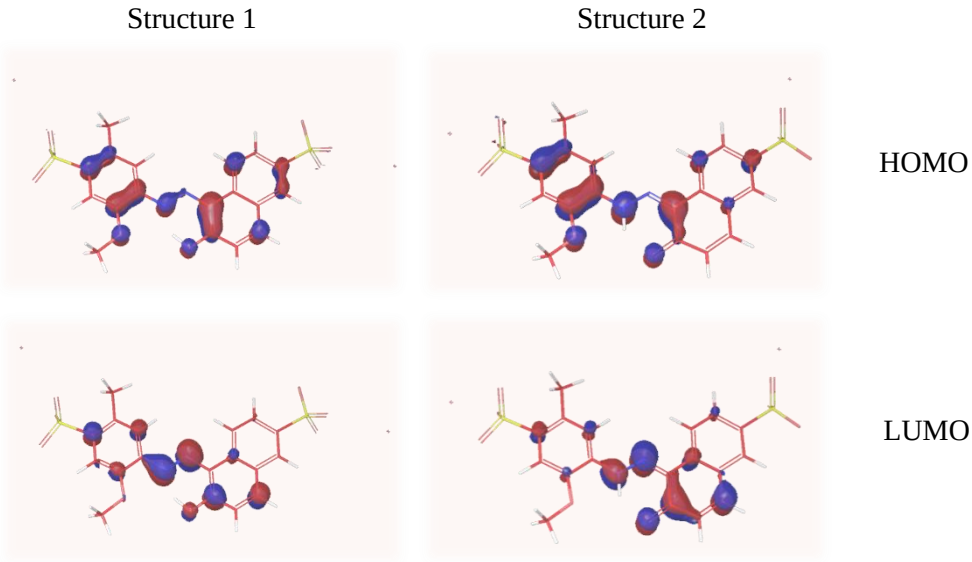

Fig. 45. FD&C Red No. 40 single-point-energy (SPE) output file containing calculated HOMO and LUMO surfaces with ethanol solvation effects

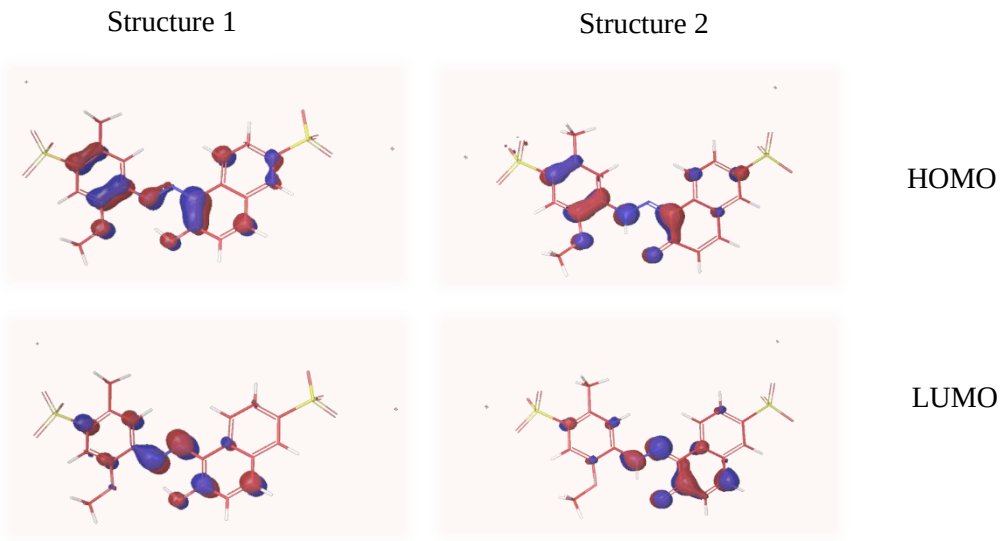

Fig. 46. FD&C Red No. 40 single-point-energy (SPE) output file containing calculated HOMO and LUMO surfaces with [BMIM]Cl ionic liquid solvation effects

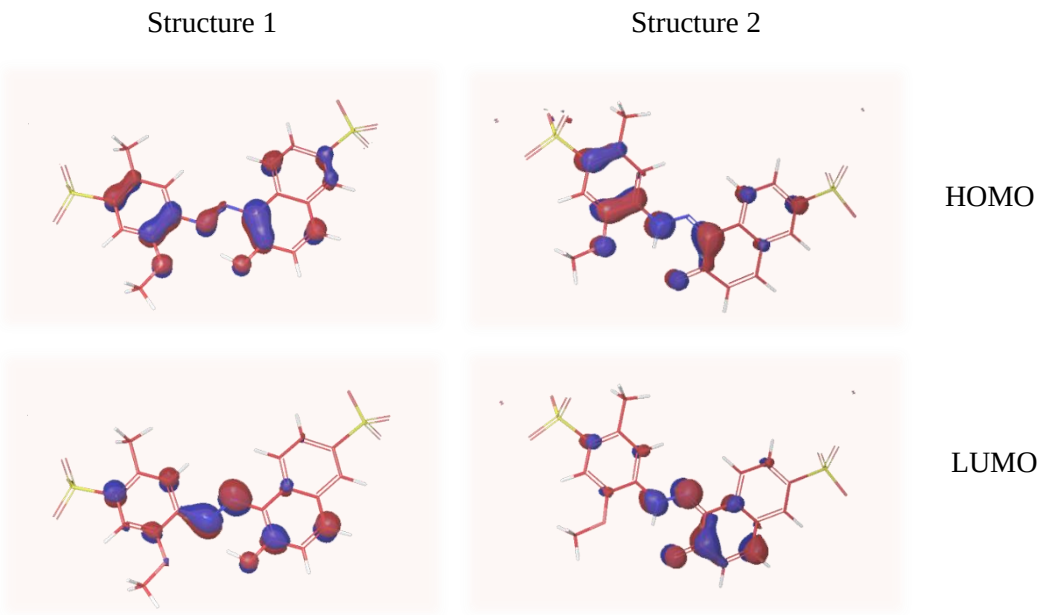

Fig. 47. FD&C Red No. 40 single-point-energy (SPE) output file containing calculated HOMO and LUMO surfaces with [BMIM]BF_4 ionic liquid solvation effects

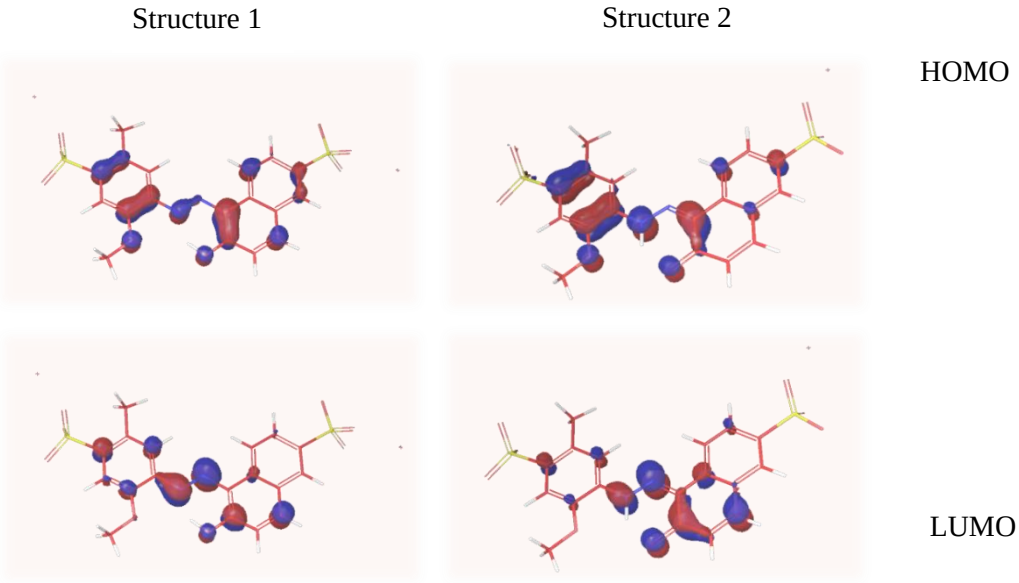

Fig. 48. FD&C Red No. 40 single-point-energy (SPE) output file containing calculated HOMO and LUMO surfaces with [EMIM]OAc (ϵ_0=12) ionic liquid solvation effects

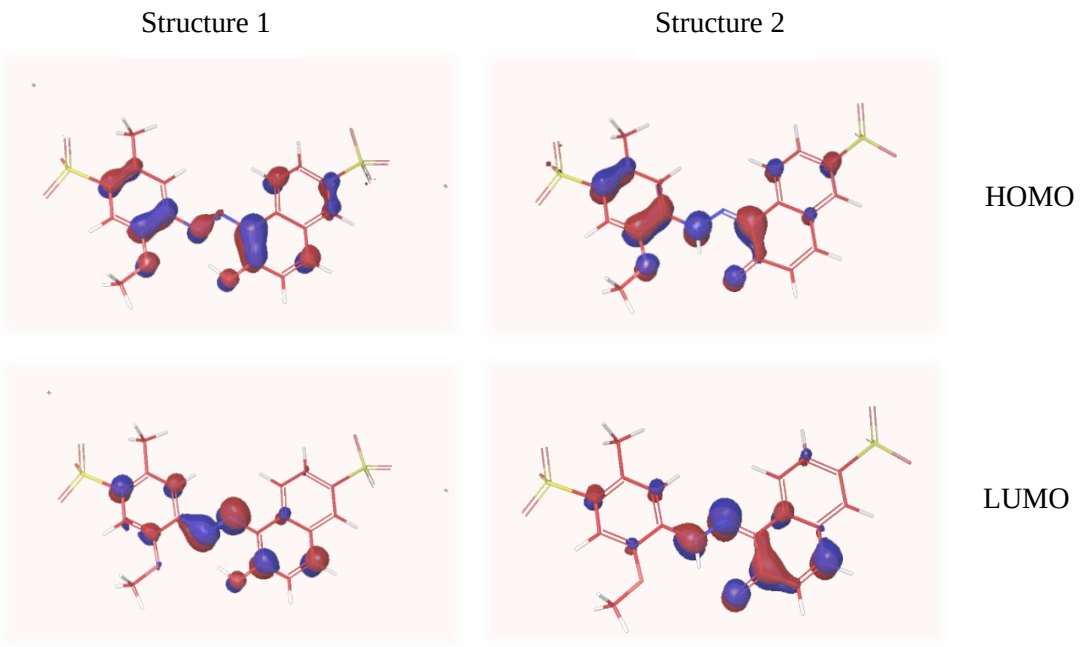

Fig. 49. FD&C Red No. 40 single-point-energy (SPE) output file containing calculated HOMO and LUMO surfaces with [EMIM]OAc (ϵ_0=14) ionic liquid solvation effects

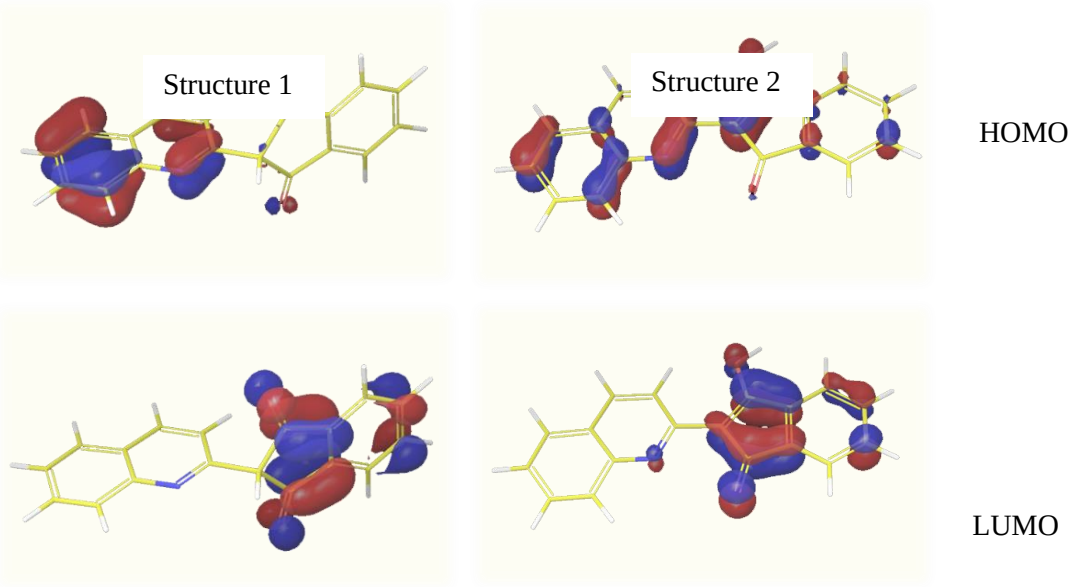

Fig. 50. D&C Yellow No. 11 single-point-energy (SPE) output file containing calculated HOMO and LUMO surfaces in vapor phase

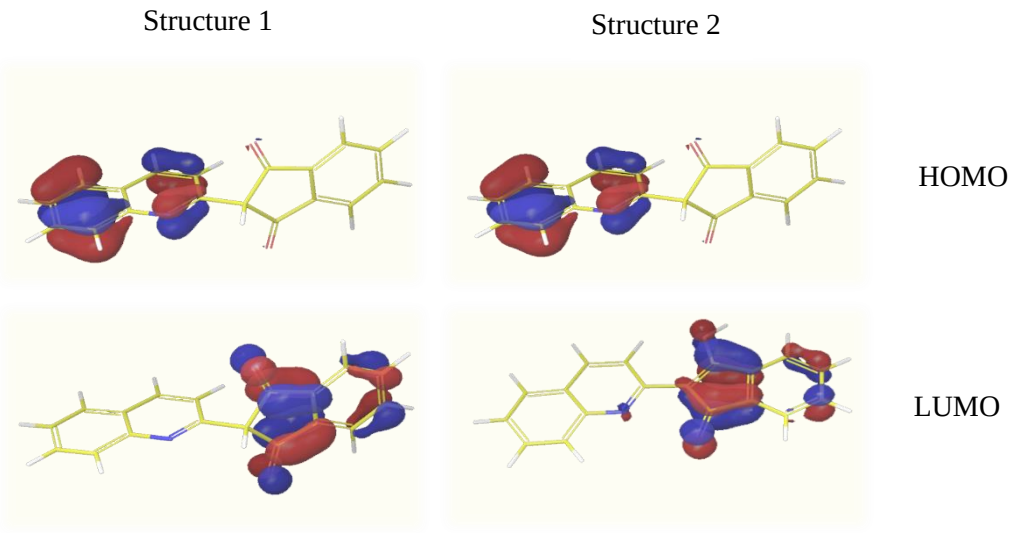

Fig. 51. D&C Yellow No. 11 single-point-energy (SPE) output file containing calculated HOMO and LUMO surfaces with ethanol solvation effects.

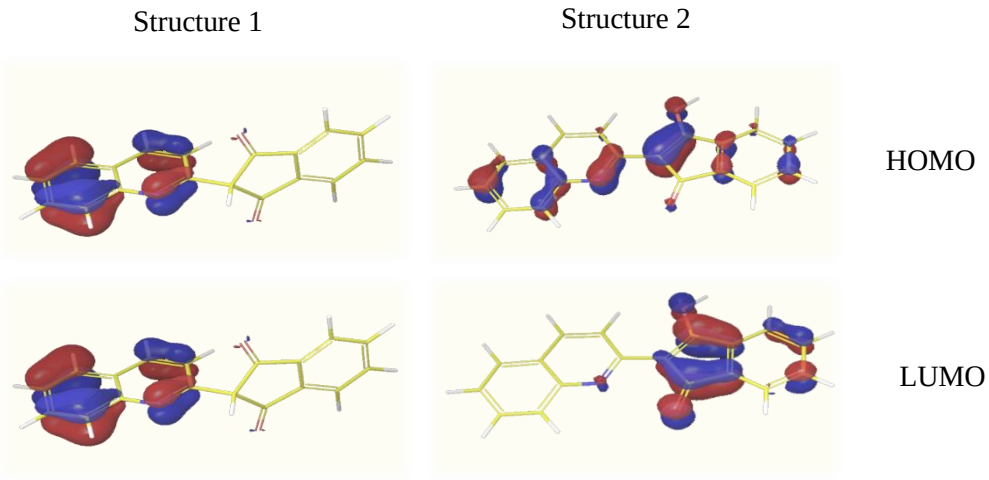

Fig. 52. D&C Yellow No. 11 single-point-energy (SPE) output file containing calculated HOMO and LUMO surfaces with [BMIM]Cl ionic liquid solvation effects

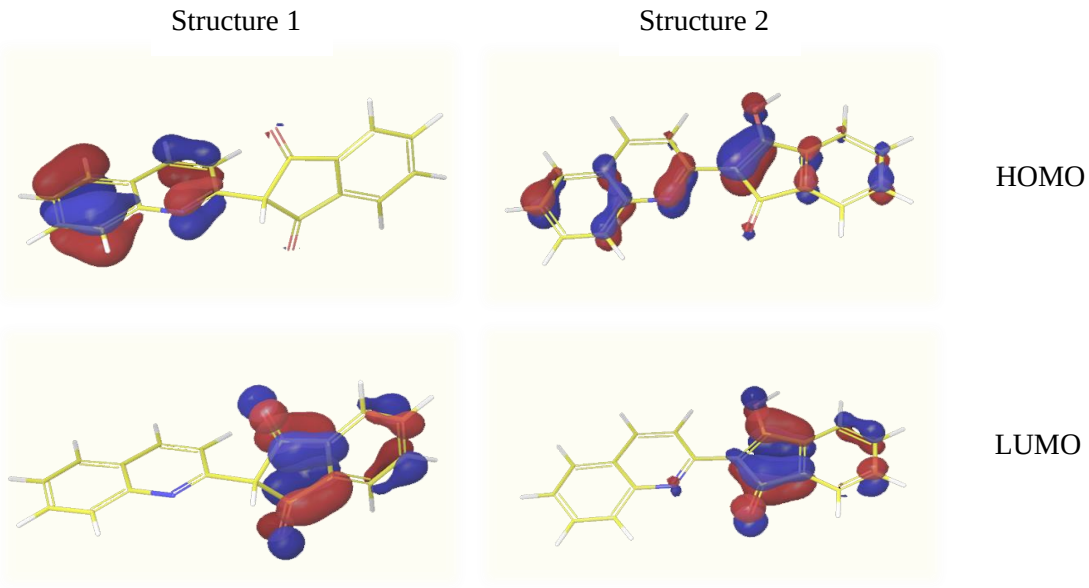

Fig. 53. D&C Yellow No. 11 single-point-energy (SPE) output file containing calculated HOMO and LUMO surfaces with [BMIM]BF_4 ionic liquid solvation effects.

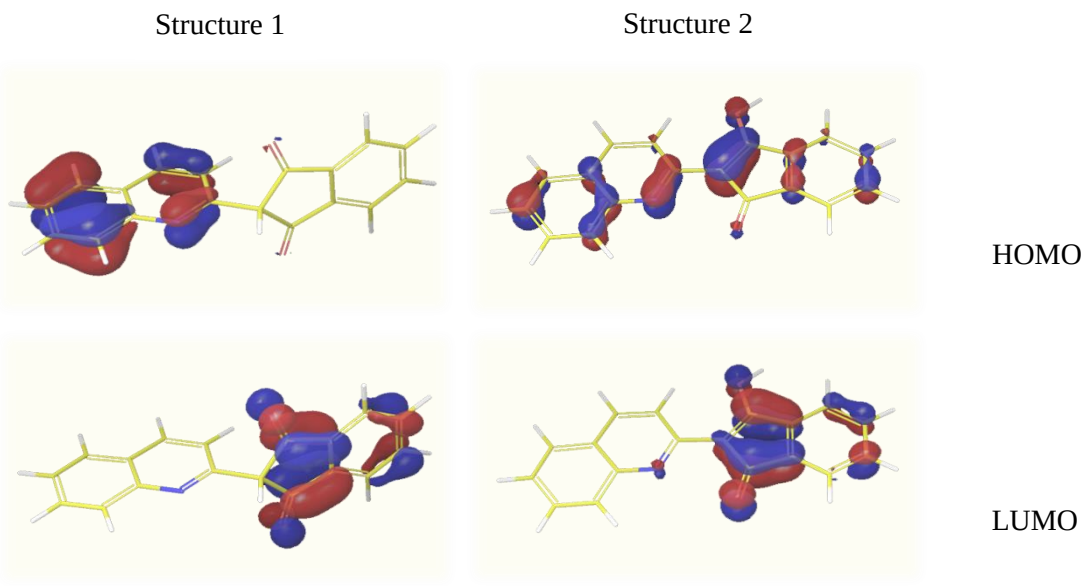

Fig. 54. D&C Yellow No. 11 single-point-energy (SPE) output file containing calculated HOMO and LUMO surfaces with [EMIM]OAc (ϵ_0=12) ionic liquid solvation effects

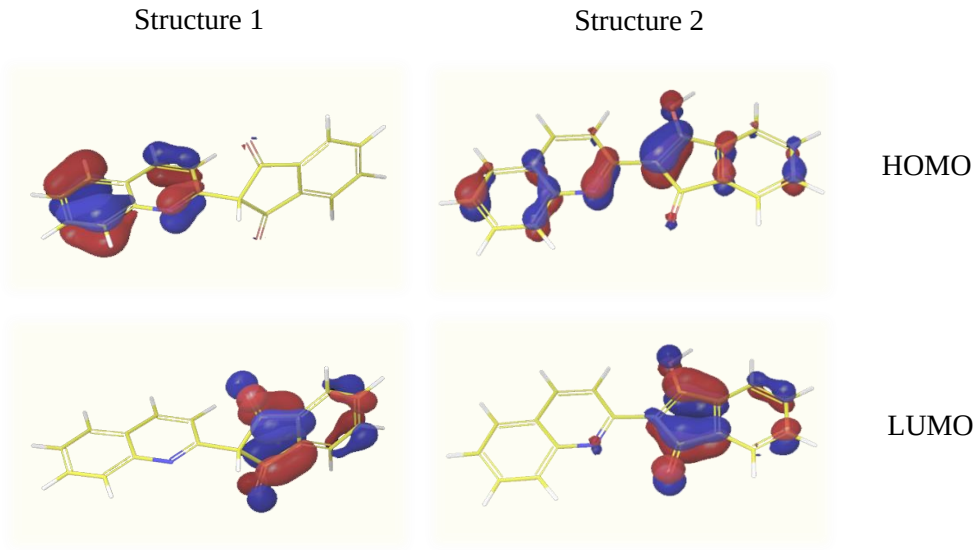

Fig. 55. D&C Yellow No. 11 single-point-energy (SPE) output file containing calculated HOMO and LUMO surfaces with [EMIM]OAc (ϵ_0=14) ionic liquid solvation effects

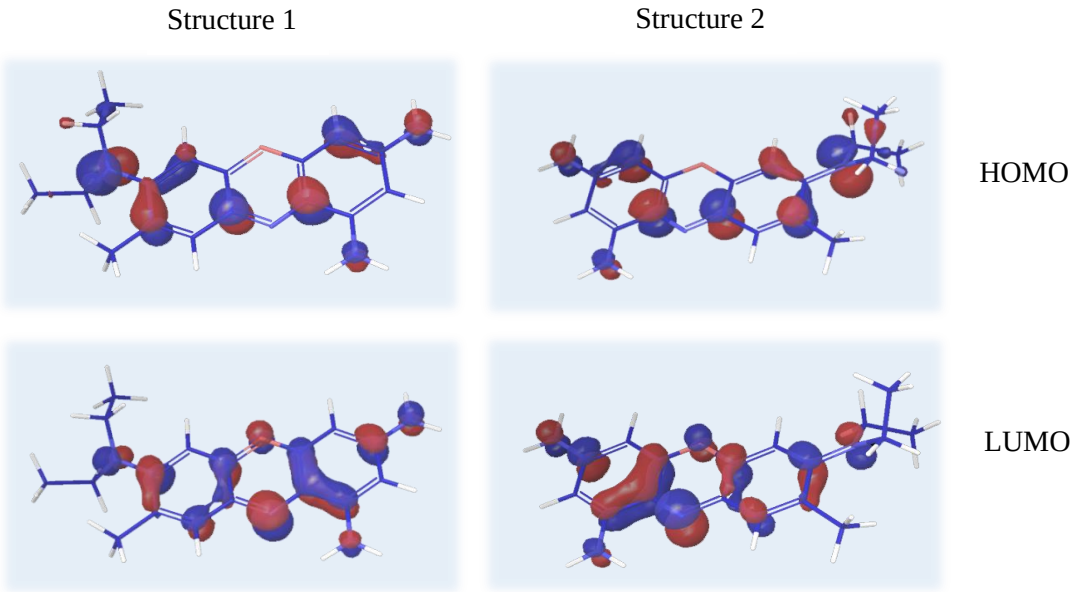

Fig. 56. Brilliant Cresyl Blue single-point-energy (SPE) output file containing calculated HOMO and LUMO surfaces in vapor phase

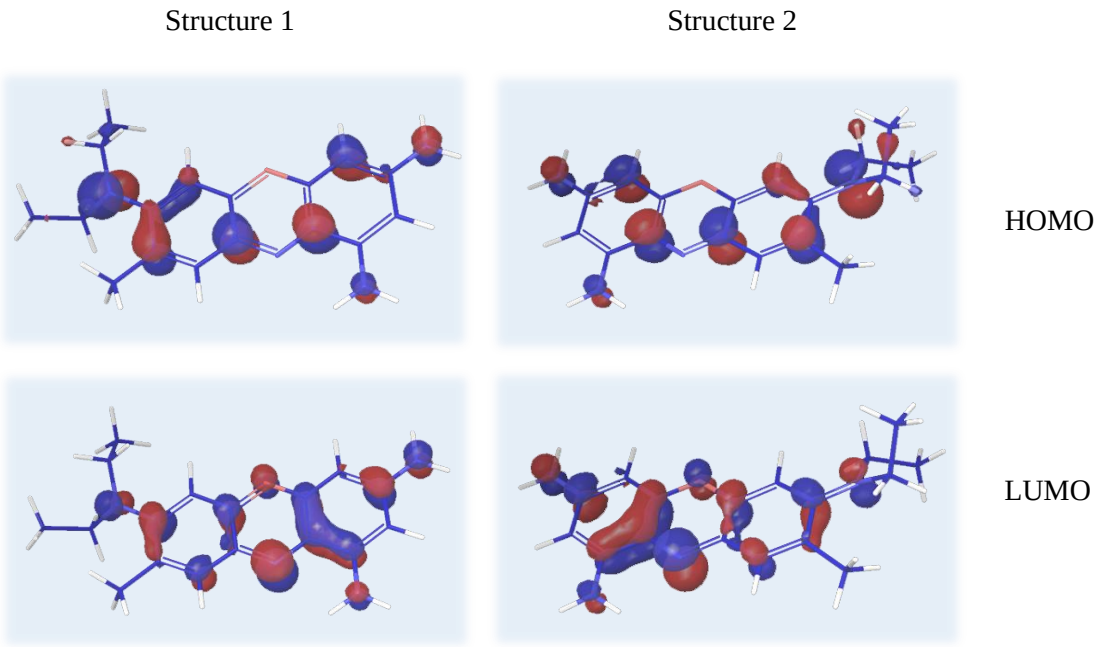

Fig. 57. Brilliant Cresyl Blue single-point-energy (SPE) output file containing calculated HOMO and LUMO surfaces with water solvation effects

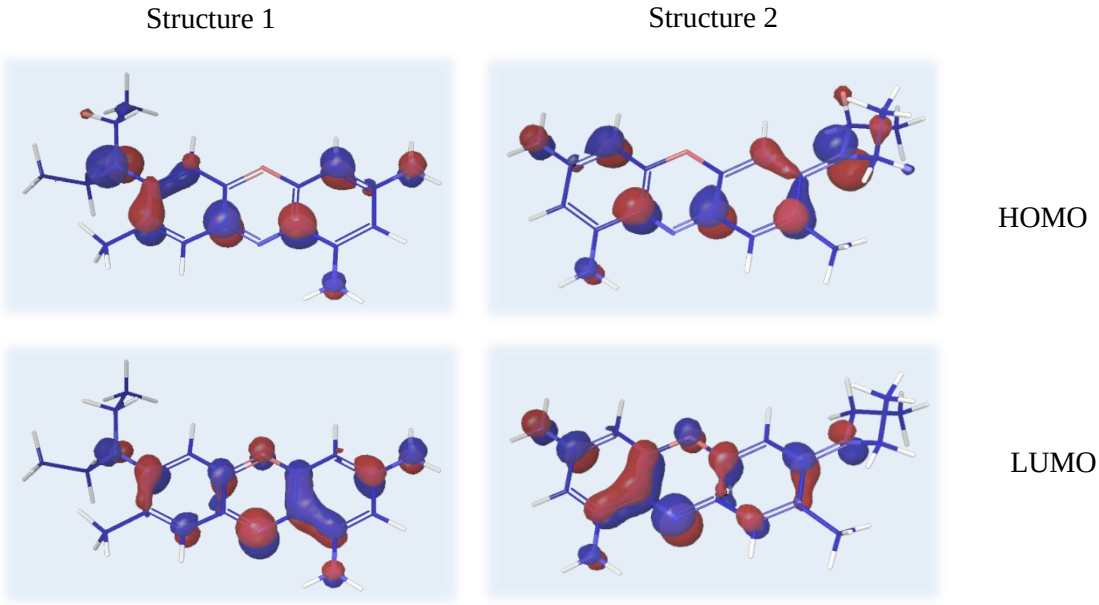

Fig. 58. Brilliant Cresyl Blue single-point-energy (SPE) output file containing calculated HOMO and LUMO surfaces with ethanol solvation effects.

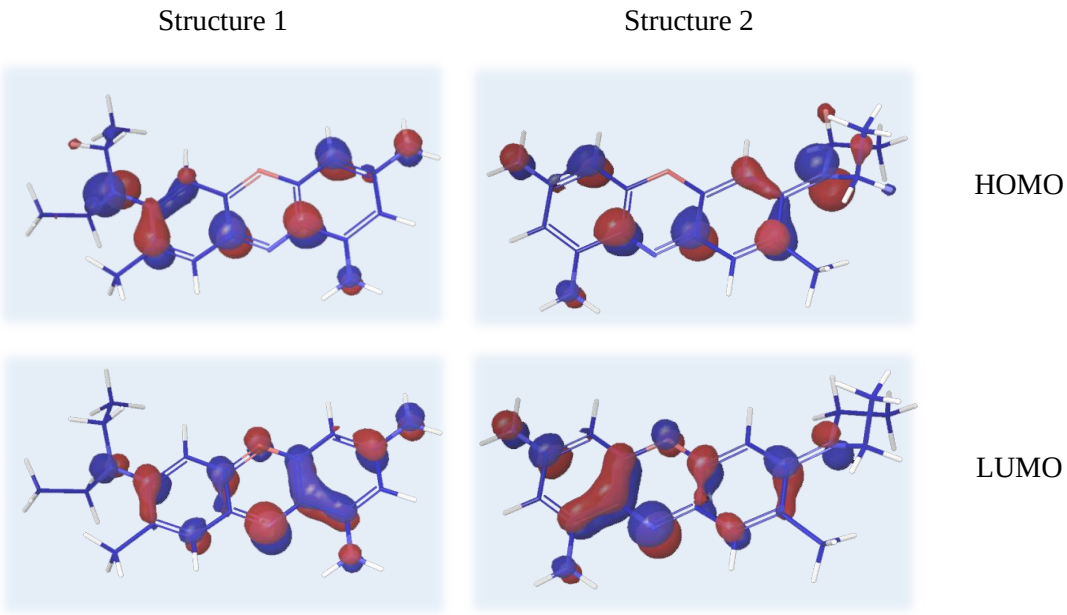

Fig. 59. Brilliant Cresyl Blue single-point-energy (SPE) output file containing calculated HOMO and LUMO surfaces with [BMIM]Cl ionic liquid solvation effects

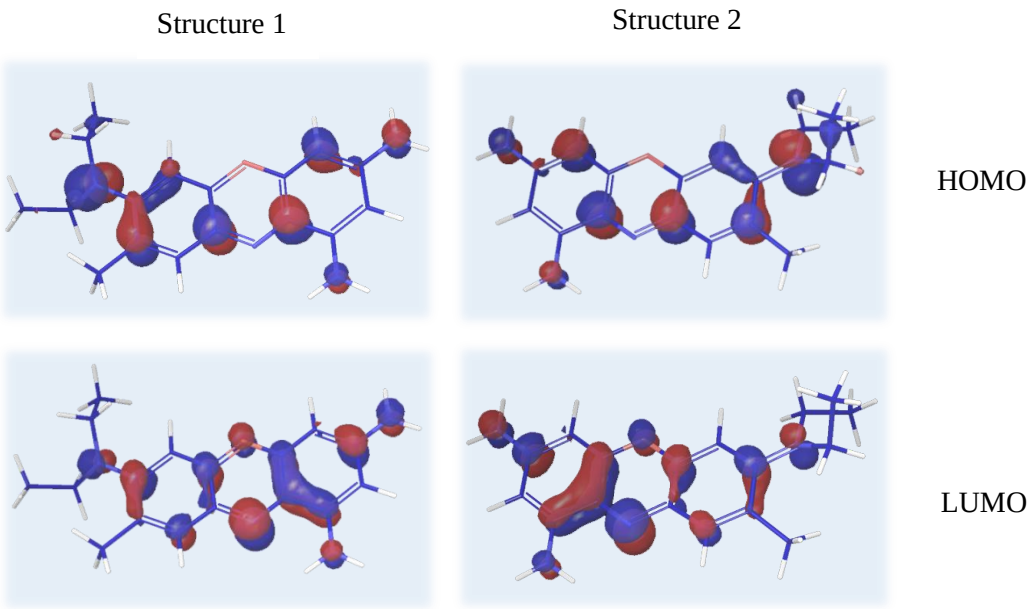

Fig. 60. Brilliant Cresyl Blue single-point-energy (SPE) output file containing calculated HOMO and LUMO surfaces with [BMIM]BF_4 ionic liquid solvation effects

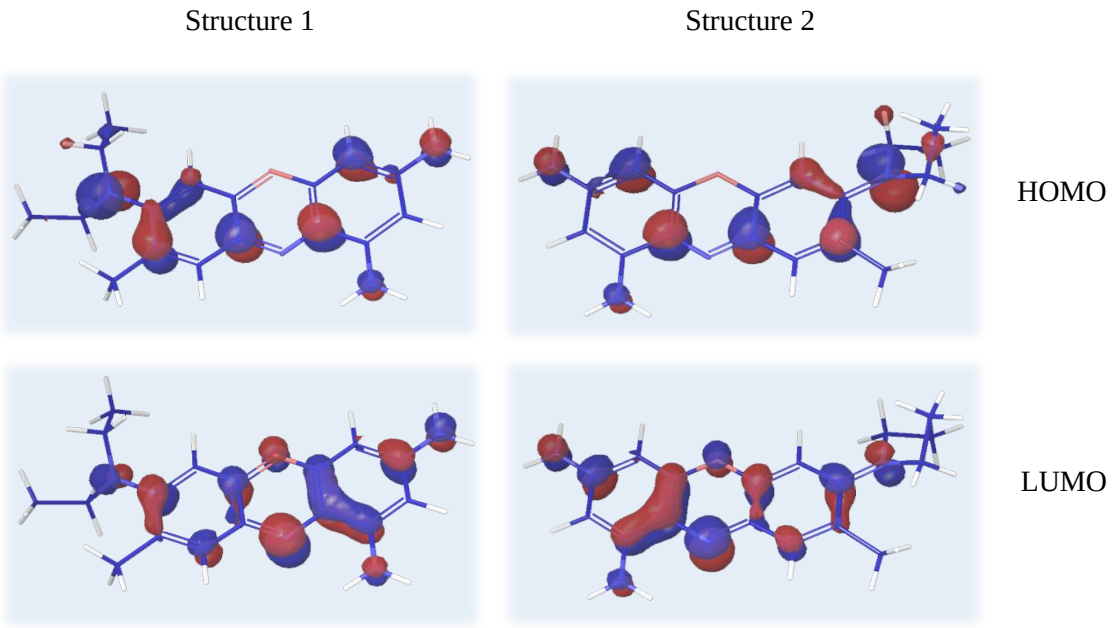

Fig. 61. Brilliant Cresyl Blue single-point-energy (SPE) output file containing calculated HOMO and LUMO surfaces with [EMIM]OAc (ϵ_0=12) ionic liquid solvation effects

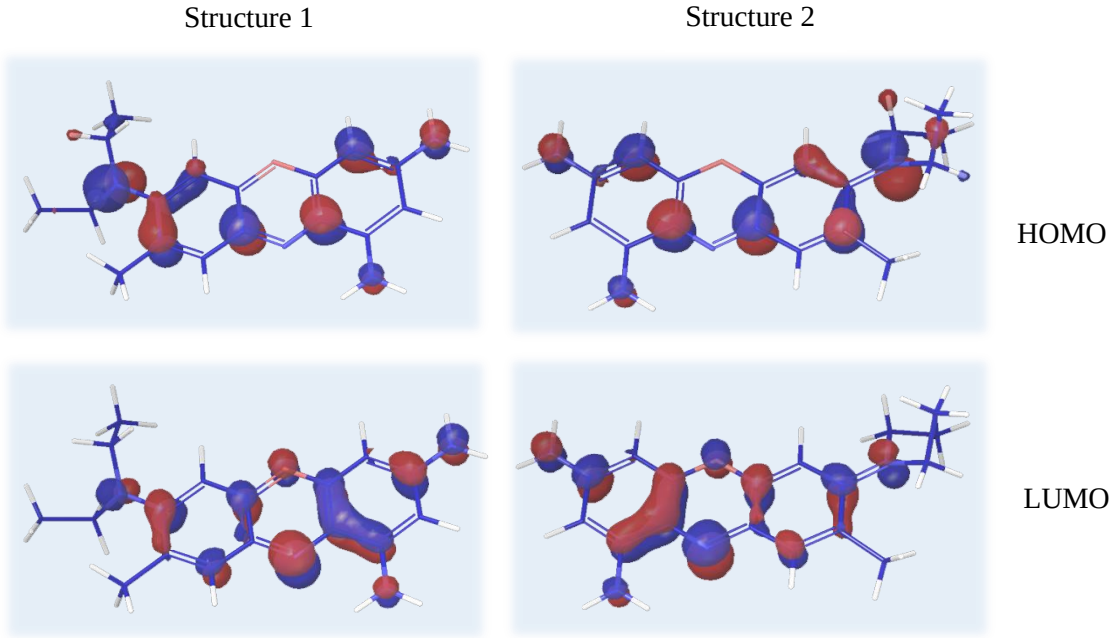

Fig. 62. Brilliant Cresyl Blue single-point-energy (SPE) output file containing calculated HOMO and LUMO surfaces with [EMIM]OAc (ϵ_0=14) ionic liquid solvation effects

Interaction Energies

Interaction energy calculations of thermodynamic qualities serve to clarify the likelihood of one structure existing in a given color additive-solvent mixture at equilibrium. This is because one of the two alternating structures analyzed is likely to be more energetically favorable than the other based on solvent effects. Changes in enthalpy (ΔH) and Gibbs Free Energy (ΔG) were calculated to mathematically approximate the likelihood of one structure to be more prevalent than the other in a chemical mixture at equilibrium. These thermodynamic qualities of a given structure vary if the molecule is immersed in solvent, and among different solvents chosen for analysis. Therefore, the energies of each color additive structure were calculated according to the representative structure (S1 or S2 as indicated) depicted in the virtual workspace based on known energy relationships and compared to the constitutional isomer or tautomer.

A prior study [158] comments that the experimental and theoretical enthalpy of formation data differs significantly from that of the value presented in the NIST database for the aromatic non-benzenoid hydrocarbon structural derivative of azulene called azuleno[2,1,8-ija]azulene. Sousa and coworkers (2014) used DFT to generate thermodynamic quantities using Gaussian03 incorporating a large basis set MP2/6-31G* and magnetic properties to describe aromatic systems calculated using wavefunctions and geometry optimizations calculated using B3LYP/6-311G** [158]. This work takes another approach by using a more contemporary Gaussian package to study different molecules containing large quantities of dissimilar atoms in order to assess the feasibility of calculating theoretical thermodynamic quantities to better predict inter- and

intramolecular interactions, as well as solvent effects, that influence the overall hue of the mixtures analyzed.

TABLE XXVI

Difference of interaction energies of FD&C Red No. 40 structures 1 and 2 calculated in vapor phase and in five solvents

Solvent	ΔE (kJ/mol)	ΔG (kJ/mol)
Vapor Phase	+19.317	-18.976
Water	-43.927	-37.052
Ethanol	-115.263	-104.247
[BMIM]Cl	-25.271	-23.972
[BMIM]BF_4	-28.110	-22.890
[EMIM]OAc (ε=12)	-26.058	-24.465
[EMIM]OAc (ε=14)	-17.642	-15.921

TABLE XXVII

Difference of interaction energies of D&C Yellow No. 11 structures 1 and 2 calculated in vapor phase and in five solvents.

Solvent	ΔE (kJ/mol)	ΔG (kJ/mol)
Vapor Phase	+60.105	+68.245
Water	X	X
Ethanol	+55.716	+62.273
[BMIM]Cl	-55.253	+61.032
[BMIM]BF_4	+55.092	+61.478
[EMIM]OAc (ϵ_0=12)	+52.033	+61.551
[EMIM]OAc (ϵ_0=14)	+55.009	+61.113

TABLE XXVIII

Difference of interaction energies of Brilliant Cresyl Blue structures 1 and 2 calculated in vapor phase and in five solvents

Solvent	ΔE (kJ/mol)	ΔG (kJ/mol)
Vapor Phase	-1.316	-0.732
Water	+7.58	+9.390
Ethanol	-0.187	+1.512
[BMIM]Cl	-2.516	-0.953
[BMIM]BF_4	-0.913	+0.294
[EMIM]OAc (ϵ_0=12)	-0.425	+1.105
[EMIM]OAc (ϵ_0=14)	-0.669	+0.318

Discussion

Tautomerism is a common phenomenon of dyes that feature phenolic components. Contemporary literature discusses the likelihood (or certainty) of alternating tautomer or tautomer- like structures in homogenous solution equilibria [40,156-172]. While this phenomenon is certainly discernible visually using two-dimensional drawings to note changes in structure that may occur during experimental trials, few studies have made the connection of specific intermolecular bonding changes to the color additive molecular structure having a direct correlation with experimental anomalies in maximum absorbance peaks. This work seeks to fill this gap in available literature by attempting to utilize computational structural models to better "pinpoint" likely molecular structural changes that may be linked to the abnormalities prevalent in experimental absorbance spectra using DFT geometry optimizations followed by theoretical absorbance spectral data generated using their time-dependent (TD-DFT) counterpart.

FD&C Red No. 40 "Allura Red". Allura Red Dye AC, more specifically referred to as FD&C Red No. 40, is a synthetic dye molecule that is made water-soluble with the addition of sulfonated salt groups $[SO_3]^-$ Na^+ on opposite sides of the molecule, as shown in Figures 30 & 37. These reactive groups increase the overall reaction rate of azo dye molecules in polar solvents, and as a result generally exhibit higher molar extinction coefficients (thus higher "intensity"), and medium-to-high fastness with regard to both light and wetness [75,173]. Given its versatility and relatively simple synthesis process compared to other dye classes [173], this molecule is an edible food dye approved for human consumption in the United States and is nearly ubiquitous in consumer products ranging from food to cosmetics and pharmaceuticals [70,75,174].

For water, ethanol, and ionic liquid solvents, FD&C Red No. 40 structures 1 & 2 exhibit azo/hydrazone tautomerism involving the transfer of electrons from the trademark, characteristic “azo” (-N=N-) group and hydroxyl groups on the phenyl ring in solvent to form an NH group and a carbonyl group on the phenyl ring, in place of the former hydroxyl group. The relevant functional groups are emphasized in Figure 63.

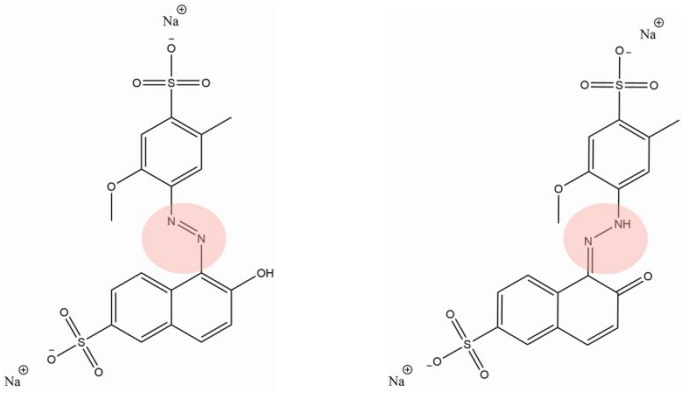

A **B**

Fig. 63. Functional groups indicative of azo/hydrazone tautomerism are emphasized in the red ovals in FD&C Red No. 40 “azo” structure 1 (a) and “hydrazone” structure 2 (b), respectively.

An increase in solvent polarity shifts tautomeric equilibrium towards the more dipolar hydrazone form[19]. In addition, NH and OH are able to form hydrogen bonds with certain solvents. In fact, the stronger hydrogen bond donor ability of the hydroxyl group compared to the nitrogen (NH) group enables this molecule to form hydrogen bonds in HBA solvents (such as pyridine which stabilizes the azo form [156]), whereas the basic “imino” group in the hydrazone form is stabilized in the HBD solvents like acetic acid. Hence, quantum mechanical calculations have indicated that the azo form is the more

[19] According to Carr [40], the hydrazone form is favored in equilibrium mixtures containing arylazonaphthol-based dyes; whereas the “true azo” form by definition is retained in mixtures containing arylazoamine-based dyes.

stable isomer in the gas phase. QM calculations performed by [175, 176] are also in agreement with the azo form being more stable in vapor phase.

The opposite trend is noticed in this work by observing that "neutral" solvents with increasing polarity (such as water and ethanol) have larger changes in both enthalpy and Gibbs free energy, indicated by larger discrepancies of ΔE and ΔG, respectively. This is because the hydrazone form dominates in HBA solvents such as acetic acid which stabilize the basic "imino" group in the hydrazone form [156]. Regarding ionic liquid solvents, it has been long understood that the anion more significantly affects the physicochemical properties of solute-solvent mixtures of these binary cation/anion combinations than does the cation. Therefore, anion effects will be treated with a more in-depth focus.

$^{-}BF_4$ is considered a rather stable anion, among one of the preliminary ions to lead to air- and water-stable room temperature ionic liquids (RTILs) [177,178]. The experimental spectra for Allura Red in this solvent shows consistent λ_{max} plateaus in 1 µM and 10 µM concentrations of Allura Red—[BMIM]BF_4 with very small (if any) change in λ_{max}. However, there is a bathochromic shift of experimental spectra of approximately 54-79 nm for experimental—theoretical S1 (azo) λ_{max} comparisons, and a slightly smaller change in λ_{max} range of 41 to 66 nm for experimental-theoretical S2 (hydrazone) λ_{max} comparisons. The overall bathochromic (red) shift in experimental spectra compared to theoretical data is likely due to the prevalence of $\pi \rightarrow \pi^*$ excited state transition states throughout the molecule. While the carbonyl enables a solvated carbonyl group $n \rightarrow \pi^*$ hypsochromic shift, the hypsochromic shift in the (S2) hydrazone form is less dramatic than that of the azo form (S1), because of the hydroxyl group in the

azo form of the dye molecule. Azo (S1) contains additional lone pairs of electrons and is a stronger nucleophile than the nitrogen atoms, thus the hypsochromic shift is higher in polar protic solvent than for the hydrazone form. In the azo structure, the hydroxyl group is able to readily form hydrogen bonds in HBA solvents, such as those that are polar and protic, causing a hypsochromic (blue) shift in theoretical data. TD-DFT overestimates the electron density in this mixture in polar solvent, which also explains the very high energy approximations in both water and ethanol solvent which are more than double and quintuple (five times)—respectively—the Gibbs free energy and enthalpy energy differences of the molecule in other solvents analyzed.

Comparison of the ionic liquid solvents paints a unique picture of color additive-solvent interaction with regard to experimental spectra and corresponding theoretical spectra and interaction energies. While ionic liquids [BMIM]BF_4 and [BMIM]Cl share a cation, their differing anions affect solvent effects more strongly. The $^{-}BF_4$ anion is considerably more stable than the Cl^- halide ion, which has a high electron density due to its larger atomic mass. In the case of [BMIM]Cl, this also leads to a greater discrepancy in the change in λ_{max} for theoretical structures S1 and S2 because TD-DFT overestimates the electron density of large anions like Cl^-. In fact, in this case effective core potential had to be applied so that theoretical calculations could better reproduce the increased stabilization of the large anion that would occur in increasingly polarizable solvents due to dispersion interactions under realistic experimental conditions. These dispersion interactions in turn contribute to increased bathochromic shifts in experimental spectra, which differ from [BMIM]BF_4 by between 3 to 6 nm despite similar-looking plateaus. The presence of the $[BMIM]^+$ cation makes two of the ionic liquids studied here

classified as hydrogen bond acceptor solvents (HBA) due to the bulky butyl group. Regardless, the cation in [BMIM]BF_4 and [BMIM]Cl ionic liquids plays less of a role in color-shifting solvatochromic effects than does their anion counterparts.

[EMIM]OAc tells an entirely different story. The ethyl imidazolium cation is considerably smaller and less sterically hindered, so it ideally plays a greater role as a hydrogen bond acceptor solvent molecule. However, the acetate ion acts as a hydrogen bond donor (HBD), causing the more basic hydrazone form (S2) to be stabilized in this solvent. The effect of this cation inducing a polar, protic-like effect is easily discernible when comparing the [EMIM]OAc λ_{max} spectra data to that of water and ethanol solvents. The change in λ_{max} for water and [EMIM]OAc is nearly identical, however the intensities are drastically different due to the presence of the HBA cation in [EMIM]OAc. Note that in the more saturated 10 micromolar Allura Red-[EMIM]OAc mixture, the experimental spectral projection appears similar to those of ethanol. In [EMIM]OAc, the hydrazone form (S2) predominates due to the prevalence of significantly larger $\pi \rightarrow \pi^*$ transitions about the hydrazone nitrogen linked to the phenyl ring, which upon electronic excitation produces large $\pi \rightarrow \pi^*$ transitions throughout the molecule. In Figures 48-49, HOMO-LUMO surface maps for FD&C Red No. 40 in EMIMOAc vividly emphasize the regions where the illustrative electronic transitions occur. In addition, the hydroxyl group in the azo form contributes to stronger hypsochromic shift than does the hydrazone solvated carbonyl group, so that the theoretical λ_{max} for the azo form is shifted further towards the left (blue range).

Based on theoretical interaction energy calculations shown in Table 26, it is evident that structure 1, the “true azo” form, is favorable in all solvent environments. It is

worth noting that theoretical calculations indicate that the hydrazone structure is only favorable in vapor phase. Based on the values presented in Table 26, the azo structure is the lower energy structure, and is also the same form to be more spontaneously generated in vapor phase. However, an increase in solvent polarity shifts tautomeric equilibrium towards the more dipolar hydrazone form [156]. This is because nitrogen (N-H) and hydroxyl (O-H) groups are able to form hydrogen bonds with solvents that can affect properties based on inherent hydrogen bond donor (HBD) or –acceptor (HBA) characteristics. The stronger hydrogen bond donor (HBD) ability of the hydroxyl group on the azo form enables this molecule to form hydrogen bonds in hydrogen bond acceptor (HBA) solvents, which stabilize the azo form. This trend is proven using computational data by showing that the azo is the higher energy structure according to enthalpy calculations, but is more spontaneously generated in vapor phase. This is due to attack of airborne singlet oxygen atoms in the atmosphere that attack the vulnerable azo coupling unit chromophoric site [40], resulting in destruction of the azo bond and shifting electrons towards the phenyl ring containing (electrophilic) OH and NH groups. These electrophilic groups in turn become sp^2-hybridized at the carbon atom once the hydrazone exists in the structure.

Ultimately, the FD&C Red No. 40 molecule produces very similar theoretical data for all solvent conditions analyzed. The hydrazone form is indicated in the more red-shifted, rightward λ_{max} or shoulder peaks, whereas the azo form is the more hypsochromic form prevalent in left-ward “blue” shifted absorbance spectra. The anomaly in this case is in vapor phase where singlet oxygen attacks cause the λ_{max} representative of the azo and hydrazone structures to be reversed.

D&C Yellow No. 11 "SS Quinoline Yellow". D&C Yellow No. 11, commonly known as SS Quinoline Yellow or CI Solvent Yellow 33, is approved for use in externally-applied drugs and cosmetic products in small quantities [70,75, 179][20]. In addition, it has been used in "colored smokes", which are volatile gases used by the United States Army to send noticeable smoke signals [179]. This molecule exhibits keto-enol tautomerism, evident in experimental trials as a result of the forked vibronic peaks of different intensities shown in Figure 35. Computational predictions have revealed that it is possible to mimic the spectral shifts that cause two different λ_{max} peaks to appear in experimental absorbance spectra. Based on theoretical comparison to experimental peaks, it seems clear that the left-most, blue-shifted peak corresponds to the keto form, while the right-most, red-shifted peak corresponds to the enol form of this yellow dye molecule.

Interaction energies indicate that [BMIM]Cl provides enthalpy and spontaneity data that is the anomaly among the solvents analyzed. The keto form is of higher total enthalpy than the enol form in the following descending order of change in energy: vapor phase (where ΔE and ΔG are the highest among all solvents analyzed), ethanol, [EMIM]OAc (ϵ_0 =12), [BMIM]BF_4, [EMIM]OAc (ϵ_0 =14). Note that this numerically-descending order is nearly identical for ΔG values, except that the order of [BMIM]BF_4 and [EMIM]OAc (ϵ_0 =12) are reversed.

In vapor phase, theoretical data exhibits an interesting change in not only spectra of S1 (keto) and enol (S2) forms but also intensity. The keto form intensity of absorbance spectra for all solvents in theoretical calculations is lower than the enol by a power of 10.

[20] D&C Yellow No. 11 is only to be used in small quantities because it is readily soluble in animal intestinal tracts and appears in feces upon animal exposure (see [179]).

Furthermore, the enol form shows a much higher intensity in vapor phase than does the keto form, which has the smallest, dullest intensity.

Despite not being soluble in water, this molecule exhibits varied solubility and intensity based on the choice of solvent and dye concentration. It is soluble in neutral, polar ethanol, however to a much lesser extent than the vibrant saturation and intensity exhibited in [EMIM]OAc ionic liquid solvent. All solvents analyzed have HOMO-LUMO transitions that invoke such high energy electronic excitation transitions that the geometry of the molecule is rotated about the z-axis (see Chapter 1 for a more thorough discussion of this phenomenon in ethanol solvent). This high energy transition contributes to the strong intensity indicated by vast peaks in experimental spectral data (see Figure 35).

Either of the D&C Yellow No. 11 keto (S1) and enol (S2) forms may dominate in solution or vapor phase based on solvent or polarity effects at play. In vapor phase, the enol form as a significantly higher intensity, yet the keto form exhibits theoretical λ_{max} values that indicate an overall leftward, hypsochromic (blue) shift. Solvent polarity has a strong effect on the prevalence of the enol form as dominating the theoretical mixtures by exhibiting higher intensity by a power of ten compared to the keto form. While the two tautomeric forms are clearly represented in (dilute) 1.0 micromolar dye concentration experimental spectra (Figure 35) as having nearly equal intensity at maximum absorbance for [EMIM]OAc with increasing concentration of solute, the enol form (rightward, bathochromic “red” shift) becomes more prevalent in the solution due to its higher intensity at λ_{max} and the minimization of the leftward peak as a $\lambda_{shoulder}$-like quantity. This indicates that with increasing solvent polarity, the enol form dominates.

Intramolecular hydrogen bonding that would otherwise occur in non-cyclic molecules (and favor the diketo-containing structure 1) is inhibited by steric hindrance. Thus, in polar hydrogen bond acceptor HBA solvents, the *trans*-enolic form dominates the solute-solvent mixture.

However, in the case of ionic liquid [EMIM]OAc, the sharp, "off the charts" rise in the left-most λ_{max} peak of the saturated 10 micromolar concentration indicates the prevalence of the keto form. As solute concentration of the cyclic diketo increases, intermolecular hydrogen bonding with acetate solvent ions compete for the same intramolecular chelation interactions that would otherwise stabilize the enol form, and thereby reduce dipole-dipole repulsion of the carbonyl group. At lower 1.0 micromolar concentrations in [EMIM]OAc, the *trans*-enolic form clearly dominates the mixture as the acetate solvent molecules act as Lewis bases and the mixture is dominated by the hydrogen bond acceptor property of solvent [156]. As a result, [EMIM]OAc acts as an electron pair donor (EPD) solvent and the enol content (S2) is strongly favored.

The λ_{max} experimental-theoretical comparison shown in Table 23 exhibits smaller differences for the keto structure data simulation in [EMIM]OAc because of transitions contributing to stronger hypsochromic shifts than in other solvents exhibiting less Lewis basicity.

HOMO-LUMO surface maps also indicate another interesting feature of the "enol" S2—additional electronic excitation transitions in the HOMO form. Both sides of the S2 molecule exhibit antibonding molecular orbital surfaces activated in vapor phase and ionic liquid solvents [BMIM]BF_4, [BMIM]Cl, and [EMIM]OAc (ϵ_0 =12 & 14).

These additional electronic transitions are induced by asymmetrical vibrations of the yellow dye molecule enabled when the center of symmetry or internuclear (z)-axis is disrupted. When this occurs, otherwise "forbidden" transitions (such as $n \rightarrow \pi^*$ for solvated carbonyl groups) are weakly allowed [180]. These additional electornic transitions, when coupled to asymmetrical vibrational modes, are nown as "vibronic" transitions [180, 181]. The more uniform, "forked" nature of the double-peaks presented in the absorbance spectral curve for D&C Yellow No. 11 likely have a strong vibronic component in addition to keto-enol tautomeric structural effects on the electronic transitions contributing to the experimental spectral anomalies observed.

TD-DFT overestimates the electronic excitation transitions for the dipole/dipole, induce dipole and specific hydrogen bond sites which contribute to noticeably hypsochromic shifts for the keto form, whereas in the theoretical calculation of λ_{max} of the enol structure, dispersion interactions in solvent are overcompensated for as bathochromic shifts. Note that the TD-DFT overcompensation of solvent effects results in overestimating of the separation of λ_{max} peaks by approximately 35 nm when the average λ_{max} in solvent are compared to vapor phase based on the methods mentioned previously as used in this study. All in all, TD-DFT overestimates the range of the change in λ_{max} for theoretical electronic transitions compared to experimental values to be approximately 44 nm to 66 nm for ethanol, [BMIM]BF_4, and [BMIM]Cl.

Interaction energies are very close in ΔG hartree calculation, differing by less than one ten-thousandth in all solvents except vapor phase. Larger changes occur in oxygen-containing solvents [EMIM]OAc, EtOH and in vapor phase as a result of increased HBA (or EPD) ability of the oxygen molecule. [BMIM]Cl favors the enol form but causes an

exothermic reaction as opposed to endothermic one because the Cl^- anion is very nucleophilic and acts as a hydrogen bond acceptor (HBA) solvent. $^-BF_4$ ion is relatively stable, and the $[BMIM]^+$ cation is rather bulky. Despite bulkiness, $[BMIM]BF_4$ shows a higher enol concentration with greater solute (dye) concentration because intramolecular chelation is not inhibited. Also, the $[BMIM]^+$ cation acts as a hydrogen bond donor, enabling EPA solvent interactions to stabilize the enol form at higher color additive molecule concentrations.

Overestimated electronic transitions due to already very high energy transitions cause DFT & TD-DFT to be very helpful, but not perfect in attributing structural characteristic of color additive molecule isomers to experimental absorbance spectral peaks. Note that larger differences in the change in λ_{max} (i.e. greater than 32 nm) are generally due to solute/solvent intermolecular forces stronger than hydrogen bonding and dipole interactions alone, thus EPA/EPD interactions likely play a large role in the λ_{max} data generated for the yellow dye molecules studied. This is especially important to take into account as novel amphoterically-charged solvents like room-temperature ionic liquids are introduced in contemporary formulation mixtures. See Table 23 for the numerical values of changes in λ_{max} based on experimental—theoretical structural comparisons.

Brilliant Cresyl Blue. Brilliant Cresyl Blue in its various structural forms (including Brilliant Cresyl Blue ALD, BB, and C) has applications throughout academic and industrial laboratories. The vast scope of its applications as an effective charge-transfer (CT) dye ranges from use as a semiconductor with other pharmaceutical or nutraceutical-like additives [32,44,182-186] to being used to observe iron transport in

laboratory animals in malnutrition studies [187,188]. The oxazine dye class includes molecules exhibiting at least two fused aromatic rings joined by a third cyclic aromatic structure containing one or more heteroatoms, usually oxygen and nitrogen [189]. Common examples encountered often in research and in literature studies include Methylene Blue, Nile Red, Nile Blue A, Cresyl Violet, and Brilliant Cresyl Blue--the final of which will be discussed in greater detail in Chapter 3. These classes of molecules exhibit charge transfer in the form of excited-state intramolecular proton transfer (abbreviated ESIPT) [190] that is clearly discernible in experimental spectra with the application of any of a variety of polar or nonpolar chemical "stock" solvents.

Brilliant Cresyl Blue is known as a "charge transfer" (CT) dye because of its inherent charged nature. This molecule exhibits a positive charge that is transferred from the oxygen atom in the Brilliant Cresyl Blue "BB" form (S1) also called 1,3-diamino-7-diethylamino-8-methylphenoxazin-5-ium chloride [77] as shown in Figures 32 and 39 to the nitrogen atom in the more widely adopted Brilliant Cresyl Blue "C" form (S2). Experimental data for this molecule indicates that maximum absorbance spectra varies with choice of solvent, meaning BCB yields different hues in different solvent mixtures. The charge transfer migration creates a "tautomer-like" effect in that the two structures are constitutional isomers in solution was first observed by Holmes [32] as his research documented a difference in blue and violet hues attributed to the chlorine anion coupling with the sp^2-hybridized nitrogen atom (using S2 form as a reference structure). Very novel/recent experimental studies performed elsewhere [44] confirm that BCB ALD, the form certified for use as a biological stain, exhibits changes in λ_{max} based on basicity of solvent and even may generate a small amount of photovoltaic charge. Other studies have

expanded on its semiconductor nature [182-187]. This work serves to verify if structural changes or bonding nature visible at the atomic level contribute to the vast color changes observed when BCB is in different solvents. Using DFT and TD-DFT calculations incorporating relevant bonding and charges indicative of each alternating structure shed light on the more intrinsic structural properties of the molecule responsible for solvatochromism as opposed to simply experimental spectral measurements.

All dye-solvent mixtures increase in intensity when the Brilliant Cresyl Blue dye molecule concentration is increased from 1.0 micromolar to 10 micromolar. In water solvent of dilute (1.0 μM) and more saturated (10 μM) concentrations, Brilliant Cresyl Blue appears its namesake hue with a λ_{max} value at approximately 588 nm and 574 nm, respectively. Strong spectral shifts occur once different solvents are utilized. Ethanol absorbance spectra places the molecule in blue-green hue absorbance spectral range with spectra comparable to [BMIM]BF_4 at high and lower dye concentration. Ethanol is a polar, protic solvent, yet the ionic liquid [BMIM]BF_4 has hydrogen bond donor (HBD) properties that produce a slight 5-6 nm rightward, bathochromic (red) shift in experimental spectral compared to ethanol. [BMIM]Cl produces experimental absorbance spectra that is dramatically shifted to the red region (right)—this bathochromic shift arises as a result of the high electron density of the halide ion, and thus the larger amount of dispersion forces required to stabilize the chlorine ion. The chlorine ion acts as a nucleophilic hydrogen bond acceptor (HBA) solvent, while the $[BMIM]^+$ cation acts as a hydrogen bond donor (HBD) or electron pair acceptor (EPA) solvent. [EMIM]OAc provides the most surprising results: the shifts in experimental spectra do not indicate a blue mixture, rather, a red hue that resembles FD&C Red No. 40 at both dilute and

saturated BCB concentrations in [EMIM]OAc. The unusual solvatochromic nature of BCB in this ionic liquid will be explored in depth here and in the following chapter. [EMIM]OAc contains an acetate ion that functions as a Lewis base. Another study [44] has indicated that more basic, anionic surfactants cause hypsochromic shifts in BCB ALD, but given the distinct bonding nature contained within the "ALD", "BB", and "C" forms of Brilliant Cresyl Blue, theoretical DFT and TD-DFT studies are still necessary to differentiate between spectral shifts caused by two of the three forms erroneously referred to interchangeably as the same molecule[21].

Theoretical calculations indicate that water and [EMIM]OAc (ϵ_0=12) have the same change in λ_{max} for both isomers and differ by only 1 nanometer. Ethanol and [BMIM]BF_4 exhibit diminutive changes in λ_{max} between structures. The largest changes in λ_{max} occur in [EMIM]OAc (ϵ_0=14) and in vapor phase (9.98 and 19.95, respectively). According to Welton and Reichardt [18], nucleophilicities in molten salts and in vapor phase follow the same order as those in dipolar hydrogen bond acceptor (HBA) solvents. The presence of oxygen atoms in each case affects the spectra depicted.

In all solvents and in vapor phase, both S1 and S2 surface maps of HOMO-LUMO transitions indicate molecular orbital transitions originate in HOMO from the nitrogen (NH) group to the outermost ring on the opposite side of the molecule in LUMO, past the cyclic oxygen atom (regardless of the charged nature of the oxygen atom). In vapor phase, singlet oxygen atoms attack the double-bonded nitrogen atom in a similar fashion to the way azo bonds are attacked in azo dyes such as FD&C Red No. 40

[21] The CAS numbers for aforementioned BCB structures are as follows: ALD = 51716-96-2, BB = 10127-36-3, and C = 10127-36-3. Note that the Brilliant Cresyl Blue BB and C CAS numbers are exactly the same, despite noticeable differences in charged atoms and bonding.

discussed earlier. Oxygen molecules are stronger competitors for the oxygen atom within the oxazine dye molecule than other airborne particles that may collide with the molecule [191]. Therefore, S2 containing the charged nitrogen atom is not spontaneously generated in vapor phase; rather, S1 is the lower energy structure prevalent in vapor phase. The energy transition is very low, indicating that little energy is required to make the transition between S1 and S2. Thus, S1 is readily formed if BCB becomes airborne.

In water, S2 containing the charged nitrogen group is prevalent in the polar protic solvent. More energy is required to form the more stable isomer because the more basic sp^2-hybridized nitrogen with a full octet is stabilized in HBD solvents such as those that have a polar or dipolar nature--water, ethanol, and [EMIM]OAc. The charged nitrogen-containing structure is also stabilized in $[BMIM]BF_4$ due to the bulky $[BMIM]^+$ cation functioning as a HBD solvent. However, in the case of this charged dye molecule, the larger shifts in ionic liquids observed experimentally are likely attributed to Lewis acidity or basicity ascribed to electron pair donor or -acceptor (EPD/EPA) interactions, respectively. The $[BMIM]^+$ cation acts as an EPA solvent, like water, thus $[BMIM]BF_4$ λ_{max} in dilute or concentrated spectra closely resembles that of ethanol with a difference of approximately 5 nm because the $^-BF_4$ anion is relatively stable due to its atypical shape. However, the slightly more numerous dispersion forces as a result of the larger size of the $[BMIM]^+$ compared to ethanol cause a bathochromic (red) shift of the spectra.

[EMIM]OAc piques interest due to the distinct shape of the absorbance curve when the static dielectric constant is set to 12 versus 14. While the other ionic liquids studied have a static dielectric constant approximated to 14 [85], *n*-ethyl-*n*-imidazolium cation binary mixtures containing an anion with an oxygen atom or similarly strong

nucleophile such as sulfur [88], exhibit a lower dielectric constant value. Closely-relevant static dielectric constants were scarcely reported in the literature, thus these computational studies ran a separate job containing [EMIM]OAc data if (ϵ_0=12), as assumed due to the nucleophilic anion, and if (ϵ_0=14) due to collective association with static dielectric constants of other room-temperature ionic liquids [87-89]. The results of this were fascinating as the TD-DFT spectra provoked a very interesting comparison. If (ϵ_0=12), the λ_{max} S1 value is identical to that of ethanol, and λ_{max} S2 closely resembles that of water, ethanol, and [BMIM]BF_4 values reported. Only one smooth curve is shown for both S1 and S2. However, if (ϵ_0=14), a $\lambda_{shoulder}$ peak occurs at approximately 400 nm, and λ_{max} S1 is hypsochromically shifted approximately 9 nm to the left. On the other hand, S2 data appears unaffected by the change in static dielectric constant. $\lambda_{shoulder}$ indicates the formation of a monomer-solvent complex, while λ_{max} indicates dimer-solvent complexation. Further discussion of this phenomenon in water solvent may be found in another study [180]. Considering the distinct hypsochromic color shift in [EMIM]OAc solvent visible in experimental trials, the Lewis base character of the acetate ion functions as an electron pair donor (EPD) solvent to stimulate interactions that are much stronger than those of water solvent (consisting of hydrogen bonding, dipole and induced dipole interactions, and van der Waals dispersion forces alone). The charged nature of both the dye molecule and the ionic liquid solvent ion binary mixture enable higher energy transitions to occur, hypsochromically (blue) shifting the experimental and theoretical absorbance spectra to indicate a red hue.

Interaction energy data for Brilliant Cresyl Blue indicates that stabilization of the alternating structures differs based on solvent effects. S1 is more spontaneously generated

in vapor phase and [BMIM]Cl solvents, whereas S2 is spontaneously generated in water, ethanol, $[BMIM]BF_4$, and in [EMIM]OAc using both static dielectric constant input values (ϵ_0 = 12 and 14). The charged oxygen atom–containing structure (S1) is more prevalent in vapor phase because singlet oxygen atoms attack the less-stable sp^2-hybridized nitrogen bond in the tautomeric structure when airborne. This interaction leads to an electron transfer to form S1, which is stabilized in air by interchelation effects with the charged oxygen atom. S1 is also more prevalent in mixtures containing ionic liquid [BMIM]Cl because the $[BMIM]^+$ cation acts as an electron pair-acceptor (EPA) solvent, so extra electrons on the less nucleophilic, charged nitrogen atom in the S2 form with a full octet are transferred to the ionic liquid cation. Therefore, the S1 structure is more spontaneously generated. In addition, the chlorine anion is also very nucleophilic, so it may supplement the electron pair-acceptor effect in the mixture due to its significant atomic mass and electron density, which strongly influence the center-of-mass ratio [88]. Thus, the chloride anion causes greater bathochromic shifts in this study due to TD-DFT overestimation of not only dispersion, but also solvent polarization effects in the mixture. S2, containing the charged nitrogen atom, is stabilized in more polar, protic solvents exhibiting hydrogen bond donor (HBD) character, namely water and ethanol. Ionic liquid cation $[BMIM]^+$ displays hydrogen bond donor (HBD), or alternatively, electron pair acceptor (EPA) character. In this case, because $[BF_4]^-$ anion is relatively stable, it does not induce significant solvent effects, so the spontaneity of S2 is more reliant on the ionic liquid cation. In ionic liquid [EMIM]OAc, the $[EMIM]^+$ cation displays greater hydrogen bond donor/electron pair acceptor (HBD/EPA) solvent characteristics because of the shorter length of the alkyl chain on the imidazolium group. More importantly, the acetate

anion functions as a Lewis base; thus, a strong dipole effect is induced in two cases: when the carbonyl group of the acetate anion is solvated, and when the α-hydroxyl group is deprotonated. The α-hydroxyl group deprotonation results in a higher frequency transition, which is indicated in absorbance spectra by a strong hypsochromic (blue, leftward) shift in both theoretical and experimental data.

Note that with increasing concentration, the intensity of the red hue of the BCB-[EMIM]OAc mixture increases as electron pair donor solute-solvent interactions become more numerous. Despite this, its intensity is rather dull compared to the intense blue and green hues exhibited by the dye-solvent interactions in other mixtures discussed. This is likely a result of the decay of the excited state that was induced by heating the ionic liquid--thus exciting electrons and ion thermal transitions with enough energy to form the kinetic product (S1), stabilized by polarization effects. This noncovalent stabilizing effect can last for several hours, however longer-term settling of the mixture allows for the thermodynamic product (S2) to form, appearing more dull (and less red) over time.

Water structure transition from S1 to S2 requires more energy because water is less protic than ethanol and the ionic liquid solvents containing charged species. As a result, the reaction in water is endothermic because it requires energy to initiate the charge-transfer isomerization that occurs more readily in more protic solvents (like ethanol) or those that have mixtures of ions. Furthermore, the lowest amount of energy (change in enthalpy, ΔE) required for the S1 to S2 transition is found in mixtures with ethyl-group containing solvent molecules, such as ethanol and 1-ethyl-3-methylimidazolium acetate. There is a lower change in enthalpy for [EMIM]OAc when (ϵ_0=12), but a higher change in Gibbs free energy (ΔG) than when (ϵ_0=14). This is

because (ϵ_0=14) assumes greater polarizability effects, but the theoretical spectra generated at this static dielectric constant input value does not emulate the single λ_{max} peak evident in experimental data. Thus, (ϵ_0=12) data is considered more comparable for experimental spectra comparison.

Static Dielectric Constant Comparison in [EMIM]OAc. Comparison of the dielectric constant input values 12 and 14 was necessary to determine the most compatible input value when theoretical spectral data output was compared to experimental spectral data collected. Scientists have tirelessly debated regarding whether or not cation or anion effects in binary mixtures of ionic liquids is of greater relevance to the static dielectric constant for over a decade, and studies exist defending one or each type of ion as being significant to the overall numerical value.

Regarding the $[EMIM]^+$ cation, results in [87] show that ϵ_0 depends on the anion, however [88] indicates that polarity mainly depends on the cation. According to Schröder (2011) [88], the dielectric constant must incorporate polarizable hydrogens which have been ignored in earlier approximations of the dielectric constant based on the Lagrangian algorithm for the Drude oscillator model, which by default neglects polarization of the hydrogen atoms. More modern works separate the translational and non-translational components of the generalized dielectric constant $\sum_0^*(v)$, known as dielectric conductivity $\vartheta_0(v)$ and dielectric permittivity $\varepsilon_0(v)$, respectively [88]. Behavior of optical frequencies is also affected by the dielectric constant [87,88], and thus it is gauged using solvatochromic dyes [33-37,87]. $[EMIM]^+$ cation in polarizable systems induces a dipole

that functions as an "inner solvent" that weakens Coulomb interactions[22]. Inclusion of polarizability weakens the attraction between unlike species and reduces the repulsion between "like" species on the mesoscopic level [192]. As a result, inclusion of polarizability shifts all dynamic processes to higher frequencies, and thus enhances the fluidity of the ionic liquid. Enhancement of fluidity in the $[EMIM]^+$ cation–containing solvents with polarization effects also influences the dielectric conductivity, $\vartheta_0(v)$, originating from the collective translational dipole moment depending on the center-of-mass and assuming the role of the Drude particle is used in computational methods. The overlap of $\vartheta_0(v)$ and $\varepsilon_0(v)$ suggests gyration of these aggregates and their translation is coupled, thus the polarization effects generated by the non- and translational dipole moments must be obtained by superposition.

Furthermore, polarization effects must be accounted for in dielectric constant values for ionic liquids. Ionic liquids are considered media of moderate polarity, and exhibit dielectric constant values of between $8.8 \leq \epsilon_0 \leq 15.2$ [87]. Polarities of ionic liquids were initially expected to be close to those of short-chain alcohols like methanol (ϵ_0=32) as in Reichardt [37]. More recently, polarities of ILs have been expected to be more moderate, corresponding to dielectric constant values akin to those of intermediate chain-length alcohols like *n*-pentanol (ϵ_0= 15.2) and *n*-octanol (ϵ_0= 8.8) [87]. In this study, the $[EMIM]^+$ cation exhibits high symmetry which decreases hydrogen bonding activity, thereby lowering the static dielectric constant value [87]; however the dipolar acetate "oxoanion" raises this value higher because of its dipolar effect on

[22] According to [88], a reduction of Coulomb energy by a factor of $(0.74)^2$ was observed by [192] without any reduction of the permanent charges indicated by the quantity $q_{i\beta}$. (88)

solvatochromic properties of the BCB molecule [85]. In particular, the internal rotation of the ethyl- and methyl chains in $[EMIM]^+$ cation require that intramolecular torsional barriers include polarizability effects in order to better reproduce experimental spectra [88]. Additionally, the collective induced dipole moment of the cations shows a stronger correlation with the permanent non-translational dipole moment of the anion, $M_D^{perm}(t)$, than with itself [88]. This indicates a strong anion cage effect around the cations; thus, may also explain the pronounced "low" frequency peak in the Optical-Kerr Effect (OKE) spectra of imidazolium ionic liquids as OKE monitors polarizability fluctuations [88,193]. The induced dipole moments of the anions "anti-correlate" with $M_D^{perm-}(t)$, and the correlation of induced dipole moments with the permanent non-translational dipole moment $M_D^{perm+}(t)$ of the cations is much weaker [88]. For these reasons, the induced dipole moments have to be accounted for in collective non-translational dipole moment and therefore become part of the dielectric permittivity as they are essential for accurate theoretical simulations.

Overall, in this work, the decision to compare 12 and 14 as static dielectric constants was made based on the relevance to experimental data produced as a "benchmark" for further investigation. Due to the larger difference in λ_{max} calculated when (ϵ_0=14), particularly for S1 quantum mechanical spectral data simulations, the (ϵ_0=12) value was regarded as generating "more accurate" data and kept consistent as data collection progressed. Future work will expand upon the charged nature of the molecule to more accurately depict spectral anomalies in diverse solvents by altering DFT and TD-DFT approximation methods utilized to better calculate electronic excitation energies for molecules and solvents with ionic character.

Conclusion

DFT and TD-DFT are helpful tools for investigating solvent-induced changes in molecular structures that contribute to solvatochromic shifts in absorbance spectra. These methods can also be used to compare energies of individual isomers that would otherwise rapidly tautomerize or undergo tautomer-like conformational changes in solvents analyzed. While amphoterically-charged azo dye molecules like FD&C Red No. 40 and neutral quinoline dye molecules such as D&C Yellow No. 11 can be modeled in their respective azo-hydrazone or keto-enol tautomeric forms to make useful inferences regarding their likely effects on hypsochromic (blue) or bathochromic (red) shifts induced by their role in solvent interactions, and in some cases attribute hypso- or bathochromic shifts to one isomer or tautomeric form or the other, charge transfer dye molecules such as BCB produce useful data only if theoretically modeled in polar solvent, or in other solvents displaying hydrogen bond acceptor (HBA) or electron pair donor (EPD)-like properties. Even in such cases, absorbance spectral data varies strongly among solvent selected for analysis. Interaction energies obtained in the ground state are useful for determining which alternating structure is more dominant in a given solute-solvent mixture. HOMO-LUMO surface mapping available in modern quantum chemical software applications also helps indicate the location and magnitude of electronic energy transitions of molecules in a given solvent or in vapor phase but exhibit such negligible differences (~1 Å) that their use is limited to visualization purposes at this time. Future research will require computational data methods more specifically tailored to the ionic nature of charge transfer molecules or neoteric solvents with inherent cationic, anionic, or amphoteric charged properties.

References

[1] *UV Atlas of Organic Compounds* New York: Plenum, 1968.

[2] A. N. Y. Victor Talrose, Alexy A. Usov, Antonina A. Goncharova, Axlexander N. Leskin, Natalia A. Messineva, Natalia V. Trusova, Margarita V. Efimkina, "UV/Visible Spectra," in *NIST Chemistry WebBook, NIST Standard Reference Database Number 69*, P. J. L. W. G. Mallard, Ed. Gaithersburg: National Institute of Standards and Technology, 2019.

[3] R. D. J. III, Ed. *NIST Computational Chemistry Comparison and Benchmark Database*, 19 ed. (NIST Standard Reference Database). Gaithersburg: National Institute of Standards and Technology.

[4] J. L. S. Gonçalves, S. R. Valandro, A. L. Poli, and C. C. Schmitt, "Influence of clay minerals on curcumin properties: Stability and singlet oxygen generation," *Journal of Molecular Structure*, vol. 1143, pp. 1-7, 2017.

[5] M. Khadem Sadigh, M. S. Zakerhamidi, S. M. Seyed Ahmadian, M. Johari-Ahar, and L. Zare Haghighi, "Environment effect on spectral and charge distribution characteristics of some drugs of folate derivatives," *Spectrochim Acta A Mol Biomol Spectrosc*, vol. 171, pp. 10-17, Jan 15 2017.

[6] M. Khadem Sadigh, M. S. Zakerhamidi, A. N. Shamkhali, and E. Babaei, "Photo-physical behaviors of various active forms of curcumin in polar and low polar environments," *Journal of Photochemistry and Photobiology A: Chemistry*, vol. 348, pp. 188-198, 2017.

[7] S. Mondal, S. Ghosh, and S. P. Moulik, "Stability of curcumin in different solvent and solution media: UV-visible and steady-state fluorescence spectral study," *J Photochem Photobiol B*, vol. 158, pp. 212-8, May 2016.

[8] A. Panja, N. Jana, A. Bauza, A. Frontera, and C. Mathoniere, "Solvent-Triggered Cis/Trans Isomerism in Cobalt Dioxolene Chemistry: Distinguishing Effects of Packing on Valence Tautomerism," *Inorg Chem*, vol. 55, no. 17, pp. 8331-40, Sep 6 2016.

[9] F. J. Avila Ferrer, J. Cerezo, J. Soto, R. Improta, and F. Santoro, "First-principle computation of absorption and fluorescence spectra in solution accounting for vibronic structure, temperature effects and solvent inhomogenous broadening," *Computational and Theoretical Chemistry*, vol. 1040-1041, pp. 328-337, 2014.

[10] J. R. Haak and J. B. F. N. Engberts, "Solvent polarity and solvation effects in highly aqueous mixed solvents. Application of the Dimroth-Reichardt ET(30) parameter," *Recueil des Travaux Chimiques des Pays-Bas*, vol. 105, no. 9, pp. 307-311, 2010.

[11] H.-F. J. Liang Shen, Hong-Yu Zhang, "A TD-DFT study on photo-physicochemical properties of hypocrellin A and its implications for elucidating the photosensitizing mechanisms of the pigment," *Journal of Photochemistry and Photobiology A: Chemistry*, vol. 180, pp. 65-68, September 21 2005 2006.

[12] C. Florindo, A. J. S. McIntosh, T. Welton, L. C. Branco, and I. M. Marrucho, "A closer look into deep eutectic solvents: exploring intermolecular interactions using solvatochromic probes," *Phys Chem Chem Phys*, vol. 20, no. 1, pp. 206-213, Dec 20 2017.

[13] K. I. Pryadarsini, "Photophysics, photochemistry and photobiology of curcumin: Studies from organic solutions, biomimetics and living cells," *Journal of photochemistry and photobiology c: photochemistry reviews*, vol. 80, pp. 81-95, May 11 2009 2009.

[14] R. Kian, M. S. Zakerhamidi, A. N. Shamkhali, and P. Nesari, "The interactional behaviors and photo-physical properties of two triarylmethane drugs in solvent media," *Journal of Molecular Liquids*, vol. 225, pp. 653-661, 2017.

[15] S. Gao, L. Zhao, L. Han, Z. Zhang, and H. Zhao, "Synthesis, structure and characterization of two solvatochromic metal–organic frameworks for chemical-sensing applications," *CrystEngComm*, vol. 20, no. 16, pp. 2237-2240, 2018.

[16] M. M. Husain, R. Sindhu, and H. C. Tandon, "Photophysical properties and estimation of ground and excited state dipole moments of 7-diethylamino and 7-diethylamino-4-methyl coumarin dyes from absorption and emission spectra," *European Journal of Chemistry*, vol. 3, no. 1, pp. 87-93, 2012.

[17] D. Loco, S. Jurinovich, L. Cupellini, M. Menger, and B. Mennucci, "The modeling of the absorption lineshape for embedded molecules through a polarizable QM/MM approach," *Photochem Photobiol Sci*, vol. 17, no. 5, pp. 552-560, May 16 2018.

[18] C. W. Reichardt, Thomas, "Solute-Solvent Interactions," in *Solvents and Solvent Effects in Organic Chemistry* 4th ed. Weinheim: Wiley-VCH, 2011, pp. 7-52.

[19] K. L. Meguellati, Sylvain; Spichty, Martin, "A conceptually improved TD-DFT approach for predicting the maximum absorption wavelength of cyanine dyes," *Dyes and Pigments*, vol. 90, pp. 114-118, December 3 2010 2010.

[20] S. Biswas, A. Pramanik, and P. Sarkar, "Effect of additional donor group on the charge transfer/recombination dynamics of a photoactive organic dye: A quantum mechanical investigation," *Computational and Theoretical Chemistry*, vol. 1103, pp. 38-47, January 10 2017 2017.

[21] E. Evangelio and D. Ruiz-Molina, "Valence Tautomerism: New Challenges for Electroactive Ligands," *European Journal of Inorganic Chemistry*, vol. 2005, no. 15, pp. 2957-2971, 2005.

[22] N. S. Xian-Fu Zhang, Xulin Lu, Wenyu Jia, "Benzoate-modified rhodamine dyes: large change in fluorescence properties due to photoinduced electron transfer," *Journal of Luminescence*, vol. 179, pp. 511-517, July 20 2016 2016.

[23] Z. Moussa, M. Chebl, and D. Patra, "Fluorescence of tautomeric forms of curcumin in different pH and biosurfactant rhamnolipids systems: Application towards on-off ratiometric fluorescence temperature sensing," *J Photochem Photobiol B*, vol. 173, pp. 307-317, Aug 2017.

[24] M. Ogawa, R. Takee, Y. Okabe, and Y. Seki, "Bio-geo hybrid pigment; clay-anthocyanin complex which changes color depending on the atmosphere," *Dyes and Pigments*, vol. 139, pp. 561-565, 2017.

[25] G.-O. Buica et al., "Azulene-ethylenediaminetetraacetic acid: A versatile molecule for colorimetric and electrochemical sensors for metal ions," *Electrochimica Acta*, vol. 263, pp. 382-390, 2018.

[26] O. S. Wolfbeis, "Solvent and Acidity Dependence of the Absorption and Fluorescence Spectra of 3-Hydroxycoumarin *," *Zeitschrift für Physikalische Chemie*, vol. 125, no. 1, pp. 15-20, 1981.

[27] S. K. Jessie A. Key, Qadir K. Timerghazin, Alex Brown, Christopher W. Cairo, "Photophysical characterization of triazole-substituted coumarin fluorophores," *Dyes and Pigments*, vol. 82, pp. 196-203, January 5 2009 2009.

[28] M. N. Kobrak, "Characterization of the solvation dynamics of an ionic liquid via molecular dynamics simulation," *J Chem Phys*, vol. 125, no. 6, p. 64502, Aug 14 2006.

[29] M. Maroncelli, X.-X. Zhang, M. Liang, D. Roy, and N. P. Ernsting, "Measurements of the complete solvation response of coumarin 153 in ionic liquids and the accuracy of simple dielectric continuum predictions," *Faraday Discuss.*, vol. 154, pp. 409-424, 2012.

[30] Z. Wang et al., "Nano self-aggregation of new benzotriazole-coumarin dyads displaying strengthened emission with huge Stokes shift," *Dyes and Pigments*, vol. 157, pp. 140-142, 2018.

[31] W. C. Holmes, "The Influence of Variation in Concentration on the Absorption Spectra of Dye Solutions," *Industrial & Engineering Chemistry*, vol. 16, no. 1, pp. 35-40, 1924.

[32] W. C. Holmes, "The Tautomerism of Brilliant Cresyl Blue," *Journal of the American Chemical Society*, vol. 50, no. 7, pp. 1989-1993, 1928.

[33] C. Reichardt, "Empirical Parameters of the Polarity of Solvents," *Angewandte Chemie International* Edition in English, vol. 4, no. 1, pp. 29-40, 1965.

[34] C. Reichardt, "Solvatochromism, thermochromism, piezochromism, halochromism, and chiro-solvatochromism of pyridinium N-phenoxide betaine dyes," *Chemical Society Reviews*, vol. 21, no. 3, 1992.

[35] C. Reichardt, "Solvatochromic Dyes as Solvent Polarity Indicators," *Chemical Reviews*, vol. 94, no. 8, pp. 2319-2358, 1994.

[36] C. Reichardt and T. Welton, *Solvents and Solvent Effects in Organic Chemistry*, 4th ed. Weinheim: Wiley-VCH, 2011, p. 692.

[37] C. Reichardt, "Polarity of ionic liquids determined empirically by means of solvatochromic pyridinium N-phenolate betaine dyes," *Green Chemistry*, vol. 7, no. 5, 2005.

[38] C. W. Reichardt, Thomas, "Solvatochromic Compounds," in *Solvents and Solvent Effects in Organic Chemistry* 4th ed. Weinheim: Wiley-VCH, 2011, pp. 360-371.

[39] H. Zollinger, "Color of Organic Compounds," in *Color Chemistry: Syntheses, Properties, and Applications of Organic Dyes and Pigments* 3 ed.: Wiley-VCH, 2001, pp. 15-50.

[40] K. Carr, "Dyes for Ink Jet Printing," in *Colorants for Non-Textile Applications*, A. T. P. H.S. Freeman, Ed. 1 ed. Amsterdam: Elsevier, 2000, pp. 1-34.

[41] M. Koel, "Solvatochromic Probes with Ionic Liquids," *Proc. Estonian Acad. Sci. Chem.*, vol. 54, no. 1, pp. 3-11, 2004.

[42] M. Koel, "Solvatochromic Study on Binary Solvent Mixtures with Ionic Liquids," 2006.

[43] A. G. Gilani, M. Salmanpour, and T. Ghorbanpour, "Solvatochromism, dichroism and excited state dipole moment of azure A and methylene blue," *Journal of Molecular Liquids*, vol. 179, pp. 118-123, 2013.

[44] C. Mall and P. P. Solanki, "Spectrophotometric and conductometric studies of molecular interaction of brilliant cresyl blue with cationic, anionic and non-ionic surfactant in aqueous medium for application in photogalvanic cells for solar energy conversion and storage," *Energy Reports*, vol. 4, pp. 23-30, 2018.

[45] D. Jacquemin, I. Duchemin, and X. Blase, "0-0 Energies Using Hybrid Schemes: Benchmarks of TD-DFT, CIS(D), ADC(2), CC2, and BSE/GW formalisms for 80 Real-Life Compounds," *J Chem Theory Comput*, vol. 11, no. 11, pp. 5340-59, Nov 10 2015.

[46] L. Shen, H.-F. Ji, and H.-Y. Zhang, "A TD-DFT study on triplet excited-state properties of curcumin and its implications in elucidating the photosensitizing mechanisms of the pigment," *Chemical Physics Letters*, vol. 409, no. 4-6, pp. 300-303, 2005.

[47] D. Jacquemin and E. A. Perpète, "Ab initio calculations of the colour of closed-ring diarylethenes: TD-DFT estimates for molecular switches," *Chemical Physics Letters*, vol. 429, no. 1-3, pp. 147-152, 2006.

[48] X. Lopez, M. A. Marques, A. Castro, and A. Rubio, "Optical absorption of the blue fluorescent protein: a first-principles study," *J Am Chem Soc*, vol. 127, no. 35, pp. 12329-37, Sep 7 2005.

[49] E. A. Perpete, C. Lambert, V. Wathelet, J. Preat, and D. Jacquemin, "Ab initio studies of the lambda(max) of naphthoquinones dyes," *Spectrochim Acta A Mol Biomol Spectrosc*, vol. 68, no. 5, pp. 1326-33, Dec 31 2007.

[50] K. L. Meguellati, Sylvain; Spichty, Martin, "A conceptually improved TD-DFT approach for predicting the maximum absorption wavelength of cyanine dyes," *Dyes and Pigments*, vol. 90, pp. 114-118, December 3 2010 2010.

[51] Y. G. S. Isa Sidir, "Experimental and Theoretical Investigation of the molecular, electronic structure and solvatohromism of phenyl salicylate: External electric field effect on the electronic structure," *Journal of Molecular Structure*, vol. 1147, pp. 206-216, June 21, 2017 2017.

[52] J. P. Denis Jacquemin, Eric A. Perpete, "A TD-DFT study of the absorption spectra of fast dye salts," *Chemical Physics Letters*, vol. 410, pp. 254-259, April 28, 2005 2005.

[53] A. D. Laurent and D. Jacquemin, "TD-DFT benchmarks: A review," *International Journal of Quantum Chemistry*, vol. 113, no. 17, pp. 2019-2039, 2013.

[54] A. Charaf-Eddin, T. Cauchy, F.-X. Felpin, and D. Jacquemin, "Vibronic spectra of organic electronic chromophores," *RSC Adv.*, vol. 4, no. 98, pp. 55466-55472, 2014.

[55] D. Jacquemin and C. Adamo, "Computational Molecular Electronic Spectroscopy with TD-DFT," *Top Curr Chem*, vol. 368, pp. 347-75, 2016.

[56] D. Jacquemin, E. Bremond, A. Planchat, I. Ciofini, and C. Adamo, "TD-DFT Vibronic Couplings in Anthraquinones: From Basis Set and Functional Benchmarks to

Applications for Industrial Dyes," *J Chem Theory Comput*, vol. 7, no. 6, pp. 1882-92, Jun 14 2011.

[57] D. Jacquemin, C. Peltier, and I. Ciofini, "Visible spectrum of naphthazarin investigated through Time-Dependent Density Functional Theory," *Chemical Physics Letters*, vol. 493, no. 1-3, pp. 67-71, 2010.

[58] D. Jacquemin, E. A. Perpete, I. Ciofini, and C. Adamo, "Accurate simulation of optical properties in dyes," *Acc Chem Res*, vol. 42, no. 2, pp. 326-34, Feb 17 2009.

[59] D. Jacquemin, E. A. Perpete, F. Maurel, and A. Perrier, "TD-DFT simulations of the electronic properties of star-shaped photochromes," *Phys Chem Chem Phys*, vol. 12, no. 28, pp. 7994-8000, Jul 28 2010.

[60] D. Jacquemin et al., "Time-dependent density functional theory investigation of the absorption, fluorescence, and phosphorescence spectra of solvated coumarins," *J Chem Phys*, vol. 125, no. 16, p. 164324, Oct 28 2006.

[61] D. Jacquemin, E. A. Perpete, G. E. Scuseria, I. Ciofini, and C. Adamo, "TD-DFT Performance for the Visible Absorption Spectra of Organic Dyes: Conventional versus Long-Range Hybrids," *J Chem Theory Comput*, vol. 4, no. 1, pp. 123-35, Jan 2008.

[62] D. Jacquemin, A. Planchat, C. Adamo, and B. Mennucci, "TD-DFT Assessment of Functionals for Optical 0-0 Transitions in Solvated Dyes," *J Chem Theory Comput*, vol. 8, no. 7, pp. 2359-72, Jul 10 2012.

[63] D. Jacquemin, J. Preat, V. Wathelet, and E. A. Perpète, "Time-dependent density functional theory determination of the absorption spectra of naphthoquinones," Chemical Physics, vol. 328, no. 1-3, pp. 324-332, 2006.

[64] E. A. Perpète and D. Jacquemin, "TD-DFT benchmark for indigoïd dyes," *Journal of Molecular Structure: THEOCHEM*, vol. 914, no. 1-3, pp. 100-105, 2009.

[65] D. Rivero, M. Á. Fernández-González, and L. M. Frutos, "Tuning molecular excitation energy with external forces," *Computational and Theoretical Chemistry*, vol. 1040-1041, pp. 106-111, 2014.

[66] K. Sakata, N. Saito, and T. Honda, "Ab initio study of molecular structures and excited states in anthocyanidins," *Tetrahedron*, vol. 62, no. 15, pp. 3721-3731, 2006.

[67] H.-F. J. Liang Shen, "Theoretical study on physicochemical properties of curcumin," *Spectrochim Acta Part A*, vol. 67, pp. 619-623, August 15 2006 2007.

[68] D. Jeevitha, K. Sadasivam, R. Praveena, and R. Jayaprakasam, "DFT study of glycosyl group reactivity in quercetin derivatives," *Journal of Molecular Structure*, vol. 1120, pp. 15-24, 2016.

[69] A. H. S. Maarten T.P. Beerepoot, Kenneth Ruud, Jogvan Magnus Haugaard Olsen, Jacob Kongsted, "Convergence of environmental polarization effects in multiscale modeling of excitation energies," *Computational and Theoretical Chemistry*, vol. 1040-1041, pp. 304-311, March 17 2014 2014.

[70] D. Marmion, "Colorants for Foods, Drugs, and Cosmetics," in *Kirk-Othmer Chemical Technology of Cosmetics*, A. Seidel, Ed. Hoboken: Wiley, 2013, pp. 501-547.

[71] PubChem. (2018, Dec 17, 2018). FDC Red No. 40. Available: https://pubchem.ncbi.nlm.nih.gov/compound/6093299#section=Top

[72] E. B. Erdal Dinc̦ , Murat Kanbur, Feyyaz Onur "Spectrophotometric multicomponent determination of sunset yellow, tartrazine and allura red in soft drink powder by double divisor-ratio spectra derivative, inverse least-squares and principal component regression methods," *Talanta*, 2002.

[73] PubChem. (2018, December 17 2018). DC Yellow No. 11. Available: https://pubchem.ncbi.nlm.nih.gov/compound/6731#section=Top

[74] ToxNet. (2012, December 17, 2018). HSDB: D & C YELLOW NO. 11 Available: https://toxnet.nlm.nih.gov/cgi-bin/sis/search2/f?./temp/~1JyHiT:2

[75] J. F. Senackerib, "Color Additives for foods, drugs, and cosmetics," in *Colorants for Non-Textile Applications*, A. T. P. H.S. Freeman, Ed. 1 ed. Amsterdam: Elsevier, 2000, pp. 131-187.

[76] H. Brockmann, "Dimethyl-2-amino-4,6-dimethyl-3-oxophenoxazine-1,9-carboxylate actinocindimethyl ester," in *UV Atlas of Organic Compounds* vol. 4. New York: Plenum, 1968.

[77] PubChem. (2018, Dec 17, 2018). 1,3-Diamino-7-(diethylamino)-8methylphenoxazin-5-ium chloride. Available: https://pubchem.ncbi.nlm.nih.gov/substance/135041161#section=Top

[78] PubChem. (2018, Dec 17 2018). 10127-36-3. Available: https://pubchem.ncbi.nlm.nih.gov/substance/254796022#section=Source-Category

[79] PubChem. (2018, December 17, 2018). 10127-36-3 (March 27, 2018 ed.). Available: https://pubchem.ncbi.nlm.nih.gov/substance/355151424#section=Top

[80] S.-A. Corporation, "Brilliant Cresyl Blue BB Safety Data Sheet," ed. Darmstadt: Merck KGaA, 2018.

[81] S.-A. Corporation. (2018, December 17, 2018). ‘Brilliant Cresyl blue’ for microscopy (Vit.), mixture of toluidine blue and waterblue. Available: https://www.sigmaaldrich.com/catalog/product/sigma/16030?lang=en&region=US

[82] P. W. Wasserscheid, T., *Ionic Liquids in Synthesis (Green Chemistry)*. Erlangen: Wiley-VCH, 2008.

[83] J. Mohen and T. D. Vaden, "Brilliant Cresyl Blue in Tunable Ionic Liquid Solvents: Comparison Between Experimental and TD-DFT Spectra," in Investigating Color Additive Molecules for Pharmaceutical and Cosmetic Applications: A Comparison of Theoretical and Experimental UV-Visible Absorbance Spectra in Tunable Solvents. Glassboro: ProQuest, 2019.

[84] A. D. Bochevarov et al., "Jaguar: A high-performance quantum chemistry software program with strengths in life and materials sciences," *International Journal of Quantum Chemistry*, vol. 113, no. 18, pp. 2110-2142, 2013.

[85] M.-M. Huang, Y. Jiang, P. Sasisanker, G. W. Driver, and H. Weingärtner, "Static Relative Dielectric Permittivities of Ionic Liquids at 25 °C," *Journal of Chemical & Engineering Data*, vol. 56, no. 4, pp. 1494-1499, 2011.

[86] H. Saba, X. Zhu, Y. Chen, and Y. Zhang, "Determination of physical properties for the mixtures of [BMIM]Cl with different organic solvents," *Chinese Journal of Chemical Engineering*, vol. 23, no. 5, pp. 804-811, 2015.

[87] C. Wakai, A. Oleinikova, M. Ott, and H. Weingartner, "How polar are ionic liquids? Determination of the static dielectric constant of an imidazolium-based ionic liquid by microwave dielectric spectroscopy," *J Phys Chem B*, vol. 109, no. 36, pp. 17028-30, Sep 15 2005.

[88] C. Schroder, T. Sonnleitner, R. Buchner, and O. Steinhauser, "The influence of polarizability on the dielectric spectrum of the ionic liquid 1-ethyl-3-methylimidazolium triflate," *Phys Chem Chem Phys*, vol. 13, no. 26, pp. 12240-8, Jul 14 2011.

[89] K. Ueno, H. Tokuda, and M. Watanabe, "Ionicity in ionic liquids: correlation with ionic structure and physicochemical properties," *Phys Chem Chem Phys*, vol. 12, no. 8, pp. 1649-58, Feb 28 2010.

[90] S. Arzhantsev, H. Jin, G. A. Baker, and M. Maroncelli, "Measurements of the complete solvation response in ionic liquids," *J Phys Chem B*, vol. 111, no. 18, pp. 4978-89, May 10 2007.

[91] P. Berton, K. Bica, and R. D. Rogers, "Ionic liquids for consumer products: Dissolution, characterization, and controlled release of fragrance compositions," *Fluid Phase Equilibria*, vol. 450, pp. 51-56, 2017.

[92] R. J. Bingham and P. Ballone, "Computational study of room-temperature ionic liquids interacting with a POPC phospholipid bilayer," *J Phys Chem B*, vol. 116, no. 36, pp. 11205-16, Sep 13 2012.

[93] K. G. Bogolitsyn, T. E. Skrebets, and T. A. Makhova, "Physicochemical properties of 1-butyl-3-methylimidazolium acetate," *Russian Journal of General Chemistry*, vol. 79, no. 1, pp. 125-128, 2009.

[94] M. Borissova, J. Gorbatsova, A. Ebber, M. Kaljurand, M. Koel, and M. Vaher, "Nonaqueous CE using contactless conductivity detection and ionic liquids as BGEs in ACN," *Electrophoresis*, vol. 28, no. 20, pp. 3600-5, Oct 2007.

[95] M. Brinkkotter, G. A. Giffin, A. Moretti, S. Jeong, S. Passerini, and M. Schonhoff, "Relevance of ion clusters for Li transport at elevated salt concentrations in [Pyr12O1][FTFSI] ionic liquid-based electrolytes," *Chem Commun (Camb)*, Apr 10 2018.

[96] A. Chaumont and G. Wipff, "Solvation of “big” spherical solutes in room temperature ionic liquids and at their aqueous interface: A molecular dynamics simulation study," *Journal of Molecular Liquids*, vol. 131-132, pp. 36-47, 2007.

[97] H. Chen, T. Yan, and G. A. Voth, "A computer simulation model for proton transport in liquid imidazole," *J Phys Chem A*, vol. 113, no. 16, pp. 4507-17, Apr 23 2009.

[98] C. Chiappe, M. Malvaldi, and C. S. Pomelli, "Ionic liquids: Solvation ability and polarity," *Pure and Applied Chemistry*, vol. 81, no. 4, pp. 767-776, 2009.

[99] M. Dandapat and D. Mandal, "Time-dependent fluorescence Stokes shift and molecular-scale dynamics in alginate solutions and hydrogels," *Chemical Physics Letters*, vol. 627, pp. 67-72, 2015.

[100] F. Endres and S. Zein El Abedin, "Air and water stable ionic liquids in physical chemistry," *Phys Chem Chem Phys*, vol. 8, no. 18, pp. 2101-16, May 14 2006.

[101] M. V. Fedorov and A. A. Kornyshev, "Ionic liquids at electrified interfaces," *Chem Rev*, vol. 114, no. 5, pp. 2978-3036, Mar 12 2014.

[102] M. H. Ghatee and Y. Ansari, "Ab initio molecular dynamics simulation of ionic liquids," *J Chem Phys*, vol. 126, no. 15, p. 154502, Apr 21 2007.

[103] A. Golabiewska et al., "Fabrication and photoactivity of ionic liquid-TiO2 structures for efficient visible-light-induced photocatalytic decomposition of organic pollutants in aqueous phase," *Beilstein J Nanotechnol*, vol. 9, pp. 580-590, 2018.

[104] Z. He and P. Alexandridis, "Nanoparticles in ionic liquids: interactions and organization," *Phys Chem Chem Phys*, vol. 17, no. 28, pp. 18238-61, Jul 28 2015.

[105] T. D. Ho, C. Zhang, L. W. Hantao, and J. L. Anderson, "Ionic liquids in analytical chemistry: fundamentals, advances, and perspectives," *Anal Chem*, vol. 86, no. 1, pp. 262-85, Jan 7 2014.

[106] J. G. Huddleston, A. E. Visser, W. M. Reichert, H. D. Willauer, G. A. Broker, and R. D. Rogers, "Characterization and comparison of hydrophilic and hydrophobic room temperature ionic liquids incorporating the imidazolium cation," *Green Chemistry*, vol. 3, no. 4, pp. 156-164, 2001.

[107] E. I. Izgorodina, "Towards large-scale, fully ab initio calculations of ionic liquids," *Phys Chem Chem Phys*, vol. 13, no. 10, pp. 4189-207, Mar 14 2011.

[108] S. G. Jones et al., "Ionic liquids through the looking glass: theory mirrors experiment and provides further insight into aromatic substitution processes," *Phys Chem Chem Phys*, vol. 12, no. 8, pp. 1873-8, Feb 28 2010.

[109] M. Kanakubo, T. Makino, and T. Umecky, "CO2 solubility in and physical properties for ionic liquid mixtures of 1-butyl-3-methylimidazolium acetate and 1-butyl-3-methylimidazolium bis(trifluoromethanesulfonyl)amide," *Journal of Molecular Liquids*, vol. 217, pp. 112-119, 2016.

[110] P. G. Katharina Bica, and Robin D. Rogers, "Ionic Liquids and Fragrances - Direct Isolation of Orange Essential Oil SUPPLEMENTAL INFORMATION," 2011.

[111] D. C. Khara and A. Samanta, "Fluorescence response of coumarin-153 in N-alkyl-N-methylmorpholinium ionic liquids: are these media more structured than the imidazolium ionic liquids?," *J Phys Chem B*, vol. 116, no. 45, pp. 13430-8, Nov 15 2012.

[112] M. N. Kobrak, "A comparative study of solvation dynamics in room-temperature ionic liquids," J Chem Phys, vol. 127, no. 18, p. 184507, Nov 14 2007.

[113] M. N. Kobrak and V. Znamenskiy, "Solvation dynamics of room-temperature ionic liquids: evidence for collective solvent motion on sub-picosecond timescales," Chemical Physics Letters, vol. 395, no. 1-3, pp. 127-132, 2004.

[114] M. N. S. Kobrak, N., "An Electrostatic Interpretation of Structure-Property Relationships in Ionic Liquids," 2015.

[115] K. Y. Lee WR, Kim JY, Kim TH, Ahn KD, Kim E., "Electro-fluorescence Switching of bis-imidazolium ionic liquids," J Nanosci Nanotechnol, vol. 8, no. 9, pp. 4630-4, 2008.

[116] K. R. J. Lovelock, "Influence of the ionic liquid/gas surface on ionic liquid chemistry," Physical Chemistry Chemical Physics, vol. 14, no. 15, 2012.

[117] K. Low, L. Wylie, D. L. A. Scarborough, and E. I. Izgorodina, "Is it possible to control kinetic rates of radical polymerisation in ionic liquids?," Chem Commun (Camb), vol. 54, no. 80, pp. 11226-11243, Oct 4 2018.

[118] R. M. Lynden-Bell, "Screening of pairs of ions dissolved in ionic liquids," Phys Chem Chem Phys, vol. 12, no. 8, pp. 1733-40, Feb 28 2010.

[119] D. R. MacFarlane and K. R. Seddon, "Ionic Liquids—Progress on the Fundamental Issues," Australian Journal of Chemistry, vol. 60, no. 1, 2007.

[120] P. K. Mandal, A. Paul, and A. Samanta, "Room Temperature Ionic Liquids as Media for Photophysical Studies," Journal of the Chinese Chemical Society, vol. 53, no. 1, pp. 247-252, 2006.

[121] P. K. Mandal, M. Sarkar, and A. Samanta, "Excitation-Wavelength-Dependent Fluorescence Behavior of Some Dipolar Molecules in Room-Temperature Ionic Liquids," The Journal of Physical Chemistry A, vol. 108, no. 42, pp. 9048-9053, 2004.

[122] M. Maroncelli, X.-X. Zhang, M. Liang, D. Roy, and N. P. Ernsting, "Measurements of the complete solvation response of coumarin 153 in ionic liquids and the accuracy of simple dielectric continuum predictions," Faraday Discuss., vol. 154, pp. 409-424, 2012.

[123] P. C. Marr and A. C. Marr, "Ionic liquid gel materials: applications in green and sustainable chemistry," Green Chemistry, vol. 18, no. 1, pp. 105-128, 2016.

[124] H. Matsumoto, S. Ikedu, T. Tosaka, Y. Nishimura, and T. Arai, "Kinetic analysis of tautomer forms of aromatic-urea compounds with acetate ions: solvent effect of excited state intermolecular proton transfer," Photochem Photobiol Sci, Apr 4 2018.

[125] M. J. Muldoon, C. M. Gordon, and I. R. Dunkin, "Investigations of solvent–solute interactions in room temperature ionic liquids using solvatochromic dyes," Journal of the Chemical Society, Perkin Transactions 2, no. 4, pp. 433-435, 2001.

[126] C. M. S. S. Neves, M. G. Freire, and J. A. P. Coutinho, "Improved recovery of ionic liquids from contaminated aqueous streams using aluminium-based salts," RSC Advances, vol. 2, no. 29, 2012.

[127] H. Niedermeyer, J. P. Hallett, I. J. Villar-Garcia, P. A. Hunt, and T. Welton, "Mixtures of ionic liquids," Chem Soc Rev, vol. 41, no. 23, pp. 7780-802, Dec 7 2012.

[128] V. H. Paschoal, L. F. O. Faria, and M. C. C. Ribeiro, "Vibrational Spectroscopy of Ionic Liquids," Chem Rev, vol. 117, no. 10, pp. 7053-7112, May 24 2017.

[129] A. Paul, P. K. Mandal, and A. Samanta, "On the optical properties of the imidazolium ionic liquids," J Phys Chem B, vol. 109, no. 18, pp. 9148-53, May 12 2005.

[130] S. S. Prasun K. Mandal, Rana Karmakar, Anunay Samanta, "Solvation Dynamics in Room Temperature Ionic Liquids: Dynamic Stokes Shift Studies of Fluorescence of Dipolar Molecules," *Current Science*, vol. 90, no. 3, pp. 301-310, Feb 10 2006 2006.

[131] G. O. B. K. Richard and S. H. Q. N. Gunaratne, "Ionic Liquid Systems," United States of America Patent US 20160376522 A1 Patent Appl. US 15/187,829, 2016. [Online]. Available: https://www.google.com/patents/US20160376522.

[132] A. Samanta, "Dynamic stokes shift and excitation wavelength dependent fluorescence of dipolar molecules in room temperature ionic liquids," *J Phys Chem B*, vol. 110, no. 28, pp. 13704-16, Jul 20 2006.

[133] M. S. Raja Shahrom, C. D. Wilfred, and A. K. Z. Taha, "CO 2 capture by task specific ionic liquids (TSILs) and polymerized ionic liquids (PILs and AAPILs)," *Journal of Molecular Liquids*, vol. 219, pp. 306-312, 2016.

[134] B. M. Sato, C. G. de Oliveira, C. T. Martins, and O. A. El Seoud, "Thermo-solvatochromism in binary mixtures of water and ionic liquids: on the relative importance of solvophobic interactions," *Phys Chem Chem Phys*, vol. 12, no. 8, pp. 1764-71, Feb 28 2010.

[135] C. Schroder, T. Rudas, and O. Steinhauser, "Simulation studies of ionic liquids: orientational correlations and static dielectric properties," *J Chem Phys*, vol. 125, no. 24, p. 244506, Dec 28 2006.

[136] M. B. Shiflett, D. W. Drew, R. A. Cantini, and A. Yokozeki, "Carbon Dioxide Capture Using Ionic Liquid 1-Butyl-3-methylimidazolium Acetate," *Energy & Fuels*, vol. 24, no. 10, pp. 5781-5789, 2010.

[137] Y. Shim, D. Jeong, M. Y. Choi, and H. J. Kim, "Rotational dynamics of a diatomic solute in the room-temperature ionic liquid 1-ethyl-3-methylimidazolium hexafluorophosphate," *J Chem Phys*, vol. 125, no. 6, p. 61102, Aug 14 2006.

[138] Y. Shim and H. J. Kim, "Vibrational energy relaxation of a diatomic molecule in a room-temperature ionic liquid," *J Chem Phys*, vol. 125, no. 2, p. 24507, Jul 14 2006.

[139] T. Singh and A. Kumar, "Static dielectric constant of room temperature ionic liquids: internal pressure and cohesive energy density approach," *J Phys Chem B*, vol. 112, no. 41, pp. 12968-72, Oct 16 2008.

[140] X. Song, "Solvation dynamics in ionic fluids: an extended Debye-Huckel dielectric continuum model," *J Chem Phys*, vol. 131, no. 4, p. 044503, Jul 28 2009.

[141] S. M. Urahata and M. C. Ribeiro, "Single particle dynamics in ionic liquids of 1-alkyl-3-methylimidazolium cations," *J Chem Phys*, vol. 122, no. 2, p. 024511, Jan 8 2005.

[142] I. J. Villar-Garcia et al., "The ionic liquid–vacuum outer atomic surface: a low-energy ion scattering study," *Chem. Sci.*, vol. 5, no. 11, pp. 4404-4418, 2014.

[143] H. Wang et al., "Fluorescence quenching of 4-tert-octylphenol by room temperature ionic liquids and its application," *J Fluoresc*, vol. 23, no. 2, pp. 323-31, Mar 2013.

[144] M. Watanabe, D. Kodama, T. Makino, and M. Kanakubo, "CO2 absorption properties of imidazolium based ionic liquids using a magnetic suspension balance," *Fluid Phase Equilibria*, vol. 420, pp. 44-49, 2016.

[145] B. Wu, H. Shirota, S. Lall-Ramnarine, and E. W. Castner, "Structure of ionic liquids with cationic silicon-substitutions," *The Journal of Chemical Physics*, vol. 145, no. 11, 2016.

[146] X. Zhang, X. Zhang, H. Dong, Z. Zhao, S. Zhang, and Y. Huang, "Carbon capture with ionic liquids: overview and progress," *Energy & Environmental Science*, vol. 5, no. 5, 2012.

[147] Q. Zhang and S. Zhu, "Ionic Liquids: Versatile Media for Preparation of Vesicles from Polymerization-Induced Self-Assembly," *ACS Macro Letters*, vol. 4, no. 7, pp. 755-758, 2015.

[148] *Ionic liquids for better separation processes* (Green Chemistry and Sustainable Technology). Heidelberg: Springer, 2016, p. 233.

[149] M. Besnard et al., "On the spontaneous carboxylation of 1-butyl-3-methylimidazolium acetate by carbon dioxide," *Chem Commun (Camb)*, vol. 48, no. 9, pp. 1245-7, Jan 30 2012.

[150] D. Coleman and N. Gathergood, "Biodegradation studies of ionic liquids," *Chem Soc Rev*, vol. 39, no. 2, pp. 600-37, Feb 2010.

[151] M. A. R. Martins, U. Domańska, B. Schröder, J. A. P. Coutinho, and S. P. Pinho, "Selection of Ionic Liquids to be Used as Separation Agents for Terpenes and Terpenoids," *ACS Sustainable Chemistry & Engineering*, vol. 4, no. 2, pp. 548-556, 2015.

[152] M. Petkovic, K. R. Seddon, L. P. Rebelo, and C. Silva Pereira, "Ionic liquids: a pathway to environmental acceptability," *Chem Soc Rev*, vol. 40, no. 3, pp. 1383-403, Mar 2011.

[153] (2019). *1-Butyl-3-Methylimidazolium Chloride Safety Data Sheet*.

[154] (2019). *1-Butyl-3-Methylimidazolium Tetrafluoroborate Safety Data Sheet*.

[155] (2019). *1-Ethyl-3-Methylimidazolium Acetate Safety Data Sheet*.

[156] C. W. Reichardt, Thomas, "Solvent Effects on Position of Homogenous Chemical Equilibrium," in *Solvents and Solvent Effects in Organic Chemistry* 4th ed. Weinheim: Wiley-VCH, 2011, pp. 107-156.

[157] S. Harfouch, "Quinoline Absorbance Peaks," J. Mohen, Ed., ed, 2017, p. 2.

[158] M. A. R. M. Clara C.S. Sousa, Victor M.F. Morais, "Energetics and stability of azulene: from experimental thermochemistry to high-level quantum chemical calculations," *J. Chem. Thermodynamics*, vol. 73, pp. 101-109, November 11 2013 2014.

[159] Y. Manolova, V. Deneva, L. Antonov, E. Drakalska, D. Momekova, and N. Lambov, "The effect of the water on the curcumin tautomerism: a quantitative approach," *Spectrochim Acta A Mol Biomol Spectrosc*, vol. 132, pp. 815-20, Nov 11 2014.

[160] K. Carr, "Dyes for Ink Jet Printing," in *Colorants for Non-Textile Applications*, A. T. P. H.S. Freeman, Ed. 1 ed. Amsterdam: Elsevier, 2000, pp. 1-34.

[161] E. Evangelio and D. Ruiz-Molina, "Valence Tautomerism: New Challenges for Electroactive Ligands," *European Journal of Inorganic Chemistry*, vol. 2005, no. 15, pp. 2957-2971, 2005.

[162] A. Dutta, B. Boruah, A. K. Manna, B. Gohain, P. M. Saikia, and R. K. Dutta, "Stabilization of diketo tautomer of curcumin by premicellar anionic surfactants: UV-Visible, fluorescence, tensiometric and TD-DFT evidences," *Spectrochim Acta A Mol Biomol Spectrosc*, vol. 104, pp. 150-7, Mar 2013.

[163] H.-J. Himmel, "Valence tautomerism in copper coordination chemistry," *Inorganica Chimica Acta*, vol. 481, pp. 56-68, 2018.

[164] S.-i. Kawano, Y. Inohana, Y. Hashi, and J.-M. Lin, "Analysis of keto-enol tautomers of curcumin by liquid chromatography/mass spectrometry," *Chinese Chemical Letters*, vol. 24, no. 8, pp. 685-687, 2013.

[165] M. Khadem Sadigh, M. S. Zakerhamidi, S. M. Seyed Ahmadian, M. Johari-Ahar, and L. Zare Haghighi, "Environment effect on spectral and charge distribution characteristics of some drugs of folate derivatives," *Spectrochim Acta A Mol Biomol Spectrosc*, vol. 171, pp. 10-17, Jan 15 2017.

[166] H. W. Liu et al., "Reversible valence tautomerism induced by a single-shot laser pulse in a cobalt-iron Prussian blue analog," *Phys Rev Lett*, vol. 90, no. 16, p. 167403, Apr 25 2003.

[167] H. Matsumoto, S. Ikedu, T. Tosaka, Y. Nishimura, and T. Arai, "Kinetic analysis of tautomer forms of aromatic-urea compounds with acetate ions: solvent effect of excited state intermolecular proton transfer," *Photochem Photobiol Sci*, Apr 4 2018.

[168] S. Mondal, S. Ghosh, and S. P. Moulik, "Stability of curcumin in different solvent and solution media: UV-visible and steady-state fluorescence spectral study," J *Photochem Photobiol B*, vol. 158, pp. 212-8, May 2016.

[169] Z. Moussa, M. Chebl, and D. Patra, "Fluorescence of tautomeric forms of curcumin in different pH and biosurfactant rhamnolipids systems: Application towards on-off ratiometric fluorescence temperature sensing," *J Photochem Photobiol B*, vol. 173, pp. 307-317, Aug 2017.

[170] A. Panja, N. Jana, A. Bauza, A. Frontera, and C. Mathoniere, "Solvent-Triggered Cis/Trans Isomerism in Cobalt Dioxolene Chemistry: Distinguishing Effects of Packing on Valence Tautomerism," *Inorg Chem*, vol. 55, no. 17, pp. 8331-40, Sep 6 2016.

[171] D. Yanagisawa et al., "Relationship between the tautomeric structures of curcumin derivatives and their Abeta-binding activities in the context of therapies for Alzheimer's disease," *Biomaterials*, vol. 31, no. 14, pp. 4179-85, May 2010.

[172] T. Tezgerevska, K. G. Alley, and C. Boskovic, "Valence tautomerism in metal complexes: Stimulated and reversible intramolecular electron transfer between metal centers and organic ligands," *Coordination Chemistry Reviews*, vol. 268, pp. 23-40, 2014.

[173] H. Zollinger, "Azo Dyes and Pigments," in *Color Chemistry: Syntheses, Properties, and Applications of Organic Dyes and Pigments* 3rd ed.: Wiley-VCH, 2001, pp. 165-253.

[174] U. S. F. a. D. Administration. (2015, November 7, 2018). *Color Additive Status List* [Online]. Available: https://www.fda.gov/ForIndustry/ColorAdditives/ColorAdditiveInventories/ucm106626.htm.

[175] G. V. Sheban, B. E. Zaitsev, and K. M. Dyumaev, "Quantum-chemical study of the tautomerism of hydroxyazobenzene derivatives," *Theoretical and Experimental Chemistry*, vol. 16, no. 2, pp. 207-211, 1980.

[176] J. O. Morley, "Theoretical Investigation of the Conformations, Tautomeric Forms, and Spectra of Donor-Acceptor (Phenylazo)arenes," *The Journal of Physical Chemistry*, vol. 98, no. 50, pp. 13177-13181, 1994.

[177] C. W. Reichardt, Thomas, "Solvent Effects on the Rates of Homogenous Chemical Reactions," in *Solvents and Solvent Effects in Organic Chemistry* 4th ed. Weinheim: Wiley-VCH, 2011, pp. 164-357.

[178] J. S. W. M. J. Zaworotko, "Air and Water Stable 1-Ethyl-3-methylimidazolium Based Ionic Liquids," *J. Chem. Soc., Chem. Commun.*, pp. 965-966, January 1, 1992 1992.

[179] (1987). Water Quality Criteria for Colored Smokes: Solvent Yellow 33 Final Report.

[180] P. F. Atkins, Ronald, "Molecular Electronic Transitions," in *Molecular Quantum Mechanics* 5th ed. Oxford: Oxford University Press, 2011, pp. 382-406.

[181] P. A. J. d. J. Keeler, "Molecular Spectroscopy," in *Physical Chemistry*11th ed. Oxford: Oxford University Press, 2018, pp. 459-469.

[182] A. Buryak and K. Severin, "Dynamic Combinatorial Libraries of Dye Complexes as Sensors," *Angewandte Chemie*, vol. 117, no. 48, pp. 8149-8152, 2005.

[183] Q. F. Zhang, Z. T. Jiang, Y. X. Guo, and R. Li, "Complexation study of brilliant cresyl blue with beta-cyclodextrin and its derivatives by UV-vis and fluorospectrometry," *Spectrochim Acta A Mol Biomol Spectrosc*, vol. 69, no. 1, pp. 65-70, Jan 2008.

[184] Y. Umasankar, T.-W. Ting, and S.-M. Chen, "Characterization of Poly(brilliant cresyl blue)-Multiwall Carbon Nanotube Composite Film and Its Application in Electrocatalysis of Vitamin B9 Reduction," *Journal of The Electrochemical Society*, vol. 158, no. 5, 2011.

[185] X. Li et al., "Ordered array of gold semishells on TiO2 spheres: an ultrasensitive and recyclable SERS substrate," *ACS Appl Mater Interfaces*, vol. 4, no. 4, pp. 2180-5, Apr 2012.

[186] R. N. Dsouza, U. Pischel, and W. M. Nau, "Fluorescent dyes and their supramolecular host/guest complexes with macrocycles in aqueous solution," *Chem Rev*, vol. 111, no. 12, pp. 7941-80, Dec 14 2011.

[187] O. TAKAHASHI, "Characteristics of Rat Platelets and Relative Contributions of Platelets and Blood Coagulation to Haemostasis," *Food Chem Toxicol*, vol. 38, pp. 203-218, 2000.

[188] E. V. Garibay et al., "Iron Absorption during Recovery from Malnutrition," *Journal of the American College of Nutrition*, vol. 20, no. 4, pp. 286-292, 2001.

[189] R. J. Nieckarz, J. Oomens, G. Berden, P. Sagulenko, and R. Zenobi, "Infrared multiple photon dissociation (IRMPD) spectroscopy of oxazine dyes," *Phys Chem Chem Phys*, vol. 15, no. 14, pp. 5049-56, Apr 14 2013.

[190] G. Wypych, *Handbook of UV degradation and stabilization*. Elsevier, 2015.

[191] F. R. S. C. Alister Vallance Jones, "Optical Emissions from Aurora," in *Aurora*, vol. 9, B. M. McCormac, Ed. (Geophysics and Astrophysics Monographs. Boston: D. Reidel, 1974, pp. 80-177.

[192] C. Schroder and O. Steinhauser, "Simulating polarizable molecular ionic liquids with Drude oscillators," *J Chem Phys*, vol. 133, no. 15, p. 154511, Oct 21 2010.

[193] T. Sonnleitner et al., "Ultra-Broadband Dielectric and Optical Kerr-Effect Study of the Ionic Liquids Ethyl and Propylammonium Nitrate," *J Phys Chem B*, vol. 119, no. 29, pp. 8826-41, Jul 23 2015.

Chapter 3

Brilliant Cresyl Blue in Tunable Ionic Liquid Solvents: A Comparison between Experimental and TD-DFT Spectra

Brilliant Cresyl Blue (BCB) is a common oxazine dye, classified within the quinone-imine class of dye molecules containing azine, oxazine, and thiazine dyes that have historically been effective for many specialized industries. BCB has pharmaceutical applications as a biological stain [1,2,3], as an indicator of malnutrition [4], in metal-ligand exchange reactions [5], and also facilitates considerable electrical output with charged solvent molecules as a photogalvanic cell due to its known charge transfer (CT) properties [2,6,7,8]. This dye molecule is encountered most commonly as Brilliant Cresyl Blue ALD [11-12], a structure certified by the Biological Stain Commission which contains a zinc (II) chloride metal ion when solvated. However, BCB also exists in the forms Brilliant Cresyl Blue C [9] and BB [10], which both differ from ALD in terms of their electronic charge distribution and the presence of a chloride ion in solution [12]. BCB C and BB are constitutional isomers based on clear distinctions in their molecular structure that affect distribution of positive charge from the sp^2-hybridized nitrogen molecule in BCB C to the oxygen atom in BCB BB charge distribution as shown in Figure 64. BCB has noteworthy aggregation properties that enable monomers of the molecule to form dimer complexes that are indicated by UV-visible absorbance spectroscopy [13,14,15] and fluorescence spectroscopy methods [2,14]. However, there are noteworthy shifts in maximum absorbance (λ_{max}) and shoulder ($\lambda_{shoulder}$) spectra values depending upon the solvent molecules selected for analysis. Table 29 lists the

maximum absorbance and “shoulder” values for BCB structures published throughout several experimental studies.

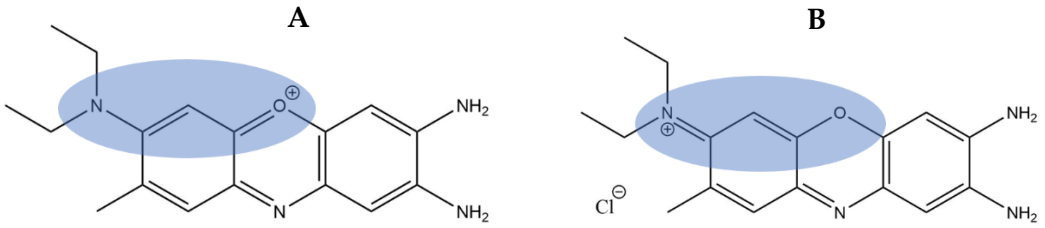

Fig. 64. Brilliant Cresyl Blue BB (a) and Brilliant Cresyl Blue C (b). Both structures are constitutional isomers, and classified under the same CAS#10127-36-3. The structures differ based on their charge distribution from the sp^2-hybridized nitrogen molecule in BCB C to the oxygen atom in BCB B

TABLE XXIX

Literature values for λ_{max} and $\lambda_{shoulder}$ of Brilliant Cresyl Blue structures in varied solvents and complexes

Dye-Solvent-Complex	λ_{max} (nm)	$\lambda_{shoulder}$ (nm)	Source
BCB–H_2O-β-CD	634	598	Zhang, Q. F.; Jiang, Z. T.; Guo, Y. X.; Li, R. Spectrochim Acta A Mol Biomol Spectrosc 2008, 69 (1), 65-70.
BCB ALD-H_2O	622	572	Gilani, A. G. et al. Spectrochim Acta A Mol Biomol Spectrosc 2011, 83 (1), 100-5.
BCB ALD-Urea (CON_2H_4)	633	594	Gilani, A. G. et al. Spectrochim Acta A Mol Biomol Spectrosc 2011, 83 (1), 100-5.
BCB BB-H_2O	636	n/a	Koel, M., Proc. Estonian Acad. Sci. Chem. 2004, 54 (1), 3-11.
BCB BB-Acetonitrile	629	n/a	Koel, M., Proc. Estonian Acad. Sci. Chem. 2004, 54 (1), 3-11.
BCB BB-Acetone	640	n/a	Koel, M., Proc. Estonian Acad. Sci. Chem. 2004, 54 (1), 3-11.
BCB BB-Propylene Carbonate	635	n/a	Koel, M., Proc. Estonian Acad. Sci. Chem. 2004, 54 (1), 3-11.
BCB BB-Benzene	607	n/a	Koel, M., Proc. Estonian Acad. Sci. Chem. 2004, 54 (1), 3-11.
BCB BB-MeOH	630	n/a	Koel, M., Proc. Estonian Acad. Sci. Chem. 2004, 54 (1), 3-11.
BCB BB-C_4MImPF_6	634	n/a	Koel, M., Proc. Estonian Acad. Sci. Chem. 2004, 54 (1), 3-11.
BCB ALD-H_2O	624.5	~575	Mall, C.; Solanki, P. P. Energy Reports 2018, 4, 23-30.
BCB ALD-CTAB-alkaline media	624.5	~580	Mall, C.; Solanki, P. P. Energy Reports 2018, 4, 23-30.
BCB ALD-SLS-alkaline media	644.5	~590	Mall, C.; Solanki, P. P. Energy Reports 2018, 4, 23-30.
BCB ALD-Tween 80-alkaline media	517.5	~630	Mall, C.; Solanki, P. P. Energy Reports 2018, 4, 23-30.
BCB BB-H_2O (Dilute, 40mg)	625	570	Holmes, W. C. Journal of the American Chemical Society 1928, 50 (7), 1989-1993.
BCB BB-H_2O (Conc. 1000mg)	575	630	Holmes, W. C. Journal of the American Chemical Society 1928, 50 (7), 1989-1993.

Literature studies present a diverse range of λ_{max} and $\lambda_{shoulder}$ values for BCB experimental spectra as shown in Table 29, which may vary considerably for several reasons ranging from dye aggregation to the unique solvent interactions as a result of dye structural characteristics. The first relevant factor affecting absorbance spectra is (i) BCB dye concentration. Dilute concentrations of BCB may indicate the presence of only the BCB monomer in solution, as opposed to a BCB dimer complex formed by self-association among more numerous dye moelcules in more saturated mixtures. This is indicated clearly by a neighboring "double-", "forked", or "shoulder" peak which increases in intensity with increasing concentration of BCB in solution. The second prevalent factor is (ii) the solvent utilized for dye-solvent mixture analysis. Deionized water has been a common choice of solvent for ionic dyes in previous works [3,7,14,15,16], and a recent study [8] has affirmed the effectiveness of charged surfactants dissolved in alkaline solutions to supplement the strong charge transfer nature of the BCB ALD cationic dye molecule for applications as a potential energy source. Previous works have considered the CT characteristic troublesome for definitive UV-visible spectra analysis [17,18]. Both of these factors have also caused an additional problem in conventional spectrophotometric analysis: (iii) it is difficult to assign the contributions of each specific monomer or dimer complex structure of BCB (dye-dye, dye-solvent, or dye-surfactant-solvent) to a characteristic λ_{max} or $\lambda_{shoulder}$ peak. A final criterion may also affect analyses of BCB in a more basic sense. Its common name (iv) is frequently used without distinction among the variety of chemical substances commercially available (and used throughout the literature) to denote its structure. While all structures previously analyzed [2,3,6-16,19] have the same core of three fused

aromatic rings and a heteroatom in the central ring, each BCB molecular structure has a distinctly different arrangement of π-bonds and alkyl groups which may in turn affect solvation properties. The different location of alkyl and aryl groups may strongly contribute to the ability of BCB to undergo successful face-to-face self-association, commonly referred to as "π-stacking" or simply "stacking". In addition, certain symmetry-forbidden electronic transitions may occur if BCB is airborne or immersed in distinct solvents. This phenomenon ultimately affects the perceived solvatochromatic properties of the dye molecule, and contributes to noticeable hypsochromic (left-most, towards ultraviolet) and bathochromic (right-most, towards IR) shifts in λ_{max} as indicated in prior studies [8, 14-16,20]. These four aspects that previously made spectrophotometric data analysis troublesome are now able to be more closely addressed in this work.

This study seeks to further explore the interaction of the versatile cationic structure of BCB C and its constitutional isomer "BB" (or "structure 1") in common formulation solvents--distilled water and ethanol--to study differences in the color perceived. In addition, the charged structure of the BCB molecule provokes interest in the use of ionic liquids (ILs) as formulation solvents. ILs are characteristically charged solvents that are binary mixtures of pairs of ions—one cation and one anion [21]. Cation and anion selection can be customized to obtain desired solution properties, hence the increasingly widespread use of ILs as "tunable" solvents [22-30]. This research explores the possible spectrum of colors that can be obtained by using isomers of a single ionic dye molecule (BCB) in ILs, and seeks to explain the possible interaction mechanisms of

specific ions on the hue and chromatic properties exhibited upon dye molecule-IL solvation.

The inconsistencies described above can be clarified by the use of computational modeling of the BCB monomer and dimer to calculate electronic excitation states to determine theoretical UV-visible absorption spectra based on simulated solvation effects. Computationally-rendered structures of individual BCB monomers and dimer complexes were generated and compared based on information available for both common solvents and less-conventional, charged solvents for novel application in pharmaceutical formulations. In this work, theoretical spectral studies have been carried out to isolate structural contributions to anomalies in experimental absorbance spectra by using density functional theory (DFT) to calculate ideal geometry optimizations in solvent, and by calculating singlet excited states of relevant monomer and dimer structures using both implicit and explicit solvation modeling using quantum mechanical calculations. Single-point-energy calculations using the time-dependent density functional theory (TD-DFT) were performed using both full-linear response (FLR) and the Tamm-Dancoff Approximation (TDA) for comparison in order to determine the optimal input settings for "realistic" simulation of theoretical absorbance spectra. Theoretical data was analyzed for its relation to multiple concentrations of dye-solvent mixtures so that the batches that most closely reflect hues that mimic the color appearance discernible in experimental batch preparations were considered accurate simulations. Explanations of the most preferable method of calculating theoretical absorbance spectra are presented, along with plausible explanations of which ions (comparatively) exhibit the strongest shifts in absorbance spectra--and as a result, color appearance--in solution containing

pharmaceutical and cosmetic formulation solvents selected for analysis. In order to isolate the contributions of molecular structures that, based on existing literature studies, have been hypothesized to exist in BCB-containing solutions, we must "work backwards" using experimental λ_{max} as a "benchmark" comparison to theoretical λ_{max} generated from specified structure and solvent parameters in a computational workspace. Such a methodology must be adopted in order to begin to explain the fascinating visual array of colors throughout the visible spectrum that are possible by simply changing the solvent ions in a mixture instead of the color additive molecule selected.

Materials and Methods

Advanced *ab initio* methods were used as described in detail in Chapter 1. However, the structures 1 and 2 as identified in Chapter 2 for the Brilliant Cresyl Blue molecule are analyzed in greater detail in this chapter to identify the solvent interactions responsible for the dramatic solvatochromic effect evident in dye-solvent mixtures containing ionic liquid solvents, particularly [EMIM]OAc. This work contrasts previous studies in that geometry conformations and restricted singlet excited states of both the BCB dye monomer and the homodimer aggregate structures were analyzed without taking molecular orbital surfaces into account (as in [20]). In this study, the goal of optimization of geometry conformations incorporating solvation effects was not only color spectral comparison. More importantly, the interaction of dye and solvent molecules implicitly or explicitly represented has been assessed to draw conclusions as to the noncovalent forces at play in mixtures containing diverse formulation solvents.

Experimental Procedure. Brilliant Cresyl Blue (CAS: 10127-36-3) solid, powder stock was purchased from Electron Microscopy Sciences located in Hatfield, Pennsylvania, USA. Dye-solvent interactions in experimental batch preparations were studied by preparing 1 mL volumes of the five various solvents using commercially-available BCB. Batches were prepared in the following millimolar (mM) and molar (M) concentrations:

TABLE XXX

Conversion chart for Brilliant Cresyl Blue dye-solvent mixture batch preparations analyzed for experimental maximum absorbance spectral peak responsivity (λ_{max}) comparison to theoretical data

Concentration	mM	M
1.0 mM	1	1×10^{-3}
0.1 mM	1×10^{-1}	1×10^{-4}
0.01 mM	1×10^{-2}	1×10^{-5}
0.001 mM	1×10^{-3}	1×10^{-6}
0.0001 mM	1×10^{-4}	1×10^{-7}
0.00001 mM	1×10^{-5}	1×10^{-8}
0.000001 mM	1×10^{-6}	1×10^{-9}

The mass of solid BCB dissolved into 1 mL solvent for the initial concentrations featured in this study was 0.033 g (0.1 mM) based on its molecular weight of 332.832 g/mol. Batches were prepared and diluted beginning from the 0.1 mM BCB solution because 1 mM concentrations were deemed too saturated for experimental UV-visible spectral analysis.

0.1 mM BCB in Formulation Solvent

0.033 g of BCB stock were weighed and transferred into an Eppendorf tube containing 0.5 mL of one of the five solvents studied—water, ethanol, [BMIM]Cl, [BMIM]BF_4, and [EMIM]OAc. Once all solid BCB was successfully transferred, an additional 0.5 mL of solvent was added to the Eppendorf tube to make 1 mL of solvent. 0.033 g BCB and 1 mL of solvent mathematically converts to a 0.1 mM dye-solvent molecule ratio. To expedite the dissolution process, the Eppendorf tube containing 1 mL dye-solvent solution was vortexed for 10 seconds and then sonicated for 20 minutes. Samples were then vortexed for an additional 10 seconds after sonication.

Solutions containing ionic liquids [BMIM]BF_4, [BMIM]Cl, and [EMIM]OAc were heated after sonication to melting point temperatures (approximately 160-175 ˚F) to ensure complete dissolution in solvent. Samples were then left at room temperature (25˚C) to cool prior to analysis.

Dye-solvent solutions were poured into quartz cuvettes for measurement of UV-visible spectra using an Agilent spectrophotometer.

0.01 mM (1 x10^{-2} mM; 1 x 10^{-5} M) BCB in Formulation Solvent

A 0.1 mL volumetric quantity of 0.1 mM BCB-solvent solution was drawn into a plastic pipette and inserted into an Eppendorf tube. Then, 0.9 mL of pure (no dye) solvent were added to the Eppendorf tube to dilute the solution by a factor of 10. To expedite the dissolution process, the Eppendorf tube containing the 1 mL dye-solvent solution was

vortexed for 10 seconds and then sonicated for 20 minutes. Samples were then vortexed for an additional 10 seconds after sonication.

Solutions containing ionic liquids [BMIM]BF_4, [BMIM]Cl, and [EMIM]OAc were heated after sonication to melting point temperatures (approximately 160-175 ˚F) to ensure complete dissolution in solvent. Samples were then left at room temperature (25˚C) to cool prior to analysis.

Dye-solvent solutions were poured into quartz cuvettes for measurement of UV-visible spectra using an Agilent spectrophotometer.

0.001 mM, 1 x 10^{-4} mM, 1 x 10^{-5} mM, and 1 x 10^{-6} mM BCB in Formulation Solvent

This dilution method was repeated to prepare the 0.001 mM, 1 x 10^{-4} mM, 1 x 10^{-5} mM, and 1 x 10^{-6} mM BCB dye-solvent batches for each of the five solutions analyzed.

Ionic liquids that were too viscous to pour at room temperature were heated, then poured into quartz cuvettes and cooled prior to analysis.

Theoretical Procedure. Quantum mechanical calculations were performed on computer-generated structures of the two constitutional isomers of the Brilliant Cresyl Blue molecule with changes in π-bonding as shown in Figure 64. Brilliant Cresyl Blue BB (referred to as “Structure 1”, Figure 64a) and Brilliant Cresyl Blue C (Figure 64b) were constructed using Schrödinger Maestro. Density functional theory (DFT) and time-dependent density functional theory (TD-DFT) quantum mechanical calculations were performed using the Jaguar software package.

Geometry optimizations to obtain the optimal conformational orientation of the BCB molecule(s) in solvent were performed using density functional theory (DFT) calculations using a double-zeta hybrid functional basis set incorporating polarization and diffuse functions, namely 6-31+G*/B3LYP. Effective core potential was utilized when necessary for large atoms (such as chlorine) using Los Alamos basis set LAV2P+*/B3LYP. Cartesian coordinates were used. Loose convergence criteria were specified for self-consistent field (SCF) convergence for up to 100 geometry iterations. Both "implicit" solvation modeling using only the Poisson-Boltzmann Finite (PBF) elements solution to the Poisson-Boltzmann Equation [31], and "explicit" solvation modeling using PBF in conjunction with solvent molecules explicitly rendered in the input file workspace containing the BCB molecule(s) were utilized in order to predict the ideal conformation of the molecules in a solvent. Implicit solvation data was generated using the values in Table 31.

TABLE XXXI

List of theoretical input parameters used for Poisson-Boltzmann Finite (PBF) elements solvation effects in DFT and TD-DFT calculations for Brilliant Cresyl Blue structures 1 and 2 monomeric and dimeric structures[23]

Solvent	ϵ_0	Molecular Weight (g/mol)	Density (g/cm^3)
Water	80.37[d]	18.02[d]	0.99823[d]
Ethanol	24.85[d]	46.07[d]	0.785[d]
[BMIM]Cl	14	174.67[c]	1.08[b,c]
[BMIM]BF_4	13.9 ± 0.4[a]	226.02[c]	1.21[c]
[EMIM]OAc	12	170.21[c]	1.027[c]

[23] Numerical values obtained from: (a) [32] (b) [22], (c) [33-35] (d) [30]

Implicit solvation utilized the Poisson-Boltzmann Finite (PBF) elements continuum model and specified variables included the static dielectric constant (ϵ_0), the molecular weight of the solvent molecule (g/mol), and the density of the solvent molecule (g/cm^3). The probe radius (Å) was calculated automatically based on these values. Explicit solvation data was generated by specifying the same criteria using PBF as well as constructing a three-dimensional structure of the solvent molecule(s) in the workspace based on a 1:1 molar ratio of their representation with the BCB monomer or dimer structure. Images are provided to illustrate this concept in Figures 65-66 for [EMIM]OAc as well as in Appendix H Figures H1-H8 for the other four solvents studied.

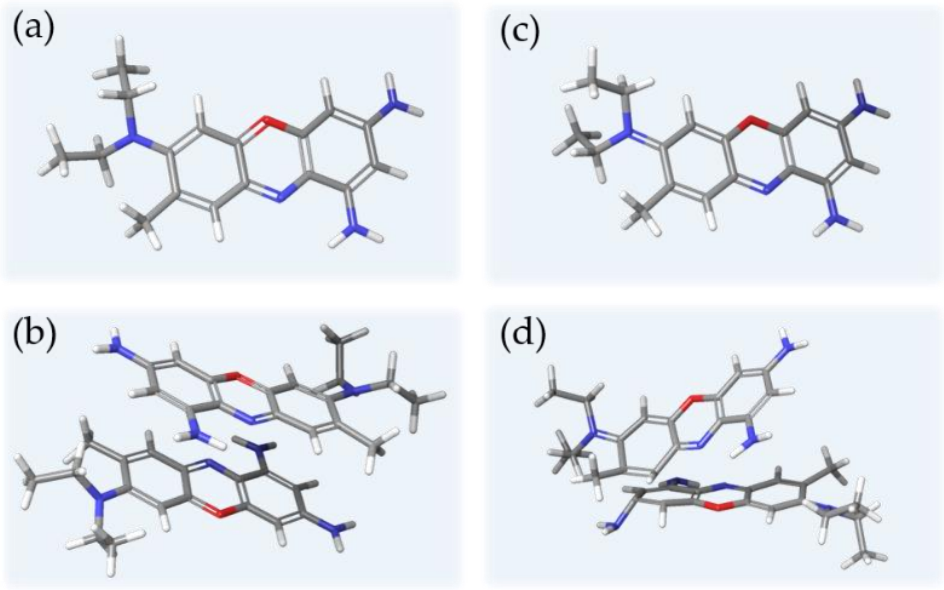

Fig. 65. Geometry conformations based on Poisson-Boltzmann Finite (PBF) elements model of implicit solvation interaction of [EMIM]OAc ionic liquid molecules with (a) BCB BB monomer, (b) BCB BB dimer, (c) BCB C monomer, and (d) BCB C dimer.

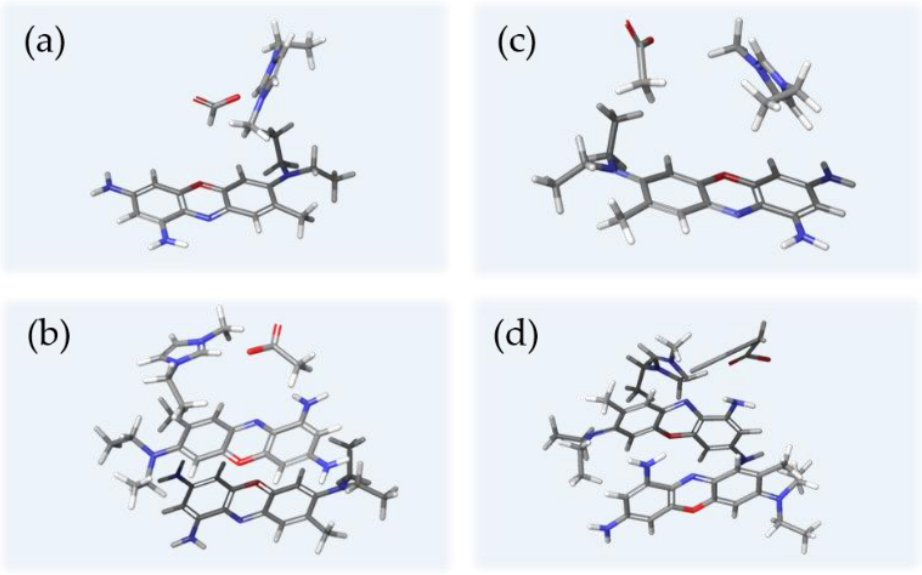

Fig. 66. Geometry conformations based on both Poisson-Boltzmann Finite (PBF) elements model and explicit solvation interaction of one set of [EMIM]OAc ionic liquid molecules with (a) BCB BB monomer, (b) BCB BB dimer, (c) BCB C monomer, and (d) BCB C dimer.

Because ionic liquids exist as binary mixtures of pairs of oppositely-charged ions in solution [21], they were constructed as shown in Figure 67 to accurately portray their structure for more realistic interaction among the color additive molecules simulated.

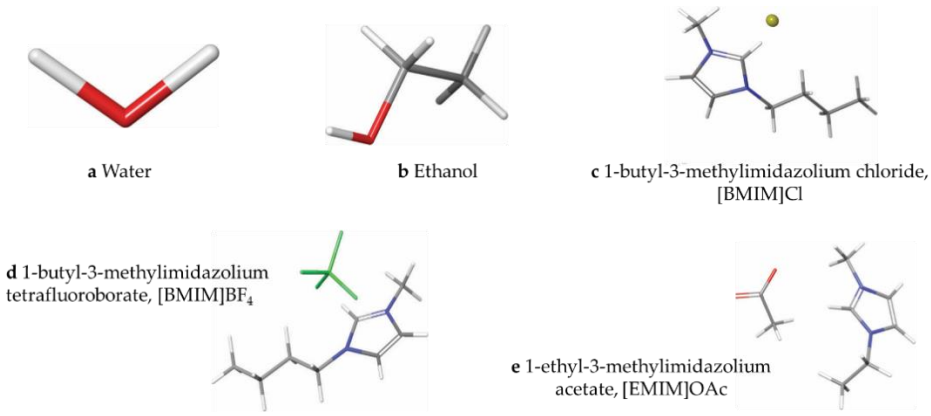

Fig. 67. Structures of solvent molecules analyzed theoretically using computational molecular modeling and quantum mechanics calculations: (a) water, (b) ethanol, (c) 1-butyl-3-methylimidazolium chloride (abbreviated [BMIM]Cl), (d) 1-butyl-3-methylimidazolium tetrafluoroborate (abbreviated [BMIM]BF_4), and (e) 1-ethyl-3-methylimidazolium acetate (abbreviated [EMIM]OAc).

Output files generated from successful geometry optimizations containing monomer and dimer complexes of BCB BB and BCB C structures were then used as input files to calculate three singlet excited states using time-dependent density functional theory (TD-DFT) which were subsequently used to determine theoretical measurements of maximum absorbance spectra within the visible region. Theoretical UV-visible absorbance spectra were generated using the same Gaussian basis set used to obtain optimized geometry conformations of each structure under implicit or explicit solvation conditions: 6-31+G*/B3LYP with effective core potential as needed (incorporated using basis set LAV2P+*/B3LYP). Systems with large anions containing atoms ranging from hydrogen (H) to krypton (Kr) which contain heavier atoms with larger numbers of electrons such that existing diffuse functions are not sufficient [36]. Three singlet excited states were calculated based on the structures explicitly represented in the workspace. The absorbance values generated computationally were incorporated into the mean Gaussian distribution function using Microsoft Excel to calculate the sum of three singlet excited states, yielding the theoretical UV-visible λ_{max} value for comparison to experimental λ_{max} obtained using measured UV-visible absorbance spectra.

Theoretical UV-visible spectra were compared to experimental UV-visible spectra measured from a range of 0.1 mM to 1 x 10^{-6} mM BCB-solvent 1 mL batch preparations to ensure accuracy of theoretical data collected. Photographs of experimental batches have been provided for direct visual comparison to experimental maximum absorbance quantities.

Experimental Data

Visual representation of the BCB-solvent mixture experimental batches clearly indicates that BCB appears its namesake color in four of the five solvents studied: water, ethanol, [BMIM]Cl, and [BMIM]BF_4. However, there is a dramatic shift in maximum absorbance spectra for BCB when added to ionic liquid solvent [EMIM]OAc. Figure 68 below shows 1 mL volumetric flasks containing preparations of the BCB-solvent mixtures used for experimental UV-visible spectroscopic analysis.

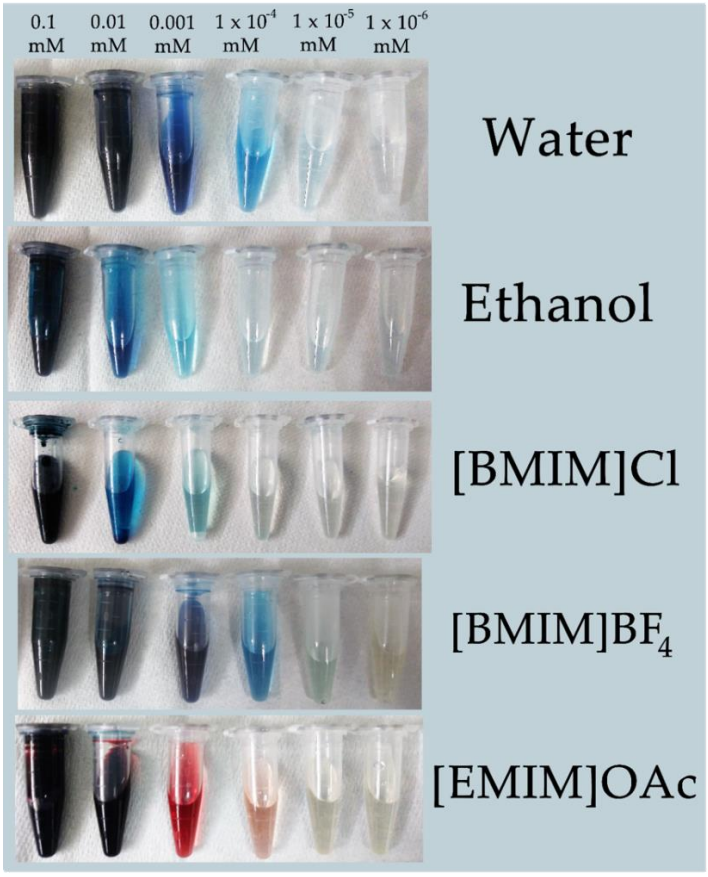

Fig. 68. Variety of hues, chroma, and saturation evident in BCB-solvent experimental batch preparations in both conventional formulation solvents and ionic liquid solvent mixtures

Experimental UV-visible spectroscopic analysis depicts the same trend in color changes as noted in the batches prior to analysis. Among the five solvents, water has the most distinct prominence of a hypsochromically-shifted "shoulder" peak, indicating the presence of the monomer, in addition to the characteristic λ_{max} peak documented in close proximity to other literature sources (see Table 29). For solvent comparison, the prominence of the $\lambda_{shoulder}$ peak decreases in the following order: water, [BMIM]BF_4, [BMIM]Cl, and ethanol solvents. [EMIM]OAc produces hypsochromically-shifted maximum absorbance spectral peak responsivity in experimental analysis that is anomalous to the bathochromically-shifted λ_{max} values of the other solvents analyzed. Theoretical studies will be necessary to assess what factors can be attributed to the noteworthy hypsochromic spectral shift of λ_{max} to reflect a distinct red hue.

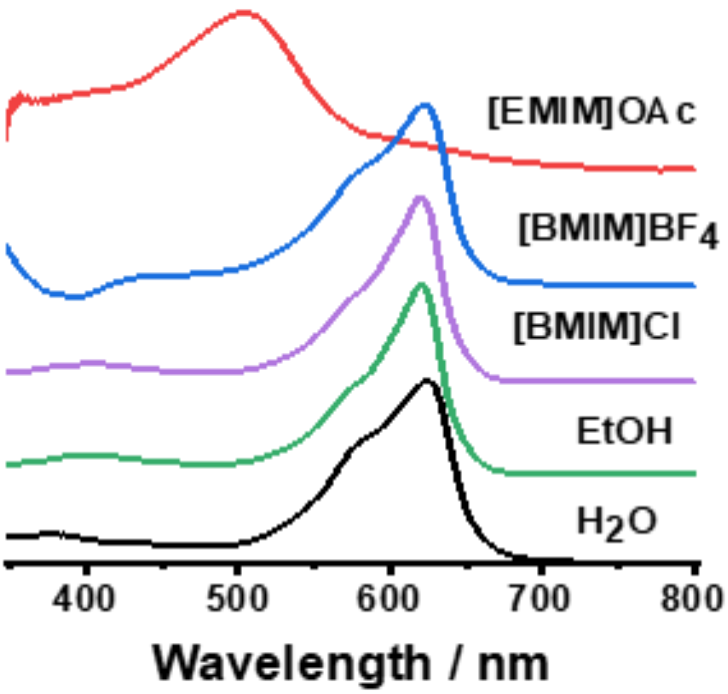

Fig. 69. Comparison of experimental λ_{max} data among all five Brilliant Cresyl Blue-solvent mixture combinations studied.

Theoretical Data

Data collected indicates that the optimal input parameters for accurate theoretical solvation of molecules in a computational workspace can vary based on the type of solvent to be analyzed. In addition, the number of dye molecules also affects the accuracy (and perhaps even precision) of theoretical-experimental λ_{max} comparison. This correlates to the known significance of dye aggregation [3,8,14,15] in which monomer-monomer or dimer complexation occurs in solution as indicated clearly by "double-", "forked", or "shoulder" peaks in experimental spectra as shown in black in Figures 70–79. A shoulder peak indicates the maximum absorbance at the highest intensity for the monomer structure in solution, and is typically found on the left-side of the graph. An isosbestic point appears when dimer complexation begins, and is visually discernable in experimental UV-visible spectra with increasing slope of the graph past the $\lambda_{shoulder}$ peak. The highest peak in all experimental graphs is the λ_{max}, which for this molecule indicates optimal formation of BCB dimer complexes in a balanced molar ratio among solvent molecules. According to Zhang, et al., experimental λ_{max} increases to its highest point when the solution containing BCB reaches equilibrium, which occurs once a 1:1 ratio of BCB dimer complexes to solvent molecules exists [15]. These observations are consistent with our theoretical spectra data. Theoretical BCB BB & C monomer spectra has a left-ward, hypsochromic shift which is comparable to the experimental $\lambda_{shoulder}$ value. BCB BB and C dimer complexation occurs at the isosbestic point shown on each graph (abbreviated "IP") and is comparable to the higher λ_{max} to the right.

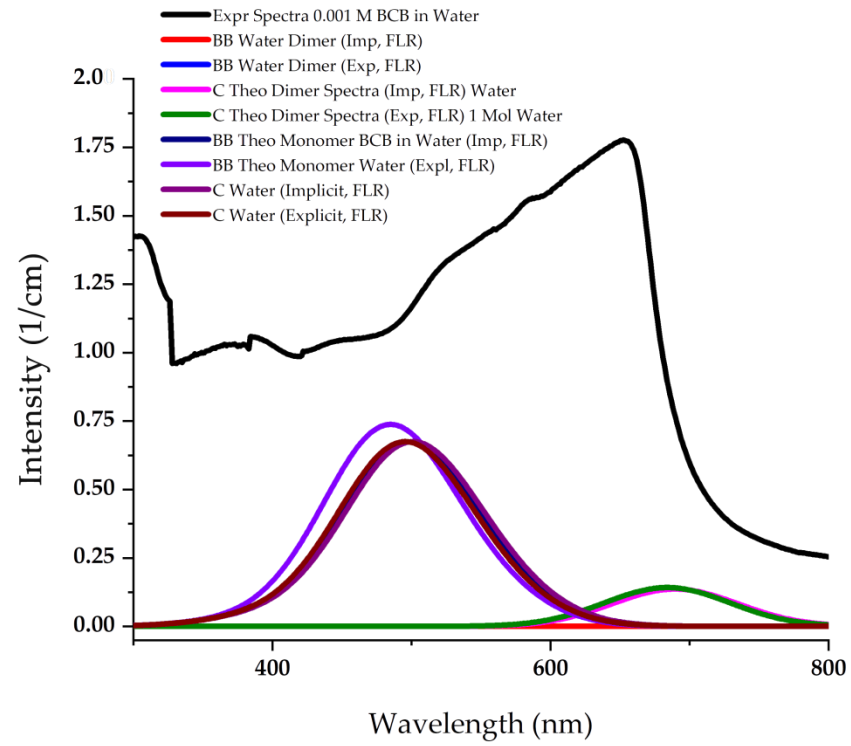

A

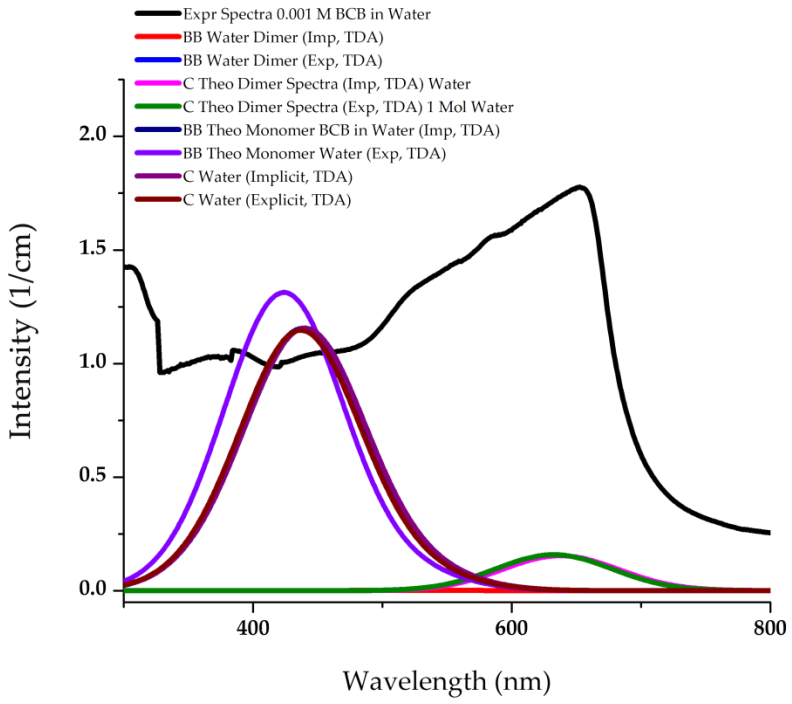

B

Fig. 70. Brilliant Cresyl Blue S1 & S2 in Water Experimental & Theoretical λ_{max} Comparison using TD-DFT with (A) Full-Linear Response (FLR) or (B) the Tamm-Dancoff Approximation (TDA) based on monomer and dimer simulations

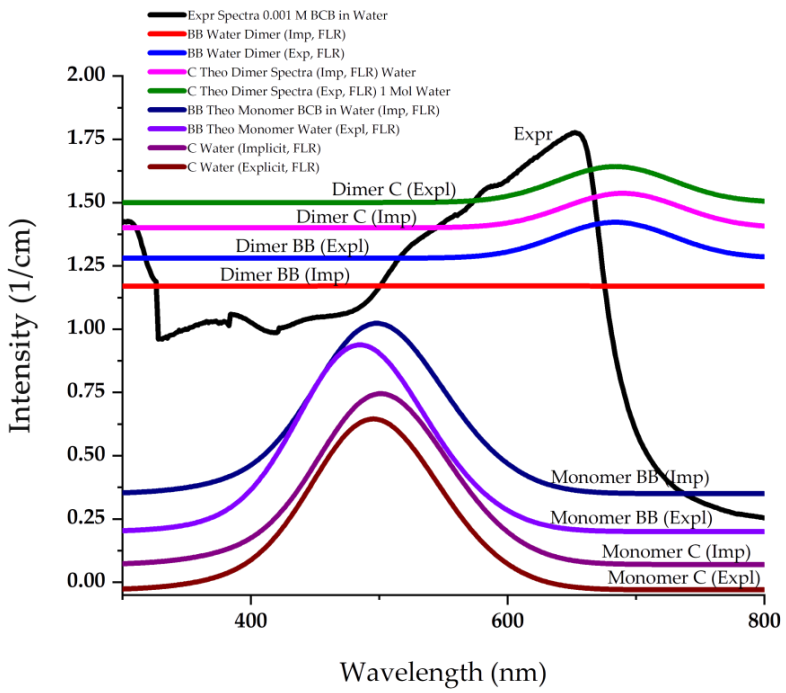

A

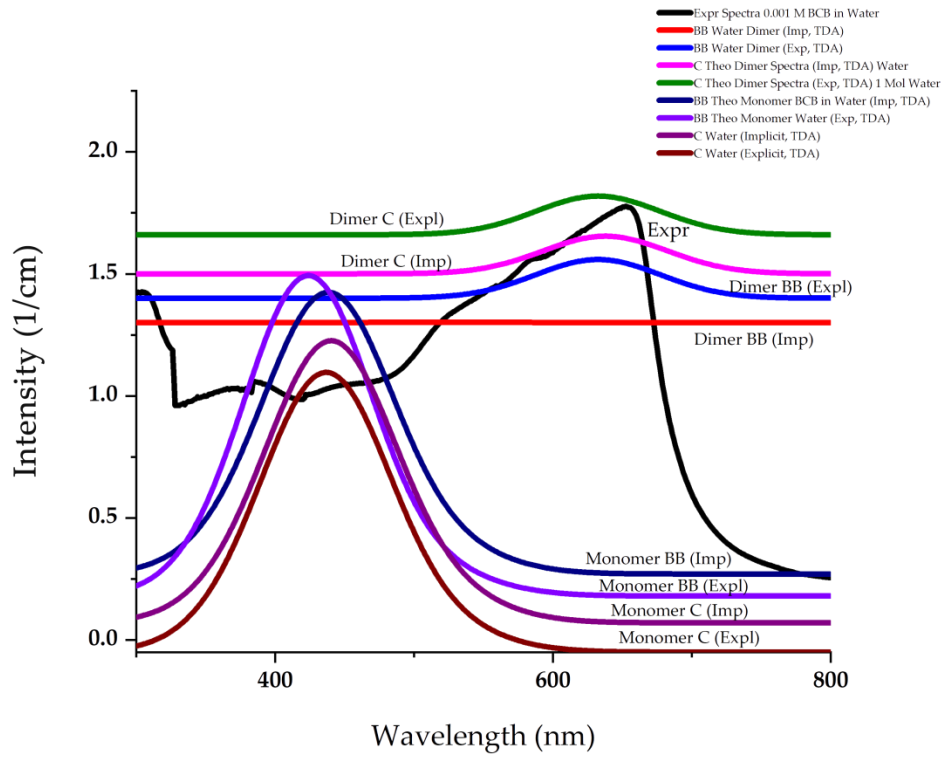

B

Fig. 71. Brilliant Cresyl Blue S1 & S2 in Water Experimental & Theoretical λ_{max} Comparison using TD-DFT with (A) Full-Linear Response (FLR) or (B) the Tamm-Dancoff Approximation (TDA) based on monomer and dimer simulations expanded along the Y-axis for ease of comparison.

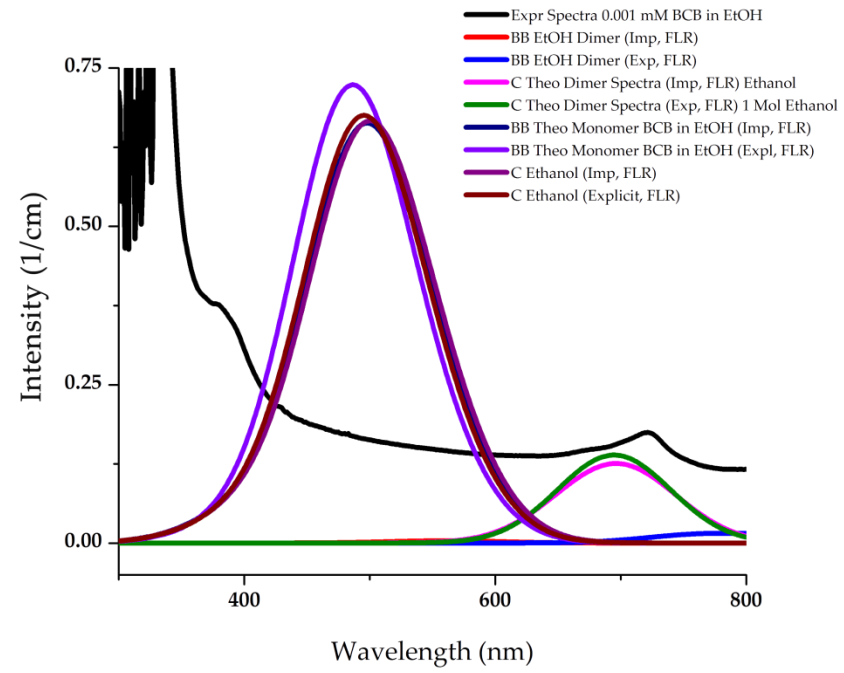

A

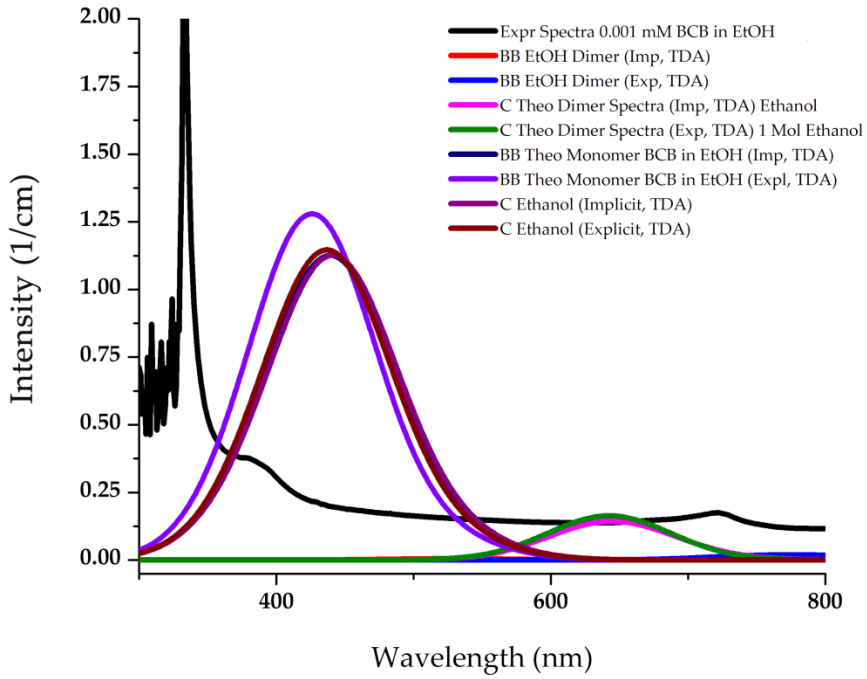

B

Fig. 72. Brilliant Cresyl Blue S1 & S2 in Ethanol Experimental & Theoretical λ_{max} Comparison using TD-DFT with (A) Full-Linear Response (FLR) or (B) the Tamm-Dancoff Approximation (TDA) based on monomer and dimer simulations

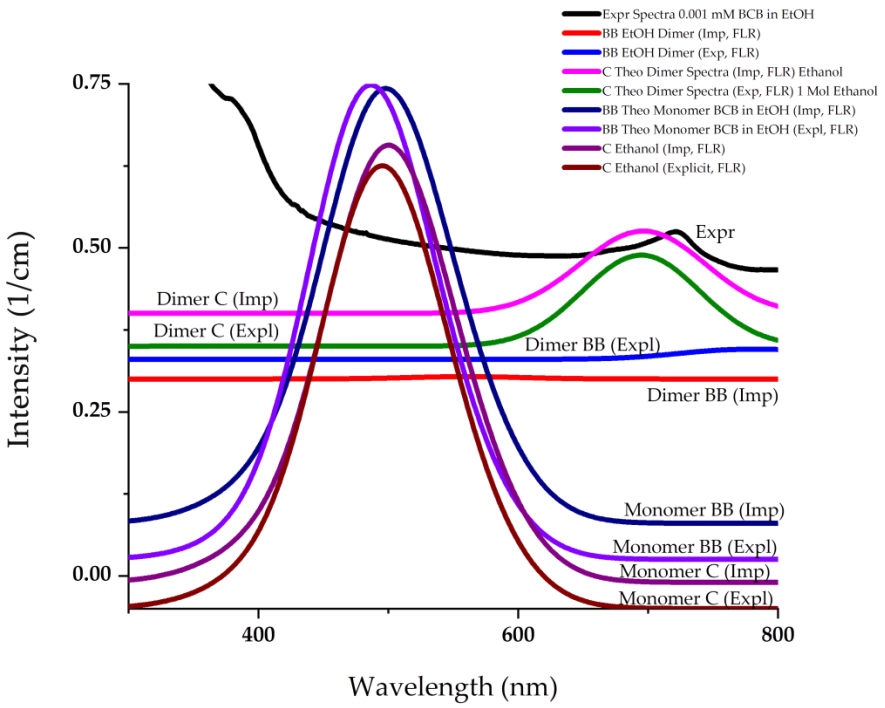

A

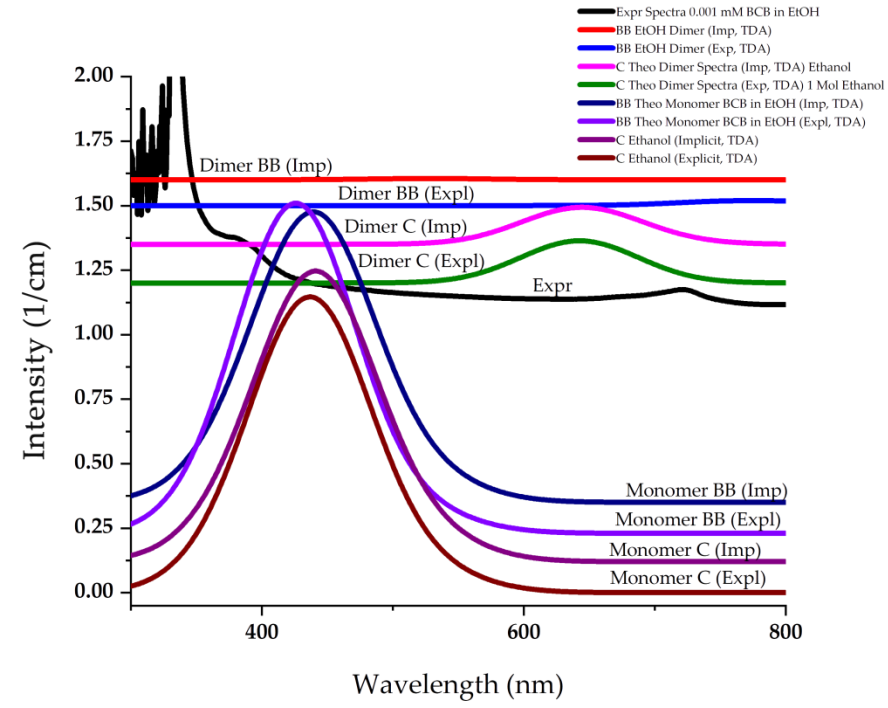

B

Fig. 73. Brilliant Cresyl Blue S1 & S2 in Ethanol Experimental & Theoretical λ_{max} Comparison using TD-DFT with (A) Full-Linear Response (FLR) or (B) the Tamm-Dancoff Approximation (TDA) based on monomer and dimer simulations expanded along the Y-axis for ease of comparison.

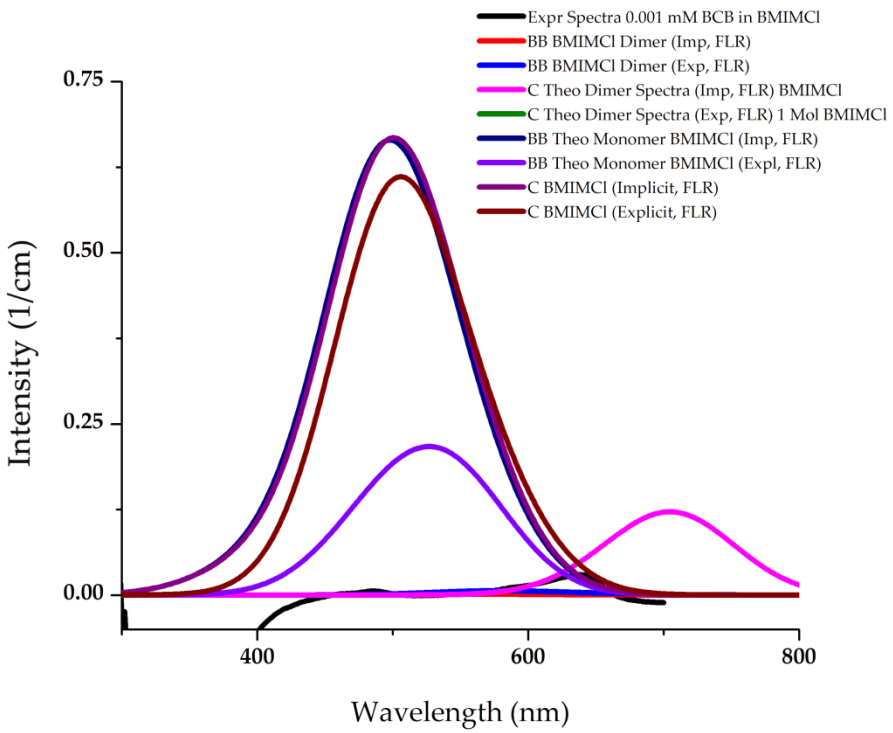

A

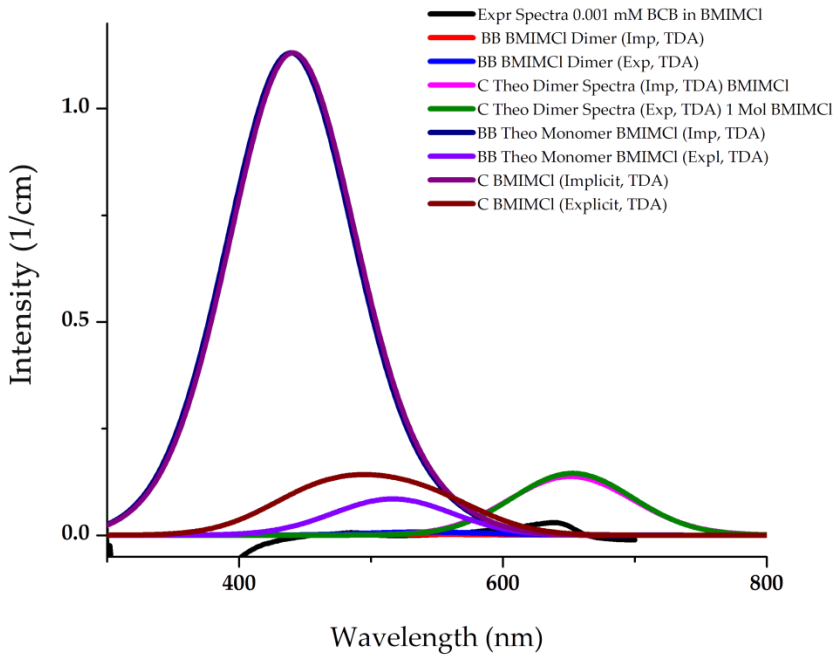

B

Fig. 74. Brilliant Cresyl Blue S1 & S2 in [BMIM]Cl Experimental & Theoretical λ_{max} Comparison using TD-DFT with (A) Full-Linear Response (FLR) or (B) the Tamm-Dancoff Approximation (TDA) based on monomer and dimer simulations

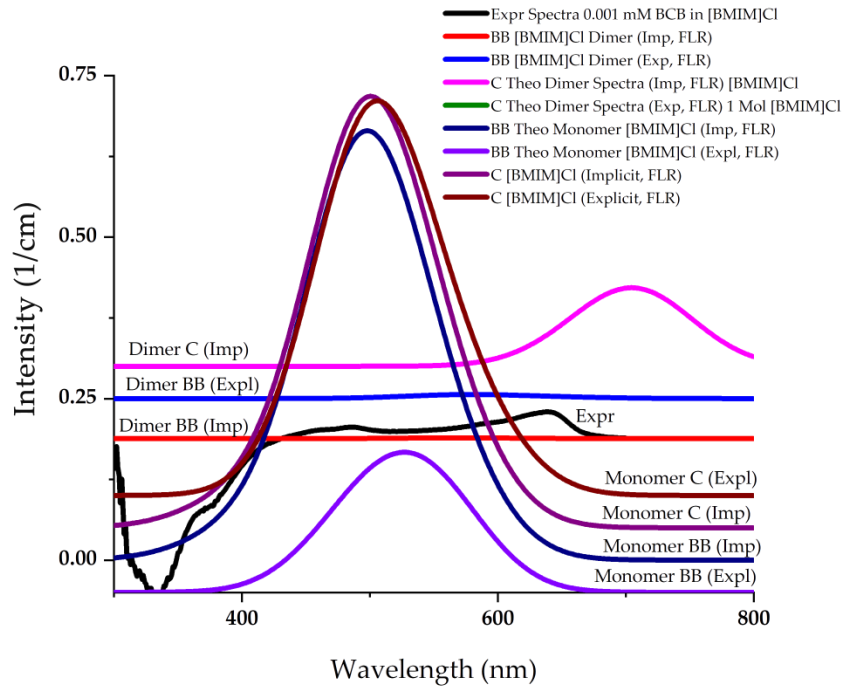

A

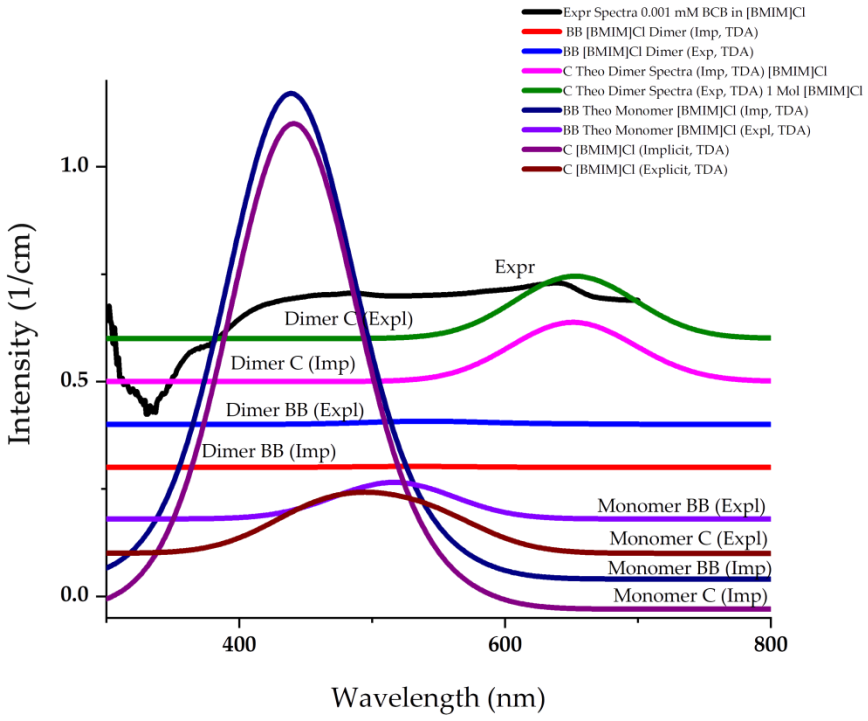

B

Fig. 75. Brilliant Cresyl Blue S1 & S2 in [BMIM]Cl Experimental & Theoretical λ_{max} Comparison using TD-DFT with (A) Full-Linear Response (FLR) or (B) the Tamm-Dancoff Approximation (TDA) based on monomer and dimer simulations expanded along the Y-axis for ease of comparison.

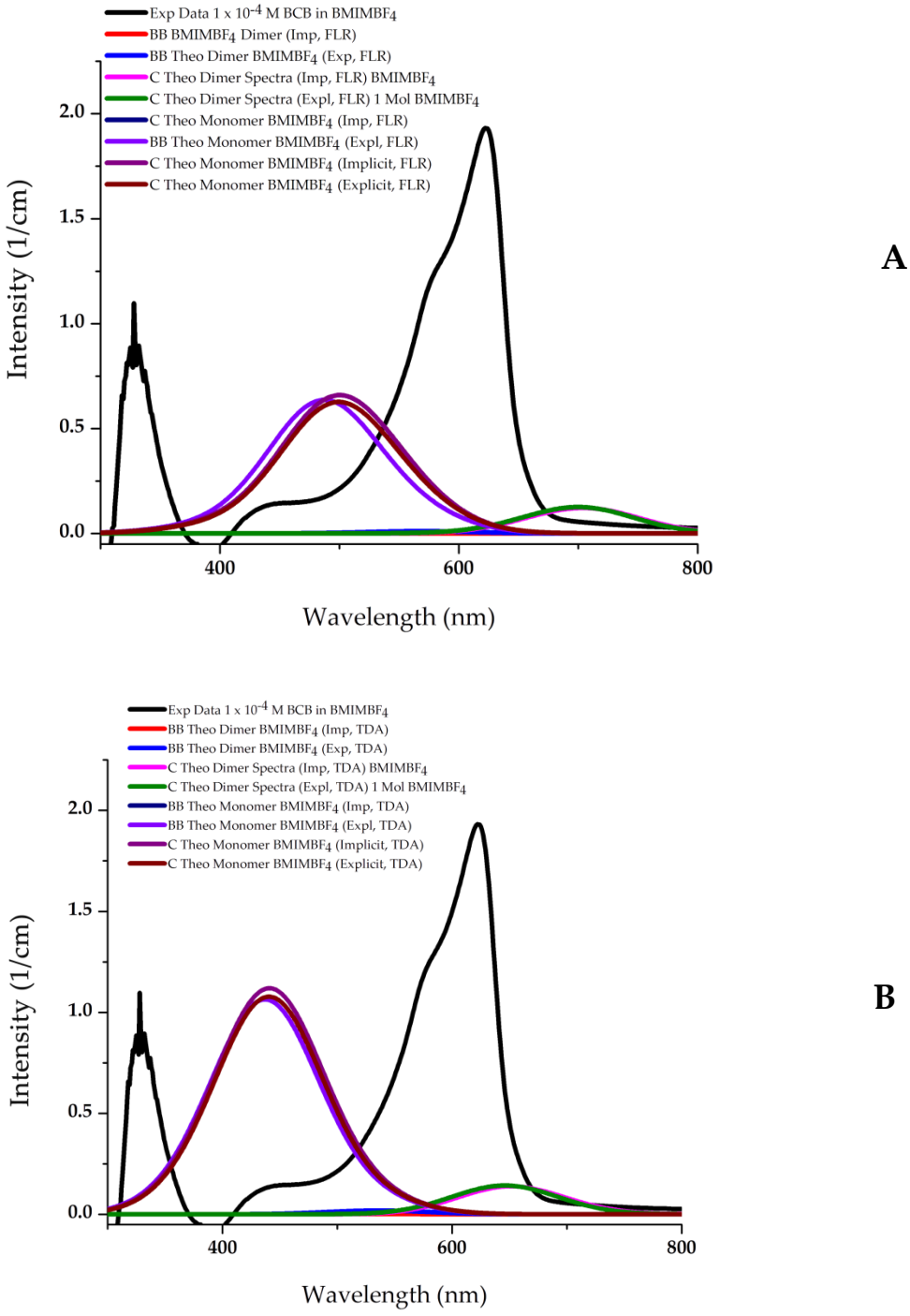

Fig. 76. Brilliant Cresyl Blue S1 & S2 in [BMIM]BF_4 Experimental & Theoretical λ_{max} Comparison using TD-DFT with (A) Full-Linear Response (FLR) or (B) the Tamm-Dancoff Approximation (TDA) based on monomer and dimer simulations.

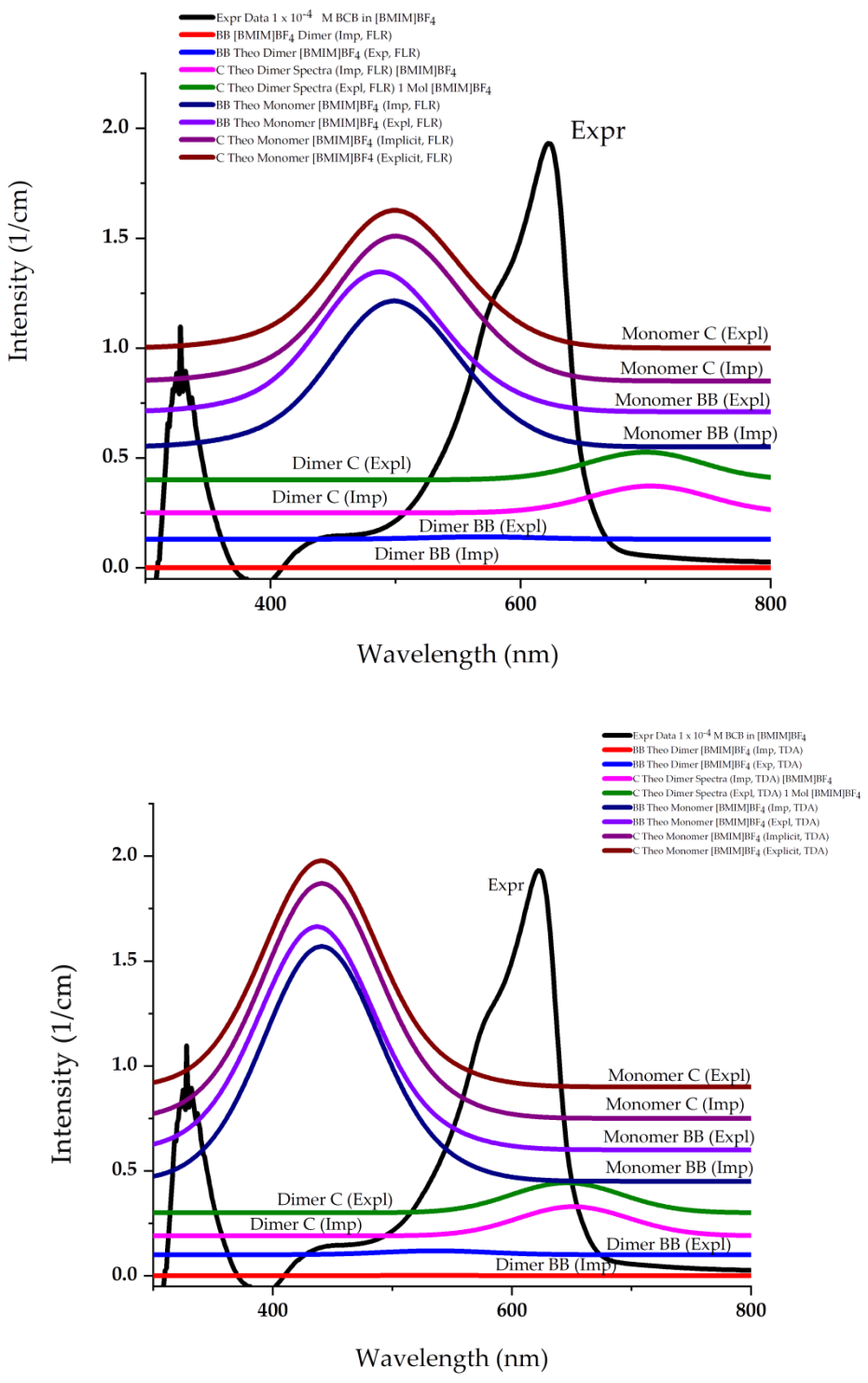

Fig. 77. Brilliant Cresyl Blue S1 & S2 in [BMIM]BF_4 Experimental & Theoretical λ_{max} Comparison using TD-DFT with (A) Full-Linear Response (FLR) or (B) the Tamm-Dancoff Approximation (TDA) based on monomer and dimer simulations expanded along the Y-axis for ease of comparison.

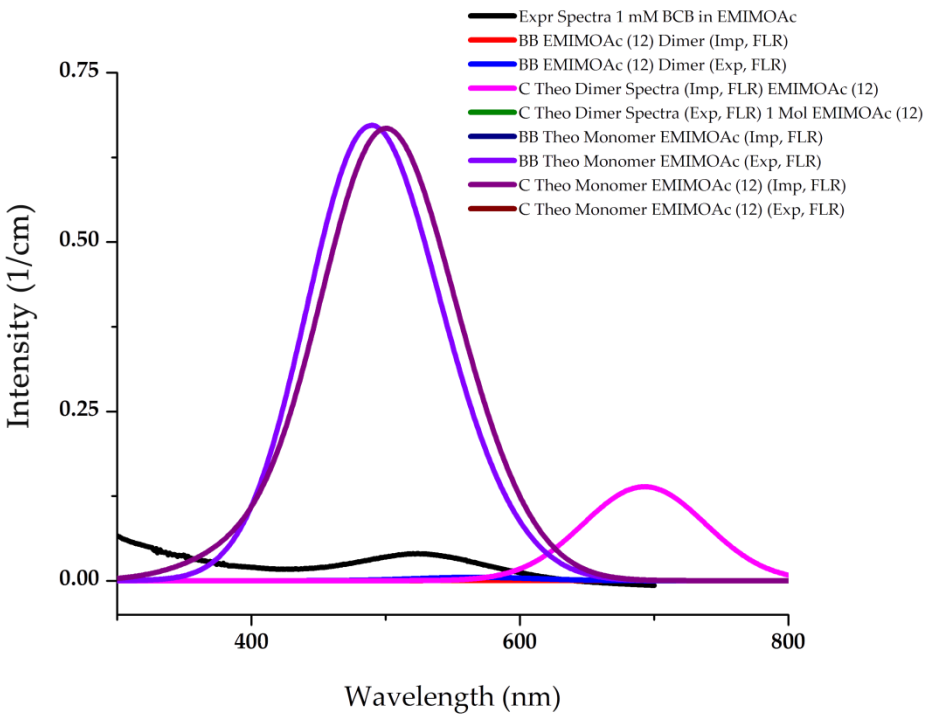

A

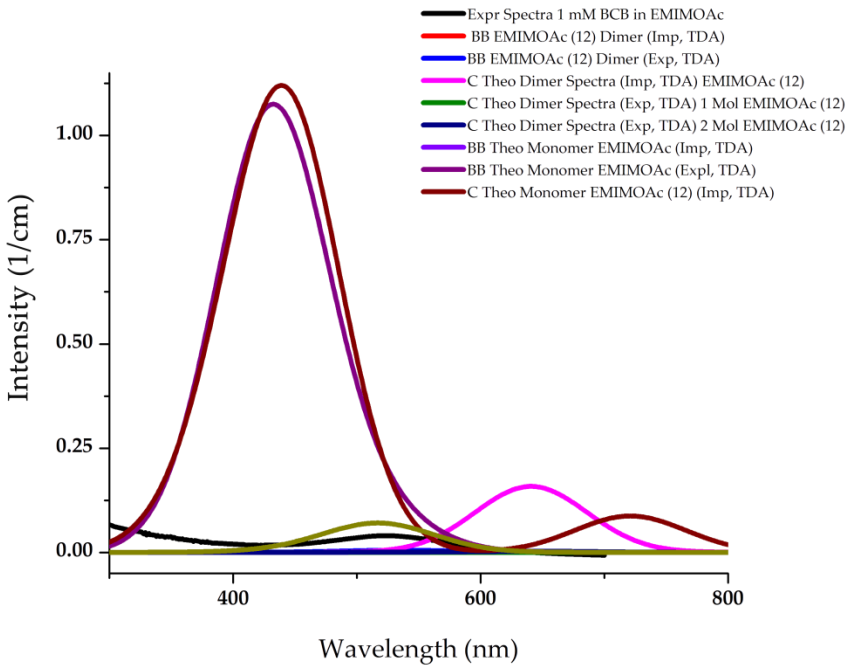

B

Fig. 78. Brilliant Cresyl Blue S1 & S2 in [EMIM]OAc Experimental & Theoretical λ_{max} Comparison using TD-DFT with (A) Full-Linear Response (FLR) or (B) the Tamm-Dancoff Approximation (TDA) based on monomer and dimer simulations.

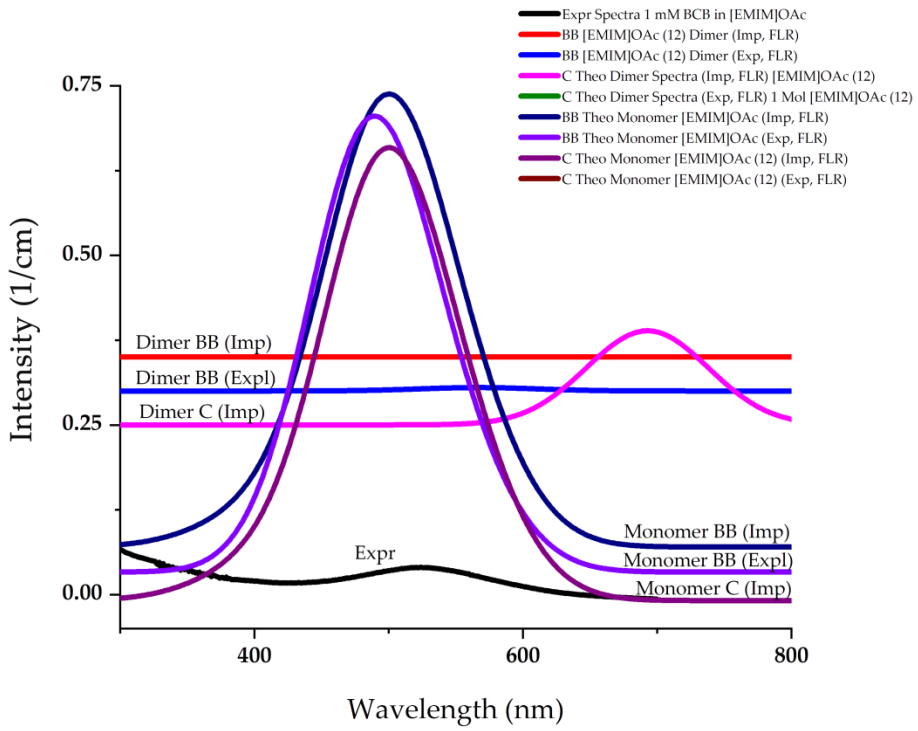

A

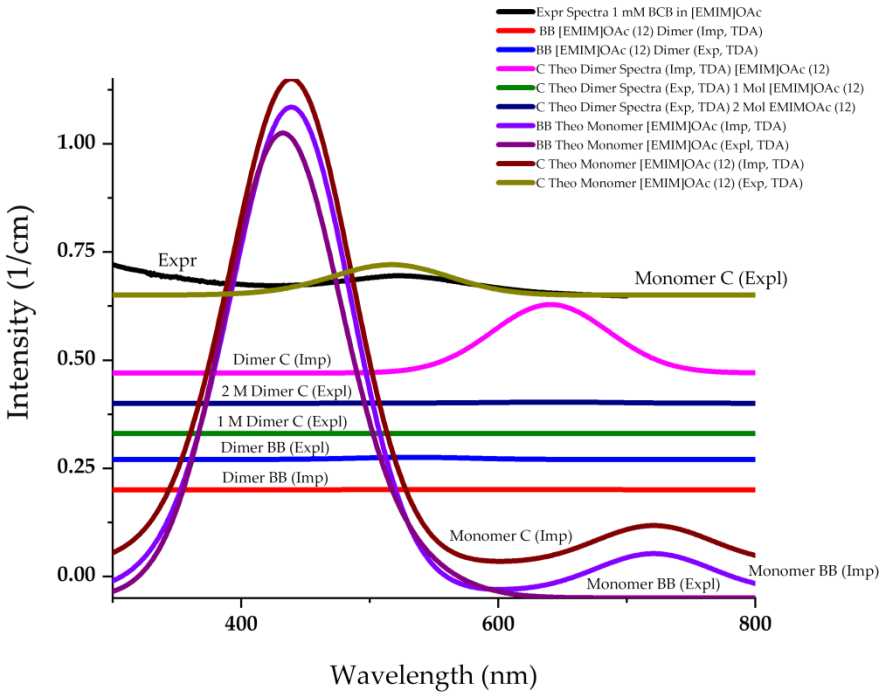

B

Fig. 79. Brilliant Cresyl Blue S1 & S2 in [EMIM]OAc Experimental & Theoretical λ_{max} Comparison using TD-DFT with (A) Full-Linear Response (FLR) or (B) the Tamm-Dancoff Approximation (TDA) based on monomer and dimer simulations expanded along the Y-axis for ease of comparison.

Observation of theoretical λ_{max} spectral shifts indicates that the most useful data for further analysis of theoretical absorbance trends is derived from the BCB dimer. Both BCB BB and BCB C dimers exhibit greater consistency in theoretical spectra peaks for comparison to one another and to the experimental λ_{max} value. The change in maximum absorbance spectra, $\Delta\lambda_{max}$, was determined by subtracting the calculated theoretical value from the measured experimental value for the solvent analyzed, using this equation:

$$\Delta\lambda_{max} = Experimental\ \lambda_{max} - Theoretical\ \lambda_{max}$$

Numerical values for λ_{max} and $\Delta\lambda_{max}$ are listed in Tables 32 and 33 for the BCB BB dimer-solvent mixtures; corresponding λ_{max} and $\Delta\lambda_{max}$ values for the BCB C dimer-solvent mixtures are listed in Tables 34 and 35, respectively. The theoretical and experimental maximum absorbance values provided help shed light on the optimal method of calculation for determining theoretical λ_{max} values for approximation of singlet electronic excitation states using time-dependent density functional theory.

TABLE XXXII

Maximum absorbance spectral peak responsivity (λ_{max}) generated by experimental batch solvation, theoretical implicit solvation using DFT and TD-DFT, and theoretical explicit solvation using DFT and TD-DFT of Brilliant Cresyl Blue BB (S1) dimer-solvent mixtures

	Brilliant Cresyl Blue BB (S1) Dimer Absorbance λ_{max} (nm)				
	Water	EtOH	[BMIM]Cl	[BMIM]BF_4	[EMIM]OAc
Experimental	624.0	620.6	639.8	623.2	523.8
Implicit, FLR	557.9	774.9	569.2	573.2	629.62
Explicit, FLR	683.8	779.0	580.5	568.8	566.5
Implicit, TDA	525.9	527.7	533.5	530.7	560.8
Explicit, TDA (1 Mol)	632.4	562.5	540.5	536.3	534.1

TABLE XXXIII

Change in maximum absorbance spectra ($\Delta\lambda_{max}$) determined by difference between experimental batch solvation λ_{max} minus theoretical TD-DFT of Brilliant Cresyl Blue BB dimer-solvent mixtures λ_{max}.

	Brilliant Cresyl Blue BB (S1) Dimer $\Delta\ \lambda_{max}$ (nm)				
	Water	EtOH	[BMIM]Cl	[BMIM]BF_4	[EMIM]OAc
Experimental	624.0	620.6	639.8	623.2	523.8
Implicit, FLR	+66.1	-154.3	+70.6	+50.0	-105.8
Explicit, FLR	-59.8	-158.4	+59.3	+54.4	-42.7
Implicit, TDA	+98.1	+92.9	+106.3	+92.5	-37.0
Explicit, TDA (1 Mol)	-8.4	+58.1	+99.3	+95.9	-10.3

Note: Plus sign indicates (leftward) hypsochromic shift, minus sign indicates (rightward) bathochromic shift of λ_{max} in TD-DFT calculations

TABLE XXXIV

Maximum absorbance spectra (λ_{max}) generated by experimental batch solvation, theoretical implicit solvation, and theoretical explicit solvation of Brilliant Cresyl Blue C dimer-solvent mixtures

Brilliant Cresyl Blue C (S2) Dimer Absorbance λ_{max} (nm)					
	Water	EtOH	[BMIM]Cl	[BMIM]BF_4	[EMIM]OAc
Experimental	624.0	620.6	639.8	623.2	523.8
Implicit, FLR	691.7	695.8	704.69	704.5	692.6
Explicit, FLR (1 Molecule)	684.3	694.1	X	700.6	X
Implicit, TDA	637.6	644.4	652.2	652.0	640.9
Explicit, TDA (1 Mol)	632.6	643.7	652.7	644.4	773.9; 666.5

TABLE XXXV

Change in maximum absorbance spectra ($\Delta\lambda_{max}$) determined by difference between experimental batch solvation λ_{max} minus theoretical TD-DFT solvation λ_{max} of Brilliant Cresyl Blue C dimer-solvent mixtures

Brilliant Cresyl Blue C (S2) Dimer $\Delta\lambda_{max}$ (nm)					
	Water	EtOH	[BMIM]Cl	[BMIM]BF_4	[EMIM]OAc
Experimental	624.0	620.6	639.8	623.2	523.8
Implicit, FLR	-67.7	-75.2	-64.9	-81.3	-168.8
Explicit, FLR	-60.3	-73.5	X	-77.4	X
Implicit, TDA	-13.6	-23.8	-12.4	-28.8	-117.1
Explicit, TDA	-12.6	-23.1	-12.9	-21.2	-142.7

Note: Plus sign indicates (leftward) hypsochromic shift, minus sign indicates (rightward) bathochromic shift of λ_{max} in theoretical calculations

It is important to note that in all spectra provided, no intensity values are given. It is well known throughout the literature [37] that time-dependent density functional theory calculations may be useful for predicting maximum absorbance spectra; however, the intensity based on oscillator strengths (*f*) generated by theoretical calculations should not be considered comparable to experimental maximum absorbance spectral measurements. However, according to Hirata and Head-Gordon, TDA has been proven to be effective for molecules containing an unstable triplet excited state that is corrected using a simplified TD-DFT correction [38]. Therefore, the BCB molecules studied may exhibit the aforementioned unstable triplet excited state, which would be a plausible explanation as to why TDA was very successful for generating accurate data for theoretical and experimental maximum absorbance spectral peak responsivity comparisons. If this were to be explored further, both singlet and triplet states would have to be calculated using the theoretical input parameters and solvation conditions mentioned, and fluorescence spectra would have to be measured for comparison. In the case of the BCB molecule, it exhibits such high saturation—even at low concentrations—that collecting useful experimental fluorescence spectra was prohibitive. For this reason, this body of work has focused strongly on experimental and theoretical maximum absorbance spectral peak responsivity and associated shoulder peaks only.

Discussion

Most theoretical data shows improved correlation with experimental data when explicit modeling of BCB dye-solvent molecules in the workspace is used, as opposed to implicit modeling. The dye and solvent molecules produce theoretical λ_{max} values with smaller differences compared to that of λ_{max} measured from experimental batches of the corresponding solutions. This is likely because the molecules are modeled as they would appear in solution—in 1:1 molar ratios of dye molecule or complex to solvent. Based on the data presented, dimer complexation is preferable for computational analysis. Therefore, two molecules of BCB should be added to the workspace in the orientation as described by Antonov and coworkers [17]. However, TD-DFT theoretical spectra trends differ for each solvent analyzed based on the nature of the solvent molecules included within the chemical system.

Brilliant Cresyl Blue in Water. Water is the most common solvent for analysis of the BCB dye molecule [2,15] and is the most common formulation solvent used globally [39-41]. For this reason, it is not surprising that the CT dye appears its characteristic blue color in distilled water. With an experimental absorbance of 624.0 nm, the BCB-water mixture falls within the range of absorbance values that absorb reddish-orange wavelengths of light and thus reflect blue light. Theoretical data for the BCB BB dimer solvated using implicit solvation (PBF only) gives a hypsochromic shift of at least 66.1 nm compared to the experimental λ_{max}. Explicit solvation modeling (PBF with solvent molecules in the workspace) gives a bathochromic shift using both full-linear response theory (FLR) and the Tamm-Dancoff Approximation (TDA). Furthermore, Explicit FLR gives a bathochromic shift of approximately the same magnitude as Implicit

FLR. Explicit TDA gives a bathochromic shift of only 8.4 nm. For water solvent, explicit solvation modeling using TDA is the most favorable method of theoretical solvation because the overall charge of all the molecules represented in the system is +1. Similarly, using the BCB C dimer in simulations involving water solvent, both implicit and explicit solvation conditions exhibit a bathochromic shift in all theoretical spectra. The smallest change in maximum absorbance is shown using explicit solvation using TDA, although this change in maximum absorbance differs by only -0.2 nm. According to Wang and coworkers [42], there are two electronic states that affect the relative energies calculated as part of the linear response of the ground state: $1L_a$ and $1L_b$. Full TD-DFT (FLR) relies on the linear response of the ground state, and underestimates the energies of the $1L_a$ state relative to the $1L_b$ state. On the other hand, TD-DFT using TDA neglects the B matrix, decoupling the ionic excited states from the description of the covalent ground state to some extent [42]. This leads to improved calculated results for the $1L_a$ state. The ionic character of the $1L_a$ state is a special case of charge transfer [37,42], in which an ionic state should be composed of some pairs of charge transfer states from the charge donor and the charge acceptor. This difference is represented in contemporary quantum chemical computational software as the difference in eigenvalues A-B. Therefore, in molecular systems in which an overall electronic charged (or "ionic") state dominates an otherwise ground, "covalent" state, the Tamm-Dancoff approximation must be used because the difference in eigenvalues determined by TD-DFT is too large for FLR to be applicable. As a result, BCB-water mixture data is best simulated using the BCB C dimer under explicit solvation conditions using the Tamm-Dancoff Approximation.

Brilliant Cresyl Blue in Ethanol. Ethanol was selected because of its ubiquitous prevalence as a popular formulation solvent [43-45]. The experimental maximum absorbance value of BCB in ethanol solvent, 620.6 nm, differs from that of water by only -3.6 nm. Theoretical λ_{max} data show that both implicit and explicit FLR calculations yield strong bathochromic shifts of over 150 nm. Implicit and explicit TDA calculations yield smaller hypsochromic shifts; however, these are much higher for the BB dimer than for the C dimer structure. Theoretical data for the BCB C dimer in ethanol solvent indicates that implicit and explicit FLR yield significant bathochromic shifts in λ_{max} of -75.2 and -73.5 nm, respectively. Once again, TDA yields comparatively smaller change in λ_{max} compared to experimental values for both implicit and explicit solvation conditions, with explicit solvation using TDA yielding the smallest change in λ_{max}. The small difference of -0.7 nm between Implicit and explicit TDA values is worth noting as an indication that either solvation method is applicable for calculating useful theoretical maximum absorbance values. The overall charge of the dimer system is +2 (because of a +1 charge for each BCB monomer) so the electronic charged, ionic state supercedes the ground, covalent state in this molecular system. Therefore, the difference in eigenvalues favors use of the Tamm-Dancoff Approximation. In particular, the explicit solvation method is the most favorable for computational analysis of the BCB C dimer given the smallest change in λ_{max}.

Brilliant Cresyl Blue in Ionic Liquids. Ionic liquids have been a hot topic in academic research due to their versatility as recyclable, “green” solvents that can be customized to attain specific physicochemical properties based on the cation/anion combination included in the binary mixture [21-22,25-30,32,46-100]. In recent years,

industrial applications of ionic liquids have increased significantly as it is possible to "tune" or tailor their properties for desired thermal stability [27-28,101-102], viscosity [22,27,65,103], and even density [21,22,27,54,64,84]. Therefore, exploration of the ability of ionic liquids to affect the experimental maximum absorbance value of charge transfer dye molecules in solution contributes to the variety of physical properties that are tunable using these "designer" solvents. Two of the ionic liquids selected have the same cation: 1-butyl-3-methylimidazolium $[BMIM]^+$, and one differs by incorporating the 1-ethyl-3-imidazolium cation $[EMIM]^+$. All three ionic liquid solvents have different anions: a halide (chloride) anion $[Cl]^-$, a tetrafluoroborate anion $[BF_4]^-$, and an acetate anion $[OAc]^-$. Experimental and theoretical data show there are clear differences in the λ_{max} measured for each ionic liquid based on its constituent ion coupling.

***BCB in 1-butyl-3-methylimidazolium chloride*.** [BMIM]Cl was analyzed in order to compare the effect of cation/anion interactions on charge transfer dye molecule BCB. The BCB-[BMIM]Cl mixture has an experimental λ_{max} value of 639.8 nm, which exhibits a -15.8 nm bathochromic shift compared to the BCB-water solvent mixture. Under theoretical solvation conditions, the BCB BB dimer structure shows large hypsochromic shifts in its change in λ_{max} with the largest leftward shift occurring for implicit solvation using FLR (+70.6 nm), followed closely by explicit solvation using FLR (+59.3 nm). Implicit and explicit solvation using TDA exhibit even larger hypsochromic shifts in change in λ_{max} than FLR of approximately +100 nm. The BCB C dimer, on the other hand, yields theoretical data that continues to exemplify the trend followed by common formulation solvents water and ethanol: TDA provides the smallest changes in λ_{max} with comparison to experimental data. Both implicit and explicit solvation conditions using

TDA have the smallest change in λ_{max} of ~12 nm, and the difference between the two values is only 0.5 nm. It is also interesting to note that the software utilized prevented successful calculation of singlet excited states for the BCB C dimer-[BMIM]Cl structure under explicit solvation conditions using FLR by issuing an error message that blatantly read "Please use TDA" due to the large difference in eigenvalues calculated. Furthermore, unlike the BCB BB dimer data for this molecule that exhibits hypsochromic shifts for theoretical absorbance spectra measured under all four conditions, all BCB C dimer theoretical λ_{max} values exhibit bathochromic shifts readily comparable to measured experimental λ_{max} of the BCB-[BMIM]Cl mixture.

BCB in 1-butyl-3-methylimidazolium tetrafluoroborate. [BMIM]BF_4 is another popular ionic liquid solvent selected for analysis. The BCB-[BMIM]BF_4 mixture has an experimental λ_{max} that is very similar to that of water. Upon initial observation of FLR to TDA, all theoretical mixtures of BCB-[BMIM]BF_4 exhibit hypsochromic (blue) shifts when TDA is used in TD-DFT. Implicit and explicit FLR changes in λ_{max} (+50.0 nm and +54.4 nm) are approximately half the magnitude of those measured for implicit and explicit solvation using TDA (+92.5 nm and +95.9 nm, respectively). All theoretical mixtures containing BCB C dimer under [BMIM]BF_4 solvation conditions exhibit changes in λ_{max} that indicate bathochromic shifts compared to BCB BB data. Furthermore, the BCB C dimer-[BMIM]BF_4 mixtures follow our overarching trend of TDA providing bathochromically-shifted λ_{max} theoretical values in closer proximity to experimental λ_{max} than FLR values. Implicit and explicit FLR theoretical absorbance spectral changes in λ_{max} exhibit bathochromic shifts of approximately -80 nm, while implicit and explicit solvation using TDA changes in λ_{max} feature bathochromic shifts of

less than 30 nm. Implicit solvation using TDA has a larger bathochromic shift than explicit solvation using TDA (-28.8 nm and -21.2 nm, respectively). Explicit solvation modeling using TDA continues to provide favorable computational results for the theoretical λ_{max} calculated by TD-DFT calculated for the BCB C dimer-[BMIM]BF_4 molecular system. These methods can nearly perfectly simulate experimental absorbance spectral data as shown in Figure 76, or expanded along the Y-axis in Figure 77 for simplified visual comparison.

BCB in 1-ethyl-3-methylimidazolium acetate. A third ionic liquid, [EMIM]OAc was selected for analysis in order to assess cation/anion interactions with less bulky functional groups. The most intriguing aspect of the BCB-[EMIM]OAc mixture is its distinct red hue, which is reflected in its experimental λ_{max} value of 523.8 nm. Furthermore, with regard to theoretical absorbance spectra, this BCB dimer-solvent system defies the trend of favoring the BCB C dimer structure in the computational workspace to approximate its theoretical maximum absorbance. While implicit and explicit solvation with FLR show large bathochromic shifts, the explicit solvation using FLR is 63.1 nm smaller than that of implicit solvation using FLR. TDA shows bathochromic shifts in theoretical spectra that are even smaller. Implicit solvation using TDA exhibits a change in λ_{max} of -37.0 nm, and explicit solvation using TDA calculates a λ_{max} value of only -10.3 nm compared to experimental λmax measured. Using the BCB C dimer—[EMIM]OAc theoretical mixture in computational studies, only bathochromic shifts are evident, which would reflect a blue color. Implicit solvation using FLR exhibits a -168.8 nm shift compared to experimental spectra, which is less useful compared to other solvation input parameters and DFT theories assessed. Theoretical maximum

absorbance spectra calculation was prohibited for explicit solvation using FLR conditions because of a computational software error message shedding light on the heart of the issue: more accurate theoretical absorbance spectra is calculated for direct comparison to experimental data when TDA is used for calculating low-lying electronic excited states for charged polycyclic molecules such as BCB.

BCB Isomer Comparison and Stability in Dye-Solvent Mixtures. A striking observation among all five solvents is that the BCB C dimer structure used in simulation presents the most accurate comparison to experimental data in all cases—except for [EMIM]OAc, where we see a distinct red hue. Experimental spectra indicate that there is indeed a leftward, hypsochromic shift in λ_{max} absorbance occurs to absorb blue so that an intense red is reflected, and our theoretical data provides insight into why this occurs. While implicit and explicit solvation using TDA for the BCB C dimer-[EMIM]OAc mixture provided theoretical spectra with smaller changes in λ_{max}, these were still much larger in comparison to those calculated using implicit and explicit solvation with TDA for the BCB BB and C monomers in [EMIM]OAc. Therefore, it is likely that the alternating BCB monomer structures, rather than their homodimers, interact with the [EMIM]OAc ions in solution to promote the dramatic color change shown in the experimental batches. Simulations of both monomer-IL and dimer-IL geometry conformations and electronic excitations reveal that more accurate λ_{max} spectra is given by BCB C monomer under explicit solvation conditions using TDA.

Kinetic vs. Thermodynamic Product Impact on Batch Hue. The hue of the Brilliant Cresyl Blue mixtures varies among the solvents analyzed due to their characteristic interactions imparted on the alternating metastable states of this charge transfer dye molecule. BCB C is the more stable, "thermodynamic" structure among the two alternating structures, as discussed previously [20]. In this theoretical comparison, this is still an accurate statement because color changes occur as a result of inhibition (or enabling) of dye aggregation via dimer complexation among the BCB metastable states. This phenomenon can be controlled by solvents containing distinct polarization effects or charged ions which compete for interaction with the charged portions of the dye molecule. While BCB BB can be prevalent in vapor phase as discussed in the prior chapter, this metastable state of the charge transfer dye is considered the "kinetic" product that must be stabilized by anions of high electron density in wall-less conditions or with large quantities of oxygen atoms that compete for interaction with the charged oxygen atom in the structure [105]. In this case, symmetry-forbidden transitions would occur that would otherwise be of lower probability in closed systems [105]. In this analysis, the five solvents were studied in closed systems, therefore the thermodynamic product dominates each mixture because of increased solvent particle collisions and the noncovalent polarization effects that stabilize the BCB C structure. Whether the BCB C monomer or dimer is most prevalent will be discussed further in terms of solvent effects that vary based on the combination of solvent molecules or one of their ions.

In four out of the five solvents studied, it is evident that both experimental and theoretical studies prove that water, ethanol, [BMIM]Cl and [BMIM]BF_4 most likely interact with the BCB C dimer structure when mixed in solution. The positively-charged

sp^2-hybridized nitrogen exhibited in BCB C is more stable than the positively-charged sp^2-hybridized oxygen shown in BCB BB. With regard to solvent molecules, water and ethanol are both neutral solvents, yet impart a strong dipolar nature that serves to stabilize the charged nitrogen atom. Furthermore, both water and ethanol are small enough to not strongly effect the process of BCB dimer self-association. For this reason, BCB appears its namesake hue in these two common formulation solvents as shown in previous literature and using the computational data presented herein. However, the minor (leftward) hypsochromic shift of λ_{max} spectra in ethanol compared to the shift observed in water may arise from the slightly bulkier ethyl group of the alcohol solvent. Ethanol atoms have greater steric hindrance due to their larger alkyl chain, which may induce more dye-solvent interactions in solution that prevent ideal BCB dimer complexation. Nonetheless, the blue color is still maintained in both solvents, albeit with a slight variation between them.

Origin of Color Variation in Ionic Liquid Solvents. The greatest color variation in the experimental trials performed arises from the use of ionic liquid solvents. Ionic liquid properties are critically dependent on cation and anion selection [21,27,106,107]. Ionic liquids present a challenge for theoretical simulation but a pleasantly vast experimental solvatochromic effect as indicated in these studies and in other works [15,16,23,106,107]. The interplay of ions in the mixture with the BCB molecule can certainly affect the overall hue of the mixture. The diverse effects that each charged particle in the binary mixture has on the charged BCB dimer can be explained by analyzing a few significant differences in interactions among the cations and anions studied.

Solvent Molecule Alkyl Chain Length. First, the shorter alkyl chain length on the $[EMIM]^+$ imidazolium ring may enable more flexible rotational movement [21,24,55,71], and thus decreasing steric hindrance of the $[EMIM]^+$ cation. The bulkier cation $[BMIM]^+$ yields steric hindrance due to its longer alkyl chain, thus increasing the unfavorable effect of unusual cation/anion molecular geometry on the solvatochromic properties of this charge transfer dye molecule in IL solvent. Studies have shown that longer alkyl chain lengths that increase branching on the imidazolium ring will increase viscosity [21,64], thermostability [28,64], and glass transition temperature [64] in addition to other physicochemical properties [71,77] of an ionic liquid [27]. Other literature has cited that more symmetrical, smaller cations can more strongly affect these properties compared to larger, asymmetrical cations [64,71]. It is likely that the size of the cation may have a role in inhibiting or delaying BCB dimer complexation interactions such that color spectra is affected. Using the experimental λ_{max} value of water as a comparison, this study indicates that hypsochromic shifts were evident for ionic liquid molecules containing an ethyl group (such as $[EMIM]^+$), and that bathochromic shifts were evident when larger alkyl chains are featured on the cation, as was the case with both ionic liquid solvents that contained the $[BMIM]^+$ cation. Further studies using additional cationic species of varied alkyl chain lengths would have to be carried out in order to verify if this pattern exists for other ionic liquid combinations.

Solvent Ion Size. Second, the anion may play a larger role in shifting color spectra than the cation. In other studies measuring physicochemical properties [64,71,81], the anion has been proven to influence ionic liquid solvent properties more than the cation. Kobrak and Sandalow discussed that the size and molecular weight of the anion

has a strong role in IL interactions with solute molecules with relevance to conductivity studies [71]. A comparison of molecular weights of anions as pertaining to this work is as follows: the $[BF_4]^-$ anion has higher molecular weight (86.8 g/mol) than both the halide anion (35.5 g/mol) and the acetate anion (59.0 g/mol). $[BF_4]^-$ can attain high conductivity for a relatively small molecular weight compared to longer-chain anions found in other ionic liquid moieties [71]; however, in this study, its bulkiness and atypical, spiked structure prevents adequate anion mobility for interaction with the planar BCB dye molecule. For this reason, there is very little change in experimental λ_{max} of the BCB-[BMIM]BF_4 mixture compared to experimental λ_{max} of the dye mixture containing neutral water. Interestingly, theoretical calculations show a bathochromic shift of BCB C dimer-[BMIM]BF_4 using explicit solvation conditions using TDA that is almost double the value of the bathochromic shift in $\Delta\lambda_{max}$ exhibited by the BCB C dimer-water explicit solvation conditions using TDA. This may indicate that some cation or anion interaction with the BCB molecule exists, most likely with the sp^2-hybridized nitrogen-containing functional group. However, this interaction is not significant enough in experimental data to strongly effect the batch hue.

Ion Molecular Weight. On the other hand, the very small molecular weight of the acetate anion and its planar structure are strong contributors to its ability to interact noncovalently with BCB. BCB dimers exhibit π-stacking in an orientation that can easily be infiltrated by small, planar acetate ions. It is clear that the negatively-charged oxygen molecule within the charged acetate anion $[OAc]^-$ of [EMIM]OAc shows unrealistic bond stretching in the computational simulations performed in this study. However, this may actually be a crude representation of proton transfer occurring in the ionic liquid solvent.

The N-H bond is weaker than the O-H bond because of the diminished electronegativity of nitrogen compared to that of oxygen, and as a result a smaller energy barrier can be overcome by proton transfer or "hopping" between nitrogen atoms and acetate anions. Acetate ions have been proven to strengthen hydrogen bond interactions by acting as bases [81], and experimental batch preparations in a previous study describe hypsochromic shifts in experimental absorbance spectra (that reflect red light) when using alkaline solvents and additives [8]. Both the $[EMIM]^+$ cation and the acetate anion have displayed strong polarization effects in other studies, therefore the strong polarization effect imparted on the BCB C structure. The dipolar "oxoanion" of the acetate ion will more readily react with the BCB C monomer than another dye molecule in solution, thus dye aggregation is prevented and the BCB monomer structure dominates the mixture—and hence provides more accurate theoretical spectra.

Ion-induced Metastable State. It is interesting to see that both BCB BB and C in [EMIM]OAc closely approximate experimental spectra of the mixture, suggesting a tautomer-like effect among these metastable structures that is essential to the overall hue. [EMIM]OAc may enhance the already-rapid ESIPT interaction occurring within BCB if the acetate ion can readily donate a proton to the neutral nitrogen atom of the BCB BB structure as soon as charge transfer takes place during electronic excitation. This "hopping" occurs as a result of the electronic charge transfer within the BCB molecule from a stable BCB C structure in the ground state to a photo-activated, less-stable "kinetic" BCB BB structure in the excited state. The very small change in λ_{max} indicated in Table 33 for the BCB BB dimer-[EMIM]OAc theoretical calculation of singlet excited states serves to verify that the BCB BB structure is essential to BCB ESIPT in this

solvent. In addition, the negatively-charged oxygen atom of the acetate anion may be attracted strongly to the positively-charged nitrogen in the imidazolium cation. In either case, the charged acetate anion may actively serve as a hydrogen bond acceptor in solution with BCB BB due to its small molecular weight, strong Lewis basicity, and well-known polarity, thereby instigating a more pronounced proton transfer than would exist in neutral solvent. As heating was also required to temporarily transport the mixture from the volumetric flask into the cuvette, an ion thermal excitation could have also excited electrons such that forbidden transitions would be enabled [105]. This effect was stabilized by the polarization imparted by the [EMIM]OAc cation/anion combination because it remained after samples were analyzed. This particular binary mixture of ions can therefore inhibit effective BCB dimer complexation and thus affects the color spectra produced when added to charge-transfer dye molecules in solution.

Ion bulkiness. The chloride ion produces a mediocre effect that falls between the drastic shift in maximum absorbance spectra exhibited by [EMIM]OAc and the noticeable similarity of BCB—[BMIM]BF_4 experimental spectra to that of BCB-water and BCB-ethanol solvent mixtures. This is because the $[BMIM]^+$ cation bulkiness produces many of the same issues as those explained above with the [BMIM]BF_4 ionic liquid. The anion activity differs strongly in this case due to the high electron density of the chlorine ion. This is due to chlorine's characteristic high electronegativity, and is further verified by the need to use both diffuse functions and effective core potential to simulate the molecule activity in this computational study. The molecule alone may have a lower molecular weight than the acetate ion which may appear to have it readily interact more quickly with the charged dye molecule, however, the BCB structure exists

in solution with a chloride ion—therefore, a "dichlorine" can form, with increased atomic mass of 70.9 g/mol. This strong attraction between chlorine atoms would pull the Cl^- anion of the ionic liquid away from the cation and the BCB dye structure, thus preventing an interesting color change experimentally. Theoretical simulations verify this by showing a smaller shift in color spectra (-12.9 nm) for BCB in [BMIM]Cl solvent. It is also worth noting that theoretical TD-DFT calculations prohibited the use of full-linear response (FLR) for an explicitly represented BCB C dimer-[BMIM]Cl in the workspace due to the distance between eigenvalues A-B being too large. This indicates that a significant ionic, charged state is exhibited by the molecules in the workspace rather than a ground, covalent state. For this reason, DFT and TD-DFT calculations can provide greater insight into the solvatochromatic trends of this molecule if the Tamm-Dancoff approximation (TDA) is used to evaluate spectral changes of charge-transfer dye molecule BCB, particularly if S2 is investigated.

ESIPT & "Proton Hopping". The molecular structure of the solvent may favor one charged dye structure over another due to a phenomenon known as excited-state intramolecular proton transfer (ESIPT). ESIPT is an extremely fast tautomerization process induced by photon absorption [104]. It is commonly noticed in charge transfer dyes containing a strong intramolecular hydrogen bond, and in cases where the most stable isomer differs at the ground state compared to the excited state [104,108]. This has been indicated in many works as comparable to a photon-induced "tautomerism" or "phototautomerism" [108] for a given charge transfer dye molecule. Contemporary research is beginning to investigate charged solvent interactions employing this mechanism with acetate ions receiving special attention in a recent publication [81].

Cation proton transfer or “proton hopping” [55] as applicable to ionic liquid alkyl imidazolium structures found in many common ionic liquids has been explored previously [23,55,71], and may be instrumental in directly affect the color change exhibited by BCB. Proton transfer or “hopping” [55] is a non-covalent interaction may occur based on the interaction visually rendered as shown in Figure 66(d). Proton transfer has been noted in previous computational *ab initio* studies of electronic structure calculations on imidazole molecules interacting with ammonia molecules, in which proton transfer may take place with a very small energy barrier. This same energy barrier is also very responsive to intermolecular nitrogen-nitrogen bond distance [55]. Steric hindrance may occur due to the aromatic ring structure of the imidazolium cation in order to prevent dimer complexation of BCB molecules from occurring readily in ionic liquid solvent. This hindrance provides the opportunity for smaller charged anion interactions to interfere strongly with the maximum absorbance spectra of a molecule that would otherwise exhibit a blue color.

FLR and TDA Basis Function Comparison. It is interesting to note that the number of basis sets calculated using FLR and TDA only varied based on the presence of solvent molecules. If solvent molecules were not explicitly represented in the workspace, theoretical simulations incorporating PBF would have calculated the restricted singlet excited states using the exact same number of basis sets throughout the four conditions emphasized as shown in Tables 36-37 for the BCB BB dimer and Tables 38-39 for the BCB C dimer.

TABLE XXXVI

Number of Basis Functions generated by experimental batch solvation, theoretical implicit solvation, and theoretical explicit solvation of Brilliant Cresyl Blue BB dimer-solvent mixtures

	Brilliant Cresyl Blue BB (S1) Dimer # of Basis Functions				
	Water	EtOH	[BMIM]Cl	[BMIM]BF_4	[EMIM]OAc
Basis Set Used	Lav2p+*	Lav2p*+	Lav2p*+	6-31g*+	6-31g*+
Implicit, FLR	876	876	876	876	876
Explicit, FLR	898	942	1094	1235	1176
Implicit, TDA	876	876	876	876	876
Explicit, TDA (1 Mol)	898	942	1094	1235	1176

TABLE XXXVII

Change in the number of basis functions (ΔBasis) determined by difference between explicit modeling minus implicit modeling of Brilliant Cresyl Blue dimer-solvent mixtures using FLR and TDA as indicated

	Brilliant Cresyl Blue BB (S1) Dimer ΔBasis				
	Water	EtOH	[BMIM]Cl	[BMIM]BF_4	[EMIM]OAc
Basis Set Used	Lav2p+*	Lav2p*+	Lav2p*+	6-31g*+	6-31g*+
Implicit, FLR	0	0	0	0	0
Explicit, FLR	+22	+66	+218	+359	+300
Implicit, TDA	0	0	0	0	0
Explicit, TDA (1 Mol)	+22	+66	+218	+359	+300

TABLE XXXVIII

Number of basis functions generated by experimental batch solvation, theoretical implicit solvation, and theoretical explicit solvation of Brilliant Cresyl Blue C dimer-solvent mixtures

Brilliant Cresyl Blue C Dimer # of Basis Functions					
	Water	EtOH	[BMIM]Cl	[BMIM]BF_4	[EMIM]OAc
Basis Set Used	Lav2p*+	Lav2p+*	Lav2P*+	Lav2p*+	Lav2p*+
Implicit, FLR	876	876	876	876	876
Explicit, FLR	943	989	1094	1235	X
Implicit, TDA	876	876	876	876	876
Explicit, TDA (1 Mol)	943	989	1094	1235	1176

TABLE XXXIX

Change in the number of basis functions (ΔBasis) determined by difference between explicit modeling minus implicit modeling of Brilliant Cresyl Blue C dimer-solvent mixtures using FLR and TDA as indicated

Brilliant Cresyl Blue C Dimer ΔBasis					
	Water	EtOH	[BMIM]Cl	[BMIM]BF_4	[EMIM]OAc
Basis Set Used	Lav2p*+	Lav2p+*	Lav2P*+	Lav2p*+	Lav2p*+
Implicit, FLR	0	0	0	0	0
Explicit, FLR	+67	+113	+218	+359	X
Implicit, TDA	0	0	0	0	0
Explicit, TDA	+67	+113	+218	+359	+300

FLR and TDA SCRF Solvation Energy Difference Among the Five BCB-Solvent Mixtures. Tables 40-43 list changes in solvation energy in kcal/mol for each dimer for comparison among the five solvents under the four theoretical conditions. In decreasing order of solvation energy, [BMIM]Cl, [BMIM]BF_4, water, ethanol, and [EMIM]OAc. [EMIM]OAc proceeds the most rapidly, alluding the prevalence of the kinetic monomer structure in solution that readily competes for solvation effects long before dye aggregation to form dimer complexes occurs.

TABLE XL

Final solvation energy (in Hartrees) converged after a number of self-consistent field iterations (SCRF iterations) as generated by theoretical implicit solvation and theoretical explicit solvation of Brilliant Cresyl Blue BB dimer-solvent mixtures

	Brilliant Cresyl Blue BB (S1) Dimer Solvation Energy (k_{cal}/mol) and (#) iterations				
	Water	EtOH	[BMIM]Cl	[BMIM]BF_4	[EMIM]OAc
Basis Set Used	Lav2p*+	Lav2p+*	Lav2P*+	Lav2p*+	Lav2p*+
Implicit, FLR	-125.326 (5)	-124.854 (5)	-124.406 (5)	-123.077 (5)	-122.330 (5)
Explicit, FLR	-137.105 (5)	-134.874 (5)	-146.564 (5)	-153.108 (5)	-155.129 (5)
Implicit, TDA	-125.326 (5)	-124.854 (5)	-124.596 (5)	-122.763 (5)	-122.217 (5)
Explicit, TDA	-137.105 (5)	-134.874 (5)	-145.915 (5)	-152.608 (5)	-155.129 (5)

TABLE XLI

Change in Final solvation energy converged after a number of self-consistent field iterations (SCRF iterations) as generated by theoretical implicit solvation and theoretical explicit solvation of Brilliant Cresyl Blue BB dimer-solvent mixtures

	Brilliant Cresyl Blue BB (S1) Dimer Change in Solvation Energy				
	Water	EtOH	[BMIM]Cl	[BMIM]BF_4	[EMIM]OAc
Basis Set Used	Lav2p*+	Lav2p+*	Lav2P*+	Lav2p*+	Lav2p*+
Implicit, FLR	0	0	0	0	0
Explicit, FLR	-9.779	-10.020	-22.158	-30.031	-33.00
Implicit, TDA	0	0	0	0	0
Explicit, TDA	-9.779	-10.020	-21.319	-29.845	-32.912

TABLE XLII

Final solvation energy (in Hartrees) converged after a number of self-consistent field iterations (SCRF iterations) as generated by theoretical implicit solvation and theoretical explicit solvation of Brilliant Cresyl Blue C dimer-solvent mixtures.

Brilliant Cresyl Blue C Dimer Solvation Energy (k_{cal}/mol) and (#) iterations					
	Water	EtOH	[BMIM]Cl	[BMIM]BF_4	[EMIM]OAc
Basis Set Used	Lav2p*+	Lav2p+*	Lav2P*+	Lav2p*+	Lav2p*+
Implicit, FLR	-125.819 (5)	-130.210 (5)	-128.142 (5)	-126.953 (5)	-123.689 (5)
Explicit, FLR	-136.420 (5)	-136.306 (5)	X	-145.033 (4)	X
Implicit, TDA	-125.819 (5)	-130.210 (5)	-128.142 (5)	-127.311 (5)	-123.689 (5)
Explicit, TDA	-136.420 (5)	-136.306 (5)	-156.018 (5)	-144.430 (4)	-123.622 (5)

TABLE XLIII

Change in Final solvation energy converged after a number of self-consistent field iterations (SCRF iterations) as generated by theoretical implicit solvation and theoretical explicit solvation of Brilliant Cresyl Blue C dimer-solvent mixtures.

Brilliant Cresyl Blue C Dimer Change in Solvation Energy					
	Water	EtOH	[BMIM]Cl	[BMIM]BF_4	[EMIM]OAc
Basis Set Used	Lav2p*+	Lav2p+*	Lav2P*+	Lav2p*+	Lav2p*+
Implicit, FLR	0	0	0	0	0
Explicit, FLR	-10.601	-6.096	X	-18.080	X
Implicit, TDA	0	0	0	0	0
Explicit, TDA	-10.601	-6.096	-27.876	-17.119	+0.067

Conclusion

Brilliant Cresyl Blue (BCB) is a charge transfer dye molecule with a wide variety of pharmaceutical and cosmetic applications. While BCB appears its namesake hue in water and ethanol solvents, BCB dimer-solvent mixtures in ionic liquids exhibit changes in maximum absorbance spectra that provoked further investigation of their solvatochromic properties. Experimental studies containing mixtures of BCB in water, ethanol, and in three common ionic liquid solvents [BMIM]Cl, [BMIM]BF_4, and [EMIM]OAc reveal that dimer complexation occurs as indicated by both a λ_{max} and a $\lambda_{shoulder}$ peak. DFT and TD-DFT calculations using Poisson-Boltzmann Finite (PBF) elements continuum model for solvation effects can be used to generate theoretical maximum absorbance spectra that is comparable to experimental batch absorbance data analyzed by a conventional UV-visible spectrophotometer.

Use of full-linear response theory (FLR) shows a larger change in λ_{max} between experimental and theoretical maximum absorbance values than does Tamm-Dancoff Approximation (TDA) due to the prevalence of an overall +2 charge state of the BCB dimer-solvent system. The efficacy of λ_{max} comparison using TD-DFT with TDA has been proven using “implicit” solvation effects featuring only the Poisson-Boltzmann Finite elements continuum model, and “explicit” solvation effects incorporating PBF and the solvent molecule explicitly represented in the computational workspace with the BCB dye structure simulated.

The differences in BCB metastable states that provoke otherwise forbidden transitions vary according to the solvent analyzed. Therefore, different solvent molecule

interactions induce clearly discernible spectral shifts that are evident in both experimental and theoretical data. BCB C is the more stable dye aggregate structure that, upon simulation as a dimer, provides more accurate theoretical λ_{max} data under explicit solvation conditions using TD-DFT with the Tamm-Dancoff Approximation for all solvents studied. However, BCB monomer data indicates that BCB BB functions as the "kinetic" product in mixtures where singlet oxygen atoms serve as stronger competitors for the charged oxygen atom metastable structure than other atoms in the mixture, (as in vapor phase), or when non-covalent interactions in solutions of high electron density stabilize the charged oxygen atom (as in [BMIM]Cl). Despite this, BCB C is the thermodynamic metastable structure that will produce the most applicable λ_{max} peak in theoretical studies intending to focus on either the BCB monomer or dimer. In addition, larger numbers of basis functions in were generated in studies including FLR with explicit solvation in water and ethanol for BCB C Dimer than for BCB BB dimer while the number of basis functions generated for BCB in ionic liquid solvents remained consistent among both structures.

References

[1] O. TAKAHASHI, "Characteristics of Rat Platelets and Relative Contributions of Platelets and Blood Coagulation to Haemostasis," *Food Chem Toxicol*, vol. 38, pp. 203-218, 2000.

[2] R. N. Dsouza, U. Pischel, and W. M. Nau, "Fluorescent dyes and their supramolecular host/guest complexes with macrocycles in aqueous solution," *Chem Rev*, vol. 111, no. 12, pp. 7941-80, Dec 14 2011.

[3] W. C. Holmes, "The Tautomerism of Brilliant Cresyl Blue," *Journal of the American Chemical Society*, vol. 50, no. 7, pp. 1989-1993, 1928.

[4] E. V. Garibay et al., "Iron Absorption during Recovery from Malnutrition," *Journal of the American College of Nutrition*, vol. 20, no. 4, pp. 286-292, 2001.

[5] A. Buryak and K. Severin, "Dynamic Combinatorial Libraries of Dye Complexes as Sensors," *Angewandte Chemie*, vol. 117, no. 48, pp. 8149-8152, 2005.

[6] Y. Umasankar, T.-W. Ting, and S.-M. Chen, "Characterization of Poly(brilliant cresyl blue)-Multiwall Carbon Nanotube Composite Film and Its Application in Electrocatalysis of Vitamin B9 Reduction," *Journal of The Electrochemical Society*, vol. 158, no. 5, 2011.

[7] X. Li et al., "Ordered array of gold semishells on TiO2 spheres: an ultrasensitive and recyclable SERS substrate," *ACS Appl Mater Interfaces*, vol. 4, no. 4, pp. 2180-5, Apr 2012.

[8] C. Mall and P. P. Solanki, "Spectrophotometric and conductometric studies of molecular interaction of brilliant cresyl blue with cationic, anionic and non-ionic surfactant in aqueous medium for application in photogalvanic cells for solar energy conversion and storage," *Energy Reports*, vol. 4, pp. 23-30, 2018.

[9] PubChem. (2018, December 17, 2018). 10127-36-3 (March 27, 2018 ed.) [Online]. Available: https://pubchem.ncbi.nlm.nih.gov/substance/355151424#section=Top.

[10] PubChem. (2018, Dec 17 2018). 10127-36-3 [Online]. Available: https://pubchem.ncbi.nlm.nih.gov/substance/254796022#section=Source-Category.

[11] Sigma-Aldrich. (2019, April 23, 2019). Brilliant Cresyl Blue ALD certified by the Biological Stain Commission [Online]. Available: https://www.sigmaaldrich.com/catalog/product/sigma/b5388?lang=en&region=US.

[12] PubChem. (2019, April 23 2019). OCKKUZVCJCWWHM-UHFFFAOYSA-L | C34H40Cl4N6O2Zn [Online]. Available: https://pubchem.ncbi.nlm.nih.gov/compound/20841696.

[13] A. G. Gilani, M. Moghadam, S. E. Hosseini, and M. S. Zakerhamidi, "A comparative study on the aggregate formation of two oxazine dyes in aqueous and aqueous urea solutions," *Spectrochim Acta A Mol Biomol Spectrosc*, vol. 83, no. 1, pp. 100-5, Dec 2011.

[14] Q. F. Zhang, Z. T. Jiang, Y. X. Guo, and R. Li, "Complexation study of brilliant cresyl blue with beta-cyclodextrin and its derivatives by UV-vis and fluorospectrometry," *Spectrochim Acta A Mol Biomol Spectrosc*, vol. 69, no. 1, pp. 65-70, Jan 2008.

[15] M. Koel, "Solvatochromic Probes with Ionic Liquids," *Proc. Estonian Acad. Sci. Chem.*, vol. 54, no. 1, pp. 3-11, 2004.

[16] G. G. L. Antonov, V. Petrov, M. Kubista, J. Nygren, "UV-Vis spectroscopic and chromometric study on the aggregation of ionic dyes in water," *Talanta*, vol. 49, pp. 99-106, 1999.

[17] A. Dreuw and M. Head-Gordon, "Failure of time-dependent density functional theory for long-range charge-transfer excited states: the zincbacteriochlorin-bacteriochlorin and bacteriochlorophyll-spheroidene complexes," *J Am Chem Soc*, vol. 126, no. 12, pp. 4007-16, Mar 31 2004.

[18] J. Fabian, "TDDFT-calculations of Vis/NIR absorbing compounds," *Dyes and Pigments*, vol. 84, no. 1, pp. 36-53, 2010.

[19] R. J. Nieckarz, J. Oomens, G. Berden, P. Sagulenko, and R. Zenobi, "Infrared multiple photon dissociation (IRMPD) spectroscopy of oxazine dyes," *Phys Chem Chem Phys*, vol. 15, no. 14, pp. 5049-56, Apr 14 2013.

[20] J. Mohen and T. D. Vaden, "Solvent Effects on Interaction Energies of Alternating Color Additive Molecular Structures in Conventional and Ionic Liquid Solvents Calculated Using TD-DFT," in *Investigating Color Additive Molecules for Pharmaceutical and Cosmetic Applications: A Comparison of Theoretical and Experimental UV-Visible Absorbance Spectra in Tunable Solvents*. Glassboro: ProQuest, 2019.

[21] P. W. Wasserscheid, T., *Ionic Liquids in Synthesis (Green Chemistry)*. Erlangen: Wiley-VCH, 2008.

[22] H. Saba, X. Zhu, Y. Chen, and Y. Zhang, "Determination of physical properties for the mixtures of [BMIM]Cl with different organic solvents," *Chinese Journal of Chemical Engineering*, vol. 23, no. 5, pp. 804-811, 2015.

[23] M. Koel, "Solvatochromic Study on Binary Solvent Mixtures with Ionic Liquids," 2006.

[24] M. N. Kobrak, "Characterization of the solvation dynamics of an ionic liquid via molecular dynamics simulation," *J Chem Phys*, vol. 125, no. 6, p. 64502, Aug 14 2006.

[25] M. A. R. Martins, U. Domańska, B. Schröder, J. A. P. Coutinho, and S. P. Pinho, "Selection of Ionic Liquids to be Used as Separation Agents for Terpenes and Terpenoids," *ACS Sustainable Chemistry & Engineering*, vol. 4, no. 2, pp. 548-556, 2015.

[26] V. H. Paschoal, L. F. O. Faria, and M. C. C. Ribeiro, "Vibrational Spectroscopy of Ionic Liquids," *Chem Rev*, vol. 117, no. 10, pp. 7053-7112, May 24 2017.

[27] K. Ueno, H. Tokuda, and M. Watanabe, "Ionicity in ionic liquids: correlation with ionic structure and physicochemical properties," *Phys Chem Chem Phys*, vol. 12, no. 8, pp. 1649-58, Feb 28 2010.

[28] B. M. Sato, C. G. de Oliveira, C. T. Martins, and O. A. El Seoud, "Thermo-solvatochromism in binary mixtures of water and ionic liquids: on the relative importance of solvophobic interactions," *Phys Chem Chem Phys*, vol. 12, no. 8, pp. 1764-71, Feb 28 2010.

[29] M. B. Shiflett, D. W. Drew, R. A. Cantini, and A. Yokozeki, "Carbon Dioxide Capture Using Ionic Liquid 1-Butyl-3-methylimidazolium Acetate," *Energy & Fuels*, vol. 24, no. 10, pp. 5781-5789, 2010.

[30] B. Wu, H. Shirota, S. Lall-Ramnarine, and E. W. Castner, "Structure of ionic liquids with cationic silicon-substitutions," *The Journal of Chemical Physics*, vol. 145, no. 11, 2016.

[31] A. D. Bochevarov et al., "Jaguar: A high-performance quantum chemistry software program with strengths in life and materials sciences," *International Journal of Quantum Chemistry*, vol. 113, no. 18, pp. 2110-2142, 2013.

[32] M.-M. Huang, Y. Jiang, P. Sasisanker, G. W. Driver, and H. Weingärtner, "Static Relative Dielectric Permittivities of Ionic Liquids at 25 °C," *Journal of Chemical & Engineering Data*, vol. 56, no. 4, pp. 1494-1499, 2011.

[33] (2019). *1-Butyl-3-Methylimidazolium Chloride Safety Data Sheet*.

[34] (2019). *1-Butyl-3-Methylimidazolium Tetrafluoroborate Safety Data Sheet*.

[35] (2019). *1-Ethyl-3-Methylimidazolium Acetate Safety Data Sheet*.

[36] japan@wavefun.com. (2014, April 2, 2017). Spartan '14 Help: Questions about Basis Sets. Available: http://www.wavefun.com/japan/support/help/BasisSetFAQ.html

[37] A. Chantzis, A. D. Laurent, C. Adamo, and D. Jacquemin, "Is the Tamm-Dancoff Approximation Reliable for the Calculation of Absorption and Fluorescence Band Shapes?," *J Chem Theory Comput*, vol. 9, no. 10, pp. 4517-25, Oct 8 2013.

[38] S. Hirata and M. Head-Gordon, "Time-dependent density functional theory within the Tamm–Dancoff approximation," *Chemical Physics Letters*, vol. 314, no. 3-4, pp. 291-299, 1999.

[39] M. M. Reiger, "Cosmetics," in *Kirk-Othmer Chemical Technology of Cosmetics*, A. Seidel, Ed. Hoboken: Wiley, 2013, pp. 1-48.

[40] E. W. Flick, *Cosmetic and Toiletry Formulations*, 2nd ed. Norwich: Noyes, 2001, p. 378.

[41] E. W. Flick, *Cosmetic and Toiletry Formulations*, 2nd ed. Park Ridge: Noyes, 1989, p. 971.

[42] Y.-L. Wang and G.-S. Wu, "Improving the TDDFT calculation of low-lying excited states for polycyclic aromatic hydrocarbons using the Tamm–Dancoff approximation," *International Journal of Quantum Chemistry*, vol. 108, no. 3, pp. 430-439, 2008.

[43] M. V. D. Michalun, Joseph, *Milady Skin Care and Cosmetic Ingredients Dictionary*, 4th ed. Clifton Park: Cengage Learning, 2015, p. 339.

[44] S. M. G. Ming Shin Neo, Tahir Mehmood Khan, Manish Gupta, "Quantification of Ethanol Content in Traditional Herbal Cough Syrups," *Pharmacogn. J.*, vol. 9, no. 6, pp. 821-827, 2017.

[45] R. U. P. E. W. J. A. R. D. Howes, "Fate of Ethanol Topically Applied To Skin," *Food Chem Toxicol*, vol. 39, no. 2, pp. 169-174, 2001.

[46] C. Wakai, A. Oleinikova, M. Ott, and H. Weingartner, "How polar are ionic liquids? Determination of the static dielectric constant of an imidazolium-based ionic liquid by microwave dielectric spectroscopy," *J Phys Chem B*, vol. 109, no. 36, pp. 17028-30, Sep 15 2005.

[47] C. Schroder, T. Sonnleitner, R. Buchner, and O. Steinhauser, "The influence of polarizability on the dielectric spectrum of the ionic liquid 1-ethyl-3-methylimidazolium triflate," *Phys Chem Chem Phys*, vol. 13, no. 26, pp. 12240-8, Jul 14 2011.

[48] S. Arzhantsev, H. Jin, G. A. Baker, and M. Maroncelli, "Measurements of the complete solvation response in ionic liquids," *J Phys Chem B*, vol. 111, no. 18, pp. 4978-89, May 10 2007.

[49] P. Berton, K. Bica, and R. D. Rogers, "Ionic liquids for consumer products: Dissolution, characterization, and controlled release of fragrance compositions," *Fluid Phase Equilibria*, vol. 450, pp. 51-56, 2017.

[50] R. J. Bingham and P. Ballone, "Computational study of room-temperature ionic liquids interacting with a POPC phospholipid bilayer," *J Phys Chem B*, vol. 116, no. 36, pp. 11205-16, Sep 13 2012.

[51] K. G. Bogolitsyn, T. E. Skrebets, and T. A. Makhova, "Physicochemical properties of 1-butyl-3-methylimidazolium acetate," *Russian Journal of General Chemistry*, vol. 79, no. 1, pp. 125-128, 2009.

[52] M. Borissova, J. Gorbatsova, A. Ebber, M. Kaljurand, M. Koel, and M. Vaher, "Nonaqueous CE using contactless conductivity detection and ionic liquids as BGEs in ACN," *Electrophoresis*, vol. 28, no. 20, pp. 3600-5, Oct 2007.

[53] M. Brinkkotter, G. A. Giffin, A. Moretti, S. Jeong, S. Passerini, and M. Schonhoff, "Relevance of ion clusters for Li transport at elevated salt concentrations in [Pyr12O1][FTFSI] ionic liquid-based electrolytes," *Chem Commun (Camb)*, Apr 10 2018.

[54] A. Chaumont and G. Wipff, "Solvation of “big” spherical solutes in room temperature ionic liquids and at their aqueous interface: A molecular dynamics simulation study," *Journal of Molecular Liquids*, vol. 131-132, pp. 36-47, 2007.

[55] H. Chen, T. Yan, and G. A. Voth, "A computer simulation model for proton transport in liquid imidazole," *J Phys Chem A*, vol. 113, no. 16, pp. 4507-17, Apr 23 2009.

[56] C. Chiappe, M. Malvaldi, and C. S. Pomelli, "Ionic liquids: Solvation ability and polarity," *Pure and Applied Chemistry*, vol. 81, no. 4, pp. 767-776, 2009.

[57] M. Dandapat and D. Mandal, "Time-dependent fluorescence Stokes shift and molecular-scale dynamics in alginate solutions and hydrogels," *Chemical Physics Letters*, vol. 627, pp. 67-72, 2015.

[58] F. Endres and S. Zein El Abedin, "Air and water stable ionic liquids in physical chemistry," *Phys Chem Chem Phys*, vol. 8, no. 18, pp. 2101-16, May 14 2006.

[59] M. V. Fedorov and A. A. Kornyshev, "Ionic liquids at electrified interfaces," *Chem Rev*, vol. 114, no. 5, pp. 2978-3036, Mar 12 2014.

[60] M. H. Ghatee and Y. Ansari, "Ab initio molecular dynamics simulation of ionic liquids," *J Chem Phys*, vol. 126, no. 15, p. 154502, Apr 21 2007.

[61] A. Golabiewska et al., "Fabrication and photoactivity of ionic liquid-TiO2 structures for efficient visible-light-induced photocatalytic decomposition of organic pollutants in aqueous phase," *Beilstein J Nanotechnol*, vol. 9, pp. 580-590, 2018.

[62] Z. He and P. Alexandridis, "Nanoparticles in ionic liquids: interactions and organization," *Phys Chem Chem Phys*, vol. 17, no. 28, pp. 18238-61, Jul 28 2015.

[63] T. D. Ho, C. Zhang, L. W. Hantao, and J. L. Anderson, "Ionic liquids in analytical chemistry: fundamentals, advances, and perspectives," *Anal Chem*, vol. 86, no. 1, pp. 262-85, Jan 7 2014.

[64] J. G. Huddleston, A. E. Visser, W. M. Reichert, H. D. Willauer, G. A. Broker, and R. D. Rogers, "Characterization and comparison of hydrophilic and hydrophobic room temperature ionic liquids incorporating the imidazolium cation," *Green Chemistry*, vol. 3, no. 4, pp. 156-164, 2001.

[65] E. I. Izgorodina, "Towards large-scale, fully ab initio calculations of ionic liquids," *Phys Chem Chem Phys*, vol. 13, no. 10, pp. 4189-207, Mar 14 2011.

[66] S. G. Jones et al., "Ionic liquids through the looking glass: theory mirrors experiment and provides further insight into aromatic substitution processes," *Phys Chem Chem Phys*, vol. 12, no. 8, pp. 1873-8, Feb 28 2010.

[67] M. Kanakubo, T. Makino, and T. Umecky, "CO2 solubility in and physical properties for ionic liquid mixtures of 1-butyl-3-methylimidazolium acetate and 1-butyl-3-methylimidazolium bis(trifluoromethanesulfonyl)amide," *Journal of Molecular Liquids*, vol. 217, pp. 112-119, 2016.

[68] D. C. Khara and A. Samanta, "Fluorescence response of coumarin-153 in N-alkyl-N-methylmorpholinium ionic liquids: are these media more structured than the imidazolium ionic liquids?," *J Phys Chem B*, vol. 116, no. 45, pp. 13430-8, Nov 15 2012.

[69] M. N. Kobrak, "A comparative study of solvation dynamics in room-temperature ionic liquids," *J Chem Phys*, vol. 127, no. 18, p. 184507, Nov 14 2007.

[70] M. N. Kobrak and V. Znamenskiy, "Solvation dynamics of room-temperature ionic liquids: evidence for collective solvent motion on sub-picosecond timescales," *Chemical Physics Letters*, vol. 395, no. 1-3, pp. 127-132, 2004.

[71] M. N. S. Kobrak, N., "An Electrostatic Interpretation of Structure-Property Relationships in Ionic Liquids," 2015.

[72] K. Y. Lee WR, Kim JY, Kim TH, Ahn KD, Kim E., "Electro-fluorescence Switching of bis-imidazolium ionic liquids," *J Nanosci Nanotechnol*, vol. 8, no. 9, pp. 4630-4, 2008.

[73] K. R. J. Lovelock, "Influence of the ionic liquid/gas surface on ionic liquid chemistry," *Physical Chemistry Chemical Physics*, vol. 14, no. 15, 2012.

[74] K. Low, L. Wylie, D. L. A. Scarborough, and E. I. Izgorodina, "Is it possible to control kinetic rates of radical polymerisation in ionic liquids?," *Chem Commun (Camb)*, vol. 54, no. 80, pp. 11226-11243, Oct 4 2018.

[75] R. M. Lynden-Bell, "Screening of pairs of ions dissolved in ionic liquids," *Phys Chem Chem Phys*, vol. 12, no. 8, pp. 1733-40, Feb 28 2010.

[76] D. R. MacFarlane and K. R. Seddon, "Ionic Liquids—Progress on the Fundamental Issues," *Australian Journal of Chemistry*, vol. 60, no. 1, 2007.

[77] P. K. Mandal, A. Paul, and A. Samanta, "Room Temperature Ionic Liquids as Media for Photophysical Studies," *Journal of the Chinese Chemical Society*, vol. 53, no. 1, pp. 247-252, 2006.

[78] P. K. Mandal, M. Sarkar, and A. Samanta, "Excitation-Wavelength-Dependent Fluorescence Behavior of Some Dipolar Molecules in Room-Temperature Ionic Liquids," *The Journal of Physical Chemistry A*, vol. 108, no. 42, pp. 9048-9053, 2004.

[79] M. Maroncelli, X.-X. Zhang, M. Liang, D. Roy, and N. P. Ernsting, "Measurements of the complete solvation response of coumarin 153 in ionic liquids and the accuracy of simple dielectric continuum predictions," *Faraday Discuss.*, vol. 154, pp. 409-424, 2012.

[80] P. C. Marr and A. C. Marr, "Ionic liquid gel materials: applications in green and sustainable chemistry," *Green Chemistry*, vol. 18, no. 1, pp. 105-128, 2016.

[81] H. Matsumoto, S. Ikedu, T. Tosaka, Y. Nishimura, and T. Arai, "Kinetic analysis of tautomer forms of aromatic-urea compounds with acetate ions: solvent effect of excited state intermolecular proton transfer," *Photochem Photobiol Sci*, Apr 4 2018.

[82] M. J. Muldoon, C. M. Gordon, and I. R. Dunkin, "Investigations of solvent–solute interactions in room temperature ionic liquids using solvatochromic dyes," *Journal of the Chemical Society*, Perkin Transactions 2, no. 4, pp. 433-435, 2001.

[83] C. M. S. S. Neves, M. G. Freire, and J. A. P. Coutinho, "Improved recovery of ionic liquids from contaminated aqueous streams using aluminium-based salts," *RSC Advances*, vol. 2, no. 29, 2012.

[84] H. Niedermeyer, J. P. Hallett, I. J. Villar-Garcia, P. A. Hunt, and T. Welton, "Mixtures of ionic liquids," *Chem Soc Rev*, vol. 41, no. 23, pp. 7780-802, Dec 7 2012.

[85] A. Paul, P. K. Mandal, and A. Samanta, "On the optical properties of the imidazolium ionic liquids," *J Phys Chem B*, vol. 109, no. 18, pp. 9148-53, May 12 2005.

[86] S. S. Prasun K. Mandal, Rana Karmakar, Anunay Samanta, "Solvation Dynamics in Room Temperature Ionic Liquids: Dynamic Stokes Shift Studies of Fluorescence of Dipolar Molecules," *Current Science*, vol. 90, no. 3, pp. 301-310, Feb 10 2006 2006.

[87] G. O. B. K. Richard and S. H. Q. N. Gunaratne, "Ionic Liquid Systems," United States of America Patent US 20160376522 A1 Patent Appl. US 15/187,829, 2016. [Online]. Available: https://www.google.com/patents/US20160376522.

[88] A. Samanta, "Dynamic stokes shift and excitation wavelength dependent fluorescence of dipolar molecules in room temperature ionic liquids," *J Phys Chem B*, vol. 110, no. 28, pp. 13704-16, Jul 20 2006.

[89] M. S. Raja Shahrom, C. D. Wilfred, and A. K. Z. Taha, "CO 2 capture by task specific ionic liquids (TSILs) and polymerized ionic liquids (PILs and AAPILs)," *Journal of Molecular Liquids*, vol. 219, pp. 306-312, 2016.

[90] C. Schroder, T. Rudas, and O. Steinhauser, "Simulation studies of ionic liquids: orientational correlations and static dielectric properties," *J Chem Phys*, vol. 125, no. 24, p. 244506, Dec 28 2006.

[91] Y. Shim, D. Jeong, M. Y. Choi, and H. J. Kim, "Rotational dynamics of a diatomic solute in the room-temperature ionic liquid 1-ethyl-3-methylimidazolium hexafluorophosphate," *J Chem Phys*, vol. 125, no. 6, p. 61102, Aug 14 2006.

[92] Y. Shim and H. J. Kim, "Vibrational energy relaxation of a diatomic molecule in a room-temperature ionic liquid," *J Chem Phys*, vol. 125, no. 2, p. 24507, Jul 14 2006.

[93] T. Singh and A. Kumar, "Static dielectric constant of room temperature ionic liquids: internal pressure and cohesive energy density approach," *J Phys Chem B*, vol. 112, no. 41, pp. 12968-72, Oct 16 2008.

[94] X. Song, "Solvation dynamics in ionic fluids: an extended Debye-Huckel dielectric continuum model," *J Chem Phys*, vol. 131, no. 4, p. 044503, Jul 28 2009.

[95] S. M. Urahata and M. C. Ribeiro, "Single particle dynamics in ionic liquids of 1-alkyl-3-methylimidazolium cations," *J Chem Phys*, vol. 122, no. 2, p. 024511, Jan 8 2005.

[96] I. J. Villar-Garcia et al., "The ionic liquid–vacuum outer atomic surface: a low-energy ion scattering study," *Chem. Sci.*, vol. 5, no. 11, pp. 4404-4418, 2014.

[97] H. Wang et al., "Fluorescence quenching of 4-tert-octylphenol by room temperature ionic liquids and its application," *J Fluoresc*, vol. 23, no. 2, pp. 323-31, Mar 2013.

[98] M. Watanabe, D. Kodama, T. Makino, and M. Kanakubo, "CO2 absorption properties of imidazolium based ionic liquids using a magnetic suspension balance," *Fluid Phase Equilibria*, vol. 420, pp. 44-49, 2016.

[99] X. Zhang, X. Zhang, H. Dong, Z. Zhao, S. Zhang, and Y. Huang, "Carbon capture with ionic liquids: overview and progress," *Energy & Environmental Science*, vol. 5, no. 5, 2012.

[100] Q. Zhang and S. Zhu, "Ionic Liquids: Versatile Media for Preparation of Vesicles from Polymerization-Induced Self-Assembly," *ACS Macro Letters*, vol. 4, no. 7, pp. 755-758, 2015.

[101] F. Endres and S. Zein El Abedin, "Air and water stable ionic liquids in physical chemistry," *Phys Chem Chem Phys*, vol. 8, no. 18, pp. 2101-16, May 14 2006.

[102] R. M. Lynden-Bell, "Screening of pairs of ions dissolved in ionic liquids," *Phys Chem Chem Phys*, vol. 12, no. 8, pp. 1733-40, Feb 28 2010.

[103] D. R. MacFarlane and K. R. Seddon, "Ionic Liquids—Progress on the Fundamental Issues," *Australian Journal of Chemistry*, vol. 60, no. 1, 2007.

[104] D. Jacquemin and C. Adamo, "Computational Molecular Electronic Spectroscopy with TD-DFT," *Top Curr Chem*, vol. 368, pp. 347-75, 2016.

[105] F. R. S. C. Alister Vallance Jones, "Optical Emissions from Aurora," in *Aurora*, vol. 9, B. M. McCormac, Ed. (Geophysics and Astrophysics Monographs. Boston: D. Reidel, 1974, pp. 80-177.

[106] C. Reichardt, "Solvatochromic Dyes as Solvent Polarity Indicators," *Chemical Reviews*, vol. 94, no. 8, pp. 2319-2358, 1994.

[107] C. Reichardt, "Polarity of ionic liquids determined empirically by means of solvatochromic pyridinium N-phenolate betaine dyes," *Green Chemistry*, vol. 7, no. 5, 2005.

[108] C. Adamo et al., "Exploring excited states using time dependent density functional theory and density-based indexes," *J Coordination Chemistry Reviews*, vol. 304, pp. 166-178, 2015.

Future Outlook

The studies provided herein have sought to fill the gap in sensory research applying computational methods to physicochemical studies. Following the contributions of Christian Reichardt throughout the 20th century to discuss experimental solvatochromism of chromophore-containing molecules using conventional solvents [1-6], several essential--but nonetheless dispersed—applications of computational advanced ab initio methods DFT and TD-DFT have helped guide our understanding of changes incurred via photoexcitation of active pharmaceutical ingredients (APIs) [7-26], biological [27-44] or bioluminescent chromophores [45-48], color additives [7-11,49-107], flavonoids [12-26,108-120], or fragrances [7-11,121]. Concurrently, advancements in neoteric solvents have brought ionic liquids to the formulator's attention as these solvents offer more widespread customization of the overall properties of a mixture based on their inherent ion coupling. Such physicochemical properties that can be affected in formulations include overall hue [4-6] and fragrance [122-124], viscosity [125-128], density [125,128-129], thermostability [125,130-132], solvation dynamics [133-139], glass transition temperature [128], melting and boiling point temperatures [128,140], conductivity [125,126,141,144], drug delivery properties [145,146], improved surface interaction during emulsification [138,145,147-149], and as separation agents [123]. Modern computational methods set a new standard in computational modeling by enabling facile application of more broadly-applicable basis sets and emerging solvation continuum models that ideally yield more "accurate" data values for further analysis. Since the 19th century, experimental benchmarks using analytical instrumentation have served as tangible approaches to readily verify emerging theoretical models. As the

human perception is unwaveringly subjective, hopefully this subjective approach will be replaced by comparison to more detailed theoretical works incorporating basis sets with functionals designed to better suit the interelectronic Coulombic and kinetic effects among constituent atoms of molecules to provide more precise mapping of HOMO-LUMO antibonding orbitals for better understanding of the significance of certain electronic transitions over others. In addition, the development and successful application of more sophisticated solvation continuum models would help to account for more diverse charge transfer effects than polarization, such as ion thermal transfer excitation. Such improvements to the currently-popular functionals would enable more intricate calculation of electronic transitions for atoms solvated in neoteric solvents in any photochemical studies. In this way, the theory will gradually generate a value that is considered not as an "approximation" value to be verified by experiment. Rather, the "theory" would become the reference model with which to compare experimental data for ensure the effectiveness of experimental methods adopted for analysis.

The progress that has been made in the beginning of the 21st century with the advent of greater processing power at a competitive price has led to efficient parallelization of DFT calculations, enabling large color molecules such as those used throughout this study to have their physicochemical properties analyzed in such a way that was considered unrealistic decades ago. Today, computational chemists are enjoying the benefits of the "Second Quantum Revolution" [150] now that quantum computing advancements enable faster calculation of the approximate values of the Schrödinger wave equation [151]. This breakthrough could lead to exact calculation of properties for molecules larger than hydrogen and helium, which would inevitably launch

advancements in computational processing availability for increasingly “more advanced” ab initio methods to be applied to larger, more complex molecular systems. Ideally, simulation of all kinds of molecular structures under more realistic conditions will be more cost-effective and approachable for software users with ever-present time constraints. In the new journal called Advanced Quantum Technologies created by Wiley in 2018 to address the growing body of research pertaining to this revolution, the editors specifically mention that “sensing” will become more feasible to mathematically model [150]. Visual mechanisms [152-173] and auditory sensations [153-161,174-180] sharing a common foundation on the study of wavelength oscillations pertaining to GPCR activation (or deactivation) have had ample literature and research contributions for several years. Richard Axel and Linda Buck’s Nobel Prize-winning contribution to our understanding of scent in 1991 has suggested a combinatorial mechanism [181-182] in its debut, but has since been challenged in more contemporary works [183-187]. Furthermore, the sensations of touch and taste have yet to be clearly defined using theoretical modeling—or even adequate experimental studies--describing a systematic mechanism where future sensory data may evolve in a rather predictive manner. As the human visual mechanism remains to be fully understood, computational models inevitably enhance our understanding but also alleviate the moral and ethical burden of chemists seeking more holistic methods to study human sensations without the sacrificial expense of human or animal organs. It may become commonplace to model the color additive molecules discussed in the previous sections in computational workspaces that capture activity at femto- [188-189], pico- [190], nano- [191-193], and even up to millisecond [194-195] time scales to better emulate natural responses to light stimuli.

Contemporary research on the long-term effects of common formulation ingredients with varied applications for both functional and aesthetic purposes has contributed to a recent bill [196] proposed on September 26, 2018. “The Safe Cosmetics and Personal Care Products Act of 2018” contains sections that legislate greater improvements on labeling, accessibility of ingredient lists, and overall consumer safety of cosmetics. According to the bill, products must have a “reasonable expectation of no harm” even at low dosages, whereas previously cosmetic additives were included (or discarded) based solely on clinical data indicating carcinogenicity, mutagenicity, and teratogenicity. While trustworthy, adequate data analysis from long-term clinical studies cannot keep up with the constantly-accelerating pace of novel sensory additive molecule development. Therefore, restriction on sensory additive molecules may occur if documented adverse effects from short-term, acute, repeated exposure have been documented in contemporary studies [196]. In addition, no formulation ingredients may be used if they contain specific hazards defined by authoritative sources such as the Environmental Protection Agency (EPA), the International Agency for Research on Cancer, the National Toxicity Program through the National Institute of Health, the California Environmental Protection Agency, and any other authoritative international, federal, or state entity as defined by the Secretary of the Departments of Energy and Commerce [196]. Furthermore, the following additives have been prohibited use in food, pharmaceutics, cosmetics, and other personal care products as of the enactment of subchapter 616(2): Benzophenones[24], octinoxate, butylated hydroxyanisole and butylated hydroxyoluen, “coal-tar” dyes (para-phenylenediamine), cocamide diethanolamine,

[24] Benzophenone, benzophenone-1, benzophenone-3 aka “oxybenzone”. [196]

dibutylated phthalate (phthalates DBP), Bis(2-ethylhexyl) phthalate (DEHP), toluene, styrene or styrene acrylates, formaldehydes[25] and formaldehyde-releasing preservatives[26], triclosan, lead acetate or other lead compounds, and the various parabens[27]. This list includes additives well-known in historical archives as dangerous or otherwise toxic but also restricts more recently-developed molecules in which the scientific community---and the interested general public—has observed or experienced adverse health effects after routine or daily exposure. Phthalates contribute to infertility [197-206]; Resveratrol, isolated from grapes used in red wine, experienced a short-lived addition and subsequent removal from lists of FDA-approved additives after discovery of its link to endometriosis, which is still debated [207-208]; overuse of antibacterial agents such as triclosan in not only household detergents and hand soap but also in wearable articles [209-224], and other additives praised for their properties to enhance formulation appearance during product development stages but are ultimately detrimental to the end-users.

Available literature pertaining to color additive molecules fluctuates similarly, from being fanatically cynical of their use to defensive of their lack of in vivo genotoxicity. Reasoning ranges widely; studies indicate that popular color additives sensitize the site of application [109], while others cite their inability to filter and dispose of a given color additive molecule long after its intended use has been fulfilled. The latter generalization applies strongly to triphenylmethane molecules such as FD&C Blue No. 1

[25] methylene glycol/methanediol/formaldehyde [196]
[26] DMDM hydantoin, diazolidinyl urea, imidazolidinyl urea, methenamine, quaternium-15, and sodium hydroxymethylglycinate [196]
[27] isopropylparaben, isobutylparaben, phenylparaben, benzylparaben, pentylparaben, propylparaben, and butylparaben [196]

known as “Brilliant Blue FCF” or “Acid Blue 9” that have been known to stain lingual mucosa and shaven skin [225] and accumulate in municipal water supplies [226-228]. Reactive dye “Brilliant Red X-3B” [229], Congo Red [230,231], and other textile dyes [232-233] also share this negative environmental implication. Erythrosine (a red xanthene dye) has been proven to cause thyroid cancer in rats [234,235], while other synthetic red and yellow dye molecules bind more readily to human serum albumin than do their natural counterparts [236]—worry not, as the effects of Sunset Yellow can be minimized by lactic acid bacteria [237], and by taurine as an organic neuroprotectant in the case of Allura Red [238]. While some other red dye molecules have great lipophilicity that they can cause staining of gastrointestinal tissue, which potentially leads to misdiagnoses of internal bleeding, Crysamine-G, a very lipophilic Congo Red analogue, has been shown to inhibit Aβ-induced toxicity in PC12 cells to be a viable therapeutic candidate for Alzheimer’s disease [239]. Yellow molecules such as Yellow No. 6 “Sunset Yellow” and Yellow No. 5 “Tartrazine” have assorted concerns according to [236,240-242] and [236,240,243-246], respectively. In addition, some researchers are wary of the aluminum component of synthetic lake pigments in high-risk groups such as infants without fully-developed kidneys to process aluminum-containing compounds due to risk of metabolic bone disease, cholestatic hepatitis, and impaired mental development [247]. Despite these separate experiments alluding to adverse human reactions to artificial or natural color addities, allergies or adverse reactions to specific color additives are in fact very rare [248,249]. To supplement this, the United States FDA has performed *in vivo* studies to justify the reputed safety of color additives Allura Red [250,251] and Tartrazine [252]. According to [234], the formulator must have access to publicly-available data in order to

make a cognizant decision as to the safety and relevance of color additive molecules prior to their selection for a specific application.

The key to effective color additive selection for any formulation end use is to determine the following: First, consider the type of delivery method of coloration desired. Is only an outer coating necessary, making a pigment the suitable choice, or is it preferable to have the color molecules dispersed equally throughout the entire formulation or solution? This may lead to choosing a dye if the final product is completely water-soluble, or a lake pigment if waxes or insoluble pigments are necessary to color the formulation. Second, understand the role that specific functional groups of the color molecule will have on the solvent(s) selected. This is now measurable prior to formulating using quantum mechanical calculations as discussed in Chapters 2 and 3. In Chapter 2, it is evident that specific tautomer-like isomers of FD&C Red No. 40, D&C Yellow No. 11, and Brilliant Cresyl Blue contribute more strongly to the observed maximum absorbance peak spectral responsivities than their alternative structures in certain solvents. Depending on the molecule, this may be due to either keto-enol tautomerism as is the case with the SS Quinoline Yellow dye, or may affect airborne detection of an azo-hydrazone tautomeric molecule as an application of Allura Red studies in vapor phase. As described in Chapter 3, solvent effects play a strong role in determining whether dye aggregation or monomer-solvent effects dominate a given mixture as shown for oxazine charge-transfer dye molecule Brilliant Cresyl Blue. Each of these aspects of color additive selection can now be verified by use of advanced *ab initio* methods which produce tangible results in a matter of hours (or days, for large systems) prior to any batch preparation.

The nearly endless number of possible combinations of ions that may constitute binary mixtures can be synthesized in reality—or simply theorized initially in a conceptual approach—to assist the formulator in achieving more desired properties. Mixtures containing formulation ingredients which call for charged particles can exhibit greater variety in maximum absorbance spectral peak responsivity—and thus wider color spectra. On the other hand, typical conventional solvents require the careful addition of costly additives in smaller quantities that have dubious benefits as "quantum sufficient" (or "q.s.") of less than one percent in typical formulations. Extensive calculations of electronic excited state properties incorporating solvent effects have historically been considered time- and cost prohibitive for the average formulator conditioned to a more simplified "cookbook" approach in creative formulation product development. Today, industrial chemists are still reluctant to incorporate the various computational approaches into their research and development methods due to a persistent fear that artificial intelligence or CPU-produced results forego the sensory aspects that are strongly influential in determining a product's approval. This fear may eventually subside if the improvements in quantum computational power were immediately compared to the trends in our contemporary expectations of hand-held device processing power—in particular, to match cosmetic product hues to our skin tone using specially-designed mobile apps in lieu of trying on shades at a department store counter [253-254]. This method of trying on shades may transition to developing pharmaceutical creams or ointments that distinctly indicate or better match the site of topical application, improving overall product appearance and likelihood of patient compliance. The ease of applicability of solvation effects on the theoretical molecules constructed in the

computational workspace strongly encourages a more creative approach to the selection of not only dye, pigment, or color additive molecules, but also of solvent chosen. The volume of reputable literature on the assortment of customizable properties of ionic liquids has advanced at an equally phenomenal rate [255], and the research provided justifies that the inclusion of combinations of ILs and color additive molecules with charge transfer properties should be further pursued as new ventures for color or photophysical "tuning" of formulations.

Furthermore, the environmentally-conscious among pharmaceutical and cosmetic consumers may appreciate the sustainability aspects of ionic liquid formulations. Active pharmaceutical ingredients (APIs) that are water-soluble become a health risk to humans and aquatic life that rely on municipal wastewater treatment to filter out drugs and additives for healthy water consumption [209]. Unfortunately, APIs such as antibiotics exist in quantities so tiny that most particle filters (1 micromolar) allow the additives of smaller particle size (usually 1 nanomolar or less) to pass through and accumulate in "filtered" water supplies [209]. Color additives similarly have been reported to accumulate in bodies of water such as the Jian River [256,257], Yangtze River [256,258-259], Wenzhou River [256,260], and Xiangbi River [256] in China (and in "waste mud" encountered in Indian aluminum plants [230-231]) as a result of large-scale industrial pollution or improper chemical waste disposal. Ionic liquids are recyclable solvents for many reasons, including biodegradability [260]. They may be recovered and immediately reused after drug or contaminant solute molecule transport [261-262], and are effective in carbon dioxide capture [263-268]. This research has found that several existing color molecule classes may indeed successfully change or intensify the color of ionic liquids,

particularly those that contain high intensity transitions or charge transfer properties. However, further studies would have to assess whether or not color additive—ionic liquid mixtures can be chemically-engineered to shed the color additive after its initial purpose has been fulfilled. As the quest for more sustainable formulation additives continues, the cradle-to-grave implications of solute-solvent interactions will become a main focus of decisions to incorporate "trendy" or classic solvents and color additives over other types of similarly aesthetic additives.

As basis sets and approximations continue to be developed regularly, thermodynamic data and total electronic excitation energies may be able to better describe properties of a more diverse array of color molecule classes than what currently exists. Other human senses may begin to be mathematically deciphered, and later accurately modeled, leading to better understanding of not only healthy or normal sensations but also abnormalities or hereditary dysfunctions. Perhaps the nerve impulses of touch could even be mapped in our lifetime. With so much ubiquitous computational equipment at our disposal, the application of density functional theory and its time-dependent counterpart to accurately portray color spectra of existing molecules paves the way for novel chromophore and pharmacophore development to better suit the ultimate goals of formulators: to create products that reflect ever-changing trends in personal care. As form follows function in all creative pursuits, these contributions to the scientific community should coincide with modern perceptions of maintaining universally-accepted values of health, beauty, and wellness in our current era.

References

[1] C. Reichardt, "Empirical Parameters of the Polarity of Solvents," *Angewandte Chemie International Edition* in English, vol. 4, no. 1, pp. 29-40, 1965.

[2] C. Reichardt, "Empirical Parameters of Solvent Polarity as Linear Free-Energy Relationships," *Angewandte Chemie International Edition* in English, vol. 18, no. 2, pp. 98-110, 1979.

[3] C. Reichardt, "Solvatochromism, thermochromism, piezochromism, halochromism, and chiro-solvatochromism of pyridinium N-phenoxide betaine dyes," *Chemical Society Reviews*, vol. 21, no. 3, 1992.

[4] C. Reichardt, "Solvatochromic Dyes as Solvent Polarity Indicators," *Chemical Reviews*, vol. 94, no. 8, pp. 2319-2358, 1994.

[5] C. Reichardt, "Polarity of ionic liquids determined empirically by means of solvatochromic pyridinium N-phenolate betaine dyes," *Green Chemistry*, vol. 7, no. 5, 2005.

[6] C. Reichardt and T. Welton, *Solvents and Solvent Effects in Organic Chemistry*, 4th ed. Weinheim: Wiley-VCH, 2011, p. 692.

[7] O. S. Wolfbeis, "Solvent and Acidity Dependence of the Absorption and Fluorescence Spectra of 3-Hydroxycoumarin *," *Zeitschrift für Physikalische Chemie*, vol. 125, no. 1, pp. 15-20, 1981.

[8] S. K. Jessie A. Key, Qadir K. Timerghazin, Alex Brown, Christopher W. Cairo, "Photophysical characterization of triazole-substituted coumarin fluorophores," *Dyes and Pigments*, vol. 82, pp. 196-203, January 5 2009 2009.

[9] M. N. Kobrak, "Characterization of the solvation dynamics of an ionic liquid via molecular dynamics simulation," *J Chem Phys*, vol. 125, no. 6, p. 64502, Aug 14 2006.

[10] M. Maroncelli, X.-X. Zhang, M. Liang, D. Roy, and N. P. Ernsting, "Measurements of the complete solvation response of coumarin 153 in ionic liquids and the accuracy of simple dielectric continuum predictions," *Faraday Discuss.*, vol. 154, pp. 409-424, 2012.

[11] Z. Wang et al., "Nano self-aggregation of new benzotriazole-coumarin dyads displaying strengthened emission with huge Stokes shift," *Dyes and Pigments*, vol. 157, pp. 140-142, 2018.

[12] A. Barik and K. Indira Priyadarsini, "Solvent dependent photophysical properties of dimethoxy curcumin," *Spectrochim Acta A Mol Biomol Spectrosc*, vol. 105, pp. 267-72, Mar 15 2013.

[13] A. Dutta, B. Boruah, A. K. Manna, B. Gohain, P. M. Saikia, and R. K. Dutta, "Stabilization of diketo tautomer of curcumin by premicellar anionic surfactants: UV-

Visible, fluorescence, tensiometric and TD-DFT evidences," *Spectrochim Acta A Mol Biomol Spectrosc*, vol. 104, pp. 150-7, Mar 2013.

[14] S.-i. Kawano, Y. Inohana, Y. Hashi, and J.-M. Lin, "Analysis of keto-enol tautomers of curcumin by liquid chromatography/mass spectrometry," *Chinese Chemical Letters*, vol. 24, no. 8, pp. 685-687, 2013.

[15] M. Khadem Sadigh, M. S. Zakerhamidi, A. N. Shamkhali, and E. Babaei, "Photo-physical behaviors of various active forms of curcumin in polar and low polar environments," *Journal of Photochemistry and Photobiology A: Chemistry*, vol. 348, pp. 188-198, 2017.

[16] L. Shen, H.-F. Ji, and H.-Y. Zhang, "A TD-DFT study on triplet excited-state properties of curcumin and its implications in elucidating the photosensitizing mechanisms of the pigment," *Chemical Physics Letters*, vol. 409, no. 4-6, pp. 300-303, 2005.

[17] H.-F. J. Liang Shen, "Theoretical study on physicochemical properties of curcumin," *Spectrochim Acta Part A*, vol. 67, pp. 619-623, August 15 2006 2007.

[18] Y. Manolova, V. Deneva, L. Antonov, E. Drakalska, D. Momekova, and N. Lambov, "The effect of the water on the curcumin tautomerism: a quantitative approach," *Spectrochim Acta A Mol Biomol Spectrosc*, vol. 132, pp. 815-20, Nov 11 2014.

[19] S. Mondal, S. Ghosh, and S. P. Moulik, "Stability of curcumin in different solvent and solution media: UV-visible and steady-state fluorescence spectral study," *J Photochem Photobiol B*, vol. 158, pp. 212-8, May 2016.

[20] Z. Moussa, M. Chebl, and D. Patra, "Fluorescence of tautomeric forms of curcumin in different pH and biosurfactant rhamnolipids systems: Application towards on-off ratiometric fluorescence temperature sensing," *J Photochem Photobiol B*, vol. 173, pp. 307-317, Aug 2017.

[21] K. I. Pryadarsini, "Photophysics, photochemistry and photobiology of curcumin: Studies from organic solutions, biomimetics and living cells," *Journal of Photochemistry and Photobiology C: Photochemistry Reviews*, vol. 80, pp. 81-95, May 11 2009 2009.

[22] C. Santezi, B. D. Reina, and L. N. Dovigo, "Curcumin-mediated Photodynamic Therapy for the treatment of oral infections-A review," *Photodiagnosis Photodyn Ther*, vol. 21, pp. 409-415, Mar 2018.

[23] D. Yanagisawa et al., "Relationship between the tautomeric structures of curcumin derivatives and their Abeta-binding activities in the context of therapies for Alzheimer's disease," *Biomaterials*, vol. 31, no. 14, pp. 4179-85, May 2010.

[24] M. Leopoldini, N. Russo, S. Chiodo, and M. Toscano, "Iron chelation by the powerful antioxidant flavonoid quercetin," *Journal of agricultural food chemistry*, vol. 54, no. 17, pp. 6343-6351, 2006.

[25] S. Fiorucci, J. Golebiowski, D. Cabrol-Bass, and S. Antonczak, "Oxygenolysis of flavonoid compounds: DFT description of the mechanism for quercetin," *Chemphyschem*, vol. 5, no. 11, pp. 1726-33, Nov 12 2004.

[26] D. Jeevitha, K. Sadasivam, R. Praveena, and R. Jayaprakasam, "DFT study of glycosyl group reactivity in quercetin derivatives," *J Mol Structure*, vol. 1120, pp. 15-24, 2016.

[27] J. Mack, Y. Asano, N. Kobayashi, and M. J. Stillman, "Application of MCD spectroscopy and TD-DFT to a highly non-planar porphyrinoid ring system. New insights on red-shifted porphyrinoid spectral bands," *J Am Chem Soc*, vol. 127, no. 50, pp. 17697-711, Dec 21 2005.

[28] M. Sun, Y. Ding, G. Cui, and Y. Liu, "S1 and S2 excited states of gas-phase Schiff-base retinal chromophores: a time-dependent density functional theoretical investigation," *J Phys Chem A*, vol. 111, no. 15, pp. 2946-50, Apr 19 2007.

[29] L. A. Montero-Cabrera et al., "CNDOL: A fast and reliable method for the calculation of electronic properties of very large systems. Applications to retinal binding pocket in rhodopsin and gas phase porphine," *J Chem Phys*, vol. 127, no. 14, p. 145102, Oct 14 2007.

[30] F. J. Avila Ferrer, F. Santoro, and R. Improta, "The excited state behavior of cytosine in the gas phase: A TD-DFT study," *Computational and Theoretical Chemistry*, vol. 1040-1041, pp. 186-194, 2014.

[31] C. S. Lopez, O. N. Faza, S. L. Estevez, and A. R. de Lera, "Computation of vertical excitation energies of retinal and analogs: scope and limitations," *J Comput Chem*, vol. 27, no. 1, pp. 116-23, Jan 15 2006.

[32] L. Pinto da Silva and J. C. Esteves da Silva, "TD-DFT/molecular mechanics study of the Photinus pyralis bioluminescence system," *J Phys Chem B*, vol. 116, no. 6, pp. 2008-13, Feb 16 2012.

[33] R. Mera-Adasme and M. Dominguez, "A computationally-derived model for the solvatochromism of p-phenolates with high predictive power," *Phys Chem Chem Phys*, vol. 20, no. 26, pp. 18127-18132, Jul 4 2018.

[34] A. Charaf-Eddin, B. Le Guennic, and D. Jacquemin, "Excited-states of BODIPY–cyanines: ultimate TD-DFT challenges?," *RSC Adv.*, vol. 4, no. 90, pp. 49449-49456, 2014.

[35] I. Duchemin, C. A. Guido, D. Jacquemin, and X. Blase, "The Bethe-Salpeter formalism with polarisable continuum embedding: reconciling linear-response and state-specific features," *Chem Sci*, vol. 9, no. 19, pp. 4430-4443, May 21 2018.

[36] J. Gierschner, H.-G. Mack, L. Lüer, and D. Oelkrug, "Fluorescence and absorption spectra of oligophenylenevinylenes: Vibronic coupling, band shapes, and solvatochromism," *J Chem Phys*, vol. 116, no. 19, 2002.

[37] C. Adamo et al., "Exploring excited states using time dependent density functional theory and density-based indexes," *J Coordination Chemistry Reviews*, vol. 304, pp. 166-178, 2015.

[38] X. Blase, I. Duchemin, and D. Jacquemin, "The Bethe-Salpeter equation in chemistry: relations with TD-DFT, applications and challenges," *Chem Soc Rev*, vol. 47, no. 3, pp. 1022-1043, Feb 5 2018.

[39] A. Charaf-Eddin, T. Cauchy, F.-X. Felpin, and D. Jacquemin, "Vibronic spectra of organic electronic chromophores," *RSC Adv.*, vol. 4, no. 98, pp. 55466-55472, 2014.

[40] Z. C. Wong, W. Y. Fan, and T. S. Chwee, "Computational modelling of singlet excitation energy transfer: a DFT/TD-DFT study of the ground and excited state properties of a syn bimane dimer system using non-empirically tuned range-separated functionals," *New Journal of Chemistry*, vol. 42, no. 16, pp. 13732-13743, 2018.

[41] C. S. Lopez, O. N. Faza, S. L. Estevez, and A. R. de Lera, "Computation of vertical excitation energies of retinal and analogs: scope and limitations," *J Comput Chem*, vol. 27, no. 1, pp. 116-23, Jan 15 2006.

[42] L. A. Montero-Cabrera et al., "CNDOL: A fast and reliable method for the calculation of electronic properties of very large systems. Applications to retinal binding pocket in rhodopsin and gas phase porphine," *J Chem Phys*, vol. 127, no. 14, p. 145102, Oct 14 2007.

[43] I. V. Rostov, R. D. Amos, R. Kobayashi, G. Scalmani, and M. J. Frisch, "Studies of the ground and excited-state surfaces of the retinal chromophore using CAM-B3LYP," *J Phys Chem B*, vol. 114, no. 16, pp. 5547-55, Apr 29 2010.

[44] I. V. Rostov, R. Kobayashi, and R. D. Amos, "Comparing long-range corrected functionals in the cis–trans isomerisation of the retinal chromophore," *Molecular Physics*, vol. 110, no. 19-20, pp. 2329-2336, 2012.

[45] C. C. Hsieh et al., "Comprehensive studies on an overall proton transfer cycle of the ortho-green fluorescent protein chromophore," *J Am Chem Soc*, vol. 133, no. 9, pp. 2932-43, Mar 9 2011.

[46] Q. K. Timerghazin, H. J. Carlson, C. Liang, R. E. Campbell, and A. Brown, "Computational prediction of absorbance maxima for a structurally diverse series of engineered green fluorescent protein chromophores," *J Phys Chem B*, vol. 112, no. 8, pp. 2533-41, Feb 28 2008.

[47] J. J. van Thor, "Photoreactions and dynamics of the green fluorescent protein," *Chem Soc Rev*, vol. 38, no. 10, pp. 2935-50, Oct 2009.

[48] L. Pinto da Silva and J. C. Esteves da Silva, "TD-DFT/molecular mechanics study of the Photinus pyralis bioluminescence system," *J Phys Chem B*, vol. 116, no. 6, pp. 2008-13, Feb 16 2012.

[49] J. Fabian, "TDDFT-calculations of Vis/NIR absorbing compounds," *Dyes and Pigments*, vol. 84, no. 1, pp. 36-53, 2010.

[50] D. Jacquemin, I. Duchemin, and X. Blase, "0-0 Energies Using Hybrid Schemes: Benchmarks of TD-DFT, CIS(D), ADC(2), CC2, and BSE/GW formalisms for 80 Real-Life Compounds," *J Chem Theory Comput*, vol. 11, no. 11, pp. 5340-59, Nov 10 2015.

[51] A. D. Katharyn Fletcher, Shirin Faraji, "Potential energy surfaces and approximate kinetic model for the excited state dynamics of Pigment Yellow 101," *Computational and Theoretical Chemistry*, vol. 1040-1041, pp. 177-185, April 4, 2014 2014.

[52] R. M. Cammi, Benedetta; Tomasi, Jacopo, "Fast Evaluation of Geometries and Properties of Excited Molecules in Solution: A Tamm-Dancoff Model with Application to 4-Dimethylaminobenzonitrile," *J. Phys. Chem. A*, vol. 104, pp. 5631-5637, 2000.

[53] S. G. Maja Parac, "A TDDFT study of the lowest excitation energies of polycyclic aromatic hydrocarbons," *Chemical Physics*, vol. 292, pp. 11-21, February 4, 2003 2003.

[54] L. Shen, H.-F. Ji, and H.-Y. Zhang, "A TD-DFT study on triplet excited-state properties of curcumin and its implications in elucidating the photosensitizing mechanisms of the pigment," *Chemical Physics Letters*, vol. 409, no. 4-6, pp. 300-303, 2005.

[55] D. Jacquemin and E. A. Perpète, "Ab initio calculations of the colour of closed-ring diarylethenes: TD-DFT estimates for molecular switches," *Chemical Physics Letters*, vol. 429, no. 1-3, pp. 147-152, 2006.

[56] A. M.-L. Samuel Frutos-Puerto, M. Elena Martin, Manuel A. Aguilar, "Theoretical study of the absorption and emission spectra of tha anionic p-coumaric methyl ester in gas phase and in solution," *Computational and Theoretical Chemistry*, pp. 287-294, April 25 2014 2014.

[57] X. Lopez, M. A. Marques, A. Castro, and A. Rubio, "Optical absorption of the blue fluorescent protein: a first-principles study," *J Am Chem Soc*, vol. 127, no. 35, pp. 12329-37, Sep 7 2005.

[58] M. A. Marques, X. Lopez, D. Varsano, A. Castro, and A. Rubio, "Time-dependent density-functional approach for biological chromophores: the case of the green fluorescent protein," *Phys Rev Lett*, vol. 90, no. 25 Pt 1, p. 258101, Jun 27 2003.

[59] N. S. U. Lourderaj; Manoj K. Harbola, "Time-dependent density functional theoretical study of low lying excited states of F2," *Chemical Physics Letters*, vol. 366, pp. 88-94, September 17 2002 2002.

[60] M. Guillaume, V. Liégeois, B. Champagne, and F. Zutterman, "Time-dependent density functional theory investigation of the absorption and emission spectra of a cyanine dye," *Chemical Physics Letters*, vol. 446, no. 1-3, pp. 165-169, 2007.

[61] S. Fantacci, F. De Angelis, A. Sgamellotti, A. Marrone, and N. Re, "Photophysical properties of [Ru(phen)2(dppz)]2+ intercalated into DNA: an integrated Car-Parrinello and TDDFT study," *J Am Chem Soc*, vol. 127, no. 41, pp. 14144-5, Oct 19 2005.

[62] M. A. R. M. Clara C.S. Sousa, Victor M.F. Morais, "Energetics and stability of azulene: from experimental thermochemistry to high-level quantum chemical calculations," *J. Chem. Thermodynamics*, vol. 73, pp. 101-109, November 11 2013 2014.

[63] J. C. Ling-Jun He, Fu-Quan Bai, Ran Jia, Jian Wang, Hong-Xing Zhang, "Fine-tuning pi-spacer for high efficiency performance DSSC: a theoretical exploration with D-pi-A based organic dye," *Dyes and Pigments*, vol. 141, pp. 251-261, February 13, 2017 2017.

[64] X. A. Thibaud Etienne, Antonio Monari, "QM/MM calculation of absorption spectra of complex systems: the case of human serum albumin," *Computational and Theoretical Chemistry*, vol. 1040-1041, pp. 360-366, January 7 2014 2014.

[65] E. C. Daniele Varsano, Olivia Pulci, Adriano Mosca Conte, Leonardo Guidoni, "Ground state structures and electronic excitations of biological chromophores at Quantum Monte Carolo/Many Body Green's Function Theory level," *Computational and Theoretical Chemistry*, vol. 1040-1041, pp. 338-346, March 6, 2014 2014.

[66] Y. Zhao and D. G. Truhlar, "Density functional for spectroscopy: no long-range self-interaction error, good performance for Rydberg and charge-transfer states, and better performance on average than B3LYP for ground states," *J Phys Chem A*, vol. 110, no. 49, pp. 13126-30, Dec 14 2006.

[67] S. D. Sema Caglar, Zerrin Heren, Orhan Buyukgungor, "Crystal structures, thermal, spectroscopic properties and DFT/TD-DFT based investigation of [M(bba)2(phen)] (M= Cu and Zn, bba = 2-benzoylbenzoato, phen = 1,10-phenanthroline)," *Polyhedron*, vol. 30, pp. 1389-1395, February 21 2011 2011.

[68] A. Chantzis, A. D. Laurent, C. Adamo, and D. Jacquemin, "Is the Tamm-Dancoff Approximation Reliable for the Calculation of Absorption and Fluorescence Band Shapes?," *J Chem Theory Comput*, vol. 9, no. 10, pp. 4517-25, Oct 8 2013.

[69] E. A. Perpete, C. Lambert, V. Wathelet, J. Preat, and D. Jacquemin, "Ab initio studies of the lambda(max) of naphthoquinones dyes," *Spectrochim Acta A Mol Biomol Spectrosc*, vol. 68, no. 5, pp. 1326-33, Dec 31 2007.

[70] K. L. Meguellati, Sylvain; Spichty, Martin, "A conceptually improved TD-DFT approach for predicting the maximum absorption wavelength of cyanine dyes," *Dyes and Pigments*, vol. 90, pp. 114-118, December 3 2010 2010.

[71] C. Loison, R. Antoine, M. Broyer, P. Dugourd, J. Guthmuller, and D. Simon, "Microsolvation effects on the optical properties of crystal violet," *Chemistry*, vol. 14, no. 24, pp. 7351-7, 2008.

[72] C. C. Maria Vega Canamares, Ronald L. Birke, John R. Lombardi, "DFT, SERS, and Single-Molecule SERS of Crystal Violet," *J. Phys. Chem. C*, vol. 112, pp. 20295-20300, Dec 17, 2018 2008.

[73] Lili Lin, Zhongjie Wang, Jianzhong Fan, and C. Want, "Theoretical insights on the electroluminescent mechanism of thermally activated delayed fluorescence emitters," *Organic Electronics*, vol. 41, pp. 17-25, December 17, 2018 2017.

[74] Y. G. S. Isa Sidir, "Experimental and Theoretical Investigation of the molecular, electronic structure and solvatohromism of phenyl salicylate: External electric field effect on the electronic structure," *Journal of Molecular Structure*, vol. 1147, pp. 206-216, June 21, 2017 2017.

[75] J. P. Denis Jacquemin, Eric A. Perpete, "A TD-DFT study of the absorption spectra of fast dye salts," *Chemical Physics Letters*, vol. 410, pp. 254-259, April 28, 2005 2005.

[76] A. H. Tobias Risthaus, Stefan Grimme, "Excited States using the simplified Tamm-Dancoff Approach for range-separated hybrid density functionals: development and application," *Physical Chemistry Chemical Physics*, vol. 16, pp. 14408-14419, 2013.

[77] R. Kian, M. S. Zakerhamidi, A. N. Shamkhali, and P. Nesari, "The interactional behaviors and photo-physical properties of two triarylmethane drugs in solvent media," *Journal of Molecular Liquids*, vol. 225, pp. 653-661, 2017.

[78] A. D. Laurent and D. Jacquemin, "TD-DFT benchmarks: A review," *International Journal of Quantum Chemistry*, vol. 113, no. 17, pp. 2019-2039, 2013.

[79] F. J. Avila Ferrer, J. Cerezo, J. Soto, R. Improta, and F. Santoro, "First-principle computation of absorption and fluorescence spectra in solution accounting for vibronic structure, temperature effects and solvent inhomogenous broadening," *Computational and Theoretical Chemistry*, vol. 1040-1041, pp. 328-337, 2014.

[80] V. Barone, M. Biczysko, J. Bloino, L. Carta, and A. Pedone, "Reprint of “Environmental and dynamical effects on the optical properties of molecular systems by time-independent and time-dependent approaches: Coumarin derivatives as test cases”," *Computational and Theoretical Chemistry*, vol. 1040-1041, pp. 144-157, 2014.

[81] D. Jacquemin and C. Adamo, "Computational Molecular Electronic Spectroscopy with TD-DFT," *Top Curr Chem*, vol. 368, pp. 347-75, 2016.

[82] D. Jacquemin, E. Bremond, A. Planchat, I. Ciofini, and C. Adamo, "TD-DFT Vibronic Couplings in Anthraquinones: From Basis Set and Functional Benchmarks to Applications for Industrial Dyes," *J Chem Theory Comput*, vol. 7, no. 6, pp. 1882-92, Jun 14 2011.

[83] D. Jacquemin, B. Mennucci, and C. Adamo, "Excited-state calculations with TD-DFT: from benchmarks to simulations in complex environments," *Phys Chem Chem Phys*, vol. 13, no. 38, pp. 16987-98, Oct 14 2011.

[84] D. Jacquemin, C. Peltier, and I. Ciofini, "Visible spectrum of naphthazarin investigated through Time-Dependent Density Functional Theory," *Chemical Physics Letters*, vol. 493, no. 1-3, pp. 67-71, 2010.

[85] D. Jacquemin, E. A. Perpete, I. Ciofini, and C. Adamo, "Accurate simulation of optical properties in dyes," *Acc Chem Res*, vol. 42, no. 2, pp. 326-34, Feb 17 2009.

[86] D. Jacquemin, E. A. Perpete, F. Maurel, and A. Perrier, "TD-DFT simulations of the electronic properties of star-shaped photochromes," *Phys Chem Chem Phys*, vol. 12, no. 28, pp. 7994-8000, Jul 28 2010.

[87] D. Jacquemin et al., "Time-dependent density functional theory investigation of the absorption, fluorescence, and phosphorescence spectra of solvated coumarins," *J Chem Phys*, vol. 125, no. 16, p. 164324, Oct 28 2006.

[88] D. Jacquemin, E. A. Perpete, G. E. Scuseria, I. Ciofini, and C. Adamo, "TD-DFT Performance for the Visible Absorption Spectra of Organic Dyes: Conventional versus Long-Range Hybrids," *J Chem Theory Comput*, vol. 4, no. 1, pp. 123-35, Jan 2008.

[89] D. Jacquemin, A. Planchat, C. Adamo, and B. Mennucci, "TD-DFT Assessment of Functionals for Optical 0-0 Transitions in Solvated Dyes," *J Chem Theory Comput*, vol. 8, no. 7, pp. 2359-72, Jul 10 2012.

[90] D. Jacquemin, J. Preat, V. Wathelet, and E. A. Perpète, "Time-dependent density functional theory determination of the absorption spectra of naphthoquinones," *Chemical Physics*, vol. 328, no. 1-3, pp. 324-332, 2006.

[91] E. A. Perpète and D. Jacquemin, "TD-DFT benchmark for indigoïd dyes," *Journal of Molecular Structure: THEOCHEM*, vol. 914, no. 1-3, pp. 100-105, 2009.

[92] E. A. Perpete, C. Lambert, V. Wathelet, J. Preat, and D. Jacquemin, "Ab initio studies of the lambda(max) of naphthoquinones dyes," *Spectrochim Acta A Mol Biomol Spectrosc*, vol. 68, no. 5, pp. 1326-33, Dec 31 2007.

[93] A. Prlj, M. E. Sandoval-Salinas, D. Casanova, D. Jacquemin, and C. Corminboeuf, "Low-Lying pipi* States of Heteroaromatic Molecules: A Challenge for Excited State Methods," *J Chem Theory Comput*, vol. 12, no. 6, pp. 2652-60, Jun 14 2016.

[94] D. Rivero, M. Á. Fernández-González, and L. M. Frutos, "Tuning molecular excitation energy with external forces," *Computational and Theoretical Chemistry*, vol. 1040-1041, pp. 106-111, 2014.

[95] K. Sakata, N. Saito, and T. Honda, "Ab initio study of molecular structures and excited states in anthocyanidins," *Tetrahedron*, vol. 62, no. 15, pp. 3721-3731, 2006.

[96] M. B. Vincenzo Barone, Camille Latouche, Andrea Pasti, "Virtual eyes for technology and cultural heritage: towards computational strategy for new and old indigo-based dyes," *Theo Chem Acc*, 2015.

[97] K. I. Pryadarsini, "Photophysics, photochemistry and photobiology of curcumin: Studies from organic solutions, biomimetics and living cells," *Journal of photochemistry and photobiology c: photochemistry reviews*, vol. 80, pp. 81-95, May 11 2009 2009.

[98] H.-F. J. Liang Shen, Hong-Yu Zhang, "A TD-DFT study on photo-physicochemical properties of hypocrellin A and its implications for elucidating the photosensitizing mechanisms of the pigment," *Journal of photochemistry and photobiology A: Chemistry*, vol. 180, pp. 65-68, September 21 2005 2006.

[99] G. G. Valentina Cantatore, Maurizio Persico, "Simulation of the pi-pi* photodynamics of azobenzene: Decoherence and solvent effects," *Computational and Theoretical Chemistry*, vol. 1040-1041, pp. 126-135, February 10 2014 2014.

[100] F. J. Avila Ferrer, J. Cerezo, J. Soto, R. Improta, and F. Santoro, "First-principle computation of absorption and fluorescence spectra in solution accounting for vibronic structure, temperature effects and solvent inhomogenous broadening," *Computational and Theoretical Chemistry*, vol. 1040-1041, pp. 328-337, 2014.

[101] D. Jeevitha, K. Sadasivam, R. Praveena, and R. Jayaprakasam, "DFT study of glycosyl group reactivity in quercetin derivatives," *Journal of Molecular Structure*, vol. 1120, pp. 15-24, 2016.

[102] A. P. Santu Biswas, Pranab Sarkar, "Effect of additional donor group on the charge transfer/recombination dynamics of a photoactive organic dye: a quantum mechanical investigation," *Computational and Theoretical Chemistry*, vol. 1103, pp. 38-47, January 10 2017 2017.

[103] N. S. Xian-Fu Zhang, Xulin Lu, Wenyu Jia, "Benzoate-modified rhodamine dyes: large change in fluorescence properties due to photoinduced electron transfer," *Journal of Luminescence*, vol. 179, pp. 511-517, July 20 2016 2016.

[104] U. R. Marika Savarese, Raolo A. Netti, Carlo Adamo, Ilaria Ciofini, Nadia Rega, "Modeling of charge transfer processes to understand photophysical signatures: The case of Rhodamine 110," *Chemical Physics Letters*, vol. 610-611, pp. 148-152, July 9 2014 2014.

[105] S. Chibani, D. Jacquemin, and A. D. Laurent, "Modelling solvent effects on the absorption and emission spectra of constrained cyanines with both implicit and explicit QM/EFP models," *Computational and Theoretical Chemistry*, vol. 1040-1041, pp. 321-327, 2014.

[106] A. H. S. Maarten T.P. Beerepoot, Kenneth Ruud, Jogvan Magnus Haugaard Olsen, Jacob Kongsted, "Convergence of environmental polarization effects in multiscale modeling of excitation energies," *Computational and Theoretical Chemistry*, vol. 1040-1041, pp. 304-311, March 17 2014 2014.

[107] G. J. Zhao et al., "Photoinduced intramolecular charge transfer and S2 fluorescence in thiophene-pi-conjugated donor-acceptor systems: experimental and TDDFT studies," *Chemistry*, vol. 14, no. 23, pp. 6935-47, 2008.

[108] D. R. Cardoso, P. Homem-de-Mello, K. Olsen, A. B. da Silva, D. W. Franco, and L. H. Skibsted, "Deactivation of triplet-excited riboflavin by purine derivatives: Important role of uric acid in light-induced oxidation of milk sensitized by riboflavin," *Journal of agricultural food chemistry*, vol. 53, no. 9, pp. 3679-3684, 2005.

[109] D. R. Cardoso, S. H. Libardi, and L. H. Skibsted, "Riboflavin as a photosensitizer. Effects on human health and food quality," *J Food function*, vol. 3, no. 5, pp. 487-502, 2012.

[110] M. Insińska-Rak et al., "New photochemically stable riboflavin analogue—3-Methyl-riboflavin tetraacetate," *Journal of Photochemistry Photobiology A: Chemistry*, vol. 186, no. 1, pp. 14-23, 2007.

[111] H.-F. Ji and L. Shen, "A DFT study on deactivation of triplet excited state riboflavin by polyphenols," *J International journal of molecular sciences*, vol. 9, no. 10, pp. 1908-1914, 2008.

[112] B. Klaumünzer, D. Kröner, and P. J. T. J. o. P. C. B. Saalfrank, "(TD-) DFT calculation of vibrational and vibronic spectra of riboflavin in solution," vol. 114, no. 33, pp. 10826-10834, 2010.

[113] E. Sikorska et al., "Spectroscopy and photophysics of flavin related compounds: Riboflavin and iso-(6, 7)-riboflavin," *J Chemical physics*, vol. 314, no. 1-3, pp. 239-247, 2005.

[114] S. Antonczak, "Electronic description of four flavonoids revisited by DFT method," *Journal of Molecular Structure: THEOCHEM*, vol. 856, no. 1-3, pp. 38-45, 2008.

[115] F. Di Meo, J. C. Sancho Garcia, O. Dangles, and P. Trouillas, "Highlights on Anthocyanin Pigmentation and Copigmentation: A Matter of Flavonoid pi-Stacking Complexation To Be Described by DFT-D," *J Chem Theory Comput*, vol. 8, no. 6, pp. 2034-43, Jun 12 2012.

[116] A. Amat, C. Clementi, C. Miliani, A. Romani, A. Sgamellotti, and S. Fantacci, "Complexation of apigenin and luteolin in weld lake: a DFT/TDDFT investigation," *Phys Chem Chem Phys*, vol. 12, no. 25, pp. 6672-84, Jul 7 2010.

[117] Y. Rong, Z. Wang, J. Wu, and B. Zhao, "A theoretical study on cellular antioxidant activity of selected flavonoids," *J Spectrochimica Acta Part A: Molecular Biomolecular Spectroscopy*, vol. 93, pp. 235-239, 2012.

[118] K. Sadasivam and R. Kumaresan, "Theoretical investigation on the antioxidant behavior of chrysoeriol and hispidulin flavonoid compounds – A DFT study," *Computational and Theoretical Chemistry*, vol. 963, no. 1, pp. 227-235, 2011.

[119] J. Tošović and S. Marković, "Reproduction and interpretation of the UV–vis spectra of some flavonoids," *J Chemical Papers*, vol. 71, no. 3, pp. 543-552, 2017.

[120] J. Tošović, Ž. Milošević, and S. Marković, "Simulation of the UV/Vis spectra of flavonoids," in *Bioinformatics and Bioengineering (BIBE)*, 2015 IEEE 15th International Conference on, 2015, pp. 1-6: IEEE.

[121] C. Raynaud, R. Poteau, L. Maron, and F. Jolibois, "Ab initio molecular dynamics simulation of the UV absorption spectrum of β-ionone," *Journal of Molecular Structure: THEOCHEM*, vol. 771, no. 1-3, pp. 43-50, 2006.

[122] G. O. B. K. Richard and S. H. Q. N. Gunaratne, "Ionic Liquid Systems," United States of America Patent US 20160376522 A1, 2016. Available: https://www.google.com/patents/US20160376522.

[123] M. A. R. Martins, U. Domańska, B. Schröder, J. A. P. Coutinho, and S. P. Pinho, "Selection of Ionic Liquids to be Used as Separation Agents for Terpenes and Terpenoids," *ACS Sustainable Chemistry & Engineering*, vol. 4, no. 2, pp. 548-556, 2015.

[124] P. Berton, K. Bica, and R. D. Rogers, "Ionic liquids for consumer products: Dissolution, characterization, and controlled release of fragrance compositions," *Fluid Phase Equilibria*, vol. 450, pp. 51-56, 2017.

[125] K. Ueno, H. Tokuda, and M. Watanabe, "Ionicity in ionic liquids: correlation with ionic structure and physicochemical properties," *Phys Chem Chem Phys*, vol. 12, no. 8, pp. 1649-58, Feb 28 2010.

[126] E. I. Izgorodina, "Towards large-scale, fully ab initio calculations of ionic liquids," *Phys Chem Chem Phys*, vol. 13, no. 10, pp. 4189-207, Mar 14 2011.

[127] D. R. MacFarlane and K. R. Seddon, "Ionic Liquids—Progress on the Fundamental Issues," *Australian Journal of Chemistry*, vol. 60, no. 1, 2007.

[128] H. Saba, X. Zhu, Y. Chen, and Y. Zhang, "Determination of physical properties for the mixtures of [BMIM]Cl with different organic solvents," *Chinese Journal of Chemical Engineering*, vol. 23, no. 5, pp. 804-811, 2015.

[129] H. Niedermeyer, J. P. Hallett, I. J. Villar-Garcia, P. A. Hunt, and T. Welton, "Mixtures of ionic liquids," *Chem Soc Rev*, vol. 41, no. 23, pp. 7780-802, Dec 7 2012.

[130] F. Endres and S. Zein El Abedin, "Air and water stable ionic liquids in physical chemistry," *Phys Chem Chem Phys*, vol. 8, no. 18, pp. 2101-16, May 14 2006.

[131] R. M. Lynden-Bell, "Screening of pairs of ions dissolved in ionic liquids," *Phys Chem Chem Phys*, vol. 12, no. 8, pp. 1733-40, Feb 28 2010.

[132] B. M. Sato, C. G. de Oliveira, C. T. Martins, and O. A. El Seoud, "Thermo-solvatochromism in binary mixtures of water and ionic liquids: on the relative importance of solvophobic interactions," *Phys Chem Chem Phys*, vol. 12, no. 8, pp. 1764-71, Feb 28 2010.

[133] X. Song, "Solvation dynamics in ionic fluids: an extended Debye-Huckel dielectric continuum model," *J Chem Phys*, vol. 131, no. 4, p. 044503, Jul 28 2009.

[134] S. M. Urahata and M. C. Ribeiro, "Single particle dynamics in ionic liquids of 1-alkyl-3-methylimidazolium cations," *J Chem Phys*, vol. 122, no. 2, p. 024511, Jan 8 2005.

[135] Y. Shim, D. Jeong, M. Y. Choi, and H. J. Kim, "Rotational dynamics of a diatomic solute in the room-temperature ionic liquid 1-ethyl-3-methylimidazolium hexafluorophosphate," *J Chem Phys*, vol. 125, no. 6, p. 61102, Aug 14 2006.

[136] S. Arzhantsev, H. Jin, G. A. Baker, and M. Maroncelli, "Measurements of the complete solvation response in ionic liquids," *J Phys Chem B*, vol. 111, no. 18, pp. 4978-89, May 10 2007.

[137] K. Low, L. Wylie, D. L. A. Scarborough, and E. I. Izgorodina, "Is it possible to control kinetic rates of radical polymerisation in ionic liquids?," *Chem Commun (Camb)*, vol. 54, no. 80, pp. 11226-11243, Oct 4 2018.

[138] J. G. Huddleston, A. E. Visser, W. M. Reichert, H. D. Willauer, G. A. Broker, and R. D. Rogers, "Characterization and comparison of hydrophilic and hydrophobic room temperature ionic liquids incorporating the imidazolium cation," *Green Chemistry*, vol. 3, no. 4, pp. 156-164, 2001.

[139] D. Jeong, M. Choi, Y. Jung, and H. J. Kim, "$1/f$ spectrum and memory function analysis of solvation dynamics in a room-temperature ionic liquid," *The Journal of chemical physics*, vol. 128, no. 17, p. 174504, 2008.

[140] M. H. Ghatee and Y. Ansari, "Ab initio molecular dynamics simulation of ionic liquids," *J Chem Phys*, vol. 126, no. 15, p. 154502, Apr 21 2007.

[141] T. Singh and A. Kumar, "Static dielectric constant of room temperature ionic liquids: internal pressure and cohesive energy density approach," *J Phys Chem B*, vol. 112, no. 41, pp. 12968-72, Oct 16 2008.

[142] M. V. Fedorov and A. A. Kornyshev, "Ionic liquids at electrified interfaces," *Chem Rev*, vol. 114, no. 5, pp. 2978-3036, Mar 12 2014.

[143] C. Schroder, T. Rudas, and O. Steinhauser, "Simulation studies of ionic liquids: orientational correlations and static dielectric properties," *J Chem Phys*, vol. 125, no. 24, p. 244506, Dec 28 2006.

[144] C. Mall and P. P. Solanki, "Spectrophotometric and conductometric studies of molecular interaction of brilliant cresyl blue with cationic, anionic and non-ionic surfactant in aqueous medium for application in photogalvanic cells for solar energy conversion and storage," *Energy Reports*, vol. 4, pp. 23-30, 2018.

[145] B. Wu, H. Shirota, S. Lall-Ramnarine, and E. W. Castner, "Structure of ionic liquids with cationic silicon-substitutions," *The Journal of Chemical Physics*, vol. 145, no. 11, 2016.

[146] Q. Zhang and S. Zhu, "Ionic Liquids: Versatile Media for Preparation of Vesicles from Polymerization-Induced Self-Assembly," *ACS Macro Letters*, vol. 4, no. 7, pp. 755-758, 2015.

[147] H. Epstein, "Skin Care Products," in *Handbook of Cosmetic Science and Technology*, A. O. P. Barel, Marc; Maibach, Howard I., Ed. 3rd ed. New York: Informa, 2009, pp. 121-134.

[148] Z. He and P. Alexandridis, "Nanoparticles in ionic liquids: interactions and organization," *Phys Chem Chem Phys*, vol. 17, no. 28, pp. 18238-61, Jul 28 2015.

[149] R. J. Bingham and P. Ballone, "Computational study of room-temperature ionic liquids interacting with a POPC phospholipid bilayer," *J Phys Chem B*, vol. 116, no. 36, pp. 11205-16, Sep 13 2012.

[150] M. E. Stournara, H. Wang, S. Hildebrandt, and M. Cavalleri, "Preparing for The Second Quantum Revolution," *Advanced Quantum Technologies*, vol. 1, no. 1, 2018.

[151] S. Borman, "Quantum computing goes beyond H and He," *C&EN Global Enterprise*, vol. 95, no. 37, pp. 4-4, 2017/09/18 2017.

[152] S. KIELICH, "Molecular Interactions in Optically Induced Nonlinearities," *IEEE J. of Quantum Electronics*, vol. 4, no. 11, pp. 744-752, November 1968 1968.

[153] M. H. Bornstein and N. O. Korda, "Discrimination and matching within and between hues measured by reaction times: Some implications for categorical perception and levels of information processing," *Psychological research*, vol. 46, no. 3, pp. 207-222, 1984.

[154] C. A. Fowler, "Auditory perception is not special: We see the world, we feel the world, we hear the world," *The Journal of the Acoustical Society of America*, vol. 89, no. 6, pp. 2910-2915, 1991.

[155] L. Kay, "Auditory perception of objects by blind persons, using a bioacoustic high resolution air sonar," *The Journal of the Acoustical Society of America*, vol. 107, no. 6, pp. 3266-3275, 2000.

[156] D. Regan and H. Spekreijse, "Auditory—Visual Interactions and the Correspondence between Perceived Auditory Space and Perceived Visual Space," *Perception*, vol. 6, no. 2, pp. 133-138, 1977.

[157] D. Regan and C. W. Tyler, "Temporal summation and its limit for wavelength changes: an analog of Bloch's law for color vision," *JOSA*, vol. 61, no. 10, pp. 1414-1421, 1971.

[158] L. D. Rosenblum, A. P. Wuestefeld, and H. M. Saldana, "Auditory looming perception: Influences on anticipatory judgments," *Perception*, vol. 22, no. 12, pp. 1467-1482, 1993.

[159] G. A. Gescheider, "Auditory and cutaneous temporal resolution of successive brief stimuli," Journal of Experimental Psychology, vol. 75, no. 4, p. 570, 1967.

[160] E. B. Goldstein and J. Brockmole, *Sensation and perception*. Cengage Learning, 2016.

[161] S. Dikker, L. J. Silbert, U. Hasson, and J. D. Zevin, "On the same wavelength: predictable language enhances speaker–listener brain-to-brain synchrony in posterior superior temporal gyrus," *Journal of Neuroscience*, vol. 34, no. 18, pp. 6267-6272, 2014.

[162] J. J. Vos and P. L. Walraven, "An analytical description of the line element in the zone-fluctuation model of colour vision—I. Basic concepts," *Vision Research*, vol. 12, no. 8, pp. 1327-1344, 1972.

[163] J. J. Vos and P. L. Walraven, "An analytical description of the line element in the zone-fluctuation model of colour vision—II. The derivation of the line element," *Vision Research*, vol. 12, no. 8, pp. 1345-1365, 1972.

[164] G. S. Wyszecki, W.S., *Color Science: Concepts and Methods, Quantitative Data and Formulae*, 2nd ed. Wiley-Interscience, 2000, p. 968.

[165] R. S. Berns, *Billmeyer and Saltzman's Principles of Color Technology*, 3rd ed. Wiley-Interscience, 2000.

[166] M. Douma. (2008, November 7, 2018). Causes of Color [Online]. Available: http://www.webexhibits.org/causesofcolor/1.html.

[167] M. Fairchild, *Color Appearance Models*, 3rd ed. Wiley, 2013.

[168] D. HOOD, BIRCH, D., "Phototransduction in Human Cones Measured Using the a-Wave of the ERG," vol. 30, no. 20, pp. 2801-2810, 1995.

[169] D. Mustafi, A. H. Engel, and K. Palczewski, "Structure of cone photoreceptors," *Prog Retin Eye Res*, vol. 28, no. 4, pp. 289-302, Jul 2009.

[170] S. D. McAlear, T. W. Kraft, and A. K. Gross, "1 rhodopsin mutations in congenital night blindness," *Adv Exp Med Biol*, vol. 664, pp. 263-72, 2010.

[171] C. Zeitz et al., "Identification and functional characterization of a novel rhodopsin mutation associated with autosomal dominant CSNB," *Invest Ophthalmol Vis Sci*, vol. 49, no. 9, pp. 4105-14, Sep 2008.

[172] F. R. S. C. Alister Vallance Jones, "Optical Emissions from Aurora," in *Aurora*, vol. 9, B. M. McCormac, Ed. (Geophysics and Astrophysics Monographs. Boston: D. Reidel, 1974, pp. 80-177.

[173] D. A. Yoblick and G. Salvendy, "Influence of frequency on the estimation of time for auditory, visual, and tactile modalities: The kappa effect," *Journal of Experimental Psychology*, vol. 86, no. 2, p. 157, 1970.

[174] T. S. Roger L. McMullen, Lidia Kulcsar, Linda Foltis, and Timothy Gillece "Evaluation of the Surface Properties of Hair with Acoustic Analysis," in *72nd Annual Society of Cosmetic Chemists Annual Meeting*, New York, 2018: Society of Cosmetic Chemists, p. 27.

[175] D. A. Yoblick and G. Salvendy, "Influence of frequency on the estimation of time for auditory, visual, and tactile modalities: The kappa effect," *Journal of Experimental Psychology*, vol. 86, no. 2, p. 157, 1970.

[176] F. J. S. Speziale, C. L. Caylor, S. Kriminski, C.-S. Zha, R. E. Thorne, and T. S. Duffy, "Sound Velocity and Elasticity of Tetragonal Lysozyme Crystals by Brillouin Spectroscopy," *Biophysical Journal*, vol. 85, pp. 3202-3213, 2003.

[177] (1996, July 25, 2018). Sound Waves and Music Review - Answers.

[178] A. Mallik, M. L. Chanda, and D. J. Levitin, "Anhedonia to music and mu-opioids: Evidence from the administration of naltrexone," *Sci Rep*, vol. 7, p. 41952, Feb 8 2017.

[179] (2018). How Chemistry Rocks Music Festivals [Online]. Available: https://cen.acs.org/sponsored-content/how-chemistry-rocks-music-festivals.html.

[180] V. N. Salimpoor, M. Benovoy, K. Larcher, A. Dagher, and R. J. Zatorre, "Anatomically distinct dopamine release during anticipation and experience of peak emotion to music," *Nat Neurosci*, vol. 14, no. 2, pp. 257-62, Feb 2011.

[181] L. Buck and R. Axel, "A novel multigene family may encode odorant receptors: a molecular basis for odor recognition," *Cell*, vol. 65, no. 1, pp. 175-187, 1991.

[182] U. J. Meierhenrich, J. Golebiowski, X. Fernandez, and D. Cabrol-Bass, "The molecular basis of olfactory chemoreception," *Angew Chem Int Ed Engl*, vol. 43, no. 47, pp. 6410-2, Dec 03 2004.

[183] J. H. Park et al., "Opsin, a structural model for olfactory receptors?," *Angew Chem Int Ed Engl*, vol. 52, no. 42, pp. 11021-4, Oct 11 2013.

[184] P. Kraft and G. Frater, "Enantioselectivity of the musk odor sensation," *Chirality*, vol. 13, no. 8, pp. 388-94, Aug 2001.

[185] O. Man, Y. Gilad, and D. Lancet, "Prediction of the odorant binding site of olfactory receptor proteins by human-mouse comparisons," *Protein Sci*, vol. 13, no. 1, pp. 240-54, Jan 2004.

[186] Z. Peterlin, S. Firestein, and M. E. Rogers, "The state of the art of odorant receptor deorphanization: a report from the orphanage," *J Gen Physiol*, vol. 143, no. 5, pp. 527-42, May 2014.

[187] L. Turin, "A Method for the Calculation of Odor Character from Molecular Structure," *Journal of Theoretical Biology*, vol. 216, no. 3, pp. 367-385, 2002.

[188] Y. Kang et al., "Crystal structure of rhodopsin bound to arrestin by femtosecond X-ray laser," *Nature*, vol. 523, no. 7562, pp. 561-7, Jul 30 2015.

[189] X. E. Zhou et al., "X-ray laser diffraction for structure determination of the rhodopsin-arrestin complex," *Sci Data*, vol. 3, p. 160021, Apr 12 2016.

[190] J. Saam, E. Tajkhorshid, S. Hayashi, and K. Schulten, "Molecular dynamics investigation of primary photoinduced events in the activation of rhodopsin," *Biophys J*, vol. 83, no. 6, pp. 3097-112, Dec 2002.

[191] J. Saam, E. Tajkhorshid, S. Hayashi, and K. Schulten, "Molecular dynamics investigation of primary photoinduced events in the activation of rhodopsin," *Biophys J*, vol. 83, no. 6, pp. 3097-112, Dec 2002.

[192] B. Trzaskowski, D. Latek, S. Yuan, U. Ghoshdastider, A. Debinski, and S. Filipek, "Action of molecular switches in GPCRs--theoretical and experimental studies," *Curr Med Chem*, vol. 19, no. 8, pp. 1090-109, 2012.

[193] D. Rodriguez and H. Gutierrez-de-Teran, "Computational Approaches for Ligand Discovery and Design in Class-A G Protein-Coupled Receptors," (in English), *Current Pharmaceutical Design*, vol. 19, no. 12, pp. 2216-2236, Apr 2013.

[194] T. E. Angel, S. Gupta, B. Jastrzebska, K. Palczewski, and M. R. Chance, "Structural waters define a functional channel mediating activation of the GPCR, rhodopsin," *Proc Natl Acad Sci U S A*, vol. 106, no. 34, pp. 14367-72, Aug 25 2009.

[195] B. Trzaskowski, D. Latek, S. Yuan, U. Ghoshdastider, A. Debinski, and S. Filipek, "Action of molecular switches in GPCRs--theoretical and experimental studies," *Curr Med Chem*, vol. 19, no. 8, pp. 1090-109, 2012.

[196] Congress, 2D Session. (2018, September 26, 2018). H.R. 6903 IH.

[197] T. Cirillo et al., "Exposure to di-2-ethylhexyl phthalate, di-n-butyl phthalate and bisphenol A through infant formulas," *J Agric Food Chem*, vol. 63, no. 12, pp. 3303-10, Apr 1 2015.

[198] M. Gong, C. J. Weschler, and Y. Zhang, "Impact of Clothing on Dermal Exposure to Phthalates: Observations and Insights from Sampling Both Skin and Clothing," *Environ Sci Technol*, vol. 50, no. 8, pp. 4350-7, Apr 19 2016.

[199] F. W. Gaspar, R. Castorina, R. L. Maddalena, M. G. Nishioka, T. E. McKone, and A. Bradman, "Phthalate exposure and risk assessment in California child care facilities," *Environ Sci Technol*, vol. 48, no. 13, pp. 7593-601, Jul 1 2014.

[200] L. You et al., "Semen phthalate metabolites, spermatozoa apoptosis, and DNA damage: a cross-sectional study in China," *Environ Sci Technol*, vol. 49, no. 6, pp. 3805-12, Mar 17 2015.

[201] M. Bartolomeu, M. Neves, M. A. F. Faustino, and A. Almeida, "Wastewater chemical contaminants: remediation by advanced oxidation processes," *Photochem Photobiol Sci*, Oct 17 2018.

[202] C. Monneret, "What is an endocrine disruptor?," *C R Biol*, vol. 340, no. 9-10, pp. 403-405, Sep - Oct 2017.

[203] B. E. Erickson. (2014, July 28, 2014) Advisers Call for New Controls on Phthalates. *C&EN*. Available: https://cen.acs.org/articles/92/i30/Advisers-Call-New-Controls-Phthalates.html

[204] M. McCoy. (2015, June 22, 2015) A Reckoning for Phthalates. *C&EN*. Available: https://cen.acs.org/articles/93/i25/Reckoning-Phthalates.html

[205] B. E. Erickson. (2017, June 26, 2017) European Union Further Restricts Four Phthalates. *C&EN* [Print]. Available: https://cen.acs.org/articles/95/i26/European-Union-further-restricts-four.html

[206] C. Hogue. (2017, October 30, 2017) U.S. To Restrict Five Phthalates in Children's Products. *C&EN*. Available: https://cen.acs.org/articles/95/i43/US-restrict-5-phthalates-childrens.html

[207] R. Kolahdouz Mohammadi and T. Arablou, "Resveratrol and endometriosis: In vitro and animal studies and underlying mechanisms (Review)," *Biomed Pharmacother*, vol. 91, pp. 220-228, Jul 2017.

[208] J. Rudzitis-Auth, M. D. Menger, and M. W. Laschke, "Resveratrol is a potent inhibitor of vascularization and cell proliferation in experimental endometriosis," *Hum Reprod*, vol. 28, no. 5, pp. 1339-47, May 2013.

[209] J.-F. Tremblay. (2017, January 16, 2017) Spotlight Grows on Antibiotic Pollution. *Chemical & Engineering News*. 18-19. Available: https://cen.acs.org/articles/95/i3/Spotlight-grows-antibiotic-pollution.html

[210] K. V. Venkatasubramanian. (2018) India Leads in Increasing Antibiotic Consumption. *Chemical & Engineering News*. Available: https://cen.acs.org/pharmaceuticals/antibiotics/India-leads-increasing-antibiotic-consumption/96/i16

[211] J. Lu et al., "Non-antibiotic antimicrobial triclosan induces multiple antibiotic resistance through genetic mutation," *Environment international*, vol. 118, pp. 257-265, 2018.

[212] J.-B. Ricco, A. Assadian, F. Schneider, and O. Assadian, "In vitro evaluation of the antimicrobial efficacy of a new silver-triclosan vs a silver collagen-coated polyester vascular graft against methicillin-resistant Staphylococcus aureus," *Journal of vascular surgery*, vol. 55, no. 3, pp. 823-829, 2012.

[213] H. P. Schweizer, "Triclosan: a widely used biocide and its link to antibiotics," *FEMS microbiology letters*, vol. 202, no. 1, pp. 1-7, 2001.

[214] B. E. Erickson. (2011, July 11, 2011) CDC Lacks Antibiotic Resistance Data. *Chemical & Engineering News*. 1. Available: https://cen.acs.org/articles/89/i28/CDC-Lacks-Antibiotic-Resistance-Data.html

[215] A. Glaser, "The ubiquitous triclosan," A common antibacterial agent exposed. *Pesticides and You*, vol. 24, pp. 12-17, 2004.

[216] R. U. Halden et al., "The florence statement on triclosan and triclocarban," *Environmental health perspectives*, vol. 125, no. 6, p. 064501, 2017.

[217] J. Kepner, "Triclosan Hazards... Continued," *Pesticides and You*. Winter, vol. 2005, no. 24, p. 4, 2004.

[218] D. G. J. Larsson et al., "Critical knowledge gaps and research needs related to the environmental dimensions of antibiotic resistance," *Environ Int*, vol. 117, pp. 132-138, Aug 2018.

[219] A. F. C. Leonard et al., "Exposure to and colonisation by antibiotic-resistant E. coli in UK coastal water users: Environmental surveillance, exposure assessment, and epidemiological study (Beach Bum Survey)," *Environment International*, vol. 114, pp. 326-333, 2018.

[220] J. Latosińska, M. Tomczak, and J. Kasprzak, "Thermal stability and molecular dynamics of triclosan in solid state studied by 35Cl–NQR spectroscopy and DFT calculations," *Chemical Physics Letters*, vol. 462, no. 4-6, pp. 284-288, 2008.

[221] (2019, April 2019) Revealing How Enzymes Turn a Toxin Into a Potential Painkiller. *Chemical & Engineering News*. Available: https://cen.acs.org/biological-chemistry/biochemistry/Revealing-enzymes-turn-toxin-potential/97/web/2019/04

[222] S. Blackmon, "Does Triclosan Exposure and Tolerance Lead to Chlorine Resistant Bacteria?," *Undergraduate Review*, vol. 7, no. 1, pp. 29-32, 2011.

[223] J. J. Braid and M. C. Wale, "The antibacterial activity of triclosan-impregnated storage boxes against Staphylococcus aureus, Escherichia coli, Pseudomonas aeruginosa, Bacillus cereus and Shewanella putrefaciens in conditions simulating domestic use," *Journal of Antimicrobial Chemotherapy*, vol. 49, no. 1, pp. 87-94, 2002.

[224] G. Dhillon et al., "Triclosan: current status, occurrence, environmental risks and bioaccumulation potential," *International journal of environmental research and public health*, vol. 12, no. 5, pp. 5657-5684, 2015.

[225] M. Lucova, J. Hojerova, S. Pazourekova, and Z. Klimova, "Absorption of triphenylmethane dyes Brilliant Blue and Patent Blue through intact skin, shaven skin and lingual mucosa from daily life products," *Food Chem Toxicol*, vol. 52, pp. 19-27, Feb 2013.

[226] M. F. a. H. Flulher, "Brilliant Blue FCF as a Dye Tracer for Solute Transport Studies--A Toxicological Overview," *J. Environmental Quality*, vol. 23, no. 5, 1993.

[227] U. Shedbalkar, R. Dhanve, and J. Jadhav, "Biodegradation of triphenylmethane dye cotton blue by Penicillium ochrochloron MTCC 517," *J Hazard Mater*, vol. 157, no. 2-3, pp. 472-9, Sep 15 2008.

[228] C. Yatome, T. Ogawa, D. Koga, and E. Idaka, "Biodegradability of Azo and Triphenylmethane dyes by Pseudomonas pseudomallei 13NA," *Journal of the Society of Dyers and Colourists*, vol. 97, no. 4, pp. 166-169, 2008.

[229] X. Lu, B. Yang, J. Chen, and R. Sun, "Treatment of wastewater containing azo dye reactive brilliant red X-3B using sequential ozonation and upflow biological aerated filter process," *J Hazard Mater*, vol. 161, no. 1, pp. 241-5, Jan 15 2009.

[230] H. Patel and R. T. Vashi, "Removal of Congo Red dye from its aqueous solution using natural coagulants," *Journal of Saudi Chemical Society*, vol. 16, no. 2, pp. 131-136, 2012.

[231] C. Namasivayam and D. J. S. E. Arasi, "Removal of congo red from wastewater by adsorption onto waste red mud," *Chemosphere*, vol. 34, no. 2, pp. 401-417, 1997.

[232] T. Ito, Y. Shimada, and T. Suto, "Potential use of bacteria collected from human hands for textile dye decolorization," *Water Resources and Industry*, vol. 20, pp. 46-53, 2018.

[233] T. K. F. S. Freitas et al., "Optimization of coagulation-flocculation process for treatment of industrial textile wastewater using okra (A. esculentus) mucilage as natural coagulant," *Industrial Crops and Products*, vol. 76, pp. 538-544, 2015.

[234] P. Amchova, H. Kotolova, and J. Ruda-Kucerova, "Health safety issues of synthetic food colorants," *Regul Toxicol Pharmacol*, vol. 73, no. 3, pp. 914-22, Dec 2015.

[235] F. M. Chequer, V. P. Venancio, M. L. Bianchi, and L. M. Antunes, "Genotoxic and mutagenic effects of erythrosine B, a xanthene food dye, on HepG2 cells," *Food Chem Toxicol*, vol. 50, no. 10, pp. 3447-51, Oct 2012.

[236] D. Masone and C. Chanforan, "Study on the interaction of artificial and natural food colorants with human serum albumin: A computational point of view," *Comput Biol Chem*, vol. 56, pp. 152-8, Jun 2015.

[237] K. Elbanna, O. M. Sarhan, M. Khider, M. Elmogy, H. H. Abulreesh, and M. R. Shaaban, "Microbiological, histological, and biochemical evidence for the adverse effects of food azo dyes on rats," *J Food Drug Anal*, vol. 25, no. 3, pp. 667-680, Jul 2017.

[238] A. Noorafshan, M. Hashemi, S. Karbalay-Doust, and F. Karimi, "High dose Allura Red, rather than the ADI dose, induces structural and behavioral changes in the medial prefrontal cortex of rats and taurine can protect it," *Acta Histochem*, vol. 120, no. 6, pp. 586-594, Aug 2018.

[239] W. E. Klunk, M. L. Debnath, A. M. Koros, and J. W. Pettegrew, "Chrysamine-G, a lipophilic analogue of Congo red, inhibits Aβ-induced toxicity in PC12 cells," Life sciences, vol. 63, no. 20, pp. 1807-1814, 1998.

[240] K. A. Amin, H. Abdel Hameid, 2nd, and A. H. Abd Elsttar, "Effect of food azo dyes tartrazine and carmoisine on biochemical parameters related to renal, hepatic function and oxidative stress biomarkers in young male rats," *Food Chem Toxicol*, vol. 48, no. 10, pp. 2994-9, Oct 2010.

[241] L. Perez-Ibarbia, T. Majdanski, S. Schubert, N. Windhab, and U. S. Schubert, "Safety and regulatory review of dyes commonly used as excipients in pharmaceutical and nutraceutical applications," *Eur J Pharm Sci*, vol. 93, pp. 264-73, Oct 10 2016.

[242] M. M. Hashem, A. H. Atta, M. S. Arbid, S. A. Nada, and G. F. Asaad, "Immunological studies on Amaranth, Sunset Yellow and Curcumin as food colouring agents in albino rats," *Food and Chemical Toxicology*, vol. 48, no. 6, pp. 1581-1586, 2010.

[243] L. Leo, C. Loong, X. L. Ho, M. F. B. Raman, M. Y. T. Suan, and W. M. Loke, "Occurrence of azo food dyes and their effects on cellular inflammatory responses," *Nutrition*, vol. 46, pp. 36-40, Feb 2018.

[244] Y. Gao, C. Li, J. Shen, H. Yin, X. An, and H. Jin, "Effect of food azo dye tartrazine on learning and memory functions in mice and rats, and the possible mechanisms involved," *J Food Sci*, vol. 76, no. 6, pp. T125-9, Aug 2011.

[245] S. K. Meyer et al., "Hepatic effects of tartrazine (E 102) after systemic exposure are independent of oestrogen receptor interactions in the mouse," *Toxicol Lett*, vol. 273, pp. 55-68, May 5 2017.

[246] B. Lab. (2007, Dec 17, 2018). The Carcinogenic Potency Project: FD&C Yellow No. 5 [Online]. Available: https://toxnet.nlm.nih.gov/cpdb/chempages/FD%20%26%20C%20YELLOW%20NO.%205.html.

[247] R. A. Yokel, "Aluminum in food–the nature and contribution of food additives," in *Food Additive*: IntechOpen, 2012.

[248] G. Feketea and S. Tsabouri, "Common food colorants and allergic reactions in children: Myth or reality?," *Food Chem*, vol. 230, pp. 578-588, Sep 1 2017.

[249] N. Martins, C. L. Roriz, P. Morales, L. Barros, and I. C. F. R. Ferreira, "Food colorants: Challenges, opportunities and current desires of agro-industries to ensure consumer expectations and regulatory practices," *Trends in Food Science & Technology*, vol. 52, pp. 1-15, 2016.

[250] M. Bastaki, T. Farrell, S. Bhusari, K. Pant, and R. Kulkarni, "Lack of genotoxicity in vivo for food color additive Allura Red AC," *Food Chem Toxicol*, vol. 105, pp. 308-314, Jul 2017.

[251] M. Honma, "Evaluation of the in vivo genotoxicity of Allura Red AC (Food Red No. 40)," *Food Chem Toxicol*, vol. 84, pp. 270-5, Oct 2015.

[252] M. Bastaki, T. Farrell, S. Bhusari, K. Pant, and R. Kulkarni, "Lack of genotoxicity in vivo for food color additive Tartrazine," *Food Chem Toxicol*, vol. 105, pp. 278-284, Jul 2017.

[253] A. Lee. (2019, Friday, February 22, 2019) The Mobile Face Race. WWD Beauty Inc. 24-25.

[254] Y. Makeup, "Beauty 3.0 AI + AR: The Next-Gen Personalized Smart Beauty Solution," *P. Corp, Ed.*, ed, 2019.

[255] P. W. Wasserscheid, T., *Ionic Liquids in Synthesis* (Green Chemistry). Erlangen: Wiley-VCH, 2008.

[256] M. Dapcevich. (2018, April 30, 2019). Investigators pinpoint what caused this river to turn blood-red (July 6, 2018 ed.) [Online]. Available: https://www.iflscience.com/environment/investigators-pinpoint-what-caused-this-river-to-turn-bloodred/.

[257] M. Jones. (2011, April 30, 2019). China's 'River of Blood': Jian Turns Red After Chemical Dump [Online]. Available: https://www.ibtimes.com/chinas-river-blood-jian-turns-red-after-chemical-dump-photos-709258.

[258] M. C. Mark Peplow, "Why has the Yangtze River Turned Red," *Nature*, p. 1, 2012.

[259] E. MacKinnon. (2012, April 30, 2019). Yangtze River Runs Mysteriously Red [Online]. Available: https://www.livescience.com/23038-yangtze-river-red.html.

[260] N. Kirkpatrick. (2014, April 30, 2019). Why did this river in China turn red? [Online]. Available: https://www.washingtonpost.com/news/morning-mix/wp/2014/07/29/why-did-this-river-in-china-turn-red/?noredirect=on&utm_term=.c2ce9c9fb997.

[261] D. Coleman and N. Gathergood, "Biodegradation studies of ionic liquids," *Chem Soc Rev*, vol. 39, no. 2, pp. 600-37, Feb 2010.

[262] M. Petkovic, K. R. Seddon, L. P. Rebelo, and C. Silva Pereira, "Ionic liquids: a pathway to environmental acceptability," *Chem Soc Rev*, vol. 40, no. 3, pp. 1383-403, Mar 2011.

[263] C. M. S. S. Neves, M. G. Freire, and J. A. P. Coutinho, "Improved recovery of ionic liquids from contaminated aqueous streams using aluminium-based salts," *RSC Advances*, vol. 2, no. 29, 2012.

[264] M. S. Raja Shahrom, C. D. Wilfred, and A. K. Z. Taha, "CO 2 capture by task specific ionic liquids (TSILs) and polymerized ionic liquids (PILs and AAPILs)," *Journal of Molecular Liquids*, vol. 219, pp. 306-312, 2016.

[265] M. B. Shiflett, D. W. Drew, R. A. Cantini, and A. Yokozeki, "Carbon Dioxide Capture Using Ionic Liquid 1-Butyl-3-methylimidazolium Acetate," *Energy & Fuels*, vol. 24, no. 10, pp. 5781-5789, 2010.

[266] M. Watanabe, D. Kodama, T. Makino, and M. Kanakubo, "CO2 absorption properties of imidazolium based ionic liquids using a magnetic suspension balance," *Fluid Phase Equilibria*, vol. 420, pp. 44-49, 2016.

[267] X. Zhang, X. Zhang, H. Dong, Z. Zhao, S. Zhang, and Y. Huang, "Carbon capture with ionic liquids: overview and progress," *Energy & Environmental Science*, vol. 5, no. 5, 2012.

[268] M. Kanakubo, T. Makino, and T. Umecky, "CO2 solubility in and physical properties for ionic liquid mixtures of 1-butyl-3-methylimidazolium acetate and 1-butyl-3-methylimidazolium bis(trifluoromethanesulfonyl)amide," *Journal of Molecular Liquids*, vol. 217, pp. 112-119, 2016.

Appendix A

Cross-Cultural Color Spectrum Table by More et al. (2009)

Color	Anglo-Saxon	Germanic	Latin	Nordic	Slavic	Chinese	Japanese	Korean	ASEAN
White	Purity Happiness	--	--	--	--	Death Mourning	Death Mourning	Death Mourning	Death Mourning
Blue	High Quality Corporate Masculine	Warm Feminine		Cold Masculine	--	High quality, Trustworthy	High quality, Trustworthy	High quality, Trustworthy	Cold Evil (Malaysia)
Green	Envy, Good Taste	--	Envy	--	--	Pure, Reliable	Love Happiness	Purity Adventure	Danger Disease (Malaysia)
Yellow	Happiness Jealousy	Envy Jealousy	Envy Infidelity	--	Envy	Pure Good taste Royalty Authority	Envy Good taste	Happiness Good taste	--
Red	Masculine Love Lust Fear Anger	Fear Anger Jealousy	Masculine	Positive	Fear Anger Jealousy	Love Happiness Lucky	Love Anger Jealousy	Love Adventure Good taste	Love Adventure
Purple	Authority Power	--	--	--	Anger Envy Jealousy	Expensive Love	Expensive Sin Fear	Expensive Love	--
Black	Expensive Fear Grief	Fear Anger Grief	Fear Anger Grief	--	Fear Anger	Expensive Powerful	Expensive Powerful	Expensive Powerful	Mourning Powerful

References

[1] A. T. S. More, R. K., "Aesthetic Considerations for pharmaceutical OTC (over-the-counter) products," in *Oxford Business & Economics Conference Program*, St. Hughes College, Oxford University, 2009, p. 22.

Appendix B

Summary of Inductive Line Element Mathematical Model of the Visual Response Mechanism of Color Vision by Vos and Walraven[28]

The description of this model has been adapted from Wyzecki and Stiles (2000) for comparative distinction from the empirical and semi-empirical line elements of theoretical maximum absorbance spectral curve generation for color-matching purposes presented throughout the main body of this thesis.

The most elaborate line element that exists to explain the sensation of color vision signal transduction has been developed by Vos and Walraven (1972a, b). There are three assumptions underlying this theory: (i) Color stimuli are processed in two stages, occurring in a Helmholtz-type three-receptor zone, followed by a Hering-type neural conversion zone in which a luminance and two antagonistic chromatic signals are formed; (ii) Color discrimination is essentially photon-noise-limited. At higher luminances, "saturation" and "supersaturation" (or channel overloading) processes occur that keep color discrimination below the limit that photon noise alone would provide; and (iii) the signals emerging from the second zone, the neural conversion zone, combine in a positive and definite (quadratic) form to generate an output signal directly proportional to a just-noticeable difference between two given input stimuli. In the case where the visual

[28] This is an abridged version--a much more detailed discussion of this and other inductive line elements of visual response mechanisms can be found elsewhere: G. S. Wyszecki, W.S., *Color Science: Concepts and Methods, Quantitative Data and Formulae*, 2nd ed. Wiley-Interscience, 2000, p. 968.

mechanism is active at low luminance levels (rods), the signal-to-noise output can be expressed as:

$$\left[\frac{Signal}{Noise}\right]_{Output} = \frac{(dN)}{\sqrt{N}}$$

Where *N* is the average number of quanta absorbed per second.

Regarding the cone mechanism, if one were to assume that the collective response of the three cone mechanisms would be equivalent to the square root of the sum of the squares of the individual cone responses, the line element would appear as such:

$$(ds)^2 = \left(\frac{dR}{\sqrt{R}}\right)^2 + \left(\frac{dG}{\sqrt{G}}\right)^2 + \left(\frac{dB}{\sqrt{B}}\right)^2$$

Where R, G, B are the responses of the three independently operating cone mechanisms.

The line element described clearly differs from that of Helmholtz but is similar to the quadratic model proposed by Schrödinger except that the separate luminance dependence factors are omitted. These factors preserve Weber's law from low to high levels of luminance and make "brightness" a linear combination of the cone responses. The line element of (equation above) on the other hand does not comply with Weber's law, as the Weber fraction increases with the square root of the luminance instead of being constant, in accordance with the now well-established transition (de Vries-Rose behavior) from absolute-threshold behavior to Weber behavior.

The most important new concept introduced by Vos and Walraven (1972a) is that the line element output signals generated by the individual cone mechanisms in the first stage of the signal transduction mechanism do not combine in the manner described above but instead are first coded in the second stage, forming two antagonistic chromatic signals and one achromatic luminance signal before a difference signal is transmitted to the brain. The coding or transformation of the R, G, B cone signals in the neural conversion zone is assumed to be as follows:

*F*irst chromatic signal:	$F = \frac{R}{G}$	(red-green)
*S*econd chromatic signal:	$S = \frac{R+G}{B} = Y/B$	(yellow-blue)
Achromatic signal:	$L = R + G + B$	(*L*uminance)

where the signals F, S, L emerging from the red-green (F), yellow-blue (S), and luminance (L) channels are then assumed to combine in the positive and definite form as shown…

$$(ds)^2 = \eta_L \left(\frac{dL}{\sigma_L}\right)^2 + \eta_F \left(\frac{dF}{\sigma_F}\right)^2 + \eta_S \left(\frac{dS}{\sigma_S}\right)^2$$

…to generate an output signal *ds* that is directly proportional to a just-noticeable color difference between two given input stimuli. In Equation (above), the quantities σ_L, σ_F, and σ_S are signal uncertainties; and η_L, η_F, and η_S are constant weighting or gain factors in the L, F, and S channels.

$$(ds)^2 = \eta_L \left[\frac{(dR + dG + dB)^2}{R + G + B}\right] + \eta_F \left[\frac{(G\,dR - R\,dG)^2}{RG(R + G)}\right]$$

$$+ \eta_S \left[\frac{\{B\,dR + B\,dG - (R + G)\,dB\}^2}{B(R_{+G})(R + G + B)}\right]$$

After sequential expansion of the line element using summations, the final signal transduction equation for color spectra at low luminance levels is:

$$\begin{aligned}(ds)^2 = (dR)^2 &\left(\frac{\eta_L}{R + G + B} + \frac{\eta_F G}{R(R + G)} + \frac{\eta_S B}{(R + G)(R + G + B)}\right) \\ &+ (dG)^2 \left(\frac{\eta_L}{R + G + B} + \frac{\eta_F R}{G(R + G)} + \frac{\eta_S B}{(R + G)(R + G + B)}\right) \\ &+ (dB)^2 \left(\frac{\eta_L}{(R + G + B)} + 0 + \frac{\eta_S (R + G)}{B(R + G + B)}\right) \\ &+ 2\,dR\,dG \left(\frac{\eta_L}{R + G + B} - \frac{\eta_F}{R + G} + \frac{\eta_S G}{(R + G)(R + G + B)}\right) \\ &+ 2\,dR\,dB \left(\frac{\eta_L}{R + G + B} + 0 - \frac{\eta_S}{R + G + B}\right) \\ &+ 2\,dG\,dB \left(\frac{\eta_L}{R + G + B} + 0 - \frac{\eta_S}{R + G + B}\right)\end{aligned}$$

If $R + G + B = L$, $\frac{R}{L} = r$, $\frac{G}{L} = g$, and $\frac{B}{L} = b$, the expanded equation becomes:

$$\begin{aligned}(ds)^2 = \frac{1}{L}\Big[&dR^2 \left\{\eta_L + \eta_F \frac{g}{r(r + g)} + \eta_S \frac{b}{r + g}\right\} + (dG)^2 \left\{\eta_L + \eta_F \frac{r}{g(r + g)} + \eta_S \frac{b}{r + g}\right\} \\ &+ (dB)^2 \left(\eta_L + \eta_S \frac{r + g}{b}\right) + 2(dR)(dG) \left\{\eta_L - \eta_F \frac{1}{r + g} + \eta_S \frac{b}{r + g}\right\} \\ &+ 2(dR\,dB + dG\,dB)\{\eta_L - \eta_S\}\Big]\end{aligned}$$

Vos and Walraven extended the applicability of the line element to the stimuli of moderate and high luminances by introducing the concept of "saturation" and "supersaturation" to their model. In this definition, "Saturation" occurs when the spike density of the neural signals increases to a level beyond which the incidents of new

spikes is prevented by the inherent refractory period (dead time) that follows each spike. A simple mathematical model of the saturation process relates the number of spikes v with the number of incident events, such as quanta *n*, as follows:

$$v = \frac{n}{1 + \frac{n}{n_0}}$$

where n_0 denotes the number of incident events ("quanta") for which saturation occurs.

In this model, it is assumed that the refractory process has a fixed time interval t_0 throughout which prevention of new spikes occurring is complete, but at the end of the dead time, the possibility of new spikes occurring is at once restored. When the number of spikes approaches its maximum, which is determined by n_0, the congestion in the neural channel increases, leading to a gradual reduction of the "accuracy of information on n". Thus, Vos and Walraven give a formula that describes the postulated "accuracy reduction" as

$$\sigma_n^2 = n\left(1 + \frac{n}{n_0}\right)$$

For high luminances, or high quanta-incidence rates, the quantity (sigma) becomes proportional to *n*. The basic steps to the final equation for moderate to high luminance in cone perception of color are as follows. First, the cone signals R, G, and B add to the following sums:

$$L = R + G + B \text{ and } Y = R + G$$

Then, the new signals saturate in accordance with:

$$v = \frac{n}{1 + \frac{n}{n_0}}$$

The accuracy of the signal transmission is governed first by Poisson statistics, the limited by saturation and supersaturation in accordance with the following:

$$\sigma_n = \sqrt{n\left(1 + \frac{n}{n_0} + \frac{n^3}{n_1^3}\right)}$$

Which provides what Vos and Walraven call the "physical line element" as shown:

$$(ds)_n^2 = \frac{(dn)^2}{n\left(1 + \frac{n}{n_0} + \frac{n^3}{n_1^3}\right)}$$

After completing the preceding steps, the signals of the two antagonistic chromatic channels are formed in accordance with

$$F = v_R/v_G \text{ and } S = v_Y/v_B$$

The general form of the line element derived in accordance with steps (i) to (iv), but expressed in terms of the initial cone signals R, G, B, is the given by the following:

$$(ds)^2 = (dR)^2\left[\eta_L f_L + \eta_F f_F G^2\left(1+\frac{G}{G_0}\right)^2 + \eta_S f_S B^2\left(1+\frac{B}{B_0}\right)^2\right]$$

$$+ (dG)^2\left[\eta_L f_L + \eta_F f_F R^2\left(1+\frac{R}{R_0}\right)^2 + \eta_S f_S B^2\left(1+\frac{B}{B_0}\right)^2\right]$$

$$+ (dB)^2\left[\eta_L f_L + \eta_S f_S Y^2\left(1+\frac{Y}{Y_0}\right)^2\right]$$

$$+ 2\,dR\,dG\left[\eta_L f_L - \eta_F f_F R\left(1+\frac{R}{R_0}\right)G\left(1+\frac{G}{G_0}\right) + \eta_S f_S B^2\left(1+\frac{B}{B_0}\right)^2\right]$$

$$+ 2\,dR\,dB\left[\eta_L f_L - \eta_S f_S B\left(1+\frac{B}{B_0}\right)Y\left(1+\frac{Y}{Y_0}\right)\right]$$

$$+ 2\,dG\,dB\left[\eta_L f_L - \eta_S f_S B\left(1+\frac{B}{B_0}\right)Y\left(1+\frac{Y}{Y_0}\right)\right]$$

….to yield f_S, f_F, and f_L as shown:

f_S

$$= \frac{\left\{\frac{B}{1+B/B_0+B^3/B_1^3}\right\}+\left\{\frac{Y}{1+Y/Y_0+Y^3/Y_1^3}\right\}}{\left[\left\{\frac{B(1-B/B_0)}{1+B/B_0+B^3/B_1^3}\right\}+\left\{\frac{Y(1+Y/Y_0)}{1+Y/Y_0+Y^3/Y_1^3}\right\}\right]^2\cdot(1+Y/Y_0+Y^3/Y_1^3)\cdot(1+B/B_0+B^3/B_1^3)YB}$$

f_F

$$= \frac{\left\{\frac{B}{1+G/G_0+G^3/G_1^3}\right\}+\left\{\frac{R}{1+R/R_0+R^3/R_1^3}\right\}}{\left[\frac{G(1-G/G_0)}{1+G/G_0+G^3/G_1^3}+\frac{R(1+R/R_0)}{1+R/R_0+R^3/R_1^3}\right]^2\cdot(1+R/R_0+R^3/R_1^3)\cdot(1+G/G_0+G^3/G_1^3)RG}$$

$$f_L = \frac{1}{L(1+L/L_0+L^3/L_1^3)}$$

Compared to experimental color discrimination data, this theory of color molecules finds reasonable agreement between prediction and experiment. Note that this is an inductive line element theory, which explains the visual mechanism of color perception rather well using a mathematical model. However, inductive models make basic assumptions about color matching. Conversely, empirical line elements, such as those by MacAdam (1942, 1943) correctly reproduce standard deviations from the mean of repeated color matches but do not attempt explain the visual response mechanism responsible for color discrimination.

References

[1] G. S. Wyszecki, W.S., Color Science: Concepts and Methods, Quantitative Data and Formulae, 2 ed. Wiley-Interscience, 2000, p. 968.

Appendix C

Supplemental Figures for Simulated TD-DFT spectra of D&C Blue No. 6, D&C Yellow No. 11, and D&C Red No. 36 Color Additive-Solvent Mixtures

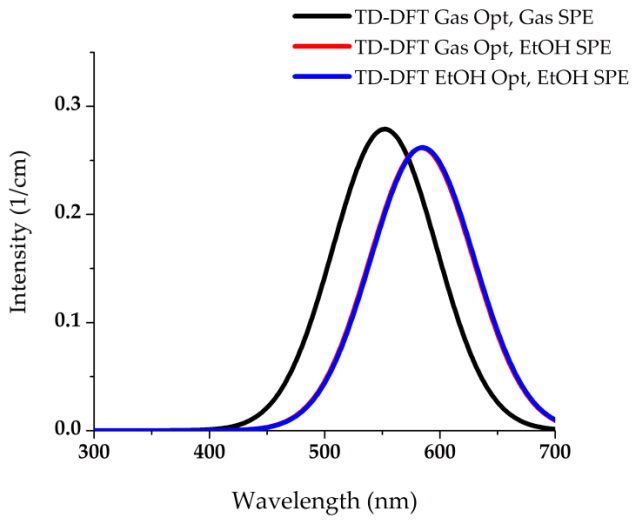

Fig. C1. D&C Blue No. 6 color additive simulated TD-DFT absorbance spectra under three optimization and single point energy calculation conditions: Gas Opt, Gas SPE; Gas Opt, EtOH SPE; EtOH Opt, EtOH SPE

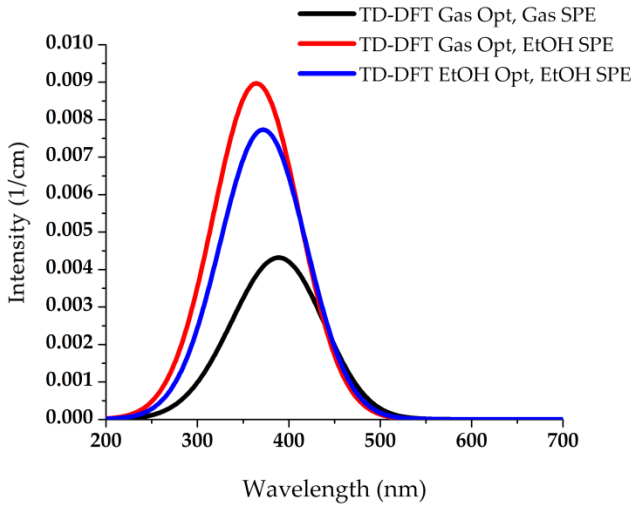

Fig. C2. D&C Yellow No. 11 color additive simulated TD-DFT absorbance spectra under three optimization and single point energy calculation conditions: Gas Opt, Gas SPE; Gas Opt, EtOH SPE; EtOH Opt, EtOH SPE

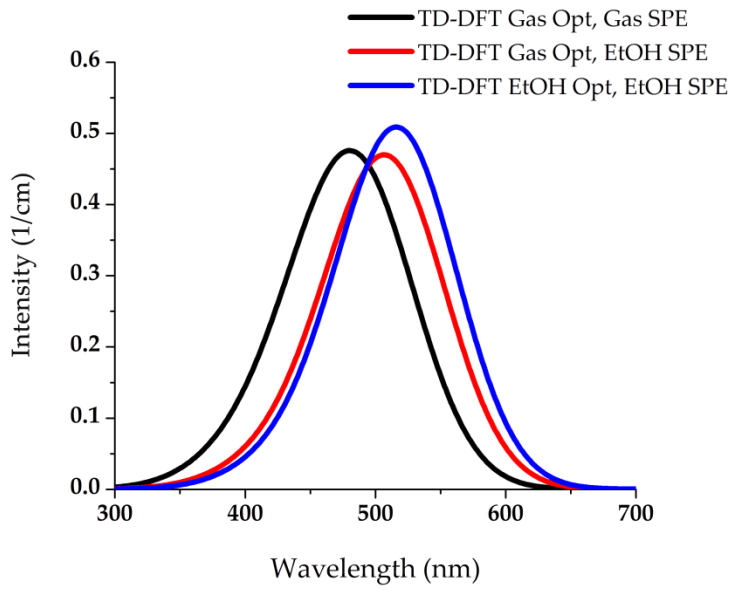

Fig. C3. D&C Red No. 36 color additive simulated TD-DFT absorbance spectra under three optimization and single point energy calculation conditions: Gas Opt, Gas SPE; Gas Opt, EtOH SPE; EtOH Opt, EtOH SPE

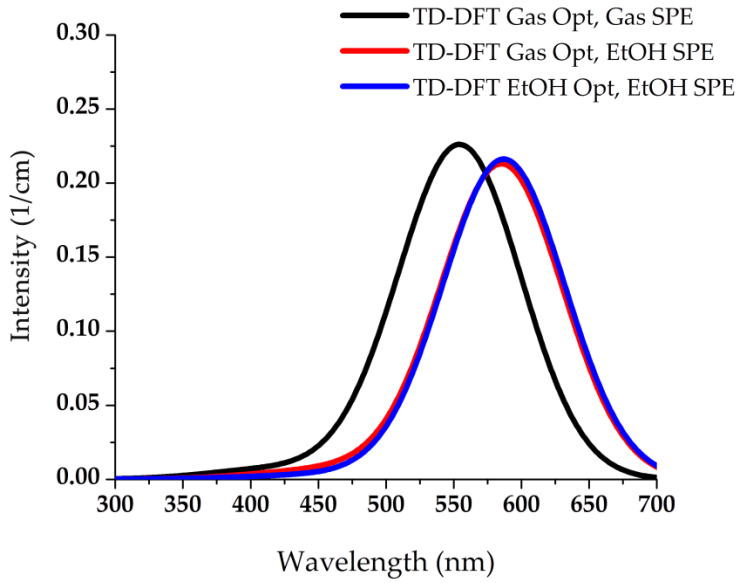

Fig. C4. D&C Blue No. 6 and D&C Yellow No. 11 simulated heterodimeric color additive mixture in three optimization and single point energy calculation conditions: Gas Opt, Gas SPE; Gas Opt, EtOH SPE; EtOH Opt, EtOH SPE

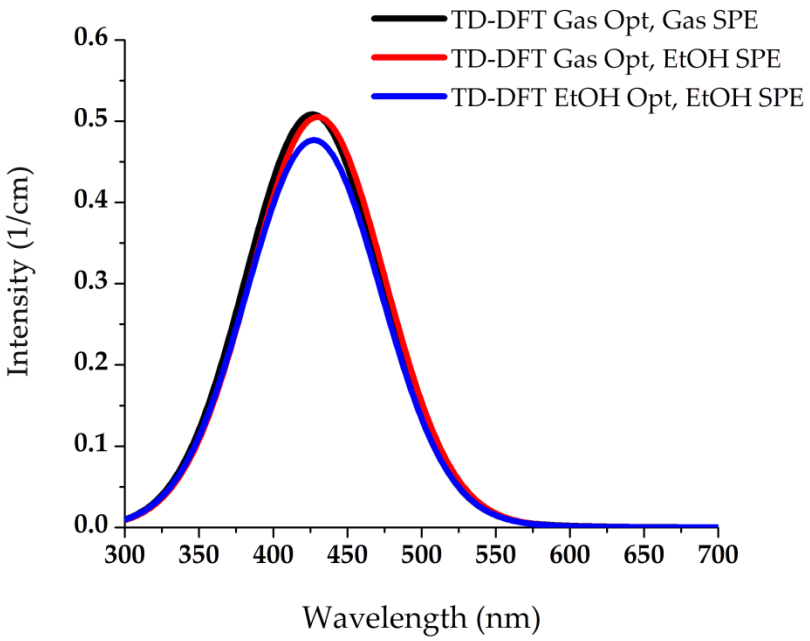

Fig. C5. D&C Yellow No. 11 and D&C Red No. 36 simulated heterodimeric color additive mixture in three optimization and single point energy calculation conditions: Gas Opt, Gas SPE; Gas Opt, EtOH SPE; EtOH Opt, EtOH SPE

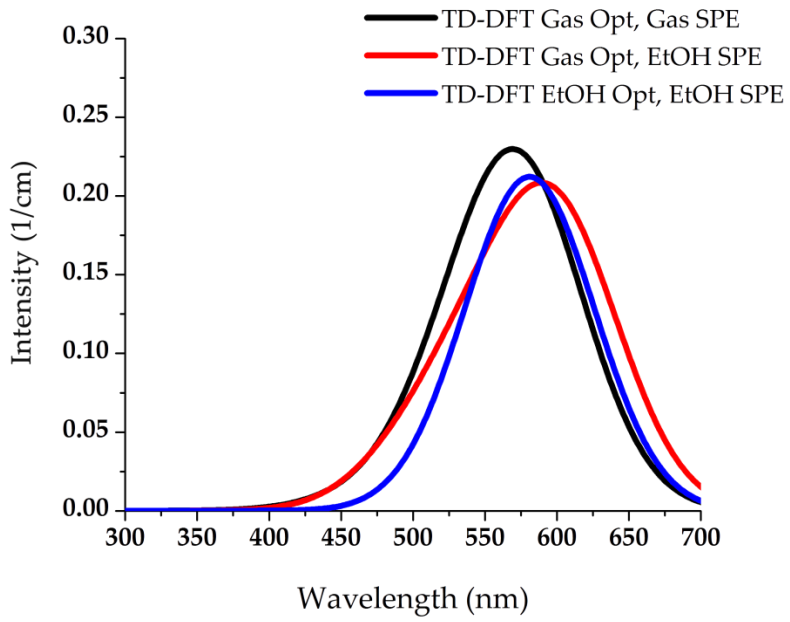

Fig. C6. D&C Blue No. 6 and D&C Red No. 36 simulated heterodimeric color additive mixture in three optimization and single point energy calculation conditions: Gas Opt, Gas SPE; Gas Opt, EtOH SPE; EtOH Opt, EtOH SPE

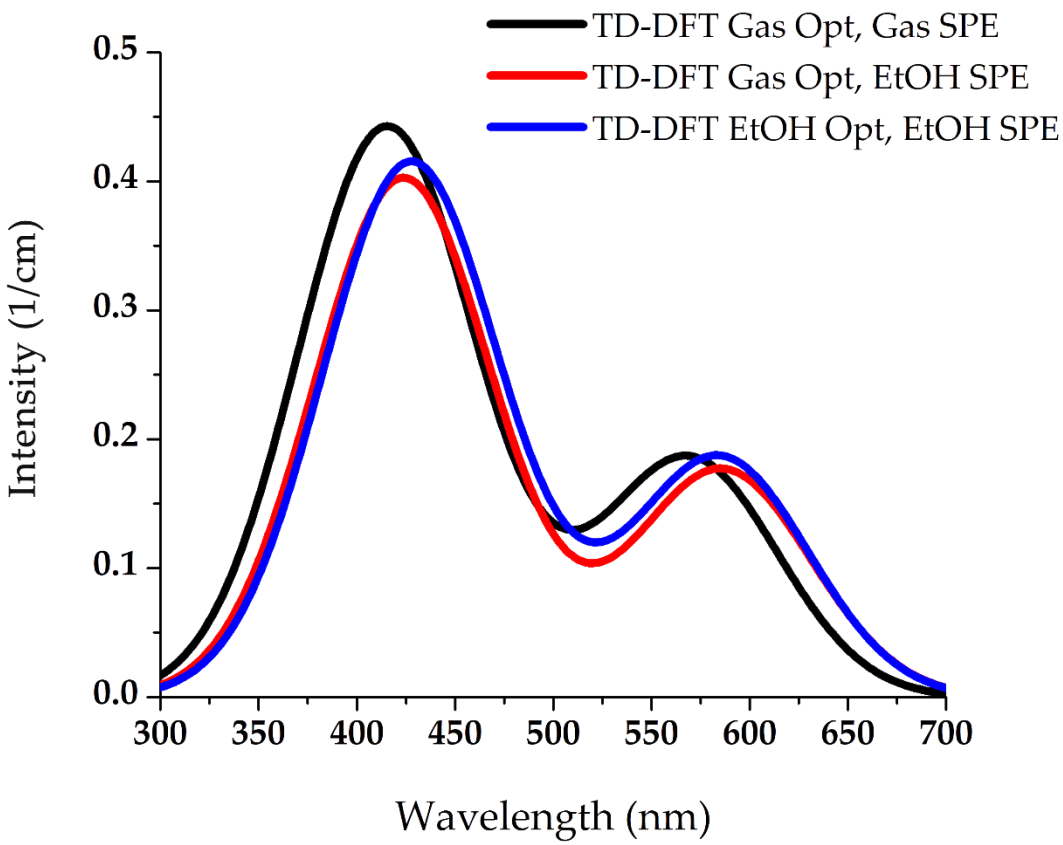

Fig. C7. D&C Blue No. 6, D&C Yellow No. 11, and D&C Red No. 36 simulated heterotrimeric color additive mixture under three optimization and single point energy calculation conditions: Gas Opt, Gas SPE; Gas Opt, EtOH SPE; EtOH Opt, EtOH SPE

Appendix D

Difference of Change between Solvent Effects and Vapor Phase Approximations based on Change in Maximum Absorbance Spectral Peaks Average of Five Solvents and in Vapor Phase for FD&C Red No. 40, D&C Yellow No. 11, and Brilliant Cresyl Blue Alternating Structures

This arithmetic indicates the color additive structures in Chapter 2 that incur quantifiable changes in theoretical maximum absorbance spectral peak responsivity (λ_{max}) as a result of implicit solvation effects using the Poisson-Boltzmann Finite (PBF) elements continuum model discussed in Chapters 1 and 2. In addition, the structures that have solvation effects that more closely resemble theoretical λ_{max} in vapor phase are also indicated with smaller changes in λ_{max}.

Formula: $\Delta\lambda_{max} Average\ of\ 5\ solvents - \Delta\lambda_{max} Vapor\ Phase =$

$Difference\ of\ change\ between\ solvent\ effects\ and\ vapor\ phase\ approximations$

FD&C Red No. 40

$14.86 - 11.83 = 3.03$

D&C Yellow No. 11

$97.96 - 62.60 = 35.36$

Brilliant Cresyl Blue

$3.07 - 19.95 = -16.88$

∴, PBF implicit solvation effects more strongly affect the color additive molecules simulated than vapor phase in the following descending order: D&C Yellow No. 11, FD&C Red No. 40, and Brilliant Cresyl Blue. D&C Yellow No. 11 changes in λ_{max} are strongly affected by solvation effects, whereas Brilliant Cresyl Blue incurs greater changes in λ_{max} with vapor phase effects alone. FD&C Red No. 40 is more stable in vapor phase and under PBF implicit solvation conditions, hence a smaller difference in changes in λ_{max} is observed when subject to comparison.

Appendix E

Solvation Energy Calculations for FD&C Red No. 40, D&C Yellow No. 11, and Brilliant Cresyl Blue Structures 1 and 2 in Varied Solvents and in Vapor Phase

FD&C Red No. 40 "Allura Red"

Solvent	*Vapor Phase*	
Structure Title	**Structure 1, "Azo" (S1)**	**Tautomer, "Hydrazone" (S2)**
SCF Solvation Energy	-1426.0219491 hartrees	-1426.0293078 hartrees
# of SCF iterations	15	17

$$Relative\ energy = SCF\ Energy_{Tautomer} - SCF\ Energy_{S1} = -0.0073587\ hartrees$$

$$\Delta E = (-0.0073587)(27.21)(1.602\ x\ 10^{-19})(6.022x10^{23}) = -19{,}316.69856\frac{J}{mol}$$

$$\therefore, \quad \Delta E = -19.317\frac{kJ}{mol}$$

Solvent	*Water*	
Structure Title	**Structure 1, "Azo" (S1)**	**Tautomer, "Hydrazone" (S2)**
SCF Solvation Energy	--1426.15627857098 hartrees	-1426.17301247708 hartrees
# of SCF iterations	2	2

$$Relative\ energy = SCF\ Energy_{Tautomer} - SCF\ Energy_{S1} = -0.016734\ hartrees$$

$$\Delta E = (-0.016734)(27.21)(1.602\ x\ 10^{-19})(6.022x10^{23}) = -43{,}926.75607\frac{J}{mol}$$

$$\therefore, \quad \Delta E = -43.927\frac{kJ}{mol}$$

Solvent	*Ethanol*	
Structure Title	**Structure 1, "Azo" (S1)**	**Tautomer, "Hydrazone" (S2)**
SCF Solvation Energy	-1426.15245823783 hartrees	-1426.19636764668 hartrees
# of SCF iterations	2	2

$$Relative\ energy = SCF\ Energy_{Tautomer} - SCF\ Energy_{S1} = -0.0439094088\ hartrees$$

$$\Delta E = (-0.0439094088)(27.21)(1.602\ x\ 10^{-19})(6.022x10^{23}) = -115{,}262.8608\frac{J}{mol}$$

$$\therefore, \quad \Delta E = -115.263\frac{kJ}{mol}$$

Solvent	*[BMIM]Cl*	
Structure Title	**Structure 1, "Azo" (S1)**	**Tautomer, "Hydrazone" (S2)**
SCF Solvation Energy	-1426.16523670733 hartrees	-1426.17486380519 hartrees

# of SCF iterations	2	2

$$Relative\ energy = SCF\ Energy_{Tautomer} - SCF\ Energy_{S1} = -0.0096270978\ hartrees$$

$$\Delta E = (-0.0096270978)(27.21)(1.602\ x\ 10^{-19})(6.022x10^{23}) = -25{,}271.27723\frac{J}{mol}$$

$$\therefore, \quad \Delta E = -25.271\frac{kJ}{mol}$$

Solvent	*[BMIM]BF$_4$*	
Structure Title	**Structure 1, "Azo" (S1)**	**Tautomer, "Hydrazone" (S2)**
SCF Solvation Energy	-1426.16412757756 hartrees	-1426.17483617803 hartrees
# of SCF iterations	2	2

$$Relative\ energy = SCF\ Energy_{Tautomer} - SCF\ Energy_{S1} = -0.0107086005\ hartrees$$

$$\Delta E = (-0.0107086005)(27.21)(1.602\ x\ 10^{-19})(6.022x10^{23}) = -28{,}110.23793\frac{J}{mol}$$

$$\therefore, \quad \Delta E = -28.110\frac{kJ}{mol}$$

Solvent	*[EMIM]OAc (ϵ_0=12)*	
Structure Title	**Structure 1, "Azo" (S1)**	**Tautomer, "Hydrazone" (S2)**
SCF Solvation Energy	-1426.17383842938 hartrees	-1425.18376509214 hartrees
# of SCF iterations	4	2

$$Relative\ energy = SCF\ Energy_{Tautomer} - SCF\ Energy_{S1} = -0.0099266628\ hartrees$$

$$\Delta E = (-0.0099266628)(27.21)(1.602\ x\ 10^{-19})(6.022x10^{23}) = -26{,}057.63967\frac{J}{mol}$$

$$\therefore, \quad \Delta E = -26.058\frac{kJ}{mol}$$

Solvent	*[EMIM]OAc (ϵ_0=14)*	
Structure Title	**Structure 1, "Azo" (S1)**	**Tautomer, "Hydrazone" (S2)**
SCF Solvation Energy	-1426.16615389141 hartrees	-1426.17287465625 hartrees
# of SCF iterations	4	2

$$Relative\ energy = SCF\ Energy_{Tautomer} - SCF\ Energy_{S1} = -0.0067207648\ hartrees$$

$$\Delta E = (-0.0067207648)(27.21)(1.602\ x\ 10^{-19})(6.022x10^{23}) = -17{,}642.10903\frac{J}{mol}$$

$$\therefore, \quad \Delta E = -17.642\frac{kJ}{mol}$$

D&C Yellow No. 11 "SS Quinoline Yellow"

Solvent	*Vapor Phase*	
Structure Title	**Structure 1, "Keto" (S1)**	**Tautomer, "Enol" (S2)**
SCF Solvation Energy	-897.7691787757 hartrees	-897.74628153464 hartrees
# of SCF iterations	13	13

$$Relative\ energy = SCF\ Energy_{Tautomer} - SCF\ Energy_{S1} = +0.0228972411\ hartrees$$

$$\Delta E = (0.0228972411)(27.21)(1.602\ x\ 10^{-19})(6.022x10^{23}) = +60{,}105.60336\frac{J}{mol}$$

$$\therefore, \quad \Delta E = +60.106\frac{kJ}{mol}$$

Solvent	*Ethanol*	
Structure Title	**Structure 1, "Keto" (S1)**	**Tautomer, "Enol" (S2)**
SCF Solvation Energy	-897.79651513733 hartrees	-897.77529000061 hartrees
# of SCF iterations	3	2

$$Relative\ energy = SCF\ Energy_{Tautomer} - SCF\ Energy_{S1} = +0.0212251367\ hartrees$$

$$\Delta E = (+0.0212251367)(27.21)(1.602\ x\ 10^{-19})(6.022x10^{23}) = +55{,}716.30423\frac{J}{mol}$$

$$\therefore, \quad \Delta E = +55.716\frac{kJ}{mol}$$

Solvent	*[BMIM]Cl*	
Structure Title	**Structure 1, "Keto" (S1)**	**Tautomer, "Enol" (S2)**
SCF Solvation Energy	-897.79562987543 hartrees	-897.77458131231 hartrees
# of SCF iterations	2	2

$$Relative\ energy = SCF\ Energy_{Tautomer} - SCF\ Energy_{S1} = -0.0210485631\ hartrees$$

$$\Delta E = (-0.0210485631)(27.21)(1.602\ x\ 10^{-19})(6.022x10^{23}) = -55{,}252.79586\frac{J}{mol}$$

$$\therefore, \quad \Delta E = -55.253\frac{kJ}{mol}$$

Solvent	*[BMIM]BF_4*	
Structure Title	**Structure 1, "Keto" (S1)**	**Tautomer, "Enol" (S2)**
SCF Solvation Energy	-897.79552592194 hartrees	-897.77453861897 hartrees
# of SCF iterations	3	2

$$Relative\ energy = SCF\ Energy_{Tautomer} - SCF\ Energy_{S1} = +0.020987303\ hartrees$$

$$\Delta E = (+0.020987303)(27.21)(1.602\ x\ 10^{-19})(6.022x10^{23}) = +55{,}091.98705\frac{J}{mol}$$

$$\therefore, \quad \Delta E = +55.092\frac{kJ}{mol}$$

Solvent	*[EMIM]OAc (ϵ_0=12)*	
Structure Title	**Structure 1, "Keto" (S1)**	**Tautomer, "Enol" (S2)**
SCF Solvation Energy	-897.79374564943 hartrees	-897.77392363461 hartrees
# of SCF iterations	6	2

$$Relative\ energy = SCF\ Energy_{Tautomer} - SCF\ Energy_{S1} = +0.01982201428\ hartrees$$

$$\Delta E = (+0.01982201428)(27.21)(1.602\ x\ 10^{-19})(6.022x10^{23}) = +52{,}033.08806\frac{J}{mol}$$

$$\therefore, \quad \Delta E = +52.033\frac{kJ}{mol}$$

Solvent	*[EMIM]OAc (ϵ_0=14)*	
Structure Title	**Structure 1, "Keto" (S1)**	**Tautomer, "Enol" (S2)**
SCF Solvation Energy	-897.79553514148 hartrees	-897.77470439646 hartrees
# of SCF iterations	3	2

$$Relative\ energy = SCF\ Energy_{Tautomer} - SCF\ Energy_{S1} = +0.020955689\ hartrees$$

$$\Delta E = (+0.020955689)(27.21)(1.602\ x\ 10^{-19})(6.022x10^{23}) = +55{,}008.9999\frac{J}{mol}$$

$$\therefore, \quad \Delta E = +55.009\frac{kJ}{mol}$$

Brilliant Cresyl Blue

Solvent	*Vapor Phase*	
Structure Title	**Structure 1, "BB" (S1)**	**Tautomer, "C" (S2)**
SCF Solvation Energy	-954.49747884732 hartrees	-954.49798028641 hartrees
# of SCF iterations	11	12

$$Relative\ energy = SCF\ Energy_{Tautomer} - SCF\ Energy_{S1}$$

$$= -5.0143909\ x\ 10^{-4}\ hartrees$$

$$\Delta E = (-5.0143909\ x\ 10^{-4})(27.21)(1.602\ x\ 10^{-19})(6.022x10^{23}) = -1{,}316.285179\frac{J}{mol}$$

$$\therefore, \quad \Delta E = -1.316\frac{kJ}{mol}$$

Solvent	*Water*	
Structure Title	**Structure 1, "BB" (S1)**	**Tautomer, "C" (S2)**
SCF Solvation Energy	-954.56697077349 hartrees	-954.56408522381 hartrees
# of SCF iterations	4	4

$$Relative\ energy = SCF\ Energy_{Tautomer} - SCF\ Energy_{S1} = +0.0028855497\ hartrees$$

$$\Delta E = (+0.0028855497)(27.21)(1.602\ x\ 10^{-19})(6.022x10^{23}) = +7{,}574.61146\frac{J}{mol}$$

$$\therefore, \quad \Delta E = +7.575\frac{kJ}{mol}$$

Solvent	*Ethanol*	
Structure Title	**Structure 1, "BB" (S1)**	**Tautomer, "C" (S2)**
SCF Solvation Energy	-954.56983372278 hartrees	-954.56990505023 hartrees
# of SCF iterations	4	3

$$Relative\ energy = SCF\ Energy_{Tautomer} - SCF\ Energy_{S1} = -7.132745\ x\ 10^{-5}\ hartrees$$

$$\Delta E = (-7.132745\ x\ 10^{-5})(27.21)(1.602\ x\ 10^{-19})(6.022x10^{23}) = -187.2356328\frac{J}{mol}$$

$$\therefore, \quad \Delta E = -0.187\frac{kJ}{mol}$$

Solvent	*[BMIM]Cl*	
Structure Title	**Structure 1, "BB" (S1)**	**Tautomer, "C" (S2)**
SCF Solvation Energy	-954.56722755657 hartrees	-954.56818585430 hartrees
# of SCF iterations	3	4

$$Relative\ energy = SCF\ Energy_{Tautomer} - SCF\ Energy_{S1}$$

$$= -9.5829773\ x\ 10^{-4}\ hartrees$$

$$\Delta E = (-9.5829773\ x\ 10^{-4})(27.21)(1.602\ x\ 10^{-19})(6.022x10^{23}) = -2{,}515.546004\frac{J}{mol}$$

$$\therefore, \quad \Delta E = -2.516\frac{kJ}{mol}$$

Solvent	*[BMIM]BF_4*	
Structure Title	**Structure 1, "BB" (S1)**	**Tautomer, "C" (S2)**
SCF Solvation Energy	-954.56795988039 hartrees	-954.56830779847 hartrees
# of SCF iterations	3	3

$$Relative\ energy = SCF\ Energy_{Tautomer} - SCF\ Energy_{S1}$$

$$= -3.4791808\ x\ 10^{-4}\ hartrees$$

$$\Delta E = (-3.4791808\ x\ 10^{-4})(27.21)(1.602\ x\ 10^{-19})(6.022x10^{23}) = -913.2902109\frac{J}{mol}$$

$$\therefore, \quad \Delta E = -0.913\frac{kJ}{mol}$$

Solvent	*[EMIM]OAc (ϵ_0=12)*	
Structure Title	**Structure 1, "BB" (S1)**	**Tautomer, "C" (S2)**
SCF Solvation Energy	-954.56701209792 hartrees	-954.56717407154 hartrees
# of SCF iterations	3	3

$$Relative\ energy = SCF\ Energy_{Tautomer} - SCF\ Energy_{S1}$$

$$= -1.6197362\ x\ 10^{-4}\ hartrees$$

$$\Delta E = (-1.6197362\ x\ 10^{-4})(27.21)(1.602\ x\ 10^{-19})(6.022x10^{23}) = -425.1831971\frac{J}{mol}$$

$$\therefore, \quad \Delta E = -0.425\frac{kJ}{mol}$$

Solvent	*[EMIM]OAc (ϵ_0=14)*	
Structure Title	**Structure 1, "BB" (S1)**	**Tautomer, "C" (S2)**
SCF Solvation Energy	-954.56792620781 hartrees	-954.56818099871 hartrees
# of SCF iterations	3	3

$$Relative\ energy = SCF\ Energy_{Tautomer} - SCF\ Energy_{S1} = -2.547909\ x\ 10^{-4}\ hartrees$$

$$\Delta E = (-2.547909\ x\ 10^{-4})(27.21)(1.602\ x\ 10^{-19})(6.022x10^{23}) = -668.8299579\frac{J}{mol}$$

$$\therefore, \quad \Delta E = -0.669\frac{kJ}{mol}$$

Appendix F

Vibrational Frequency DFT Calculations of Translational, Rotational, Vibrational, Electronic, and Total Energies of FD&C Red No. 40, D&C Yellow No. 11, and Brilliant Cresyl Blue Structures 1 and 2 in Varied Solvents and in Vapor Phase

FD&C Red No. 40 Vibrational Frequency Energy Data (T=298.15 K)

Vapor Phase (Structure 1)

Energy	*U*	C_v	*S*	*H*	*G*	*ln(Q)*
Translational	0.889	2.981	44.492	1.481	-11.784	19.88898
Rotational	0.889	2.981	38.311	0.889	-10.534	17.77879
Vibrational	17.053	105.954	116.354	17.053	-17.638	29.76873
Electronic	0.000	0.000	0.000	0.000	0.000	0.000
Total	18.831	111.915	199.156	19.423	-39.955	67.43651

Total Internal Energy, U_{total} $(SCFE + ZPE + U)$ = -1425.685703 hartrees

Total Enthalpy, H_{total} $(U_{total} + pV)$ = -1425.684759 hartrees

Total Gibbs free energy, G_{total} $(H_{total} - T \cdot S)$ = -1425.779384 hartrees

Vapor Phase (Structure 2 or Tautomer)

Energy	*U*	C_v	*S*	*H*	*G*	*ln(Q)*
Translational	0.889	2.981	44.492	1.481	-11.784	19.88898
Rotational	0.889	2.981	38.337	0.889	-10.541	17.79196
Vibrational	17.167	106.160	117.793	17.167	-17.953	30.30081
Electronic	0.000	0.000	0.000	0.000	0.000	0.000
Total	18.945	112.121	200.621	19.537	-40.278	67.98176

Total Internal Energy, U_{total} $(SCFE + ZPE + U)$ = -1425.692236 hartrees

Total Enthalpy, H_{total} $(U_{total} + pV)$ = -1425.691292 hartrees

Total Gibbs free energy, G_{total} $(H_{total} - T \cdot S)$ = -1425.786613 hartrees

$$\Delta G_{VP} = G_{Tautomer} - G_{S1} = (-1425.786613) - (-1425.779384) = -0.007229\ hartrees$$

$$\Delta G_{VP,J} = (-0.007229\ hartrees)(27.21)(1.602\ x\ 10^{-19})(6.022\ x\ 10^{23})$$

$$= -18{,}976.2341 \frac{J}{mol}$$

$$\Delta G_{VP,kJ} = -18.976\ kJ/mol$$

FD&C Red No. 40 Vibrational Frequency Energy Data (at T = 298.15 K)

Water (Structure 1)

Energy	*U*	C_v	*S*	*H*	*G*	*ln(Q)*
Translational	0.889	2.981	44.492	1.481	-11.784	19.88898
Rotational	0.889	2.981	38.598	0.889	-10.619	17.92322
Vibrational	16.740	103.093	114.173	16.740	-17.301	29.20077
Electronic	0.000	0.000	0.000	0.000	0.000	0.000
Total	18.517	109.055	197.262	19.109	-39.704	67.01298

Total Internal Energy, U_{total} $(SCFE + ZPE + U)$ = -1425.823606 hartrees

Total Enthalpy, H_{total} $(U_{total} + pV)$ = -1425.822662 hartrees

Total Gibbs free energy, G_{total} $(H_{total} - T \cdot S)$ = -1425.916387 hartrees

Water (Structure 2 or Tautomer)

Energy	*U*	C_v	*S*	*H*	*G*	*ln(Q)*
Translational	0.889	2.981	44.492	1.481	-11.784	19.88898
Rotational	0.889	2.981	38.672	0.889	-10.641	17.96045
Vibrational	16.714	103.292	111.779	16.714	-16.613	28.03988
Electronic	0.000	0.000	0.000	0.000	0.000	0.000
Total	18.491	109.254	194.942	19.084	-39.038	65.88931

Total Internal Energy, U_{total} $(SCFE + ZPE + U)$ = -1425.838823 hartrees

Total Enthalpy, H_{total} $(U_{total} + pV)$ = -1425.837879 hartrees

Total Gibbs free energy, G_{total} $(H_{total} - T \cdot S)$ = -1425.930502 hartrees

$$\Delta G_{Water} = G_{Tautomer} - G_{S1} = (-1425.930502) - (-1425.916387)$$
$$= -0.014115\ hartrees$$

$$\Delta G_{Water,J} = (-0.014115\ hartrees)(27.21)(1.602\ x\ 10^{-19})(6.022\ x\ 10^{23})$$
$$= -37{,}052.08803 \frac{J}{mol}$$

$$\Delta G_{Water,kJ} = -37.052\ kJ/mol$$

FD&C Red No. 40 Vibrational Frequency Energy Data (at T = 298.15 K)

Ethanol (Structure 1)

Energy	*U*	C_v	*S*	*H*	*G*	*ln(Q)*
Translational	0.889	2.981	44.492	1.481	-11.784	19.88898
Rotational	0.889	2.981	38.626	0.889	-10.628	17.93733
Vibrational	16.708	103.200	111.432	16.708	-16.515	27.87439
Electronic	0.000	0.000	0.000	0.000	0.000	0.000
Total	18.486	109.162	194.550	19.078	-38.927	65.70071

Total Internal Energy, U_{total} $(SCFE + ZPE + U)$ = -1425.819866 hartrees

Total Enthalpy, H_{total} $(U_{total} + pV)$ = -1425.818921 hartrees

Total Gibbs free energy, G_{total} $(H_{total} - T \cdot S)$ = -1425.911358 hartrees

Ethanol (Structure 2 or Tautomer)

Energy	*U*	C_v	*S*	*H*	*G*	*ln(Q)*
Translational	0.889	2.981	44.492	1.481	-11.784	19.88898
Rotational	0.889	2.981	38.447	0.889	-10.574	17.84737
Vibrational	16.095	101.228	104.538	16.095	-15.073	25.44048
Electronic	0.000	0.000	0.000	0.000	0.000	0.000
Total	17.872	107.189	187.476	18.465	-37.431	63.17684

Total Internal Energy, U_{total} $(SCFE + ZPE + U)$ = -1425.862939 hartrees

Total Enthalpy, H_{total} $(U_{total} + pV)$ = -1425.861995 hartrees

Total Gibbs free energy, G_{total} $(H_{total} - T \cdot S)$ = -1425.951071 hartrees

$$\Delta G_{EtOH} = G_{Tautomer} - G_{S1} = (-1425.951071) - (-1425.911358)$$
$$= -0.039713\ hartrees$$

$$\Delta G_{EtOH,J} = (-0.039713\ hartrees)(27.21)(1.602\ x\ 10^{-19})(6.022\ x\ 10^{23})$$
$$= -104{,}247.2244 \frac{J}{mol}$$

$$\Delta G_{EtOH,kJ} = -104.247\ kJ/mol$$

FD&C Red No. 40 Vibrational Frequency Energy Data (at T = 298.15 K)

[BMIM]Cl (Structure 1)

Energy	*U*	C_v	*S*	*H*	*G*	*ln(Q)*
Translational	0.889	2.981	44.492	1.481	-11.784	19.88898
Rotational	0.889	2.981	38.552	0.889	-10.606	17.90013
Vibrational	16.145	101.150	106.159	16.145	-15.507	26.17217
Electronic	0.000	0.000	0.000	0.000	0.000	0.000
Total	17.922	107.111	189.202	18.515	-37.896	63.96129

Total Internal Energy, U_{total} $(SCFE + ZPE + U)$ = -1425.833464 hartrees

Total Enthalpy, H_{total} $(U_{total} + pV)$ = -1425.832520 hartrees

Total Gibbs free energy, G_{total} $(H_{total} - T \cdot S)$ = -1425.922416 hartrees

[BMIM]Cl (Structure 2 or Tautomer)

Energy	*U*	C_v	*S*	*H*	*G*	*ln(Q)*
Translational	0.889	2.981	44.492	1.481	-11.784	19.88898
Rotational	0.889	2.981	38.590	0.889	-10.617	17.91928
Vibrational	16.211	101.436	107.085	16.211	-15.717	26.52664
Electronic	0.000	0.000	0.000	0.000	0.000	0.000
Total	17.988	107.397	190.166	18.581	-38.118	64.33490

Total Internal Energy, U_{total} $(SCFE + ZPE + U)$ = -1425.842138 hartrees

Total Enthalpy, H_{total} $(U_{total} + pV)$ = -1425.841194 hartrees

Total Gibbs free energy, G_{total} $(H_{total} - T \cdot S)$ = -1425.931548 hartrees

$$\Delta G_{[BMIM]Cl} = G_{Tautomer} - G_{S1} = (-1425.931548) - (-1425.922416)$$
$$= -0.009132\ hartrees$$

$$\Delta G_{[BMIM]Cl,J} = (-0.009132\ hartrees)(27.21)(1.602\ x\ 10^{-19})(6.022\ x\ 10^{23})$$
$$= -23{,}971.63782 \frac{J}{mol}$$

$$\Delta G_{[BMIM]Cl,kJ} = -23.972\ kJ/mol$$

FD&C Red No. 40 Vibrational Frequency Energy Data (at T = 298.15 K)

[BMIM]BF_4 (Structure 1)

Energy	*U*	C_v	*S*	*H*	*G*	*ln(Q)*
Translational	0.889	2.981	44.492	1.481	-11.784	19.88898
Rotational	0.889	2.981	38.544	0.889	-10.603	17.89618
Vibrational	16.754	103.329	113.129	16.975	-16.975	28.65105
Electronic	0.000	0.000	0.000	0.000	0.000	0.000
Total	18.532	109.291	196.165	19.124	-39.362	66.43620

Total Internal Energy, U_{total} $(SCFE + ZPE + U)$ = -1425.831638 hartrees

Total Enthalpy, H_{total} $(U_{total} + pV)$ = -1425.830694 hartrees

Total Gibbs free energy, G_{total} $(H_{total} - T \cdot S)$ = -1425.923898 hartrees

[BMIM]BF_4 (Structure 2 or Tautomer)

Energy	*U*	C_v	*S*	*H*	*G*	*ln(Q)*
Translational	0.889	2.981	44.492	1.481	-11.784	19.88898
Rotational	0.889	2.981	38.583	0.889	-10.615	17.91553
Vibrational	16.307	101.506	109.631	16.307	-16.380	27.64565
Electronic	0.000	0.000	0.000	0.000	0.000	0.000
Total	18.084	107.467	192.705	18.677	-38.778	65.45016

Total Internal Energy, U_{total} $(SCFE + ZPE + U)$ = -1425.842002 hartrees

Total Enthalpy, H_{total} $(U_{total} + pV)$ = -1425.841058 hartrees

Total Gibbs free energy, G_{total} $(H_{total} - T \cdot S)$ = -1425.932618 hartrees

$$\Delta G_{[BMIM]BF4} = G_{Tautomer} - G_{S1} = (-1425.932618) - (-1425.923898)$$
$$= -0.00872\ hartrees$$

$$\Delta G_{[BMIM]BF4,J} = (-0.00872\ hartrees)(27.21)(1.602\ x\ 10^{-19})(6.022\ x\ 10^{23})$$
$$= -22{,}890.13161 \frac{J}{mol}$$

$$\Delta G_{[BMIM]BF4,kJ} = -22.890\ kJ/mol$$

FD&C Red No. 40 Vibrational Frequency Energy Data (at T = 298.15 K)

[EMIM]OAc (ϵ_0=12) (Structure 1)

Energy	*U*	C_v	*S*	*H*	*G*	*ln(Q)*
Translational	0.889	2.981	44.492	1.481	-11.784	19.88898
Rotational	0.889	2.981	38.466	0.889	-10.580	17.85670
Vibrational	15.542	99.148	98.542	15.542	-13.838	23.35601
Electronic	0.000	0.000	0.000	0.000	0.000	0.000
Total	17.320	105.110	181.500	17.912	-36.202	61.10169

Total Internal Energy, U_{total} $(SCFE + ZPE + U)$ = -1425.843068 hartrees

Total Enthalpy, H_{total} $(U_{total} + pV)$ = -1425.842124 hartrees

Total Gibbs free energy, G_{total} $(H_{total} - T \cdot S)$ = -1425.928360 hartrees

[EMIM]OAc (ϵ_0=12) (Structure 2 or Tautomer)

Energy	*U*	C_v	*S*	*H*	*G*	*ln(Q)*
Translational	0.889	2.981	44.492	1.481	-11.784	19.88898
Rotational	0.889	2.981	38.504	0.889	-10.591	17.87572
Vibrational	15.635	99.394	99.799	15.635	-14.120	23.83166
Electronic	0.000	0.000	0.000	0.000	0.000	0.000
Total	17.412	105.356	182.794	18.005	-36.495	61.59637

Total Internal Energy, U_{total} $(SCFE + ZPE + U)$ = -1425.851773 hartrees

Total Enthalpy, H_{total} $(U_{total} + pV)$ = -1425.850829 hartrees

Total Gibbs free energy, G_{total} $(H_{total} - T \cdot S)$ = -1425.937680 hartrees

$$\Delta G_{[EMIM]OAc\,(12)} = G_{Tautomer} - G_{S1} = (-1425.937680) - (-1425.928360)$$
$$= -0.00932\ hartrees$$

$$\Delta G_{[EMIM]OAc\,(12),J} = (-0.00932\ hartrees)(27.21)(1.602\ x\ 10^{-19})(6.022\ x\ 10^{23})$$
$$= -24{,}465.14066 \frac{J}{mol}$$

$$\Delta G_{[EMIM]OAc\,(12),kJ} = -24.465\ kJ/mol$$

FD&C Red No. 40 Vibrational Frequency Energy Data (at T = 298.15 K)

[EMIM]OAc (ϵ_0=14) (Structure 1)

Energy	*U*	C_v	*S*	*H*	*G*	*ln(Q)*
Translational	0.889	2.981	44.492	1.481	-11.784	19.88898
Rotational	0.889	2.981	38.535	0.889	-10.600	17.89137
Vibrational	16.229	101.244	108.501	16.229	-16.120	27.20734
Electronic	0.000	0.000	0.000	0.000	0.000	0.000
Total	18.007	107.206	191.527	18.599	-38.504	64.98770

Total Internal Energy, U_{total} $(SCFE + ZPE + U)$ = -1425.835366 hartrees

Total Enthalpy, H_{total} $(U_{total} + pV)$ = -1425.834422 hartrees

Total Gibbs free energy, G_{total} $(H_{total} - T \cdot S)$ = -1425.925422 hartrees

[EMIM]OAc (ϵ_0=14) (Structure 2 or Tautomer)

Energy	*U*	C_v	*S*	*H*	*G*	*ln(Q)*
Translational	0.889	2.981	44.492	1.481	-11.784	19.88898
Rotational	0.889	2.981	38.597	0.889	-10.619	17.92252
Vibrational	16.817	103.487	113.927	16.817	-17.151	28.94724
Electronic	0.000	0.000	0.000	0.000	0.000	0.000
Total	18.594	109.448	197.016	19.187	-39.554	66.75874

Total Internal Energy, U_{total} $(SCFE + ZPE + U)$ = -1425.838823 hartrees

Total Enthalpy, H_{total} $(U_{total} + pV)$ = -1425.837879 hartrees

Total Gibbs free energy, G_{total} $(H_{total} - T \cdot S)$ = -1425.931487 hartrees

$$\Delta G_{[EMIM]OAc\,(14)} = G_{Tautomer} - G_{S1} = (-1425.931487) - (-1425.925422)$$
$$= -0.006065\ hartrees$$

$$\Delta G_{[EMIM]OAc\,(14),J} = (-0.006065\ hartrees)(27.21)(1.602\ x\ 10^{-19})(6.022\ x\ 10^{23})$$
$$= -15{,}920.71654 \frac{J}{mol}$$

$$\Delta G_{[EMIM]OAc\,(14),kJ} = -15.921\ kJ/mol$$

D&C Yellow No. 11 Vibrational Frequency Energy Data (at T = 298.15 K)

Vapor Phase (Structure 1)

Energy	*U*	C_v	*S*	*H*	*G*	*ln(Q)*
Translational	0.889	2.981	42.713	1.481	-11.254	18.99377
Rotational	0.889	2.981	33.938	0.889	-9.230	15.57804
Vibrational	7.841	55.558	51.582	7.841	-7.538	12.72227
Electronic	0.000	0.000	0.000	0.000	0.000	0.000
Total	9.619	61.519	128.232	10.211	-28.021	47.29407

Total Internal Energy, U_{total} $(SCFE + ZPE + U)$ = -897.511368 hartrees

Total Enthalpy, H_{total} $(U_{total} + pV)$ = -897.510424 hartrees

Total Gibbs free energy, G_{total} $(H_{total} - T \cdot S)$ = -897.571351 hartrees

Vapor Phase (Structure 2 or Tautomer)

Energy	*U*	C_v	*S*	*H*	*G*	*ln(Q)*
Translational	0.889	2.981	42.713	1.481	-11.254	18.99377
Rotational	0.889	2.981	34.009	0.889	-9.251	15.61382
Vibrational	7.365	54.736	43.440	7.365	-5.587	9.42960
Electronic	0.000	0.000	0.000	0.000	0.000	0.000
Total	9.142	60.697	120.162	9.735	-26.091	44.03719

Total Internal Energy, U_{total} $(SCFE + ZPE + U)$ = -897.489204 hartrees

Total Enthalpy, H_{total} $(U_{total} + pV)$ = -897.488260 hartrees

Total Gibbs free energy, G_{total} $(H_{total} - T \cdot S)$ = -897.545353 hartrees

$$\Delta G_{VP} = G_{Tautomer} - G_{S1} = (-897.545353) - (-) = -2.79\ x\ 10^{-4}\ hartrees$$

$$\Delta G_{VP,J} = (-2.79\ x\ 10^{-4} hartrees)(27.21)(1.602\ x\ 10^{-19})(6.022\ x\ 10^{23})$$

$$= -732.3792108 \frac{J}{mol}$$

$$\Delta G_{VP,kJ} = -0.732\ kJ/mol$$

D&C Yellow No. 11 Vibrational Frequency Energy Data (at T = 298.15 K)

Ethanol (Structure 1)

Energy	*U*	C_v	*S*	*H*	*G*	*ln(Q)*
Translational	0.889	2.981	42.713	1.481	-11.254	18.99377
Rotational	0.889	2.981	33.946	0.889	-9.232	15.58225
Vibrational	7.692	55.189	48.308	7.692	-6.711	11.32683
Electronic	0.000	0.000	0.000	0.000	0.000	0.000
Total	9.469	61.150	124.966	10.062	-27.197	45.90285

Total Internal Energy, U_{total} $(SCFE + ZPE + U)$ = -897.538855 hartrees

Total enthalpy, H_{total} $(U_{total} + pV)$ = -897.537911 hartrees

Total Gibbs free energy, G_{total} $(H_{total} - T \cdot S)$ = -897.597286 hartrees

Ethanol (Structure 2 or Tautomer)

Energy	*U*	C_v	*S*	*H*	*G*	*ln(Q)*
Translational	0.889	2.981	42.713	1.481	-11.254	18.99377
Rotational	0.889	2.981	34.019	0.889	-9.254	15.61913
Vibrational	7.163	53.896	41.805	7.163	-5.301	8.94675
Electronic	0.000	0.000	0.000	0.000	0.000	0.000
Total	8.941	59.858	118.536	9.533	-25.808	43.55965

Total Internal Energy, U_{total} $(SCFE + ZPE + U)$ = -897.518187 hartrees

Total enthalpy, H_{total} $(U_{total} + pV)$ = -897.517242 hartrees

Total Gibbs free energy, G_{total} $(H_{total} - T \cdot S)$ = -897.573563 hartrees

$$\Delta G_{EtOH} = G_{Tautomer} - G_{S1} = (-897.573563) - (-897.597286) = +0.023723\ hartrees$$

$$\Delta G_{EtOH,J} = (+0.023723\ hartrees)(27.21)(1.602\ x\ 10^{-19})(6.022\ x\ 10^{23})$$

$$= +62{,}273.23304 \frac{J}{mol}$$

$$\Delta G_{EtOH,kJ} = +62.273\ kJ/mol$$

D&C Yellow No. 11 Vibrational Frequency Energy Data (at T = 298.15 K)

[BMIM]Cl (Structure 1)

Energy	*U*	C_v	*S*	*H*	*G*	*ln(Q)*
Translational	0.889	2.981	42.713	1.481	-11.254	18.99377
Rotational	0.889	2.981	33.946	0.889	-9.232	15.58217
Vibrational	7.690	55.185	48.294	7.690	-6.708	11.32228
Electronic	0.000	0.000	0.000	0.000	0.000	0.000
Total	9.468	61.147	124.952	10.060	-27.194	45.89821

Total Internal Energy, U_{total} $(SCFE + ZPE + U)$ = -897.537849 hartrees

Total enthalpy, H_{total} $(U_{total} + pV)$ = -897.536905 hartrees

Total Gibbs free energy, G_{total} $(H_{total} - T \cdot S)$ = -897.596273 hartrees

[BMIM]Cl (Structure 2 or Tautomer)

Energy	*U*	C_v	*S*	*H*	*G*	*ln(Q)*
Translational	0.889	2.981	42.713	1.481	-11.254	18.99377
Rotational	0.889	2.981	34.018	0.889	-9.254	15.61855
Vibrational	7.164	53.895	41.800	7.164	-5.299	8.94317
Electronic	0.000	0.000	0.000	0.000	0.000	0.000
Total	8.941	59.857	118.530	9.534	-25.806	43.55549

Total Internal Energy, U_{total} $(SCFE + ZPE + U)$ = -897.517650 hartrees

Total enthalpy, H_{total} $(U_{total} + pV)$ = -897.516706 hartrees

Total Gibbs free energy, G_{total} $(H_{total} - T \cdot S)$ = -897.573023 hartrees

$$\Delta G_{[BMIM]Cl} = G_{Tautomer} - G_{S1} = (-897.573023) - (-897.596273) = +0.02325\ hartrees$$

$$\Delta G_{[BMIM]Cl,J} = (+0.02325\ hartrees)(27.21)(1.602\ x\ 10^{-19})(6.022\ x\ 10^{23})$$

$$= +61{,}031.6009 \frac{J}{mol}$$

$$\Delta G_{[BMIM]Cl,kJ} = +61.032\ kJ/mol$$

D&C Yellow No. 11 Vibrational Frequency Energy Data (at T = 298.15 K)

[BMIM]BF_4 (Structure 1)

Energy	*U*	C_v	*S*	*H*	*G*	*ln(Q)*
Translational	0.889	2.981	42.713	1.481	-11.254	18.99377
Rotational	0.889	2.981	33.945	0.889	-9.232	15.58176
Vibrational	7.689	55.187	48.228	7.689	-6.690	11.29154
Electronic	0.000	0.000	0.000	0.000	0.000	0.000
Total	9.466	61.148	124.885	10.059	-27.176	45.86706

Total Internal Energy, U_{total} $(SCFE + ZPE + U)$ = -897.537839 hartrees

Total enthalpy, H_{total} $(U_{total} + pV)$ = -897.536895 hartrees

Total Gibbs free energy, G_{total} $(H_{total} - T \cdot S)$ = -897.596232 hartrees

[BMIM]BF_4 (Structure 2 or Tautomer)

Energy	*U*	C_v	*S*	*H*	*G*	*ln(Q)*
Translational	0.889	2.981	42.713	1.481	-11.254	18.99377
Rotational	0.889	2.981	34.018	0.889	-9.254	15.61855
Vibrational	7.164	53.897	41.808	7.164	-5.301	8.94641
Electronic	0.000	0.000	0.000	0.000	0.000	0.000
Total	8.942	59.858	118.538	9.534	-25.808	43.55872

Total Internal Energy, U_{total} $(SCFE + ZPE + U)$ = -897.517434 hartrees

Total enthalpy, H_{total} $(U_{total} + pV)$ = -897.516490 hartrees

Total Gibbs free energy, G_{total} $(H_{total} - T \cdot S)$ = -897.572812 hartrees

$$\Delta G_{[BMIM]BF4} = G_{Tautomer} - G_{S1} = (-897.572812) - (-897.596232)$$
$$= +0.02342\ hartrees$$

$$\Delta G_{[BMIM]BF4,J} = (+0.02342\ hartrees)(27.21)(1.602\ x\ 10^{-19})(6.022\ x\ 10^{23})$$
$$= +61{,}477.85346 \frac{J}{mol}$$

$$\Delta G_{[BMIM]BF4,kJ} = +61.478\ kJ/mol$$

D&C Yellow No. 11 Vibrational Frequency Energy Data (at T = 298.15 K)

[EMIM]OAc (ϵ_0=12) (Structure 1)

Energy	*U*	C_v	*S*	*H*	*G*	*ln(Q)*
Translational	0.889	2.981	42.713	1.481	-11.254	18.99377
Rotational	0.889	2.981	33.945	0.889	-9.232	15.58163
Vibrational	7.693	55.193	48.292	7.693	-6.706	11.31782
Electronic	0.000	0.000	0.000	0.000	0.000	0.000
Total	9.470	61.155	124.950	10.063	-27.191	45.89321

Total Internal Energy, U_{total} $(SCFE + ZPE + U)$ = -897.537231 hartrees

Total enthalpy, H_{total} $(U_{total} + pV)$ = -897.536287 hartrees

Total Gibbs free energy, G_{total} $(H_{total} - T \cdot S)$ = -897.595655 hartrees

[EMIM]OAc (ϵ_0=12) (Structure 2 or Tautomer)

Energy	*U*	C_v	*S*	*H*	*G*	*ln(Q)*
Translational	0.889	2.981	42.713	1.481	-11.254	18.99377
Rotational	0.889	2.981	34.018	0.889	-9.254	15.61875
Vibrational	7.167	53.925	41.801	7.167	-5.296	8.93901
Electronic	0.000	0.000	0.000	0.000	0.000	0.000
Total	8.944	59.886	118.532	9.537	-25.804	43.55153

Total Internal Energy, U_{total} $(SCFE + ZPE + U)$ = -897.516832 hartrees

Total enthalpy, H_{total} $(U_{total} + pV)$ = -897.515888 hartrees

Total Gibbs free energy, G_{total} $(H_{total} - T \cdot S)$ = -897.572207 hartrees

$$\Delta G_{[EMIM]OAc\,(12)} = G_{Tautomer} - G_{S1} = (-897.572207) - (-897.595655)$$
$$= +0.023448\ hartrees$$

$$\Delta G_{[EMIM]OAc\,(12),J} = (+0.023448\ hartrees)(27.21)(1.602\ x\ 10^{-19})(6.022\ x\ 10^{23})$$
$$= +61{,}551.35389\ \frac{J}{mol}$$

$$\Delta G_{[EMIM]OAc\,(12),kJ} = +61.551\ kJ/mol$$

D&C Yellow No. 11 Vibrational Frequency Energy Data (at T = 298.15 K)

[EMIM]OAc (ϵ_0=14) (Structure 1)

Energy	*U*	C_v	*S*	*H*	*G*	*ln(Q)*
Translational	0.889	2.981	42.713	1.481	-11.254	18.99377
Rotational	0.889	2.981	33.945	0.889	-9.232	15.58171
Vibrational	7.690	55.188	48.242	7.690	-6.694	11.29750
Electronic	0.000	0.000	0.000	0.000	0.000	0.000
Total	9.467	61.150	124.899	10.060	-27.179	45.87297

Total Internal Energy, U_{total} $(SCFE + ZPE + U)$ = -897.537855 hartrees

Total enthalpy, H_{total} $(U_{total} + pV)$ = -897.536911 hartrees

Total Gibbs free energy, G_{total} $(H_{total} - T \cdot S)$ = -897.596254 hartrees

[EMIM]OAc (ϵ_0=14) (Structure 2 or Tautomer)

Energy	*U*	C_v	*S*	*H*	*G*	*ln(Q)*
Translational	0.889	2.981	42.713	1.481	-11.254	18.99377
Rotational	0.889	2.981	34.018	0.889	-9.254	15.61851
Vibrational	7.164	53.893	41.002	7.164	-5.300	8.94490
Electronic	0.000	0.000	0.000	0.000	0.000	0.000
Total	8.941	59.855	118.533	9.534	-25.807	43.55718

Total Internal Energy, U_{total} $(SCFE + ZPE + U)$ = -897.517598 hartrees

Total enthalpy, H_{total} $(U_{total} + pV)$ = -897.516654 hartrees

Total Gibbs free energy, G_{total} $(H_{total} - T \cdot S)$ = -897.572973 hartrees

$$\Delta G_{[EMIM]OAc\,(14)} = G_{Tautomer} - G_{S1} = (-897.572973) - (-897.596254)$$
$$= +0.023281\ hartrees$$

$$\Delta G_{[EMIM]OAc\,(14),J} = (+0.023281\ hartrees)(27.21)(1.602\ x\ 10^{-19})(6.022\ x\ 10^{23})$$
$$= +61{,}112.97637\,\frac{J}{mol}$$

$$\Delta G_{[EMIM]OAc\,(14),kJ} = +61.113\ kJ/mol$$

Brilliant Cresyl Blue Vibrational Frequency Energy Data (at T = 298.15 K)

Vapor Phase (Structure 1)

Energy	*U*	C_v	*S*	*H*	*G*	*ln(Q)*
Translational	0.889	2.981	42.965	1.481	-11.329	19.12059
Rotational	0.889	2.981	34.717	0.889	-9.462	15.97045
Vibrational	11.345	76.712	70.190	11.345	-9.582	16.17277
Electronic	0.000	0.000	0.000	0.000	0.000	0.000
Total	13.122	82.673	147.871	13.715	-30.373	51.26381

Total Internal Energy, U_{total} $(SCFE + ZPE + U)$ = -954.114145 hartrees

Total enthalpy, H_{total} $(U_{total} + pV)$ = -954.113201 hartrees

Total Gibbs free energy, G_{total} $(H_{total} - T \cdot S)$ = -954.183460 hartrees

Vapor Phase (Structure 2 or Tautomer)

Energy	*U*	C_v	*S*	*H*	*G*	*ln(Q)*
Translational	0.889	2.981	42.965	1.481	-11.329	19.12059
Rotational	0.889	2.981	34.740	0.889	-9.469	15.98182
Vibrational	11.315	76.645	70.081	11.315	-9.579	16.16796
Electronic	0.000	0.000	0.000	0.000	0.000	0.000
Total	13.093	82.607	147.786	13.685	-30.377	51.27038

Total Internal Energy, U_{total} $(SCFE + ZPE + U)$ = -954.11446 hartrees

Total enthalpy, H_{total} $(U_{total} + pV)$ = -954.113522 hartrees

Total Gibbs free energy, G_{total} $(H_{total} - T \cdot S)$ = -954.183739 hartrees

$$\Delta G_{VP} = G_{Tautomer} - G_{S1} = (-954.183739) - (-954.183460) = -2.79\ x\ 10^{-4}\ hartrees$$

$$\Delta G_{VP,J} = (-2.79\ x\ 10^{-4} hartrees)(27.21)(1.602\ x\ 10^{-19})(6.022\ x\ 10^{23})$$

$$= -732.3792108 \frac{J}{mol}$$

$$\Delta G_{VP,kJ} = -0.732\ kJ/mol$$

Brilliant Cresyl Blue Vibrational Frequency Energy Data (at T = 298.15 K)

Water (Structure 1)

Energy	*U*	C_v	*S*	*H*	*G*	*ln(Q)*
Translational	0.889	2.981	42.965	1.481	-11.329	19.12059
Rotational	0.889	2.981	34.734	0.889	-9.467	15.97891
Vibrational	10.921	75.064	68.773	10.921	-9.584	16.17609
Electronic	0.000	0.000	0.000	0.000	0.000	0.000
Total	12.698	81.025	146.472	13.290	-30.380	51.27559

Total Internal Energy, U_{total} $(SCFE + ZPE + U)$ = -954.184075 hartrees

Total enthalpy, H_{total} $(U_{total} + pV)$ = -954.183131 hartrees

Total Gibbs free energy, G_{total} $(H_{total} - T \cdot S)$ = -954.252724 hartrees

Water (Structure 2 or Tautomer)

Energy	*U*	C_v	*S*	*H*	*G*	*ln(Q)*
Translational	0.889	2.981	42.965	1.481	-11.329	19.12059
Rotational	0.889	2.981	34.761	0.889	-9.475	15.99231
Vibrational	10.889	75.082	67.473	10.889	-9.228	15.57501
Electronic	0.000	0.000	0.000	0.000	0.000	0.000
Total	12.667	81.044	145.199	13.259	-30.032	50.68791

Total Internal Energy, U_{total} $(SCFE + ZPE + U)$ = -954.181103 hartrees

Total enthalpy, H_{total} $(U_{total} + pV)$ = -954.180158 hartrees

Total Gibbs free energy, G_{total} $(H_{total} - T \cdot S)$ = -954.249147 hartrees

$$\Delta G_{Water} = G_{Tautomer} - G_{S1} = (-954.249147) - (-954.252724) = +0.003577\ hartrees$$

$$\Delta G_{Water,J} = (+0.003577\ hartrees)(27.21)(1.602\ x\ 10^{-19})(6.022\ x\ 10^{23})$$

$$= +9{,}389.678986 \frac{J}{mol}$$

$$\Delta G_{Water,kJ} = +9.390\ kJ/mol$$

Brilliant Cresyl Blue Vibrational Frequency Energy Data (at T = 298.15 K)

Ethanol (Structure 1)

Energy	*U*	C_v	*S*	*H*	*G*	*ln(Q)*
Translational	0.889	2.981	42.965	1.481	-11.329	19.12059
Rotational	0.889	2.981	34.735	0.889	-9.468	15.97934
Vibrational	10.925	75.160	68.192	10.925	-9.406	15.87569
Electronic	0.000	0.000	0.000	0.000	0.000	0.000
Total	12.703	81.122	145.892	13.295	-30.202	50.97562

Total Internal Energy, U_{total} $(SCFE + ZPE + U)$ = -954.187056 hartrees

Total enthalpy, H_{total} $(U_{total} + pV)$ = -954.186111 hartrees

Total Gibbs free energy, G_{total} $(H_{total} - T \cdot S)$ = -954.255429 hartrees

Ethanol (Structure 2 or Tautomer)

Energy	*U*	C_v	*S*	*H*	*G*	*ln(Q)*
Translational	0.889	2.981	42.965	1.481	-11.329	19.12059
Rotational	0.889	2.981	34.761	0.889	-9.475	15.99248
Vibrational	10.884	75.133	67.098	10.884	-9.121	15.39423
Electronic	0.000	0.000	0.000	0.000	0.000	0.000
Total	12.662	81.095	144.823	13.254	-29.925	50.50730

Total Internal Energy, U_{total} $(SCFE + ZPE + U)$ = -954.186987 hartrees

Total enthalpy, H_{total} $(U_{total} + pV)$ = -954.186042 hartrees

Total Gibbs free energy, G_{total} $(H_{total} - T \cdot S)$ = -954.254853 hartrees

$$\Delta G_{EtOH} = G_{Tautomer} - G_{S1} = (-954.254853) - (-954.255429) = +5.76\ x\ 10^{-4}\ hartrees$$

$$\Delta G_{EtOH,J} = (+5.76\ x\ 10^{-4} hartrees)(27.21)(1.602\ x\ 10^{-19})(6.022\ x\ 10^{23})$$

$$= +1{,}512.008693 \frac{J}{mol}$$

$$\Delta G_{EtOH,kJ} = +1.512\ kJ/mol$$

Brilliant Cresyl Blue Vibrational Frequency Energy Data (at T = 298.15 K)

[BMIM]Cl (Structure 1)

Energy	*U*	C_v	*S*	*H*	*G*	*ln(Q)*
Translational	0.889	2.981	42.965	1.481	-11.329	19.12059
Rotational	0.889	2.981	34.734	0.889	-9.467	15.97884
Vibrational	10.941	75.230	68.288	10.941	-9.419	15.89823
Electronic	0.000	0.000	0.000	0.000	0.000	0.000
Total	12.718	81.191	145.987	13.311	-30.215	50.99766

Total Internal Energy, U_{total} $(SCFE + ZPE + U)$ = -954.184411 hartrees

Total enthalpy, H_{total} $(U_{total} + pV)$ = -954.183467 hartrees

Total Gibbs free energy, G_{total} $(H_{total} - T \cdot S)$ = -954.252830 hartrees

[BMIM]Cl (Structure 2 or Tautomer)

Energy	*U*	C_v	*S*	*H*	*G*	*ln(Q)*
Translational	0.889	2.981	42.965	1.481	-11.329	19.12059
Rotational	0.889	2.981	34.759	0.889	-9.475	15.99140
Vibrational	10.885	75.108	67.188	10.885	-9.147	15.43781
Electronic	0.000	0.000	0.000	0.000	0.000	0.000
Total	12.663	81.070	144.912	13.255	-29.950	50.54980

Total Internal Energy, U_{total} $(SCFE + ZPE + U)$ = -954.185284 hartrees

Total enthalpy, H_{total} $(U_{total} + pV)$ = -954.184340 hartrees

Total Gibbs free energy, G_{total} $(H_{total} - T \cdot S)$ = -954.253193 hartrees

$$\Delta G_{[BMIM]Cl} = G_{Tautomer} - G_{S1} = (-954.253193) - (-954.252830)$$
$$= -3.63\ x\ 10^{-4}\ hartrees$$

$$\Delta G_{[BMIM]Cl,J} = (-3.63\ x\ 10^{-4} hartrees)(27.21)(1.602\ x\ 10^{-19})(6.022\ x\ 10^{23})$$
$$= -952.8804785 \frac{J}{mol}$$

$$\Delta G_{[BMIM]Cl,kJ} = -0.953\ kJ/mol$$

Brilliant Cresyl Blue Vibrational Frequency Energy Data (at T = 298.15 K)

[BMIM]BF_4 (Structure 1)

Energy	*U*	C_v	*S*	*H*	*G*	*ln(Q)*
Translational	0.889	2.981	42.965	1.481	-11.329	19.12059
Rotational	0.889	2.981	34.734	0.889	-9.467	15.97882
Vibrational	10.945	75.216	68.434	10.945	-9.459	15.96434
Electronic	0.000	0.000	0.000	0.000	0.000	0.000
Total	12.722	81.178	146.132	13.315	-30.255	51.06375

Total Internal Energy, U_{total} $(SCFE + ZPE + U)$ = -954.185141 hartrees

Total enthalpy, H_{total} $(U_{total} + pV)$ = -954.184197 hartrees

Total Gibbs free energy, G_{total} $(H_{total} - T \cdot S)$ = -954.253629 hartrees

[BMIM]BF_4 (Structure 2 or Tautomer)

Energy	*U*	C_v	*S*	*H*	*G*	*ln(Q)*
Translational	0.889	2.981	42.965	1.481	-11.329	19.12059
Rotational	0.889	2.981	34.759	0.889	-9.475	15.99156
Vibrational	10.913	75.133	67.854	10.913	-9.318	15.72719
Electronic	0.000	0.000	0.000	0.000	0.000	0.000
Total	12.690	81.094	145.578	13.283	-30.122	-50.83933

Total Internal Energy, U_{total} $(SCFE + ZPE + U)$ = -954.185292 hartrees

Total enthalpy, H_{total} $(U_{total} + pV)$ = -954.184348 hartrees

Total Gibbs free energy, G_{total} $(H_{total} - T \cdot S)$ = -954.253517 hartrees

$$\Delta G_{[BMIM]BF4} = G_{Tautomer} - G_{S1} = (-954.253517) - (-954.253629)$$
$$= +1.12\,x\,10^{-4}\ hartrees$$

$$\Delta G_{[BMIM]BF4,J} = (+1.12\,x\,10^{-4} hartrees)(27.21)(1.602\,x\,10^{-19})(6.022\,x\,10^{23})$$
$$= +294.0016903\,\frac{J}{mol}$$

$$\Delta G_{[BMIM]BF4,kJ} = +0.294\ kJ/mol$$

Brilliant Cresyl Blue Vibrational Frequency Energy Data (at T = 298.15 K)

[EMIM]OAc (ϵ_0=12) (Structure 1)

Energy	*U*	C_v	*S*	*H*	*G*	*ln(Q)*
Translational	0.889	2.981	42.965	1.481	-11.329	19.12059
Rotational	0.889	2.981	34.734	0.889	-9.467	15.97857
Vibrational	10.941	75.185	68.257	10.941	-9.410	15.88165
Electronic	0.000	0.000	0.000	0.000	0.000	0.000
Total	12.719	81.147	145.956	13.311	-30.205	50.98081

Total Internal Energy, U_{total} $(SCFE + ZPE + U)$ = -954.184228 hartrees

Total enthalpy, H_{total} $(U_{total} + pV)$ = -954.183284 hartrees

Total Gibbs free energy, G_{total} $(H_{total} - T \cdot S)$ = -954.252632 hartrees

[EMIM]OAc (ϵ_0=12) (Structure 2 or Tautomer)

Energy	*U*	C_v	*S*	*H*	*G*	*ln(Q)*
Translational	0.889	2.981	42.965	1.481	-11.329	19.12059
Rotational	0.889	2.981	34.759	0.889	-9.475	15.99160
Vibrational	10.900	75.176	67.347	10.900	-9.180	15.49385
Electronic	0.000	0.000	0.000	0.000	0.000	0.000
Total	12.677	81.138	145.071	13.270	-29.983	50.60604

Total Internal Energy, U_{total} $(SCFE + ZPE + U)$ = -954.184227 hartrees

Total enthalpy, H_{total} $(U_{total} + pV)$ = -954.183283 hartrees

Total Gibbs free energy, G_{total} $(H_{total} - T \cdot S)$ = -954.252211 hartrees

$$\Delta G_{[EMIM]OAc\,(12)} = G_{Tautomer} - G_{S1} = (-954.252211) - (-954.252632)$$
$$= +4.21\ x\ 10^{-4}\ hartrees$$

$$\Delta G_{[EMIM]OAc\,(12),J} = (+4.21\ x\ 10^{-4} hartrees)(27.21)(1.602\ x\ 10^{-19})(6.022\ x\ 10^{23})$$
$$= +1{,}105.131354 \frac{J}{mol}$$

$$\Delta G_{[EMIM]OAc\,(12),kJ} = +1.105\ kJ/mol$$

Brilliant Cresyl Blue Vibrational Frequency Energy Data (at T = 298.15 K)

[EMIM]OAc (ϵ_0=14) (Structure 1)

Energy	*U*	*C_v*	*S*	*H*	*G*	*ln(Q)*
Translational	0.889	2.981	42.965	1.481	-11.329	19.12059
Rotational	0.889	2.981	34.734	0.889	-9.467	15.97874
Vibrational	10.933	75.155	68.160	10.933	-9.389	15.84720
Electronic	0.000	0.000	0.000	0.000	0.000	0.000
Total	12.710	81.117	145.858	13.303	-30.185	50.94653

Total Internal Energy, U_{total} $(SCFE + ZPE + U)$ = -954.185150 hartrees

Total enthalpy, H_{total} $(U_{total} + pV)$ = -954.184206 hartrees

Total Gibbs free energy, G_{total} $(H_{total} - T \cdot S)$ = -954.253508 hartrees

[EMIM]OAc (ϵ_0=14) (Structure 2 or Tautomer)

Energy	*U*	*C_v*	*S*	*H*	*G*	*ln(Q)*
Translational	0.889	2.981	42.965	1.481	-11.329	19.12059
Rotational	0.889	2.981	34.760	0.889	-9.475	15.99176
Vibrational	10.914	75.171	67.720	10.914	-9.277	15.65734
Electronic	0.000	0.000	0.000	0.000	0.000	0.000
Total	12.691	81.132	145.444	13.284	-30.080	50.76969

Total Internal Energy, U_{total} $(SCFE + ZPE + U)$ = -954.185226 hartrees

Total enthalpy, H_{total} $(U_{total} + pV)$ = -954.184282 hartrees

Total Gibbs free energy, G_{total} $(H_{total} - T \cdot S)$ = -954.253387 hartrees

$$\Delta G_{[EMIM]OAc\,(14)} = G_{Tautomer} - G_{S1} = (-954.253387) - (-954.253508)$$
$$= +1.21\ x\ 10^{-4}\ hartrees$$

$$\Delta G_{[EMIM]OAc\,(14),J} = (+1.21\ x\ 10^{-4} hartrees)(27.21)(1.602\ x\ 10^{-19})(6.022\ x\ 10^{23})$$
$$= +317.6268262 \frac{J}{mol}$$

$$\Delta G_{[EMIM]OAc\,(14),kJ} = +0.318\ kJ/mol$$

Appendix G

Color Appearance Experimental Data for FD&C Blue No. 1, FD&C Yellow No. 5, and FD&C Red No. 40 Color Additive Mixtures in Ethanol

The following data was collected to analyze the interaction of water-soluble color additive molecules containing comparatively large sulfonated salt groups ($[SO_3]^-$). Three color additive molecules were selected for experimental analysis of their solvent interactions in ethanol:

(i) FD&C Yellow No. 5, or "Tartrazine",

(ii) FD&C Red No. 40, or "Allura Red", and

(iii) FD&C Blue No. 1, "Acid Blue 9".

All three of these color additives have been approved for use in food, drug or pharmaceutical, and cosmetic products by the Food and Drug Administration in the United States (hence "FD&C" in their nomenclature, respectively) [1,2], and in other nations that abide by FDA regulations [3]. While computational data generation of restricted singlet excited states to simulate theoretical maximum absorbance curves proved prohibitive when the B3LYP/6-31+G* basis set was applied in the methods discussed throughout Chapters 1, 2, and 3, it is still interesting to provide a brief discussion of the overall hue of experimental batch mixtures containing three of the most common color additive molecules with widespread applications in diverse consumer products available in today's market.

Fig. G1. Individual color additive molecules mixed in ethanol solvent with corresponding 0.1 mm path length cuvette sample preparation. From left to right: FD&C Yellow No. 5, “Tartrazine”; FD&C Red No. 40 “Allura Red”, and FD&C Blue No. 1 “Acid Blue 9”

Figure G1 shows the color appearance of a molar equivalent of each individual color additive molecule in ethanol solvent and a corresponding sample prepared for UV-visible spectroscopic analysis using a 0.1 mm path length cuvette. Note that each of these color additive mixtures is translucent upon mixture in transparent ethanol solvent—particularly the Tartrazine mixture (left). This is because the “dye” molecules shown are known to exhibit great solubility in ethanol and water solvent [3, 4], thereby justifying their widespread use in mass-market and specialty formulations containing water and ethanol, which are the two most popular solvents for industrial use today [5-10].

Fig. G2. Heterodimeric mixtures of individual color additives in ethanol solvent. From left to right: FD&C Yellow No. 5 and FD&C Red No. 40 (Tartrazine—Allura Red), FD&C Yellow No. 5 and FD&C Blue No. 1 (Tartrazine—Acid Blue 9), and FD&C Blue No. 1 and FD&C Red No. 40 (Acid Blue 9—Allura Red) in ethanol solvent.

The heterodimeric mixtures of molar equivalents of two color additive molecules in ethanol solvent shown in Figure G2 reveal that the translucent quality of the individual color additive batches is preserved when additional color additive molecules are added to the mixture. The path length cuvettes further illustrate this concept.

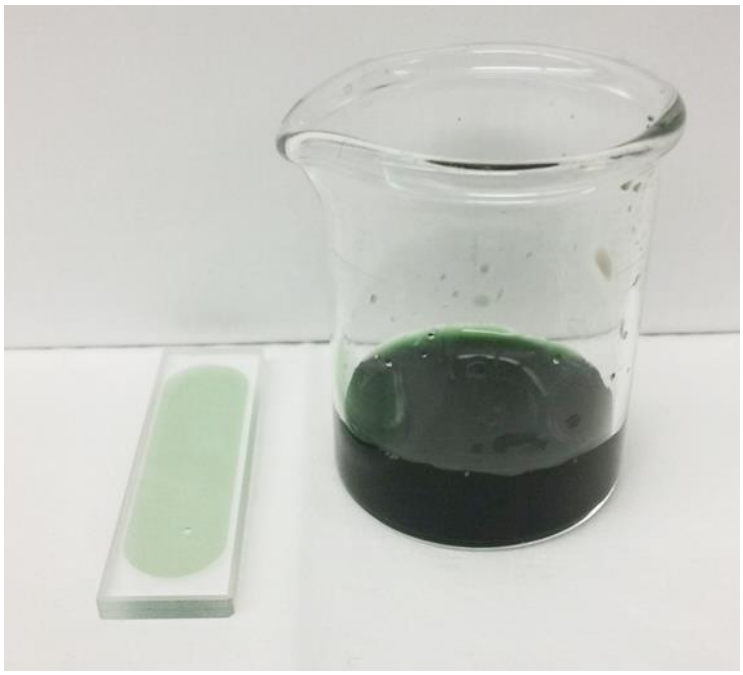

Fig. G3. Heterotrimeric mixture of all three color additives in ethanol solvent, including FD&C Blue No. 1, FD&C Yellow No. 5, and FD&C Red No. 40 (Acid Blue 9—Tartrazine—Allura Red).

The heterotrimeric mixture provokes an intriguing observation. Despite the subtractive method of color mixing indicating that molar equivalencies of the primary colors should yield a dull brown or black hue upon mixing [11], this mixture appears dark green. In order to clarify the interesting visual effects implied in Figure G3, an adequate basis set and functional equipped to handle the bulky water-soluble sulfonated salt groups inherent in the structure of each of the FD&C dye molecules shown would be necessary for theoretical analysis in a future computational study.

References

[1] U. S. F. a. D. Administration. (2015, November 7, 2018). *Color Additive Status List* [Online]. Available: https://www.fda.gov/ForIndustry/ColorAdditives/ColorAdditiveInventories/ucm106626.htm.

[2] J. N. B. A. L. L. C. J. Bailey. (2003, November 7, 2018). *Color Additives: FDA's Regulatory Process and Historical Perspectives*.

[3] J. F. Senackerib, "Color Additives for foods, drugs, and cosmetics," in *Colorants for Non-Textile Applications*, A. T. P. H.S. Freeman, Ed. 1 ed. Amsterdam: Elsevier, 2000, pp. 131-187.

[4] D. Marmion, "Colorants for Foods, Drugs, and Cosmetics," in *Kirk-Othmer Chemical Technology of Cosmetics*, A. Seidel, Ed. Hoboken: Wiley, 2013, pp. 501-547.

[5] M. M. Reiger, "Cosmetics," in *Kirk-Othmer Chemical Technology of Cosmetics*, A. Seidel, Ed. Hoboken: Wiley, 2013, pp. 1-48.

[6] E. W. Flick, *Cosmetic and Toiletry Formulations*, 2nd ed. Norwich: Noyes, 2001, p. 378.

[7] E. W. Flick, *Cosmetic and Toiletry Formulations*, 2nd ed. Park Ridge: Noyes, 1989, p. 971.

[8] M. V. D. Michalun, Joseph, *Milady Skin Care and Cosmetic Ingredients Dictionary*, 4th ed. Clifton Park: Cengage Learning, 2015, p. 339.

[9] S. M. G. Ming Shin Neo, Tahir Mehmood Khan, Manish Gupta, "Quantification of Ethanol Content in Traditional Herbal Cough Syrups," *Pharmacogn. J.*, vol. 9, no. 6, pp. 821-827, 2017.

[10] R. U. P. E. W. J. A. R. D. Howes, "Fate of Ethanol Topically Applied To Skin," *Food Chem Toxicol*, vol. 39, no. 2, pp. 169-174, 2001.

[11] R. S. Berns, "Producing Color," in *Billmeyer and Saltzman's Principles of Color Technology* 3rd ed.: Wiley, 2000, pp. 149-197.

Appendix H

Brilliant Cresyl Blue Structure 1 and 2 Monomer and Dimer Geometry Conformations Optimized using DFT with Implicit or Explicit Solvation Effects in Five Solvents

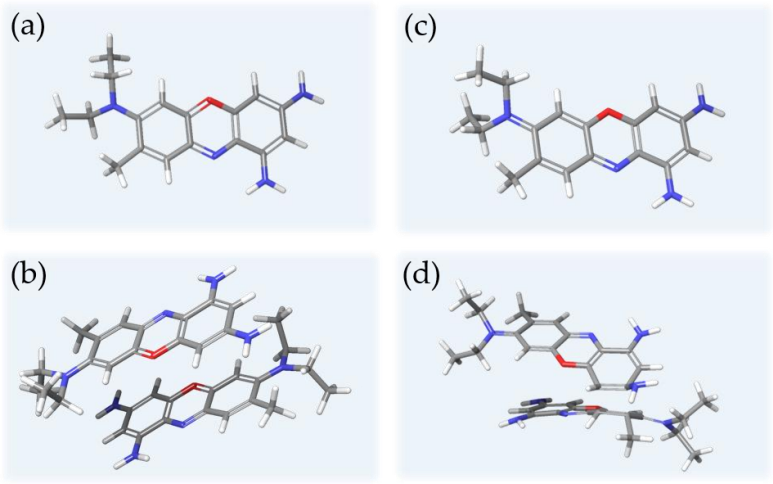

Fig. H1. Geometry conformations based on Poisson-Boltzmann Finite (PBF) elements model of implicit solvation interaction of water molecules with (a) BCB BB monomer, (b) BCB BB dimer, (c) BCB C monomer, and (d) BCB C dimer.

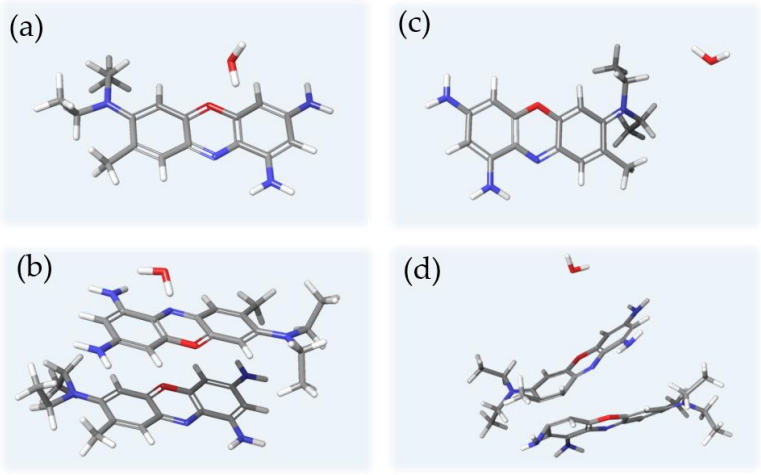

Fig. H2. Geometry conformations based on both Poisson-Boltzmann Finite (PBF) elements model and explicit solvation interaction of water molecules with (a) BCB BB monomer, (b) BCB BB dimer, (c) BCB C monomer, and (d) BCB C dimer with one water molecule

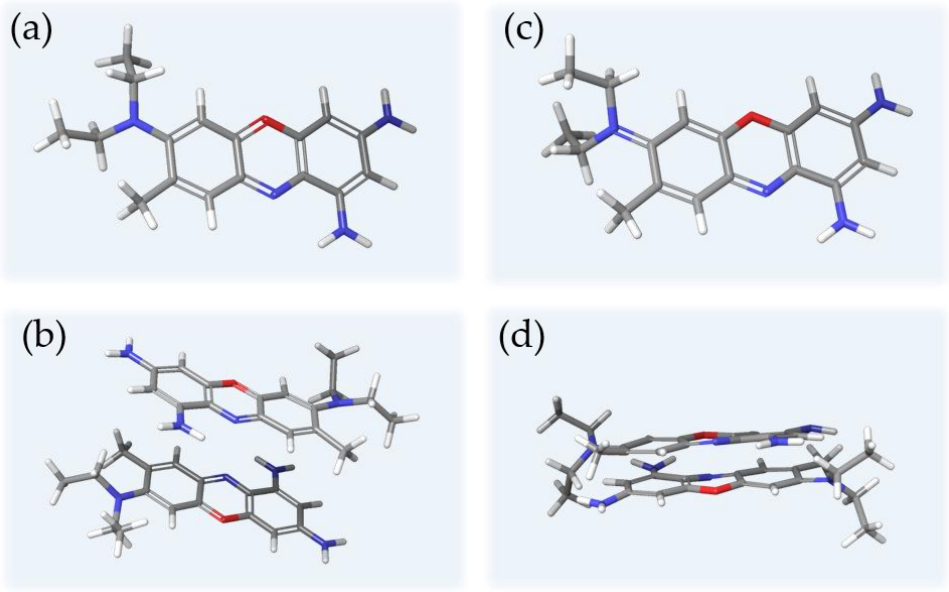

Fig. H3. Geometry conformations based on Poisson-Boltzmann Finite (PBF) elements model of implicit solvation interaction of ethanol molecules with (a) BCB BB monomer, (b) BCB BB dimer, (c) BCB C monomer, and (d) BCB C dimer.

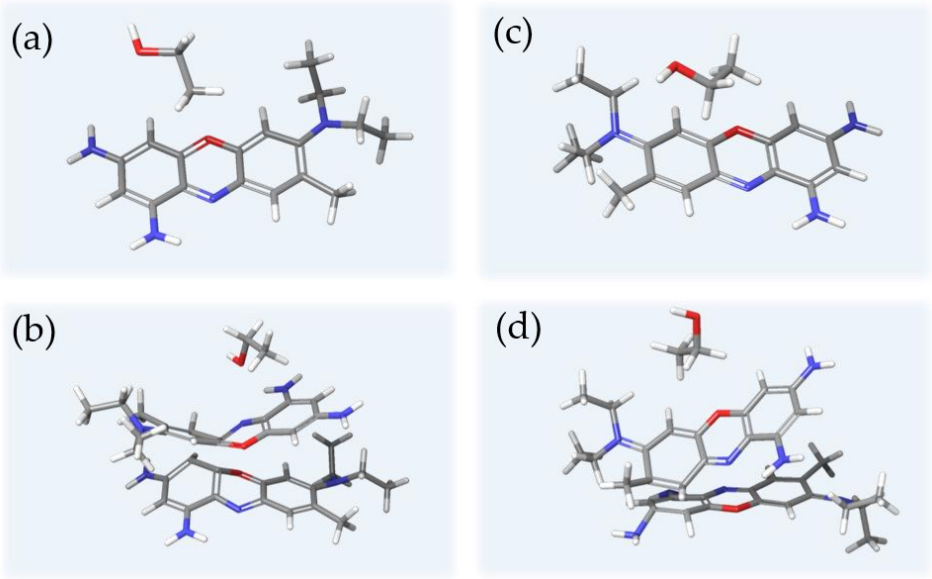

Fig. H4. Geometry conformations based on both Poisson-Boltzmann Finite (PBF) elements model and explicit solvation interaction of one ethanol molecule with (a) BCB BB monomer, (b) BCB BB dimer, (c) BCB C monomer, and (d) BCB C dimer.

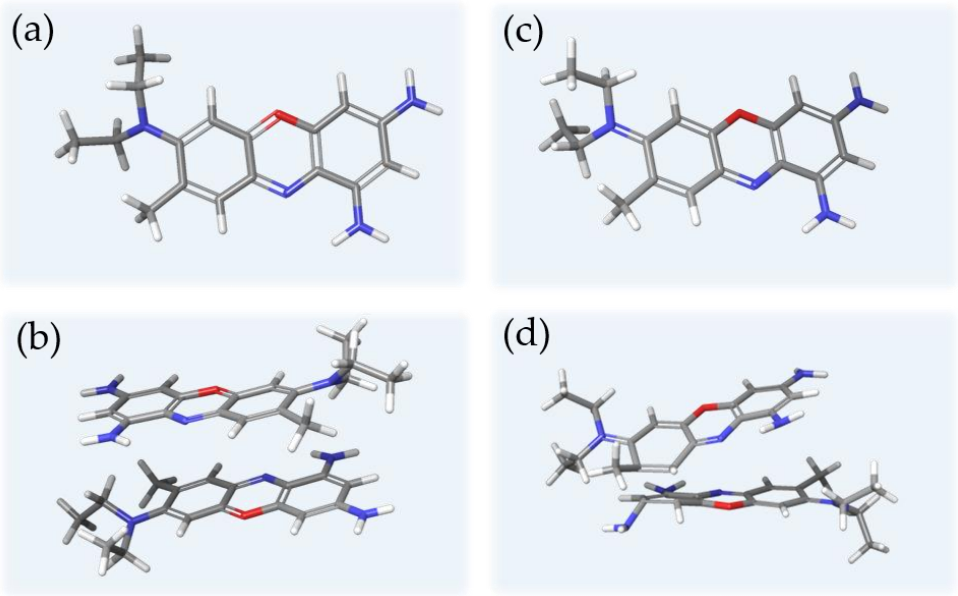

Fig. H5. Geometry conformations based on Poisson-Boltzmann Finite (PBF) elements model of implicit solvation interaction of [BMIM]Cl ionic liquid molecules with (a) BCB BB monomer, (b) BCB BB dimer, (c) BCB C monomer, and (d) BCB C dimer.

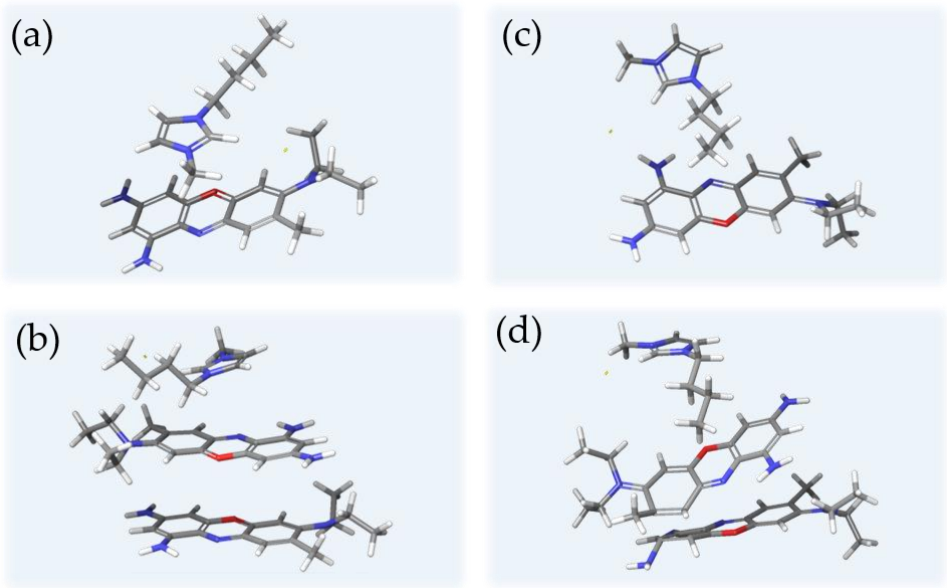

Fig. H6. Geometry conformations based on both Poisson-Boltzmann Finite (PBF) elements model and explicit solvation interaction of one set of [BMIM]Cl ionic liquid molecules with (a) BCB BB monomer, (b) BCB BB dimer, (c) BCB C monomer, and (d) BCB C dimer.

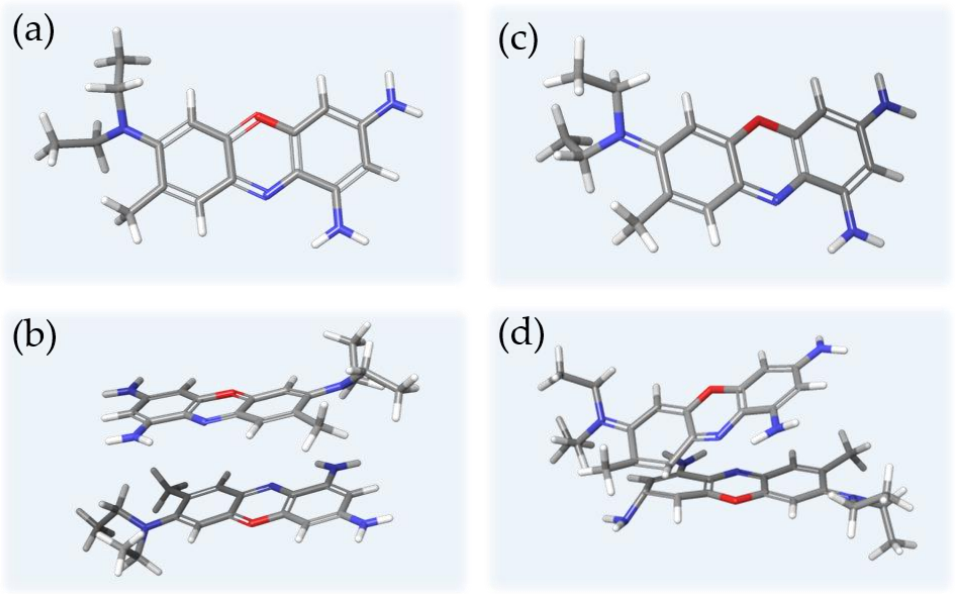

Fig. H7. Geometry conformations based on Poisson-Boltzmann Finite (PBF) elements model of implicit solvation interaction of $[BMIM]BF_4$ ionic liquid molecules with (a) BCB BB monomer, (b) BCB BB dimer, (c) BCB C monomer, and (d) BCB C dimer.

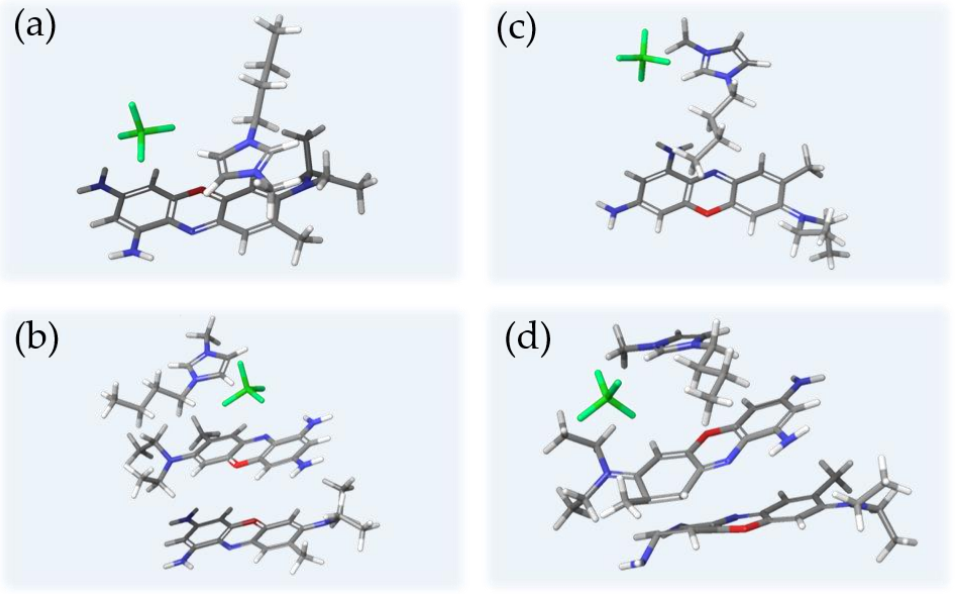

Fig. H8. Geometry conformations based on both Poisson-Boltzmann Finite (PBF) elements model and explicit solvation interaction of one set of $[BMIM]BF_4$ ionic liquid molecules with (a) BCB BB monomer, (b) BCB BB dimer, (c) BCB C monomer, and (d) BCB C dimer.

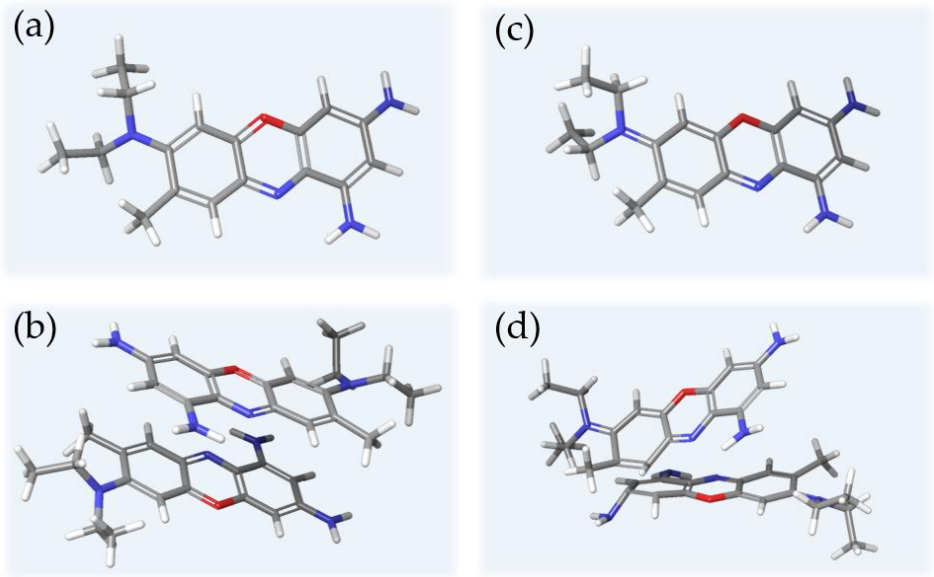

Fig. H9. Geometry conformations based on Poisson-Boltzmann Finite (PBF) elements model of implicit solvation interaction of [EMIM]OAc ionic liquid molecules with (a) BCB BB monomer, (b) BCB BB dimer, (c) BCB C monomer, and (d) BCB C dimer.

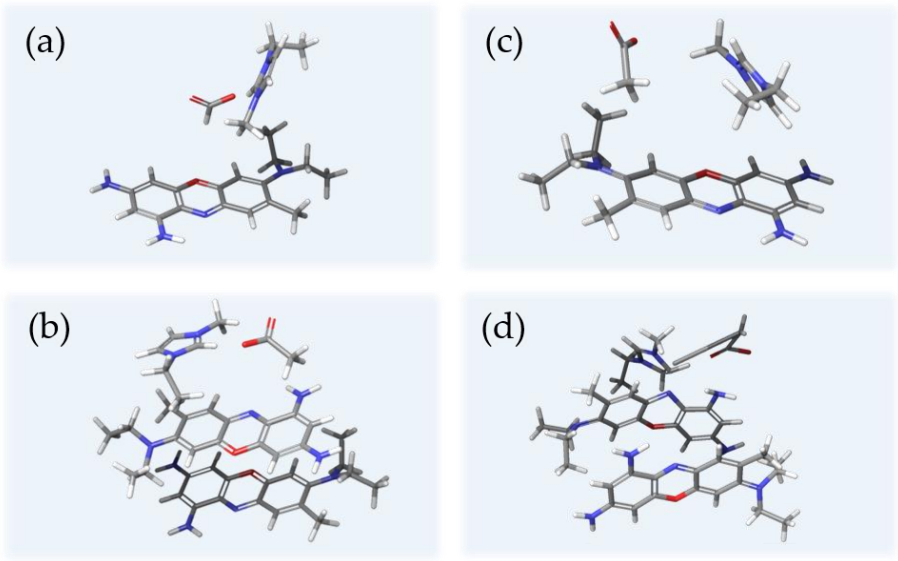

Fig. H10. Geometry conformations based on both Poisson-Boltzmann Finite (PBF) elements model and explicit solvation interaction of one set of [EMIM]OAc ionic liquid molecules with (a) BCB BB monomer, (b) BCB BB dimer, (c) BCB C monomer, and (d) BCB C dimer.

Appendix I

Color Wheel[29] Used to Compare Experimental and Theoretical Maximum Absorbance Spectral Peak Responsivity (λ_{max}) Data

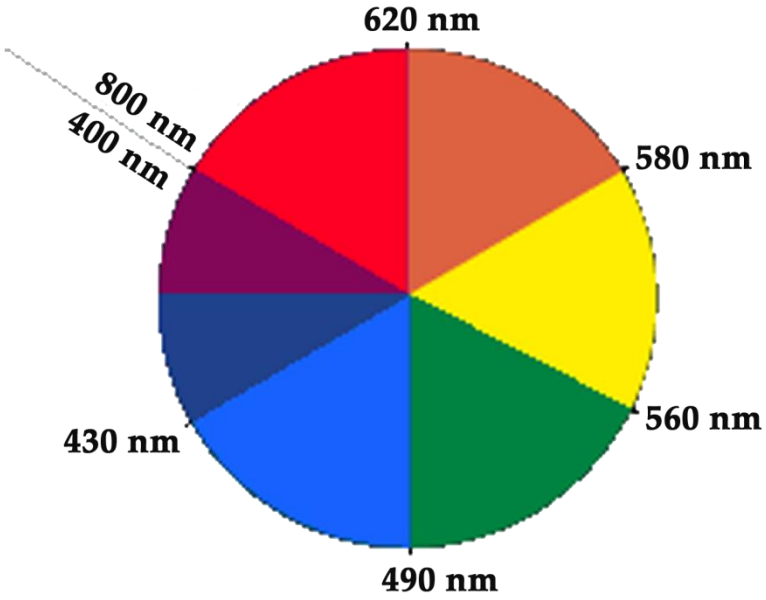

Fig. I1. [1] Color Wheel used to compare experimental and theoretical maximum absorbance spectral peak responsivity (λ_{max}) data.

[29] Adapted from [1] W. Reusch. (2013, May 27, 2019). *Visible and Ultraviolet Spectroscopy* [Online]. Available: https://www2.chemistry.msu.edu/faculty/reusch/virttxtjml/spectrpy/uv-vis/spectrum.htm.

References

[1] W. Reusch. (2013, May 27, 2019). *Visible and Ultraviolet Spectroscopy* [Online]. Available: https://www2.chemistry.msu.edu/faculty/reusch/virttxtjml/spectrpy/uv-vis/spectrum.htm.